ABSTRACT

Title of Document: TOPOGRAPHIC SIGNATURES IN THE HIMALAYA: A GEOSPATIAL SURVEY OF THE INTERACTION BETWEEN TECTONICS AND EROSION IN THE MODI KHOLA VALLEY, CENTRAL NEPAL

Lisa S. Walsh, M.S., 2009

Directed By: Assistant Professor Aaron Martin, Department of Geology

Spurred by the recognition that lithologic resistivity to erosion influences the steepness of terrain, the purpose of this study is to enhance our understanding of feedbacks between erosion and tectonics in the Himalaya. Using spatial statistics, within a Geographic Information Systems (GIS) framework, this study extracts steepness and curvature values from the terrain to identify the unique spatial signature of lithologic units in the Annapurna Range. The spatial relationship of faults and significant changes in river steepness (k_{sn}) and concavity (θ) are examined in this project using high resolution digital elevation models (DEMs), derived from a variety of interpolation methods. Through these quantifications, I explore the possibility of a new model for tectonic activity in central Nepal, in an effort to improve our understanding of how surface processes sculpt the landscape.

TOPOGRAPHIC SIGNATURES IN THE HIMALAYA: A GEOSPATIAL SURVEY OF THE INTERACTION BETWEEN TECTONICS AND EROSION IN THE MODI KHOLA VALLEY, CENTRAL NEPAL

By

Lisa S. Walsh

Thesis submitted to the Faculty of the Graduate School of the
University of Maryland, College Park, in partial fulfillment
of the requirements for the degree of
Master of Science
2009

Advisory Committee:
Assistant Professor Aaron J. Martin, Chair
Assistant Professor Saswata Hier-Majumder
Associate Professor Karen L. Prestegaard
Assistant Professor Naijun Zhou

Dedication

To Ben Walsh, my husband,

for exploring life and the world's landscapes with me

and continuously supporting my research.

Acknowledgements

Knowledge in science is attained by exploring unanswered questions and eliminating unreasonable results. The wisdom and dedication of several people fueled the completion of this thesis.

My advisor, Aaron Martin, initiated several insightful discussions and provided an ideal environment where I could finally synthesize geology and geographic information systems (GIS). I greatly appreciate his patience and unprecedented dedication to our research. Tank Ojha supplied the digitized contour lines I used as the main data source in this project and taught me the basics of contour line error correction methods used in GIS. Tank Ojha's excitement and dedication to producing digital data for Nepal was contagious and enhanced my inspiration for this project. I also thank workers in Nepal who initially digitized the contour lines from the topographic maps I used in this project. Ofori Pearson provided us with an alternative dataset for the Modi Khola valley, which became helpful for assessing the uncertainty of the dataset and examining land cover change. This work would not have been possible without Tom Fedenczuk, who I met at the ExxonMobil Student Education Program at the SEG, and Karl Schleicher, my father, who created high quality digital interpolations of the elevation data. Bodo Bookhagen kindly provided us with the TRMM precipitation data implemented in this project.

I appreciate the time and dedication put forth by the members of my committee. Saswata Hier-Majumder introduced the diffusion model to me and helped me devise a series of equations to model erosion of lithologies in the Modi Khola valley. This model, which began as a class project, inspired me and initiated the idea

of this project. Naijun Zhou, my GIS professor, offered the essential GIS perspective needed to bolster my project. Naijun Zhou advanced my understanding of problems with geographic data, taught me the basics of GIS, and emphasized the importance of scale in geographic data. I greatly appreciate the time Naijun Zhou has spent helping me with my research, even though I am not part of the geography department. Karen Prestegaard offered her expertise in river morphology, and invoked several interesting questions at grad talks which drove important aspects of my research.

Nadine McQuarrie's GSA short course notes greatly aided in my understanding of the ArcGIS stream profiler tool I used to extract k_{sn} and θ values. Bruce Hart, Kurt Marfurt, Chuck Blumentritt, and Karl Schleicher aided greatly in my understanding of curvature calculations and applications. The curvature program that was used to derive the curvature grids in this analysis was provided by Bruce Hart. Josh Roering provided important information about his GIS data of the Oregon Coast Range, allowing me to compare the results from his research in Oregon to our data in the Modi Khola valley. Kate Burgy allowed me to virtually visit and visualize the Modi Khola valley through georectification of her field photographs. Questions and advice from Laurent Montesi significantly improved my project and continuously stimulated my thinking. I also thank all members of the Tectonics Reading Group who provided insight to my research and enlightening discussions of scientific papers.

I am grateful to all graduate students who make the University of Maryland a good place to investigate the geosciences. I thank the geology department for funding my research with a teaching assistantship, eliminating the difficult task of balancing an outside job and research. I also recognize our departmental secretaries Sandy

Romeo, Dorothy Brown, Jeanne Martin, and Wafaa Von Blon for assisting me with my unending questions about paperwork, problems with copy machines, and scheduling. I thank John Merck, Bill McDonough, and Aaron Martin for their helpful discussions concerning teaching philosophy and also my undergraduate advisor, Bill Miller, for introducing me to geologic research at UNC Asheville.

I deeply appreciate the love and support my family has provided me throughout my entire education. I thank my Mom, Kay Schleicher, and my Dad, Karl Schleicher, for always encouraging me to pursue my interests. I am fortunate to have experienced camping and hiking trips as a kid, which drove my fascination with the environment and ultimately my decision to study geology. I will never forget canoe trips to collect petrified wood on the Brazos River, in Texas, with the Houston Gem and Mineral Society. These adventures introduced me to geology, and though I pursued other studies for several years, eventually brought me back to the world of Earth Science. I am also grateful to my Aunt, Mimi Schleicher, for discussing my research and for her helpful advice during this process. Jennifer Schleicher, my sister, offered excellent artistic assistance with my understanding of digital image creation and provided a helpful critique of a poster I presented, from which several figures in this paper are derived. My husband, Ben Walsh, inexhaustibly supported me during this process by being a constant sounding board, keeping me sane, and helping me refine my thesis by several edits and grammatical corrections. His encouragement and support is what allowed me to complete this thesis.

Lisa S. Walsh

July 13, 2009

Table of Contents

Thesis Chapter Guide

Chapter 1: Introduction
The first chapter introduces the research project and describes its place in relation to other studies that use topographic data to examine feedbacks between tectonics and erosion.

Chapter 2: Topographic signatures in the Modi Khola valley of central Nepal reveal spatial changes in lithology, erosion, and rock uplift
The second chapter is the core of the thesis and is written as a standalone document for submission to a professional journal. All subsequent chapters offer additional information that elaborates on the information in this chapter.

Chapter 3: Data acquisition
The third chapter illustrates methods for producing a high resolution DEM from contour lines with the aid of a variety of interpolation methods.

Chapter 4: Uncertainty in geographical information
The fourth chapter describes the selection of a DEM to use for this analysis based on elevation uncertainty determined by RMSE and the reduction of flat irregular terraces.

Chapter 5: DEM derivatives
The fifth chapter explains how slope and curvature are mathematically derived from a DEM.

Chapter 6: Topographic signatures of Modi Khola lithologies
The sixth chapter describes the application of spatial statistics to quantitatively characterize different rock types by values of slope and curvature.

Chapter 7: River steepness analysis
The seventh chapter discusses the background of tectonic geomorphology, parameters and methods implemented in the river profile analysis, comparison of river analysis results with slope and curvature grids, and uncertainty of k_{sn} and θ values.

Chapter 8: Discussion
The eighth chapter summarizes all the information acquired in this analysis and reveals the main conclusions of this project.

List of Tables

List of Figures

Chapter 1: Introduction

1.1 Background information

Geologic studies within the last decade offer a more comprehensive understanding of lithology, bedrock structure, and climate in the Himalaya. These recent improvements present the opportunity to decipher how complex interactions of tectonics, climate, and erosion sculpt mountainous terrains. Incorporating geologic mapping and topographic data into a Geographic Information System (GIS) framework offers the chance to examine aspects of the landscape quantitatively.

In the traditional tectonic model for the Himalaya, fault activity began in the north then progressed south over time towards current deformation at the Main Frontal thrust (MFT) (Hodges, 2000). The mean convergence rate across central Nepal is approximately 19 $\pm$ 1.5 mm/yr, according to global positioning system (GPS) measurements (Bettinelli et al., 2006). The Siwalik Hills of southern Nepal, where the MFT reaches the surface (Figure 1) are commonly estimated to accommodate most of the convergence in central Nepal (Pandey et al., 1995; Lave and Avouac, 2000; Wobus et al., 2005; Hodges et al., 2004).

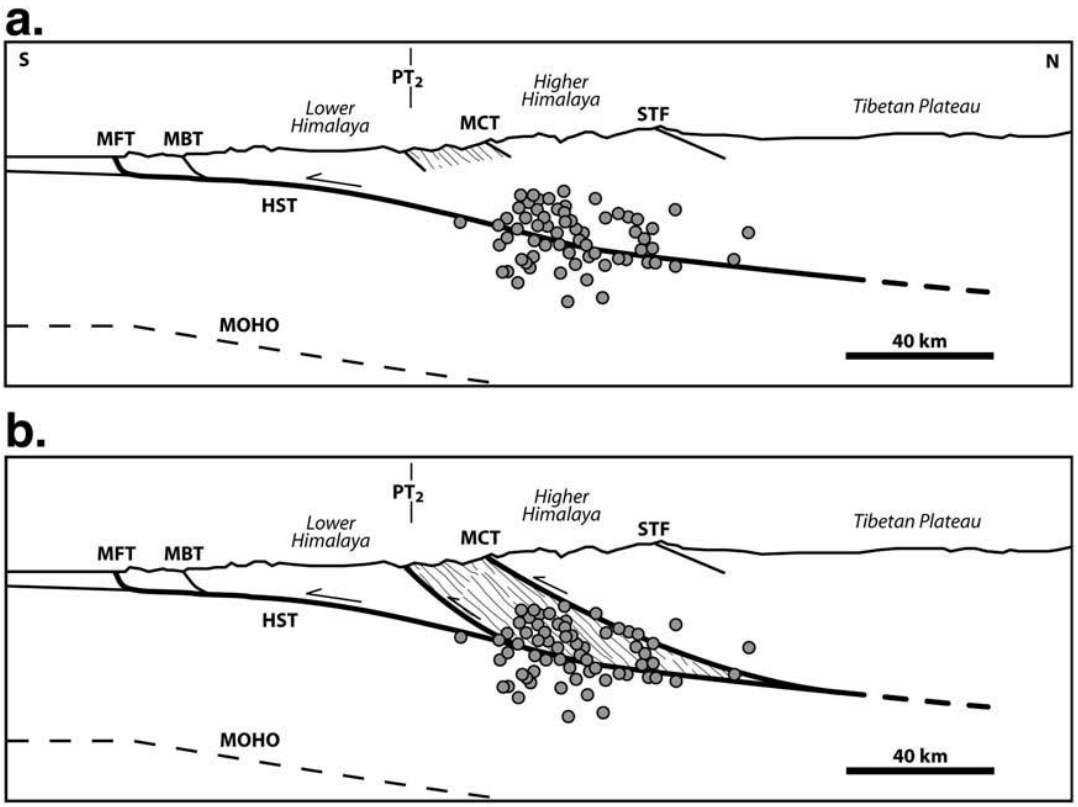

Figure 1: Two tectonic models of the Himalaya
Models of Holocene thrust activity for the Himalaya. Earthquakes are shown on each model with gray circles. Major faults: HST - Himalayan Sole thrust, MFT - Main Frontal thrust, MBT - Main Boundary thrust, MCT - Main Central thrust, and STF - South Tibetan fault. The Lesser Himalayan duplex is bound to the north by the MCT and shown by the patterned zone on each model above. The active fault system is shown in bold for each model. According to Hodges et al. (2004), both models may be correct at different times during the Quaternary period. (a) Evolutionary 'passive' model which Holocene convergence is accommodated predominately at the MFT at the front of the range. Uplift beneath the central Himalaya is entirely related to the movement of hanging wall rocks over a ramp in the HST at depth. Between seismic events, when the HST is locked, uplift is thought to be related to strain accumulation over the ramp. (b) Alternative 'active' model: uplift is related to surface breaking faults near PT_2. Reactivated segments of the MCT and a new and reactivated structure of the Lesser Himalayan duplex accommodate recent rock uplift in this model. (Figure from Hodges et al., 2004)

Seeber and Gornitz (1983) were the first to utilize discontinuities in river profiles to recognize a major tectonic boundary between the Higher and Lower Himalaya (Figure 2). Trans-Himalayan river profiles in the central Himalaya exhibit low gradients in the Tibetan Plateau, steep gradients traversing the High Himalaya, and low gradients in the Lesser Himalaya. Several researchers delineated a sharp morphologic break in the topography of the central Nepalese Himalaya, referred to as physiographic transition 2 (PT_2) (Lave and Avouac, 2000; Wobus et al., 2005; Hodges et al., 2004; Seeber and Gornitz, 1983; Burbank et al., 2003; Burbank et al., 2005; Wobus et al., 2003; Wobus et al., 2006a; Wobus et al., 2006b). Cosmogenic radionuclides and $^{40}Ar/^{39}Ar$ ages from detrital muscovites indicate a transition in bedrock mineral cooling ages, suggesting a change in rock uplift at PT_2 (Figure 3) (Wobus et al., 2003; Wobus et al., 2005; Wobus et al., 2006b). These discoveries introduce a new tectonic model for the spatial distribution of thrust activity in central Nepal. This alternative tectonic model incorporates active surface breaking faults at reactivated segments of the Main Central thrust (MCT) near PT_2 (Figure 1) (Hodges et al., 2004).

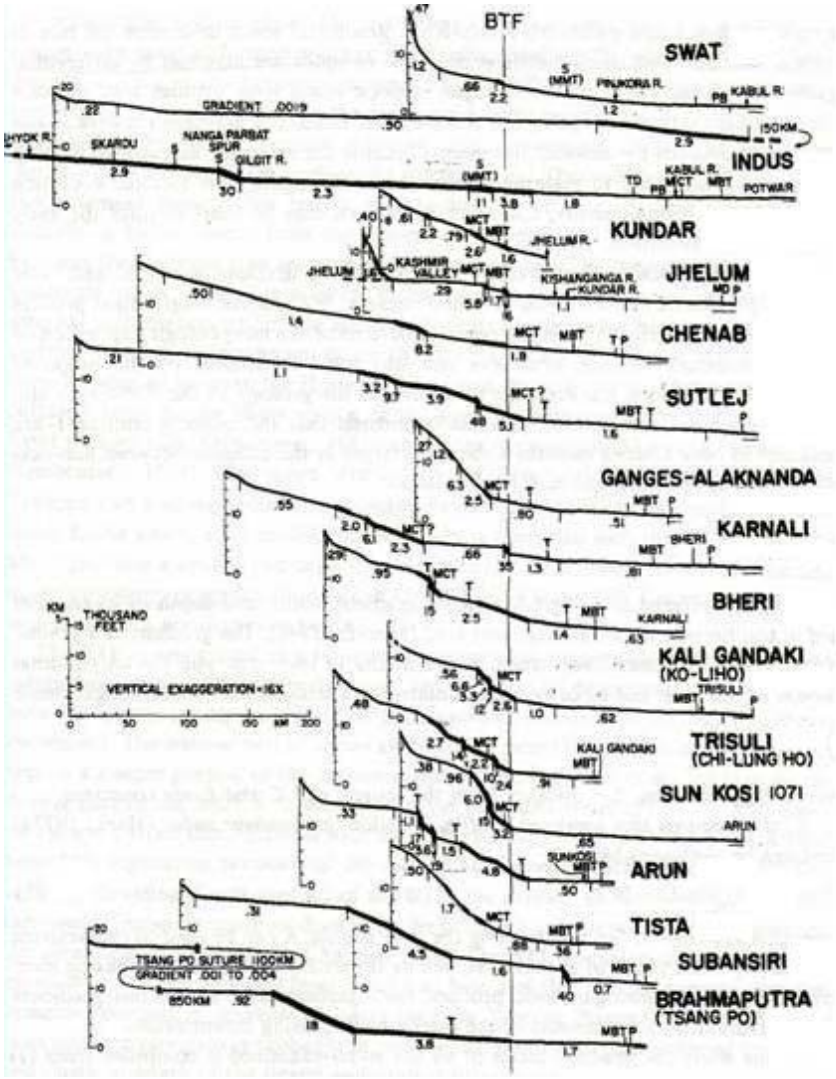

Figure 2: Longitudinal profiles of major Himalayan rivers
Longitudinal profiles of most of the major Himalayan rivers arranged from west (on top) to east (on bottom). Steep sections of each river profile are shown by wider bands. S - suture zone, T - thrust, and P - entrance into Indo-Gangetic plains, MMT - Main Mantle thrust, MBT - Main Basal thrust, and MCT - Main Central thrust. The vertical line is the BTF (Basement Thrust Front) as defined by the seismic belt and the topographic break. (Figure from Seeber and Gornitz, 1981)

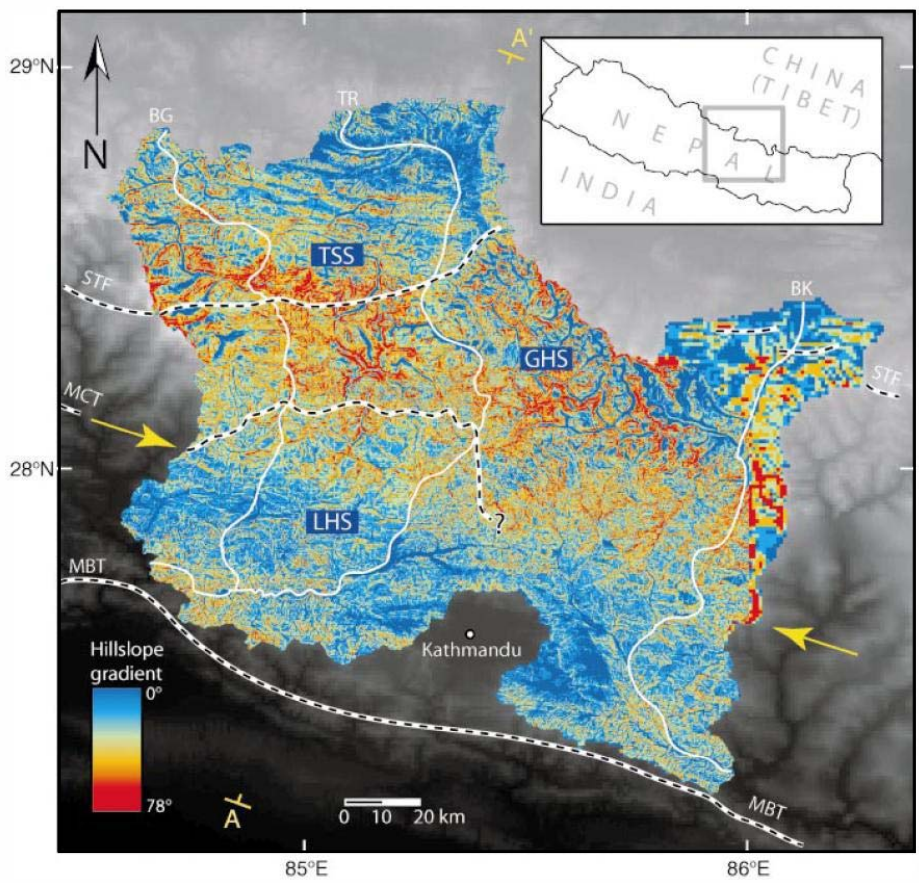

Figure 3: PT_2 in slope map from Wobus et al. (2003) study
Site location map (inset) and slope map for topography studied by Wobus et al. (2003), which is located west of the Modi Khola valley investigated in this thesis. Physiographic transition, PT_2, is prominent break in hillslope gradient shown by change of colors on the slope map and by the yellow arrows. Structural and lithotectonic units: TSS—Tibetan Sedimentary Sequence; GHS—Greater Himalayan Sequence; LHS—Lesser Himalayan Sequence. Rivers: BG—Burhi Gandaki; TR—Trisuli; BK—Bhote Kosi. (Figure from Wobus et al., 2003)

1.2 Motivation for this research

Spatial statistics and GIS offer the opportunity to measure changes in slope, curvature, and river steepness in central Nepal over larger spatial scales and at quicker rates than traditional methods of topographic analysis. This analysis focuses on developing a high resolution digital elevation model (DEM) and robust spatial statistics to characterize lithologies, regions around faults, and steepness transitions in the topography. This investigation examines the topographic changes in the Modi Khola valley in the Annapurna range of central Nepal (Figure 4). Intense erosion generated by an average rainfall of 3 m/yr and several mapped faults make the Modi Khola valley an interesting location to study topography. Martin et al. (2009) created a very detalied geologic map of the Modi Khola valley, which allows me to compare changes in river steepness with the location of lithologic contacts and faults at a smaller spatial scale than previously examined in central Nepal. This interdisciplinary project assimilates geologic and geospatial data, presenting new methods for evaluating the interaction of tectonics and erosion. Through the use of a high resolution topographic dataset, detailed aspects of the terrain will be illuminated for the first time. The procedures established in this analysis are broadly applicable to deciphering landscape dynamics worldwide, advancing our understanding of mountain belt evolution.

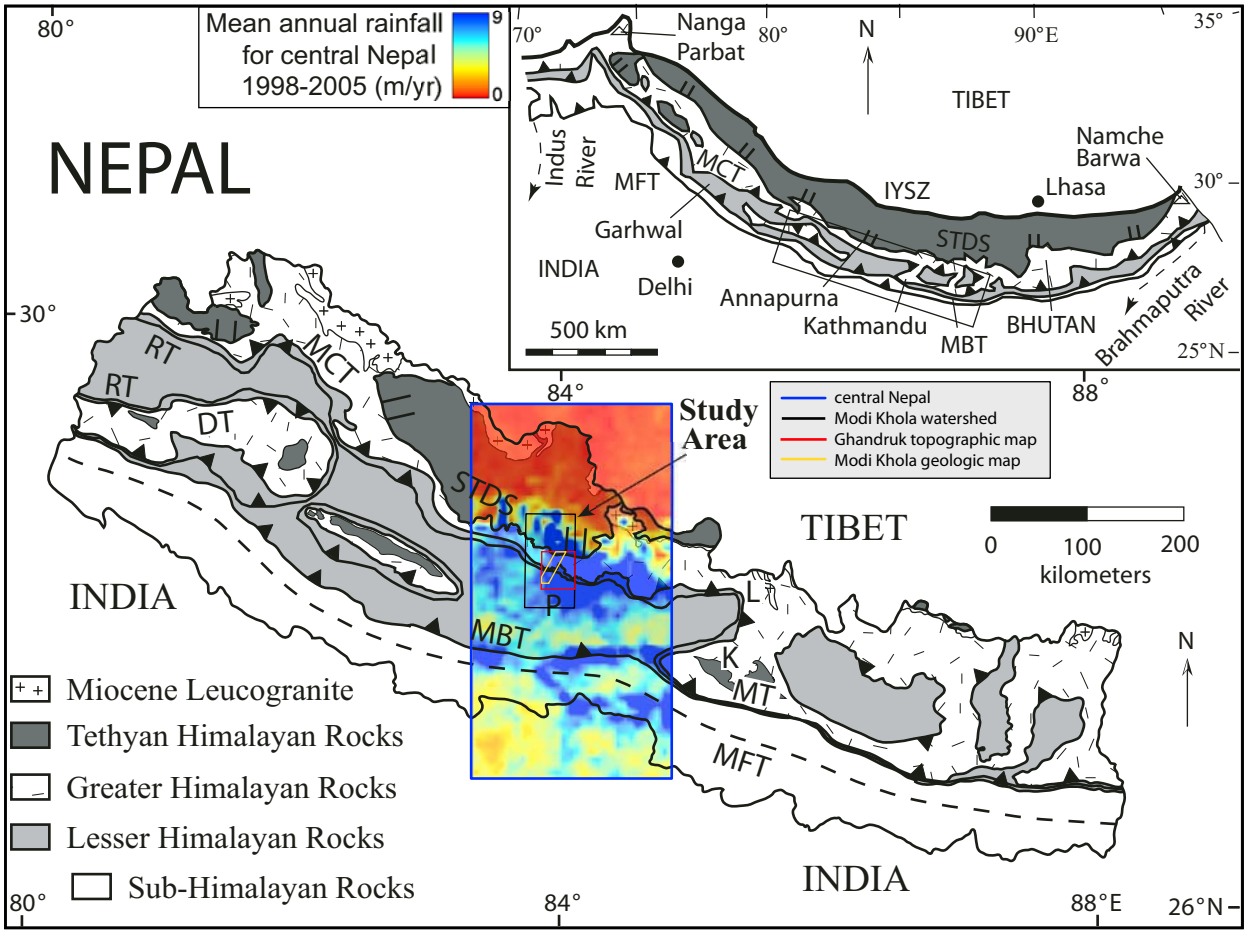

Figure 1: Location of study site with precipitation values
Location of Modi Khola valley is shown by the yellow polygon. Generalized geologic map of Nepal modified from Amatya and Jnawali (1994) and was extracted from Figure 1 in Martin et al. (2005). The precipitation data are from the Tropical Rainfall Measurement Mission (TRMM), which has a spatial resolution of ~5 x 5 km for the Himalaya (Bookhagen 2006). Bodo Bookhagen kindly provided the TRMM precipitation data shown in this figure.

1.3 Geologic Setting

The diverse range of steepness across the central Nepalese Himalaya makes it a spectacular mountain range for topographic research. Recent field mapping by Martin et al. (2005; 2009) provides a more detailed geologic map of the Modi Khola valley, allowing this project to incorporate new and more detailed lithologic mapping into a geospatial analysis (Figure 5).

This study focuses in the region around the MCT, where Greater Himalayan rocks are thrust on top of Lesser Himalayan rocks. The protolith boundary between Greater Himalayan and Lesser Himalayan rocks is visually indistinguishable in the field, and typically mapped using an approximation within the boundary of known Greater Himalayan (kyanite/sillimanite) gneiss and Lesser Himalayan schist (Martin et al., 2005). Field and microscopic observations combined with whole rock Nd isotopic and U-Pb detrital zircon data by Martin et al. (2005) place the MCT 1 km south of the location it is normally mapped on the basis of lithology (Figure 6). These new data allow mapping of the MCT with spatial accuracy previously unattainable in the Annapurna Range and is used as the basis for the location of the MCT in this project.

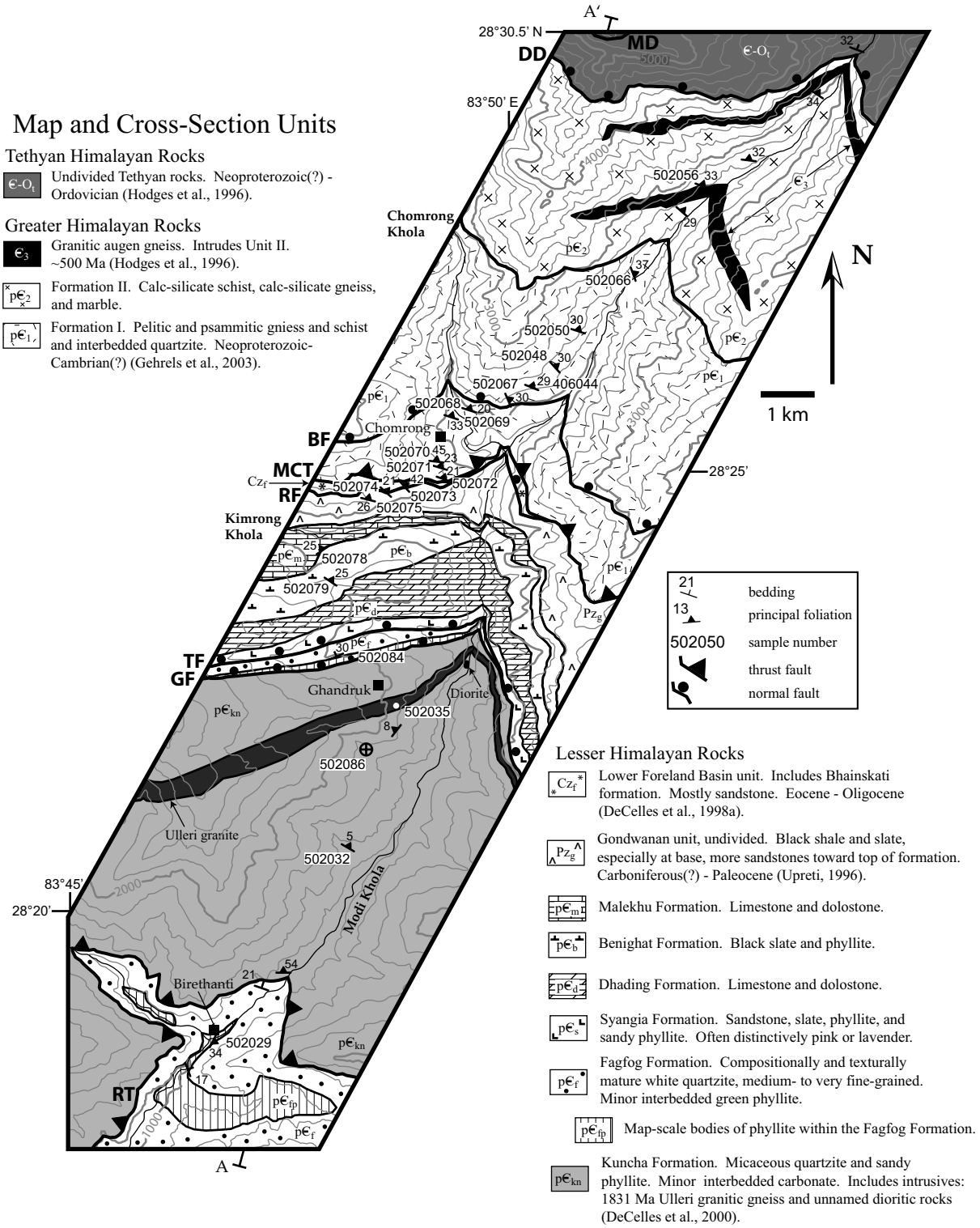

Figure 5: Geologic map of Modi Khola valley
Geologic Map of the Modi Khola (river) valley by Martin et al. (2009). MD—Macchapucchare Detachment, DD—Deorali Detachment, FRM II - FRM I— Formation II - Formation I lithologic contact, BF— Bhanuwa Fault, MCT—Main Central thrust, RF—Romi Fault, TF—Tobro Fault, GT—Ghandruk thrust, RT—Ramgarh thrust. Contour interval is 200 meters.

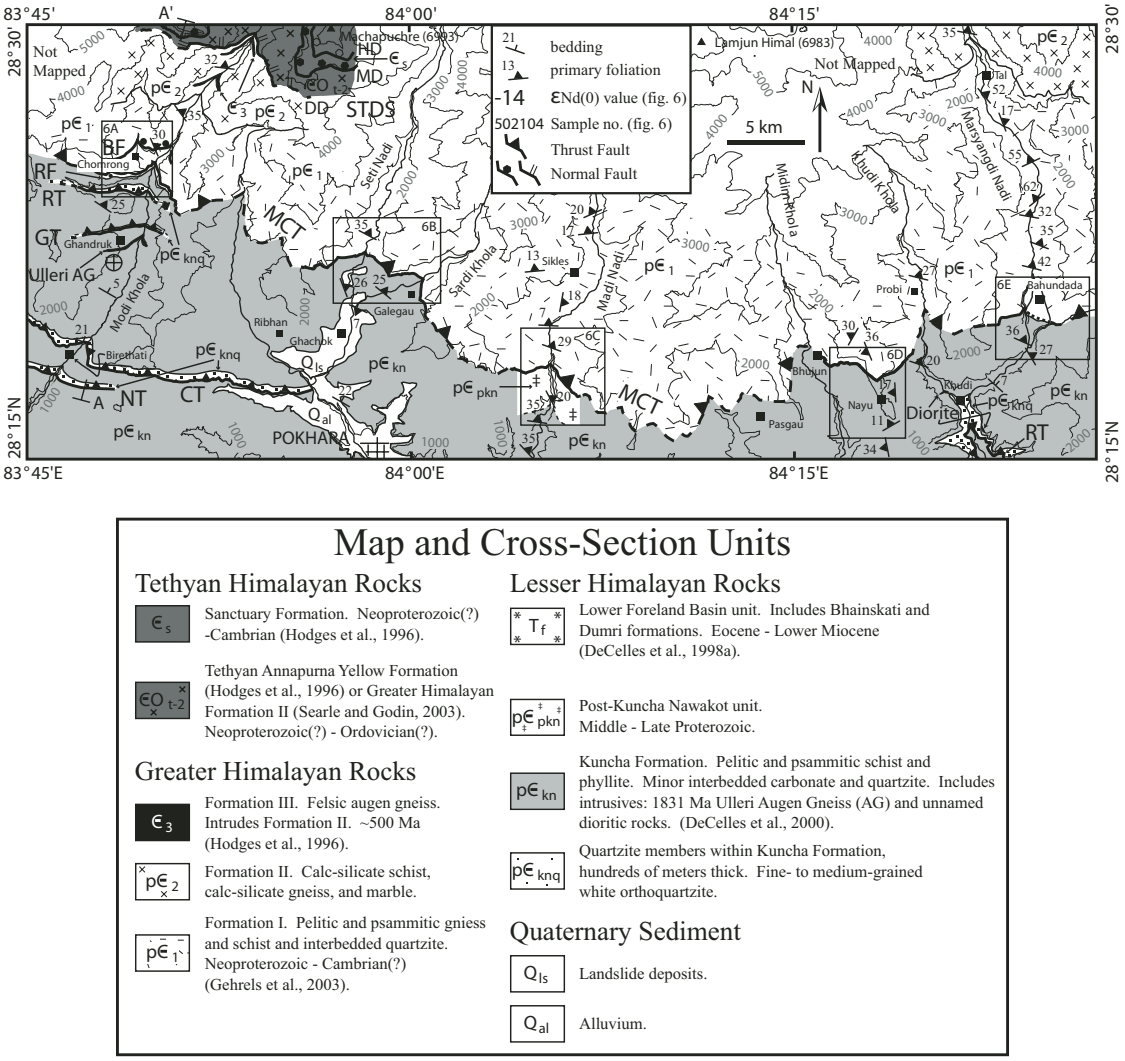

Map and Cross-Section Units

Tethyan Himalayan Rocks

ϵ_s — Sanctuary Formation. Neoproterozoic(?) -Cambrian (Hodges et al., 1996).

ϵO_{t-2} — Tethyan Annapurna Yellow Formation (Hodges et al., 1996) or Greater Himalayan Formation II (Searle and Godin, 2003). Neoproterozoic(?) - Ordovician(?).

Greater Himalayan Rocks

ϵ_3 — Formation III. Felsic augen gneiss. Intrudes Formation II. ~500 Ma (Hodges et al., 1996).

$p\epsilon_2$ — Formation II. Calc-silicate schist, calc-silicate gneiss, and marble.

$p\epsilon_1$ — Formation I. Pelitic and psammitic gniess and schist and interbedded quartzite. Neoproterozoic - Cambrian(?) (Gehrels et al., 2003).

Lesser Himalayan Rocks

T_f — Lower Foreland Basin unit. Includes Bhainskati and Dumri formations. Eocene - Lower Miocene (DeCelles et al., 1998a).

$p\epsilon_{pkn}$ — Post-Kuncha Nawakot unit. Middle - Late Proterozoic.

$p\epsilon_{kn}$ — Kuncha Formation. Pelitic and psammitic schist and phyllite. Minor interbedded carbonate and quartzite. Includes intrusives: 1831 Ma Ulleri Augen Gneiss (AG) and unnamed dioritic rocks. (DeCelles et al., 2000).

$p\epsilon_{knq}$ — Quartzite members within Kuncha Formation, hundreds of meters thick. Fine- to medium-grained white orthoquartzite.

Quaternary Sediment

Q_{ls} — Landslide deposits.

Q_{al} — Alluvium.

Figure 6: MCT in southern Annapurna Range

Geologic map of the southern Annapurna range from Martin et al., 2005. Main faults in the Modi Khola valley are shown including the Bhanuwa fault (BF), Chandrakot thrust (CT), Deorali detachment (DD), Ghandruk thrust (GT), Hiunchuli detachment (HD), Machhapuchhre detachment (MD), Nayapur thrust (NT), Romi fault (RF), Ramgarh thrust (RT), and South Tibetan Detachment System (STDS). Trace of the Main Central thrust (MCT) is shown across several valleys west of the Modi Khola, including the Seti Nadi, Madi Nadi, Midim Khola, and Marsyandi Nadi. Contours: 1000 m. (Figure from Martin et al., 2005.)

1.4 Aims of this study

1.4.1 Hypotheses

Hypothesis 1: Lithology and Topography

Values of steepness and curvature characterize and distinguish lithologic units in the Modi Khola valley of central Nepal.

Explanation: This hypothesis is based on the idea that each lithology exhibits a unique resistivity to erosion. The composition of each rock type determines its resistivity level, ultimately determining the level of steepness in the topography a lithology can withhold.

Hypothesis 2: Faults and Topography

Contacts between lithologies with different resistances to erosion can explain breaks in river steepness and concavity near the MCT in the Modi Khola valley of central Nepal.

Explanation: This hypothesis incorporates the notion that spatial changes in lithology impacts gradients in the topography, instead of rock uplift of the terrain caused by fault activity.

1.4.2 Tests of Hypotheses

Tests of Hypothesis 1: Lithology and Topography

Slope variability within a particular lithology was quantified using spatial statistics. Values of slope and curvature were measured at 25 x 25 m grid cells within the each lithologic unit. Probability density plots were created to quantify and illustrate

slope variability for each lithology. Slope vs. curvature plots were also utilized in the search for spatial signatures that characterize rock type. This process was executed for each lithology in the study site in order to characterize each lithologic unit by slope variation. If the characteristics of average slope variability allow different lithologies to be distinguished, then it will be inferred that lithology contributes to slope changes. If slope variability characteristics are indistinguishable, then other factors such as tectonic structure, hydrology, and climate may have a greater impact on the landscape architecture.

A river profile analysis will examine correlations between changes in river steepness and lithologic contacts in the Modi Khola valley (Wobus et al., 2006a; Wobus et al., 2006b; Martin et al., 2005). The river steepness indexes, k_{sn}, were calculated for the Modi Khola using the techniques described by Wobus et al. (2006a) and Whipple et al. (2007). The k_{sn} values were then examined to identify sharp topographic changes in the river profile, called knickpoints. If river knickpoints coincide with lithologic contacts then a causative relationship between the two can be inferred. If no correlation between river knickpoints and lithologic contacts is observed, then lithologic contacts may not play a significant role in the formation of river knickpoints in this area, suggesting other factors such as tectonics and structure may play a greater role in landscape evolution.

Tests of Hypothesis 2: Faults and Topography

Digital maps of slope, curvature, relief, and river steepness (k_{sn}) were created for the southern Annapurna Range between the Modi and Marsyandi rivers. The extent of this study site encompassed the trace of the MCT mapped by Martin et al. (2005) and detailed geologic maps located in the Modi Khola valley (Figure 5). If the area north of the MCT has an identifiable spatial signature of slope and curvature

values that are distinguishable from the area south of the MCT, then the hypothesis passes. If the areas north and south of the MCT do not have statistically different spatial signatures, then topography in this area may not be related to the location of the MCT. It is possible that normal faults or other faults in the area are more related to the most recent topographic signature. In this case, other faults and tectonic features in the area were examined to determine any relationship to the current landscape. The topography was sampled from north to south across the study site to search for distinct changes in slope or curvature. Then the proximity of these transition zones to mapped faults or lithologic contacts structures will be examined in detail.

A river profile analysis examined correlations between changes in river steepness and the MCT, or other mapped faults, in the Modi Khola valley. This process utilized the methods described by Wobus et al. (2006a) and Whipple et al. (2007). A high resolution DEM was used to search for changes in steepness and concavity in the study site. If river knickpoints coincide with the MCT and other mapped faults, then a relationship between river incision at knickpoints, faulting, and topographic uplift was inferred. If no correlation between river knickpoints and faults are inferred, then faults may not be contributing to the local relief. The influence of other factors such as precipitation, vegetation, land use, or other environmental conditions may play a larger role in river incision and knickpoint formation and were observed in closer detail.

Chapter 2: Geospatial investigation of the Modi Khola valley in central Nepal reveals spatial changes in lithology, erosion, and rock uplift

ABSTRACT

To investigate the relation of lithology and structures with changes in normalized river steepness and concavity, I compare high resolution digital topography with detailed geologic maps of the Modi Khola valley in central Nepal. The trace of the Bhanuwa fault, a large normal fault, persistently coincides with the steepest location on the river profile where k_{sn} reaches 884 $m^{0.9}$. Transitions in k_{sn} also occur at 1) the Romi fault, another normal fault, 2) within the Kuncha formation, 3) within Greater Himalayan rocks at the Formation I – Formation II boundary, and 4) between quartzite- and phyllite-rich parts of the Fagfog Formation. I assess mechanisms for k_{sn} transitions on the Modi Khola by examining the influence of precipitation variability, glacial and landslide dams, tributary junctions, changes in lithology, and rock uplift on the topography. Although changes in lithology and/or landslide dams potentially explain all major k_{sn} extrema and transitions, these changes in river steepness consistently occur at normal faults suggesting possible recent motion on some of them. In detail, the Main Central thrust appears not to be the location of a major steepness change. Correlations of k_{sn} with normal faults may exhibit an important topographic feedback initiated by interactions between tectonics and erosion in the Modi Khola valley.

Keywords: tectonic geomorphology, GIS, central Nepalese Himalaya, river steepness, concavity

2.1 Introduction

The interaction between tectonics and erosion sculpt the landscape, creating a complex expression scientists define as topography. The recent explosion of Geographic Information Systems (GIS) tools and digital data allow quantitative evaluations of the terrain, illuminating information about mountain belt evolution. Bedrock river profiles adjust rapidly to intense precipitation, glacial and landslide damming, rock resistance, and active rock uplift and reflect recent morphological changes on the Earth's surface (Whipple and Tucker, 1999; Keller, 2002; Whipple, 2004; Bookhagen and Burbank, 2006; VanLaningham et al., 2006; Korup and Montgomery, 2008). Two indices derived from river profiles, river steepness (k_{sn}) and concavity (θ), are helpful in examining the dynamic interactions between tectonics and erosion (Snyder et al., 2000; Kirby and Whipple, 2001; Kirby and Whipple, 2003; Wobus et al., 2003; Hodges et al., 2004; Whipple, 2004; Schoenbohm et al., 2009).

In central Nepal, river profile analyses by several research groups reveal a prominent morphologic break in the landscape south of the Main Central thrust (MCT), referred to as physiographic transition 2 (PT_2) (Seeber and Gornitz, 1983; Burbank et al., 2003; Wobus et al., 2003; Hodges et al., 2004; Wobus et al., 2005; Wobus et al., 2006a; Wobus et al., 2006b). These researchers infer rock uplift at PT_2, delineating a zone of active deformation at the base of the High Himalaya and propose a tectonic model for thrust activity in central Nepal that incorporates active surface breaking faults near the MCT and PT_2 (Hodges et al., 2004; Wobus et al., 2003; Wobus et al., 2006b). In the traditional model of Himalayan tectonics (Pandey

et al., 1995; Cattin and Avouac, 2000; Hodges, 2000; Lave and Avouac, 2000), the Main Frontal thrust (Figure 7, Nepal geologic map inset) accommodates approximately 19 ± 1.5 mm yr^{-1} (Bettinelli, 2006). The discovery of a distinct topographic break near the MCT spurred the development of alternative tectonic models designed to explain landscape morphology in central Nepal (Wobus et al., 2006b).

I examine correlations between river morphology, small scale faulting mechanisms, and lithologic contacts in the Modi Khola valley of central Nepal using detailed geologic maps (Martin et al., 2009) and a high resolution digital elevation model (DEM). Although active thrust faulting is one good explanation for river steepness changes near the MCT, the possibility that lithologic contacts change measurable aspects of the topography remains underexplored in the Himalaya. Contacts between lithologies with different resistances to erosion may explain breaks in river steepness and concavity near the MCT in the Modi Khola valley. The discovery of changes in river steepness only at lithologic contacts, with no repetitions or omissions of stratigraphy, might resolve steepness breaks in the topography without the need for active faults. Combinations of rock type change and normal fault activity might also explain topographic changes near the MCT.

In contrast to other research, my analyses reveal strong correlations between topographic changes and normal faults and identify locations on the Modi Khola where river steepness is dependent on lithologic composition. Detailed analysis of local geologic changes in the topography provides an avenue for understanding intricate relations between tectonics and erosion, enhancing our understanding of how

surface processes carve the landscape. A thorough examination of topography and detailed geologic maps is required to determine all the parameters needed to build realistic models of mountain belt evolution. My analyses suggest the structural geometry of normal faults may play a pivotal role in recent landscape processes occurring in the Himalaya.

2.2 Geologic setting

The diverse range of steepness and the presence of several mapped faults and ductile shear zones make the central Nepalese Himalaya a spectacular location for topographic research. I focus my study of the topography in the Modi Khola valley where large displacement 30° north-dipping thrust-sense and normal-sense faults and ductile shear zones dominate the landscape. In the Modi Khola valley, the slope of topography north of the Bhanuwa fault reaches near vertical and maintains slopes with a mean that is 11 degrees greater than terrain south of the Bhanuwa fault (Figure 7). Recent field mapping by Martin et al. (2009) allows incorporation of a more detailed lithologic map into a geospatial analysis (Figure 8, Figure 9). The Modi Khola valley centers on an exposed band of Tethyan Himalayan sedimentary rocks, Greater Himalayan metasedimentary rocks, and Lesser Himalayan metasedimentary rocks in the center of the Himalayan fold-thrust belt (Figure 7, upper left map inset).

The South Tibetan Detachment System, a series of north-dipping normal faults and ductile shear zones with cumulative slip of several tens of kilometers, bounds the structural top of the Greater Himalayan series (Burchfiel et al., 1992; Searle et al., 2003; Martin et al., 2005; Martin et al., 2007; Martin et al., 2009). The Deorali and Macchpucchare detachments are strands of the South Tibetan

Detachment System. The Deorali detachment places Tethyan sedimentary rocks on Greater Himalayan metasedimentary rocks in the Modi Khola valley (Martin et al., 2009). Greater Himalayan rocks are divided into two units: Formation I, a lower pelitic, semi-pelitic, and psammitic unit, and Formation II, an upper calcareous unit (Lefort, 1975; Searle and Godin, 2003; Martin et al., 2009). Detrital zircons from Formation I samples record a youngest age range of 900-640 Ma (Martin et al., 2009). A granitic augen gneiss intruded Formation II circa 500 Ma (Hodges et al., 1996; Martin et al. 2007; Martin et al., 2009). A large normal fault, the Bhanuwa fault, subdivides Formation I into two distinguishable units. Although the Bhanuwa fault has not been recognized in the field, Martin et al. (2009) identified it based on a 4 kilobar pressure difference between the hanging wall and foot wall rocks, comparison of garnet retrograde diffusion profiles in the hanging wall and foot wall rocks, and the presence of kyanite in the hanging wall rocks but not the foot wall rocks. Peak temperatures and pressures in the hanging wall of the Bhanuwa fault are 720 °C and 11 kilobars and are 720 °C and 15 kilobars in the footwall (Martin et al., 2009).

The MCT, a ductile shear zone which placed high-grade metasedimentary Greater Himalayan rocks on medium-grade metasedimentary Lesser Himalayan rocks, bounds the structural base of the Greater Himalayan series. Field and microscopic observations combined with whole rock Nd isotopic and U-Pb detrital zircon data by Martin et al. (2005) allow mapping of the MCT with spatial accuracy previously unattainable in the Annapurna Range, and I used their location of the MCT in this paper. The MCT accommodated at least 160 km of slip (Pearson, 2002;

Robinson, 2008; Martin et al., 2009). Lesser Himalayan rocks are cut by several major thrust-sense and normal-sense faults, most importantly the Ramgarh thrust which accommodated at least 120 km of slip and is the roof thrust for a large Lesser Himalayan duplex (DeCelles et al., 2001; Pearson et al., 2002; Robinson et al., 2003; Robinson, 2008; Martin et al., 2005; Martin et al., 2009). Rocks between the MCT and Ramgarh thrust experienced peak temperatures of about 575 °C and corresponding pressures of approximately 9 kilobars (Martin et al., 2009). The Romi fault lies directly south of the MCT and juxtaposes phyllitic quartzites of the Eocene-Oligocene foreland basin unit against slates of the Gondwanan strata. South of the Romi fault, the Tobro fault places phyllite and sandy phyllite of the Syangia Formation on the quartzite rich Fagfog Formation. Further south, the Ghandruk fault places map-scale bodies of phyllite within the Fagfog Formation on micaceous quartzites and sandy phyllites of the Kuncha formation. Martin et al. (2009) reveal only a small peak temperature and pressure change across the Romi, Tobro, and Ghandruk faults suggesting these faults probably only experienced minor amounts of dip-slip, though the amount of strike-slip is unknown.

2.3 Methods

River incision into bedrock is often modeled as a power-law function of local contributing drainage area and channel gradient (Snyder et al., 2000; Kirby and Whipple, 2001; Wobus et al., 2006a) expressed by:

$$S = k_s A^{-\theta}, \quad (1)$$

where S is local channel slope, k_s is the local steepness index, A represents the upstream drainage area, and θ is the concavity index. A single slope-area index may

characterize the entire length of a stream profile, but different values of k_s and θ often characterize discrete river segments (Hack, 1973, Snyder et al., 2000; Keller, 2002; Wobus et al., 2006a). Variations of k_s and θ values reflect spatial or temporal variations in rock uplift rate, climatic factors, or a rock unit's resistivity to erosion (Whipple and Tucker, 1999; Kirby and Whipple, 2001; Wobus et al., 2003; Whipple et al., 2004; Whipple, 2004; Hodges et al., 2004; Wobus et al., 2005; VanLaningham, 2006; Whittaker et al., 2008). Employing a reference concavity (θ_{ref}) allows the comparison of different stream segments through a normalized steepness value (k_{sn}) since k_s and θ strongly correlate at any single position on the stream. When log slope – log drainage area data are plotted for designated stream segments, k_s and θ can be determined by regression. I inserted the reference concavity into the following equation to find k_{sn} (Wobus et al., 2006a):

$$k_{sn} = k_s A_{cent}^{(\theta_{ref} - \theta)} \qquad (2)$$

with

$$A_{cent} = 10^{(\log A_{\max} + \log A_{\min})/2}, \qquad (3)$$

where k_s and θ are determined by equation 1, A_{min} and A_{max} bound the river segment analyzed, and A_{cent} is the midpoint value for the segment analyzed. Typically, the θ_{ref} value used in river profile analyses is the regional mean of observed θ values in undisturbed channel segments. These channel segments do not show signs of any knickpoints, uplift rate gradients, or changes in lithology. The range for reference concavities falls between 0.35-0.65 (Snyder et al., 2000; Kirby and Whipple, 2001; Wobus et al., 2005; Wobus et al., 2006a). I used a reference concavity of 0.45 since it representative of the average concavity on the Modi Khola and was used by other

researchers on streams near the Modi Khola (Wobus et al., 2005; Wobus et al., 2006a).

I extracted quantitative topographic measurements from the Modi Khola using an ArcGIS stream profiler toolbar and Matlab codes acquired from http://www.geomorphtools.org (Whipple et al., 2007). Studies of topography often obtain DEMs from satellite data such as the Shuttle Radar Topography Mission data (SRTM). However, the near vertical slopes and glaciated regions typical in the Himalaya produced large data void regions in the SRTM data for central Nepal (Figure 10). To mitigate the problem of data voids in the Modi Khola valley, digitized contour lines with a 40 m interval from the Ghandruk topographic map were obtained from the Nepal Department of Mining and Geology in order to produce a high resolution 25 m DEM. I converted the contour lines to points and created an interpolated surface using the multiquadric radial basis function, allowing us to avoid irregular flat terraces produced using the TIN grid interpolation in ArcGIS (Fedenczuk, 2008, personal communication; Hardy, 1990; Ware, 1998; Buhmann, 2003).

Local slope and drainage area data were extracted at points along the river profile using a 1.5 km smoothing window and an 8 m contour interval as parameter inputs for the stream profiler tool. I isolated and eliminated regions of data covered by glaciers drawn on the topographic map for the Modi Khola valley. I then identified a high concavity zone on the Modi Khola (Figure 11) and delineated distinct transitions in k_{sn} and θ, within the high concavity zone on the log slope – distance plot using at least squares regression (Figure 12, Table 1). I superimposed a

detailed geologic map of the Modi Khola created by Martin et al. (2009) on the river profile allowing comparison of the changes in k_{sn} and θ with the location of faults and lithologic contacts (Figure 8, Figure 11).

2.4 Results

The Modi Khola crosses a zone of high concavity exceeding 70 times the concavity of the surrounding region (Figure 11). The zone of high concavity maintains a mean θ of 2.12, while the mean θ to the north is only 0.03. Maxima and minima k_{sn} indices range between 165 and 884 $m^{0.9}$ within the high concavity zone (Figure 7, Figure 11).

Detailed analyses of the high concavity zone on the Modi Khola transect reveal four prominent river steepness peaks along with concordant steepness minima and transitions (Figure 12, Table 1). The most notable k_{sn} extrema occur at the interface of Formation II and medium grade Formation I rocks, the Bhanuwa fault, within the Kuncha formation south of the Ulleri granite, and at the contact between the quartzite and phyllite members of the Fagfog formation (Figure 8, Figure 13, Table 2). Reaches of the Modi Khola within Greater Himalayan rocks maintain high k_{sn} values ranging 424 to 884 $m^{0.9}$, while k_{sn} in the Lesser Himalayan rocks range 165 to 404 $m^{0.9}$ (Table 1).

Near the northern edge of the study site, another local maximum k_{sn} of 858 $m^{0.9}$ occurs near the Deorali detachment. South of the detachment system, within Formation II, k_{sn} drops from 858 to 582 $m^{0.9}$ and θ drops from 5.79 to -16.59.

At the interface of Formation II (calc-silicate schist, calc-silicate gneiss, and marble) and Formation I (pelitic and psammitic gneiss and schist and interbedded

quartzite) k_{sn} increases from 434 to 556 $m^{0.9}$ and θ dramatically shifts from 12.52 to -430.81 (Figure 13: location 1, Table 2). Overall the contact between Formation II and Formation I corresponds to a local k_{sn} minimum as river steepness increases both north and south of location 1.

Normalized river steepness (k_{sn}) peaks to a global maximum of 884 $m^{0.9}$ at the trace of the Bhanuwa fault and then consistently drops to 317 $m^{0.9}$ across a short distance of only 9 km. At the Bhanuwa fault the concavity index plummets from approximately 10 to an extremely negative value of -350 (Figure 13: location 2, Table 2). To the north of the Bhanuwa fault, k_{sn} values fluctuate several times (ranging 850 to 650 $m^{0.9}$) before dropping to a k_{sn} of 434 $m^{0.9}$ in the trough at location 1. A dramatic increase of k_{sn} (632 to 835 $m^{0.9}$) and decrease of θ (26.6 to -47.69) occurs north of the Bhanuwa fault and south of the Formation II – Formation I boundary. South of the Bhanuwa fault, k_{sn} truncates at the Romi fault and decreases consistently to about 0.5 km south of the Ulleri granite from 835 to 740 $m^{0.9}$. The most abrupt decrease in river steepness (740 to 424 $m^{0.9}$) occurs at the Romi fault, with no evident relationship to the MCT. The concavity index also drops drastically from 30 to 5 at the Romi fault.

Though changes in lithology coincide with subtle k_{sn} transitions south of the Romi fault, k_{sn} values almost monotonically decrease towards the south. Normalized steepness decreases across the stream profile in a stair step-like pattern across the Gondwanan Unit, and the Malekhu, Benighat, and Dhading Formations. Changes in k_{sn} correlate strikingly well along the lithologic interface of the Malekhu – Benighat (404 $m^{0.9}$ - 352 $m^{0.9}$), and the Benighat – Dhading (352 $m^{0.9}$ - 317 $m^{0.9}$) (Figure 14).

At location 3, k_{sn} increases to a local maximum of 398 $m^{0.9}$ at a subtle, yet visible peak of k_{sn} in the Kuncha formation.

South of the peak at location 3, k_{sn} decreases to a local minimum of 165 $m^{0.9}$. River steepness then increases gradually by intervals of 15 $m^{0.9}$ to a peak of 215 $m^{0.9}$ (location 4) that centers on a contact between the quartzite and phyllite members of the Fagfog formation (Figure 13, Table 2). The concavity of the k_{sn} peak at location 4 reacts in the opposite manner, decreasing to a low θ value at 58.41.

2.5 Interpretations

Precipitation variability, glacial dams, landslide dams, tributary junctions, changes in lithology, and recent rock uplift on faults each provide possible mechanisms to explain the distinct changes in k_{sn} and θ observed in the Modi Khola valley. The degree to which each of these mechanisms controls the topography is addressed in the following text.

2.5.1 Precipitation variability in the Modi Khola valley

Several researchers emphasize the important connection between topography and the spatial variability of precipitation in the Himalaya (Montgomery et al., 2002; Burbank et al., 2003; Gabet et al., 2004; Hodges et al., 2004; Anders et al., 2006; Bookhagen and Burbank, 2006; Garzanti et al., 2007). Models of orographic precipitation demonstrate direct relations to slope and have been used as a proxy for determining erosion rates, river discharge, and fluvial incision (Finlayson et al., 2002; Roe et al., 2002; Anders et al., 2006). The distribution of precipitation and temporal

variability related to the seasons may influence topographic expressions of river profiles (Snyder et. al., 2000; Tucker et al., 2000; Roe et al., 2002).

Annual satellite rainfall measurements from the Tropical Rainfall Measurement Mission (TRMM) depict two along-strike bands of rainfall maxima across the southern extent of the Lesser and Greater Himalaya (Bookhagen and Burbank, 2006). The Modi Khola valley rests in the northern rainfall maximum band where precipitation accumulates to an intense amount of rainfall, averaging 3 m/yr (from TRMM data). With a spatial resolution of ~1 x 1 km (sub sampled from ~5 x 5 km), TRMM data depict spatial variations in rainfall ranging from 2.8 to 4.1 m/yr along the Modi Khola profile (Figure 15). Local precipitation maxima in the northern reach of the Modi Khola might be responsible for the drop in k_{sn} (858 to 582 $m^{0.9}$) occurring at location A within Formation II. The local minimum in k_{sn} (165 $m^{0.9}$) between locations 3 and 4 may also reflect a topographic response to a local precipitation maximum.

Anders et al. (2006) estimate that errors in TRMM-derived precipitation data range from 15-50% and demonstrate that the relationship between precipitation patterns and the topography is observable at spatial scales larger than 10 km. Since the Modi Khola valley extends over a small spatial scale, only 40 km, the precipitation variations locally present in the TRMM data could be subject to greater error. An account of the distribution of precipitation must be carried out as temperatures, prevailing winds, and topographic changes extending across the Himalaya from India to the Tibetan plateau drive large-scale climate processes (Roe et al., 2002). Further investigations of the spatial variability of rainfall across the tributaries and hillslopes

surrounding the Modi Khola, which contribute to total river discharge, must be carried out before local precipitation changes can be interpreted.

The acquisition of higher resolution precipitation measurements, with at least 25 m resolution, from rain gauges would greatly facilitate interpretation of the effect of rainfall variability on the Modi Khola profile. Annual meteorological field measurements or the installation of permanent meteorological stations, which do not currently exist in the Modi Khola valley, would improve our understanding of climatic relations to the topography at our field site (Barros et al., 2000; Burbank et al., 2003; Hodges et al., 2004).

2.5.2 Glacial damming of the Modi Khola

Korup and Montgomery (2008) propose a possible mechanism for the preservation of the edge of southeast Tibet, in which glacial dams impede river incision by generating upstream impoundment and interglacial aggradation. The main mechanism proposed by Korup and Montgomery (2008) incorporates glaciers which created ice and moraine dams, and debris flows in adjacent tributary basins. Glacial material from tributaries extended down from the side of the trunk stream, blocking stream flow and inhibiting river incision. A U-shaped glacial valley dominates the terrain north of location 1, extending to only 1 km north of the border of the Modi Khola geologic map (Figure 7). The stream profile may still be adjusting to glacial processes that dominated the landscape in the late Quaternary. Hanging valleys which mark the potential extent of glaciated terrain extend into the Modi Khola valley approximately 4 km, traversing Tethyan rocks and Formation II.

Glaciation potentially affected topography north of Formation II and across the Formation I – Formation II contact (Figure 7).

Steep topography and abundant precipitation result in poor preservation of moraines, terraces, and landslide deposits (Owen et al., 2005; Zech et al., 2009). Rainfall in the Modi Khola valley exceeds 3 m/yr and potentially washed away any recently deposited glacial dams or associated stream terraces (Bookhagen and Burbank, 2006). The possibility that the Modi Khola profile is still adjusting to damming from glacial features cannot be ruled out. Since location A lies within possible U-shaped glaciated terrain determined from photography and a precipitation maximum occurs at location A, it is possible that changes in k_{sn} within the northern extent of the Modi Khola reflect topographic responses to glacial and climatic processes.

Stream blockage from a glacial moraine would generate steep topography south of the moraine and gentle topography north of the moraine. Although k_{sn} values between the Formation I – Formation II contact and the Bhanuwa fault reflect gentle to steep transition in the topography, field work, photographs of the Modi Khola valley, and analysis of digital topography show no noticeable evidence of glacial moraines. Glacial damming would create terraces, which remain undetected in the Modi Khola. Due to uncertainty in recent river profile adjustment to glaciation, I choose not to further interpret changes in k_{sn} north of the Formation I – Formation II boundary.

2.5.3 Landslide damming on the Modi Khola

Landslide events create natural dams on rivers, which trap incoming sediment and inhibit fluvial bedrock incision (Korup and Tweed, 2007). Several researchers consider the effect of mass-wasting processes on the topography to be underestimated (Roering et al., 2005; Korup and Tweed, 2007; Zech et al., 2009) and important for landscape processes in the Annapurna range (Fort, 2000; Korup et al., 2006; Weidinger et al., 2006; Korup et al., 2007). Studies by Zech et al. (2009) indicate deposits from the Dhampu-Chooya landslide dammed the Kali Gandaki circa 4.1±0.6 ka. Subsequent dam failure resulted in 600 m of sediment build up in the Kali Gandaki valley, drastically impacting river discharge and erosion rates. ^{10}Be surface exposure rates from boulders show large landslides and related debris flows may account for discrepancies between high denundation rates and low erosion rates observed in the Marsyandi valley (Zech et al., 2009). ^{14}C dating of wood fragments and stratigraphic analysis of landslide deposits, which formed a >400 m tall dam in the Marsyandi, indicate aggregation and subsequent incision occurs rapidly, over ~500 years after the landslide event (Pratt-Sitaula et al., 2007). Korup et al. (2006) demonstrate an abrupt increase in steepness and concavity at the Kalopani rockslide dam near the South Tibetan Detachment Zone. The Modi Khola drains into the Kali Gandaki and traverses the Annapurna Range, like the Marsyandi, and possibly experienced similar mass-wasting events and consequent disturbance to its river profile.

Known landslides in the Modi Khola valley fail to coincide with any steepness transitions I detected in my analysis, though intense rainfall may have washed away

landslide deposits. Steepness maxima, minima, and transitions were observed at four mapped geologic boundaries, including two faults: the Formation I – Formation II contact, the quartzite- and phyllite-rich members of the Fagfog formation, Eocene-Oligocene foreland basin deposits and Gondwanan strata are juxtaposed by the Romi fault, and compositionally different members of Formation I are juxtaposed at the Bhanuwa fault. Although we cannot rule out the possibility that landslide dams caused any or all of the topographic features we observe, it would be extremely coincidental for the effects of landslides to only be observed at fault and lithologic boundaries and nowhere else on the Modi Khola profile. A landslide could be responsible for the steepness transition observed within the Kuncha formation at location 3, as it can not be explained by lithologic contacts or faults. Before determining the impact of landslide damming on the Modi Khola profile, a field examination of past and recent landslides is necessary at all steepness extrema and transitions.

2.5.4 Tributary junctions

An increase of bedrock incision rate at tributary junctions, due to an increase in drainage area, generates knickpoints, or steep stream reaches in the topography (Crosby et al., 2006; Wobus et al., 2006a). Water and sediment inputs at tributary junctions generate local perturbations in a stream's longitudinal profile (Keller, 2002). Near the town of Birethanti, the Bhurundi Khola joins the Modi Khola, increasing drainage area by 21% (Figure 8, Figure 16). The Bhurundi Khola tributary junction coincides with the contact between the phyllite and quartzite members of the Fagfog Formation and may have played a role in the creation of the small steepness

maximum at location 4 (Figure 13). The Chomrong Khola and Kimrong Khola tributary junctions increase drainage area only a few hundred meters and a few kilometers, respectively, from the Romit fault (Figure 13, Figure 16). Drainage area increases by 4.03 x 10^7 m^2 at the Chomrong Khola tributary junction and by 6.14 x 10^7 m^2 at the Kimrong Khola tributary junction. These large changes in drainage area potentially explain the lack of increase in k_{sn} at the Dhading limestone, which is expected due to changes in rock resistance (Keller, 2002; Korup, 2008). The Chomrong Khola intersects with the Modi Khola within close proximity to the Romi fault and the MCT, approximately 3 km downstream of location 2. Although the increase in drainage area at the Chomrong Khola tributary junction is possibly responsible for the drop in k_{sn} at the Romi fault, knickpoints generated by a change in drainage area tend to occur less than 1 km upstream, not downstream, of large tributary junctions (Crosby et al., 2006). Although it is possible an increase in drainage area created the continuous drop in steepness south of location 2 and at the Romi fault, the prominent steepness maximum at the Bhanuwa fault does not correlate with any tributary junctions. The Bhanuwa fault traverses the Modi Khola north of the Chomrong and Kimrong tributary junctions. Perhaps combinations of recent rock uplift occurring at the Bhanuwa and Romi faults, spatial changes in lithology, and an increase in drainage area generated the systematic drop in k_{sn} extending from the Bhanuwa fault.

2.5.5 Changes in lithology

Stream profiles adjust depending on a lithologic unit's resistivity to erosion over short geologic timescales (Keller 2002). Several studies document topographic

correlations with different lithologic resistivities to erosion (Hack, 1973; Belt et al., 2005; Roering et al., 2005; VanLaningham et al., 2005; Korup, 2008).

Along-stream changes in substrate properties or spatial and temporal differences in rock uplift rate produce extreme concavities (negative or >1) (VanLangingham, 2003; Whipple, 2004). An extreme negative concavity value and local k_{sn} minimum occurs near the Formation II and Formation I contact (Figure 13: location 1, Table 2). The presence of a fault between Formation II and Formation I is suggested by Martin et al. (2009), but remains uncertain. Since Formation II is rich in calcite and Formation I contains mostly pelitic material and quartz, I suggest the k_{sn} minimum at location 1 reflects a change in rock type. Concavity also drops to an extreme negative concavity (from 35 to -75) and k_{sn} maximizes at 398 $m^{0.9}$ within the Kuncha formation south of the Ulleri granite (Figure 13: location 3, Table 2). The Kuncha formation is consistently comprised of phyllite and gritty phyllite, with the exception of the Ulleri granite and sparse patches of diorite (Martin et al., 2005). The igneous – metasedimentary transition of the Ulleri granite to the Kuncha may be responsible for the local steepness maximum at location 3 (VanLangingham, 2003), though the location of this contact does not precisely correlate with location 3. In general, schist-rich lithologies erode more easily than quartzite (Whipple et al., 2000; Attal et al., 2006). Since the quartzite of the Fagfog formation likely is highly resistant to erosion, it is possible that the quartzite – phyllite contact within the Fagfog formation generated the small steepness maximum at location 4.

Lithologies juxtaposed by the Bhanuwa and Romi faults contain different compositions, which alone could account for changes in the topography across the

faults, with no recent motion on them necessarily to explain the data. Formation I rocks south of the Bhanuwa fault contain the peak assemblage quartz + muscovite + biotite + plagioclase + garnet, while Formation I rocks north of the Bhanuwa fault contain an aluminosilicate phase (kyanite) within the peak assemblage quartz + muscovite + biotite + plagioclase ± garnet ± kyanite (Martin et al., 2009). Similarly, the Romi fault places phyllitic quartzites of the Eocene-Oligocene foreland basin unit against slates of the Gondwanan unit. The abrupt transition in metamorphic grade from Greater Himalayan to Lesser Himalayan rocks at the MCT, located between the Romi and Bhanuwa faults, could explain abrupt changes in k_{sn} between locations 2 and 3 (Figure 13).

Studies in the western Alps delineate numerous knickpoints along the Drac River which correlate with more resistant bedrock, such as Mesozoic reef limestone and Paleozoic micaschist (Brocard et al., 2006). Studies by VanLaningham 2006 derived quantifiable relationships between rock type and concavity, indicating high θ values characterize sedimentary rocks and low values associate with more resistant volcanic rocks. The stream reach south of the Romi fault traverses repeating stretches of resistant limestone. Although previous research suggests k_{sn} and θ should fluctuate from high to low values, I observe a continuous drop in k_{sn} and an increase of θ from north to south even though the river traverses highly resistant strata at two locations on the river profile (the Malekhu and Dhading limestone) (Figure 14).

2.5.6 Recent rock uplift on faults

Log slope vs. log drainage area data analyses on regions where movement on faults are well constrained such as the Mendocino triple junction in Northern

California, the Red River fault in China, across active normal faults in the Central Apennines of Italy, and the Siwalik Hills along the Main Frontal thrust (Figure 7, inset in upper left corner) of southern Nepal confirm that regions of rapid rock uplift produce high concavity zones (Snyder et al., 2000; Kirby and Whipple, 2001; Schoenbohm et al., 2004; Wobus et al., 2006a; Whittaker et al., 2008). Following England and Molnar (1990), I define rock uplift as the displacement of rocks with respect to the geoid. Whittaker et al. (2008) show that faults have undergone an increase in throw rate within the last 1 My maintain significant river profile convexities, while streams crossing no faults or faults with constant slip rate exhibit concave-up profiles. High concavity values ranging from 0.7 to 2.1 characterize river channels traversing the Main Frontal thrust in the Siwalik Hills of southern Nepal (Kirby and Whipple, 2001). River profile investigations further north, in central Nepal near the MCT, detected breaks in normalized river steepness and reaches of high concavity zones on the Trisuli, Burhi Gandaki, and Marsyandi rivers (Wobus et al., 2003; Hodges et al., 2004; Wobus et al., 2006a). The Modi Khola traverses several faults and reflects a reach of significantly high concavity at 2.2, which is approximately 70 times greater than the mean concavity of the surrounding region. The presence of a high concavity zone suggests that perhaps faults in the Modi Khola valley experienced slip during the last 1 My. If recent rock uplift on faults dominates landscape evolution processes in the Modi Khola valley, topographic signatures related to rock type may become undetectable (Korup, 2008; Keller, 2002).

The global k_{sn} maximum at the Bhanuwa fault and the abrupt k_{sn} transition at the Romi fault depict an interesting relationship between river morphology and

normal faulting on the Modi Khola. The global maximum and drop of k_{sn} consistently occur at the trace of the Bhanuwa and Romi faults, respectively, regardless of smoothing window size (Figure 17). In the Modi Khola valley, the trace of the MCT lies less than 1 km from the Romi fault. While sample locations allow the location of the MCT to fluctuate by less than 1 m and the DEM resolution allows stream profile data to shift 25 m, my data constantly reveal an abrupt transition at the Romi fault, not the MCT. A similar k_{sn} maximum and drop appear at the Deorali detachment system, another series of normal faults, though landslides and glacial processes potentially altered the topography in the northern margin of the study site. A newly developed or unmapped active fault could possibly account for the k_{sn} maximum occurring within the Kuncha formation at location 3.

A maximum and a large transition in river steepness occur at normal faults, where steepness peaks at the Bhanuwa fault and drops at the Romi fault. Although other studies associate changes in river steepness with active thrusting south of the MCT (Burbank et al., 2003; Hodges et al., 2004; Wobus et al., 2006b), in the Modi Khola spatial changes in river steepness correlate better with the location of mapped normal faults, not thrusts. If differential rock uplift is occurring in the Modi Khola, normal faults likely accommodate motion required for recent rock exhumation and topographic steepening.

The identification and location of faults is critical to my interpretation, even if the same DEM is used to locate extrema and transitions in k_{sn} and θ. Hodges et al. (1996) place the MCT further north near the trace of the Bhanuwa fault as mapped by Martin et al. (2009). I would reach different conclusions if the Hodges et al. (1996)

geologic map was implemented in this project. Although the topographic data I examined might support recent uplift on normal faults, there is no record of earthquakes in the Modi Khola. Also no k_{sn} transition is observed at the Ghandruk or Tobro faults, other normal-sense faults located south of the Romi fault. Mid-crustal temperatures experienced during metamorphism also determined the location of the Bhanuwa fault (Martin et al., 2009), which is somewhat abstracted from active faulting. Recent movement on the Bhanuwa fault and Romi fault needs to be confirmed using techniques such as GPS, seismology, and low temperature thermochonology.

2.6 Implications

The Modi Khola displays a complex topographic expression, reflecting a dynamic landscape response to rock resistance, geologic structures, precipitation variability, and intensified erosion. Landslide damming potentially explains any or all of the steepness extrema or transitions in the Modi Khola valley (Figure 13: 1 through 4, Table 2). Changes in lithology also explain all distinct changes in river steepness except the local peak in river steepness at location 3. Conversely, rock uplift on normal faults, spatial changes in lithology, and an unmapped active fault at location 3 also explain topographic changes on the Modi Khola. Distinct compositional differences between Formation I and Formation II and between the quartzite- and phyllite-rich members of the Fagfog Formation could explain k_{sn} transitions at locations 1 and 4. A large change in drainage area may also contribute to the local steepness maximum at location 4 and the distinct drop at the Romi fault. Rock uplift on faults would be a more plausible explanation for the abrupt change of

k_{sn}, at location 2, since the rocks juxtaposed by the Bhanuwa fault contain only subtle compositional differences. River steepness of the Modi Khola correlates with normal faults, not thrusts. Therefore, normal faulting may play a pivotal role in recent landscape evolution driven by interactions between tectonics and erosion. Although, a thrust potentially exist at the Formation I – Formation II contact. The landscape in the Modi Khola valley likely reflects and has experienced topographic feedbacks generated by each of these mechanisms to some extent.

Interactions between the forward propagating thrust system of the Himalayan arc, recent normal fault activity, and intense erosion may drive landscape morphology in the central Nepalese Himalaya. According to numerical models of shear zone sensitivity, thrust reactivation in the internal part of orogenic wedges is triggered by surface processes, strain softening, or weak inclusions (Selzer et al., 2007). Since the Romi fault truncates at depth with the MCT and exhibits a distinct drop in k_{sn} (740 to 424 $m^{0.9}$), normal-sense reactivation of the MCT is plausible. Balanced cross sections from western Nepal invoke speculation that the onset of the Asian monsoon (12-10 Ma) created rapid erosion, initiating the formation of the Lesser Himalayan duplex in the late Miocene (Robinson et al., 2006). Studies of critical taper and balanced cross sections in the central Andes also demonstrate strong correlations between climate and deformation (McQuarrie et al., 2008). Local normal faulting events in the Modi Khola valley may reflect minor adjustments to the geometry of the orogenic wedge required to maintain critical taper and promote the southward propagation of the Himalayan thrust belt (Davis et al., 1983; Dahlen, 1990; DeCelles and DeCelles, 2001; Thiede et al., 2004; Whipple and Meade, 2004; Hoth et al., 2006; Robinson et

al., 2006; Roe et al., 2006; Stolar et al., 2006; McQuarrie et al., 2008; Robinson, 2008). The instigation of normal-sense motion in response to the intense erosion may play a crucial role in mountain building processes that continuously control the architecture of the Himalayan landscape.

2.7 Conclusions

Detailed evaluation of distinct changes in river steepness and concavity indices on the Modi Khola transect support the following conclusions:

(1) A high concavity zone where k_{sn} ranges between 165 and 884 $m^{0.9}$ traverses the Modi Khola, indicating fault movement possibly occurred in the last 1 My.

(2) Significant differences in schistocity and composition might explain transitions of k_{sn} occurring at the interface of medium grade Formation I and Formation II rocks, and between the quartzite and phyllite members of the Fagfog formation.

(3) Major transitions in normalized river steepness occur at normal faults in the Modi Khola valley. The steepest reach of the stream and a large decrease in concavity coincide with the trace of the Bhanuwa fault. The most abrupt decrease in steepness occurs at the Romi fault. Localization of recent river incision on the Modi Khola profile, and potentially rock uplift, occurs at the trace of the Bhanuwa and Romi faults.

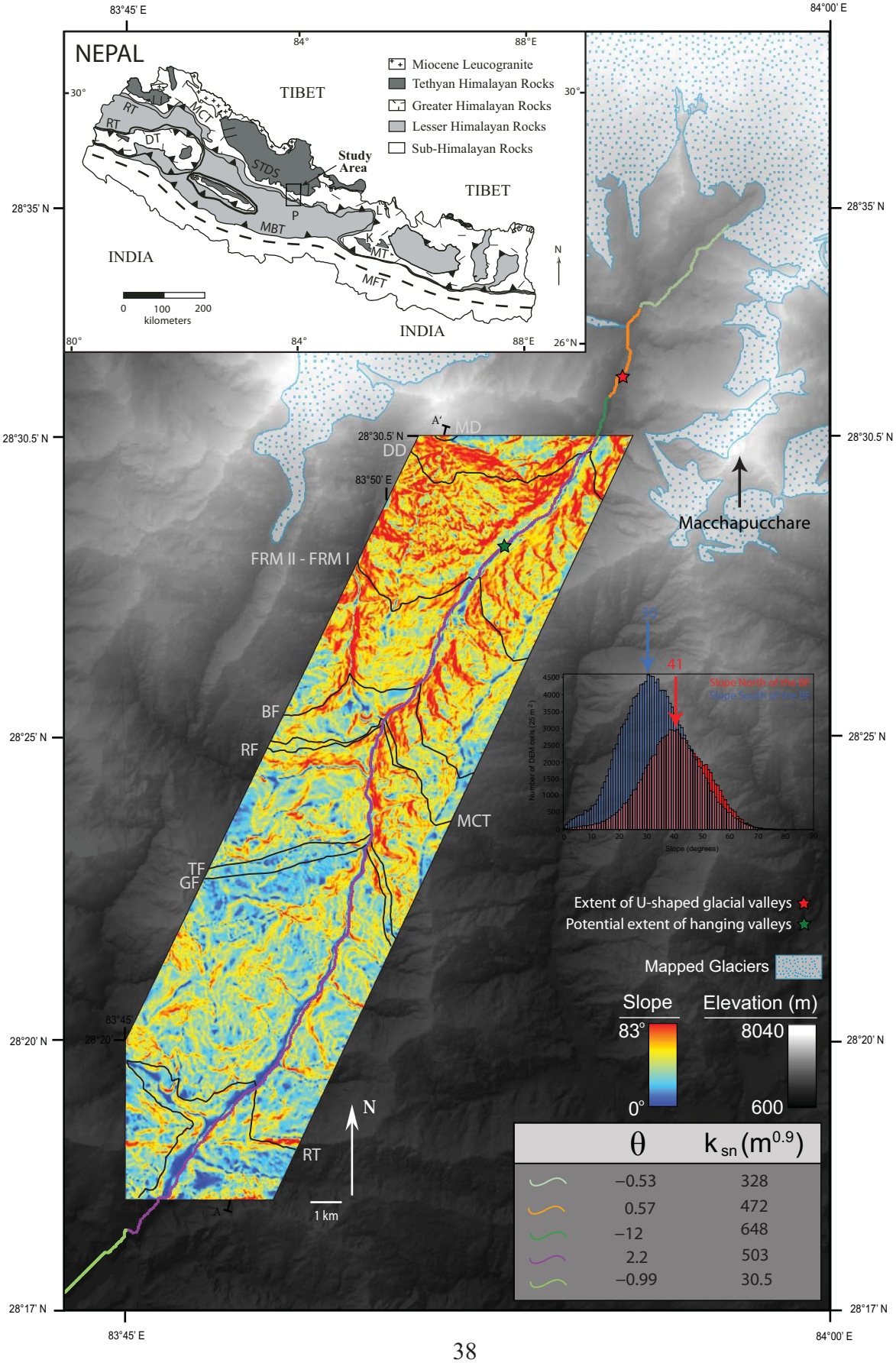
NEPAL
Miocene Leucogranite
Tethyan Himalayan Rocks
Greater Himalayan Rocks
Lesser Himalayan Rocks
Sub-Himalayan Rocks
TIBET
INDIA
Study Area
STDS
MCT
RT
DT
MBT
MFT
0 100 200
kilometers
83°45' E
84°00' E
28°35' N
28°30.5' N
28°25' N
28°20' N
28°17' N
A
A'
MD
DD
FRM II - FRM I
BF
RF
MCT
TF
GF
RT
1 km
Macchapucchare
Slope North of the BF
Slope South of the BF
Number of DEM cells (25 m²)
Slope (degrees)
Extent of U-shaped glacial valleys
Potential extent of hanging valleys
Mapped Glaciers
Slope
Elevation (m)
83°
0°
8040
600
θ
k sn (m0.9)
−0.53 328
0.57 472
−12 648
2.2 503
−0.99 30.5

Figure on previous page

Figure 7: Changes in θ across the Modi Khola profile
The purple stream segment marks the high concavity zone, where θ is approximately 70 times greater than the surrounding topography. Variations of k_{sn} within the high concavity zone are illustrated in Figures 8 and 12. MD—Macchapucchare Detachment, DD—Deorali Detachment, FRM II - FRM I—Formation II - Formation I lithologic contact, BF— Bhanuwa Fault, MCT—Main Central thrust, RF—Romi Fault, TF—Tobro Fault, GT—Ghandruk thrust, RT—Ramgarh thrust. Macchapucchare marks highest summit on the map at 6993 m. The border around the slope map shows the boundary of the geologic map from Martin et al. (2009), shown in Figure 8. The topography of the Modi Khola valley maintains an average slope of 41° north of the Bhanuwa fault and 30° south of the Bhanuwa fault. The background shows a digital elevation model (DEM) in grey scale at 25 m resolution. A hillshade is superimposed beneath the DEM to show the topography in three-dimensions. The terrain beneath mapped glaciers was excluded from the river profile analysis. A U-shaped glacial valley extends approximately 2 km north of the geologic map border (red star). The green star marks the potential extent of hanging valleys. Generalized geologic map of Nepal in top left corner shows location of Modi Khola valley study site modified from Martin et al. (2009). Generalized geologic map of Nepal is originally from Amatya and Jnawali (1994). On generalized Nepal geologic map: K—Kathmandu, P—Pokhara, L—Langtang region, STDS—South Tibetan Detachment System, MCT—Main Central thrust, DT—Dadeldhura thrust, MT—Mahabarat thrust, RT—Ramgarh thrust, MBT—Main Boundary thrust, MFT—Main Frontal thrust. Geographic coordinate system: WGS 1984 UTM Zone 44N. Projection: Transverse Mercator.

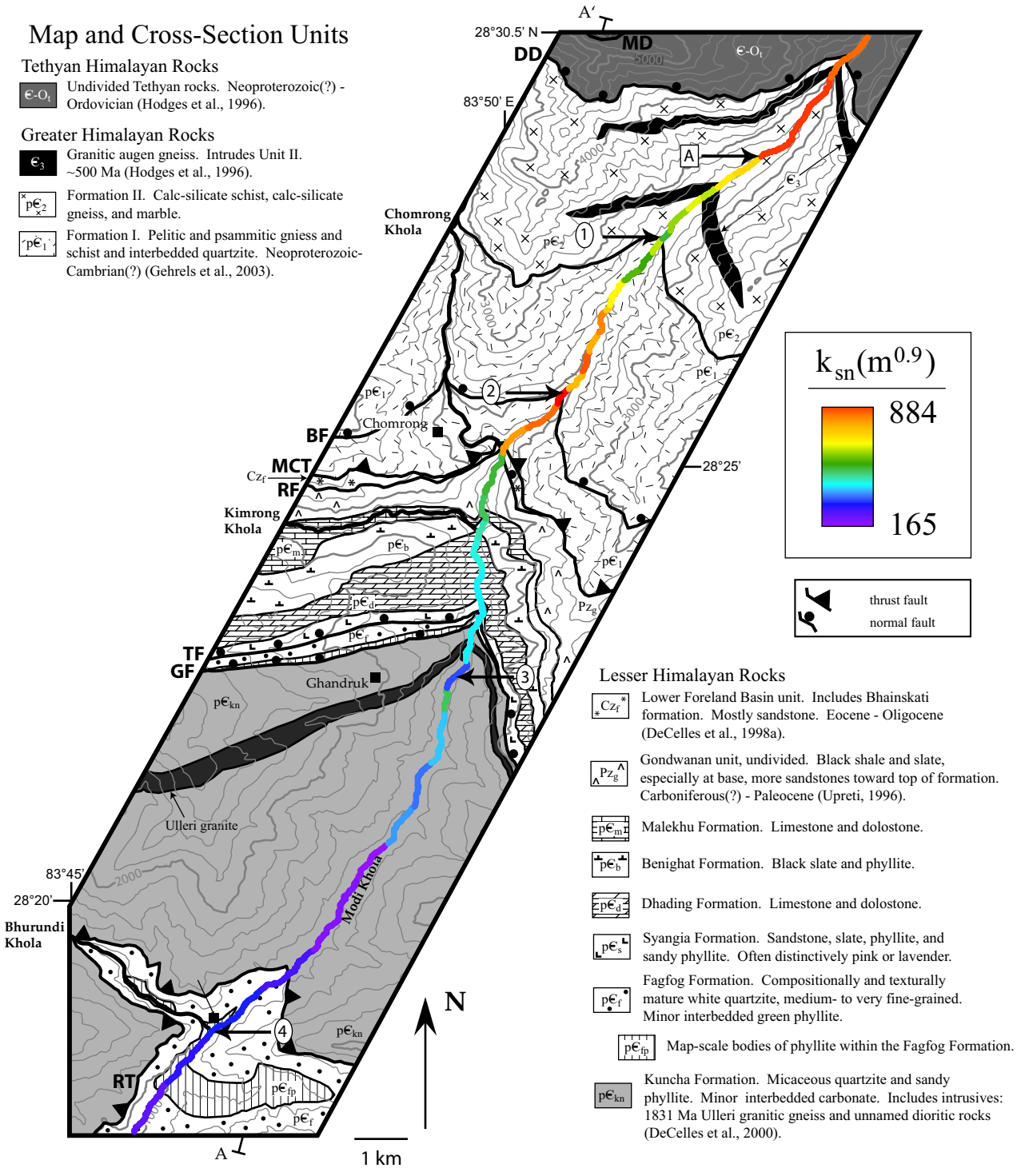

Figure 8: Geologic map of the Modi Khola valley with k_{sn}
Geologic map of the Modi Khola valley modified from Martin et al. (2009). The red to green gradient shown k_{sn} values calculated for segments of the Modi Khola profile. Locations 1-4 and A mark abrupt and significant transitions of k_{sn} discussed in the text. MD—Macchapucchare Detachment, DD—Deorali Detachment, FRM II - FRM I— Formation II - Formation I lithologic contact, BF— Bhanuwa Fault, MCT—Main Central thrust, RF—Romi Fault, TF—Tobro Fault, GT—Ghandruk thrust, RT—Ramgarh thrust. Contour interval is 200 meters.

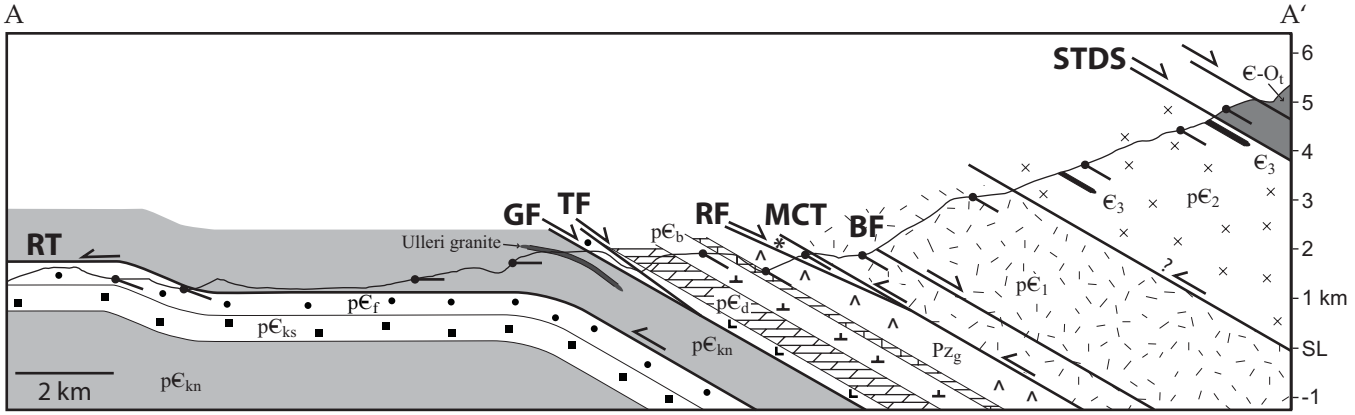

Figure 9: Cross-section of the Modi Khola valley
Cross-section of the Modi Khola valley from Martin et al. (2009). Transect taken from A-A' on geologic map of the Modi Khola valley shown in Figure 8.

.

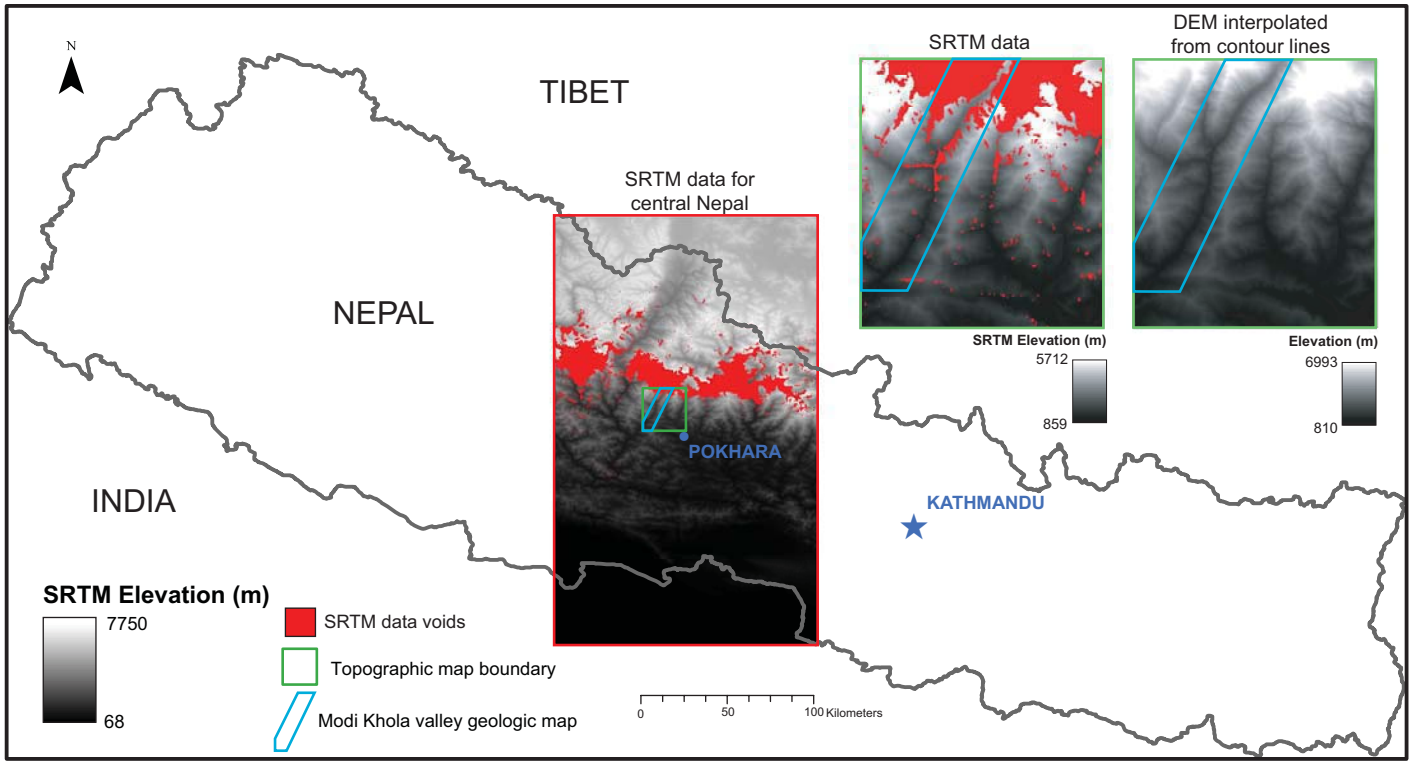

Figure 10: Problem with SRTM data in central Nepal
SRTM data for central Nepal contain data voids in glaciated regions and locations of near vertical terrain. The green box shows the extent of the topographic map region required to produce a slope map which covers the Modi Khola valley. Blue line marks the border of the Modi Khola geologic map shown in Figure 8. Voids in the topographic map make SRTM data unusable for our study site in the Modi Khola valley. To mitigate this problem we created a 25 m DEM from digitized contour lines. Geographic coordinate system: GCS Everest India Nepal.

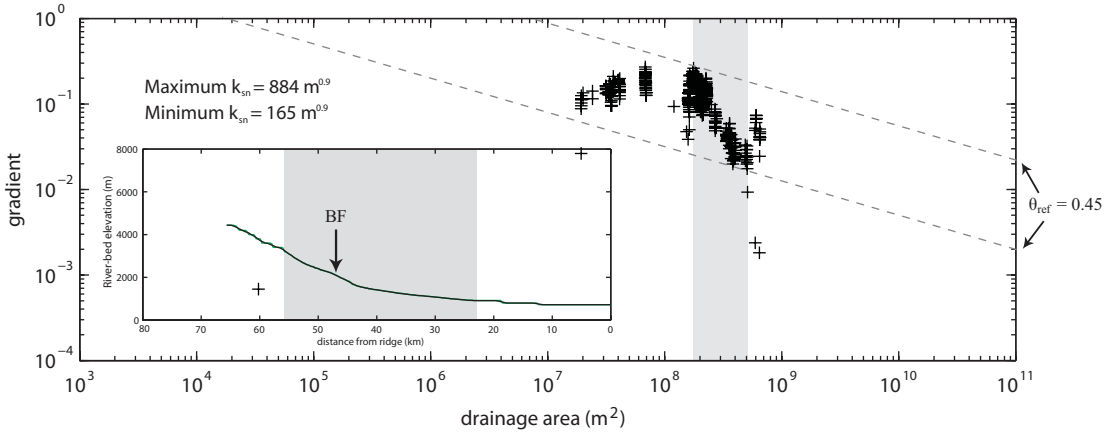

Figure 11: Plot of log slope versus log drainage area for the Modi Khola profile
Plot of log slope versus log drainage area data for the Modi Khola profile. Grey bands mark the extent of a locally high concavity zone on the Modi Khola profile. Concavity is shown by the slope of the data on the plot. The grey box shows the zone of high concavity where concavity is 2.2, which is 70 larger than the surrounding topography. Dashed lines show maximum and minimum k_{sn} values calculated with a reference concavity of 0.45. Inset shows the Modi Khola profile. The Bhanuwa Fault (BF) is the steepest location on Modi Khola profile.

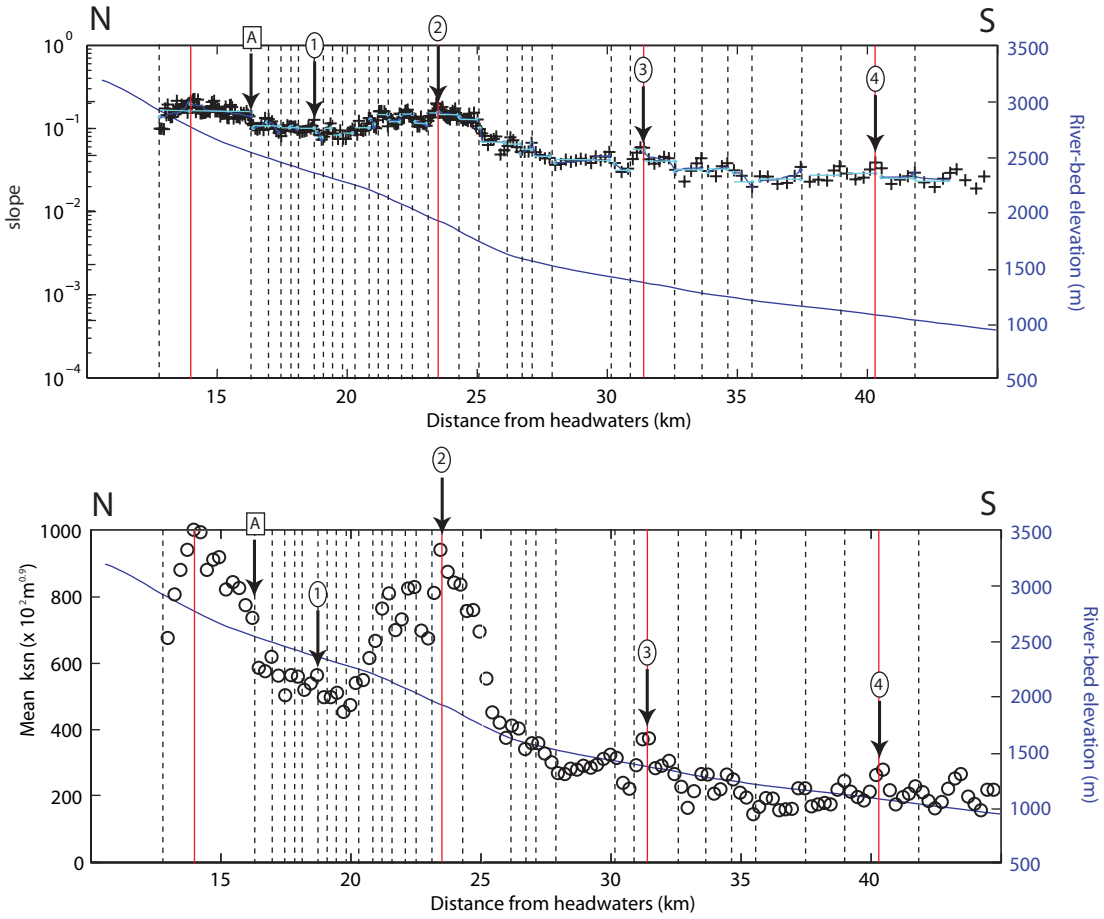

Figure 12: River steepness extrema and transitions on the Modi Khola profile
Top plot displays log slope versus distance data for locations sampled every 25 m along the Modi Khola profile is shown by the black plus marks. Open circles in bottom plot represent values of k_{sn} based on log slope versus distance data for the Modi Khola over a 0.5 km window with an assumed reference concavity of 0.45. Dashed black vertical lines mark the bounds for each segment used to calculate k_{sn}. Solid red vertical lines mark locations of steepness maxima. The two northern steepness maxima maintain large changes in steepness, while the two southern steepness maxima maintain only small changes in steepness. The blue segments show regressed channel concavity for a particular segment, while cyan lines show reference concavity, θ_{ref}, used to calculate k_{sn}. River-bed elevation for the stream profile is delineated by the dark blue line. Letter A and numbers 1 through 4 mark locations of notable steepness extrema or transitions discussed in the text.

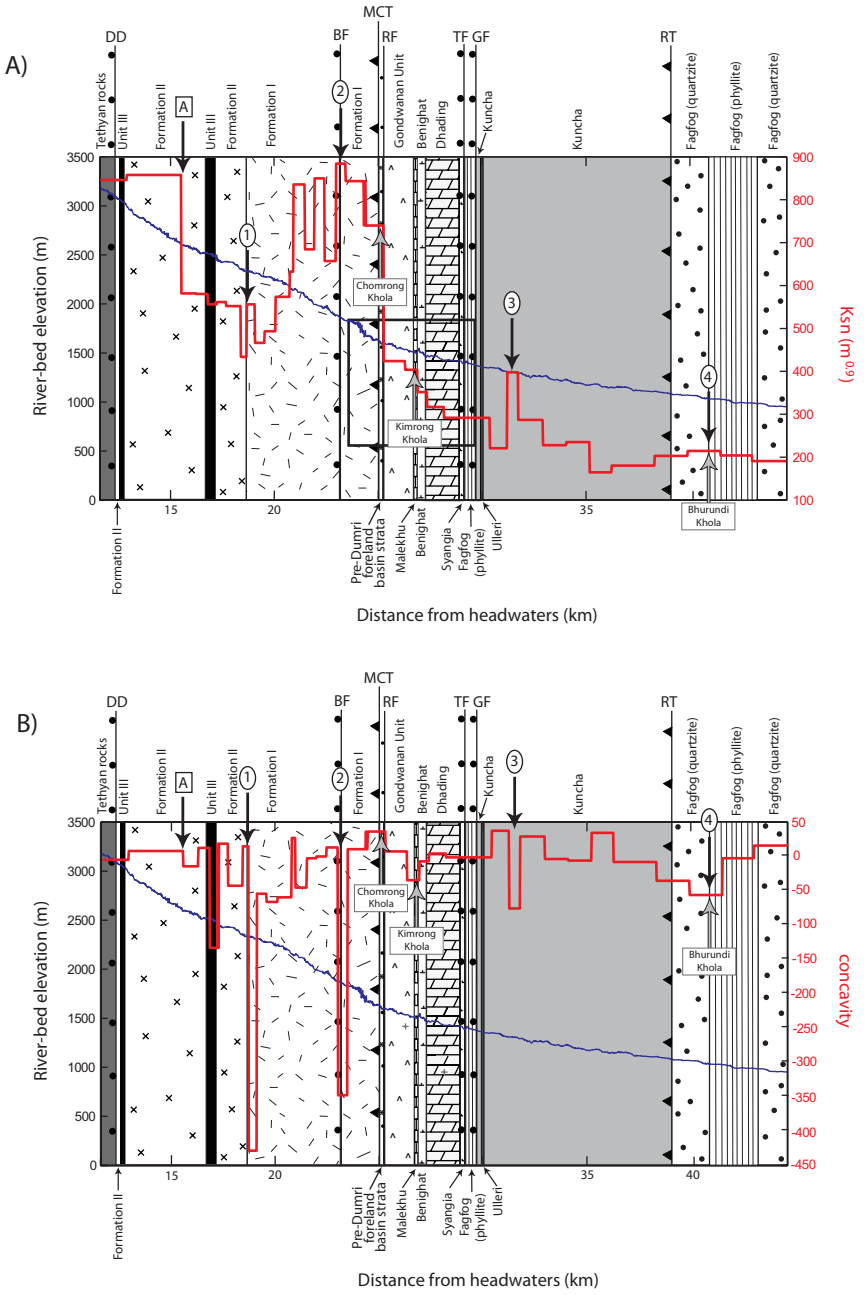

Figure 13: River steepness and concavity compared to geology on the Modi Khola profile Correlations of lithologic contacts and faults with river steepness (k_{sn}) and concavity (θ). Elevation of river bed shown is shown in blue. Lithologic unit patterns and faults correspond to descriptions in Figure 8. Black arrows pointing down show 1ocations 1-4 and A, which represent significant changes in k_{sn} discussed in the text. Location A marks and abrupt drop in k_{sn} and is excluded from the analysis because the topography in this region was potentially affected by glacial activity in the geologic past. Location 2 marks the steepest location on the Modi Khola profile at the trace of the Bhanuwa fault. Grey arrows pointing up represent major tributary junctions. A) Red line shows k_{sn} values determined by regression on the log slope vs. distance plot in Figure 12. Horizontal segments represent k_{sn} or θ value calculated for designated stream segments while vertical lines connect segments to show changes in k_{sn} values. Black box marks location of inset shown in Figure 14. B) Same as A, but shows θ values instead of k_{sn}.

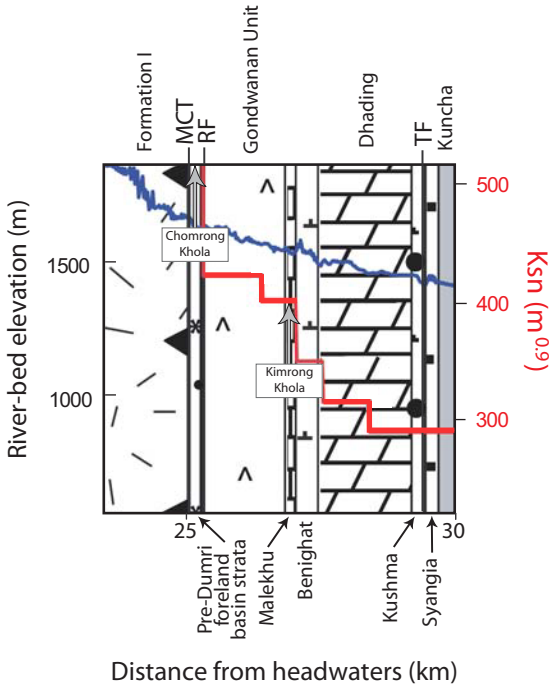

Figure 14: River steepness changes across limestone
Inset from Figure 13 that shows a magnification of k_{sn} changes across the Malekhu and Dhading limestones. Symbology same as in Figure 13.

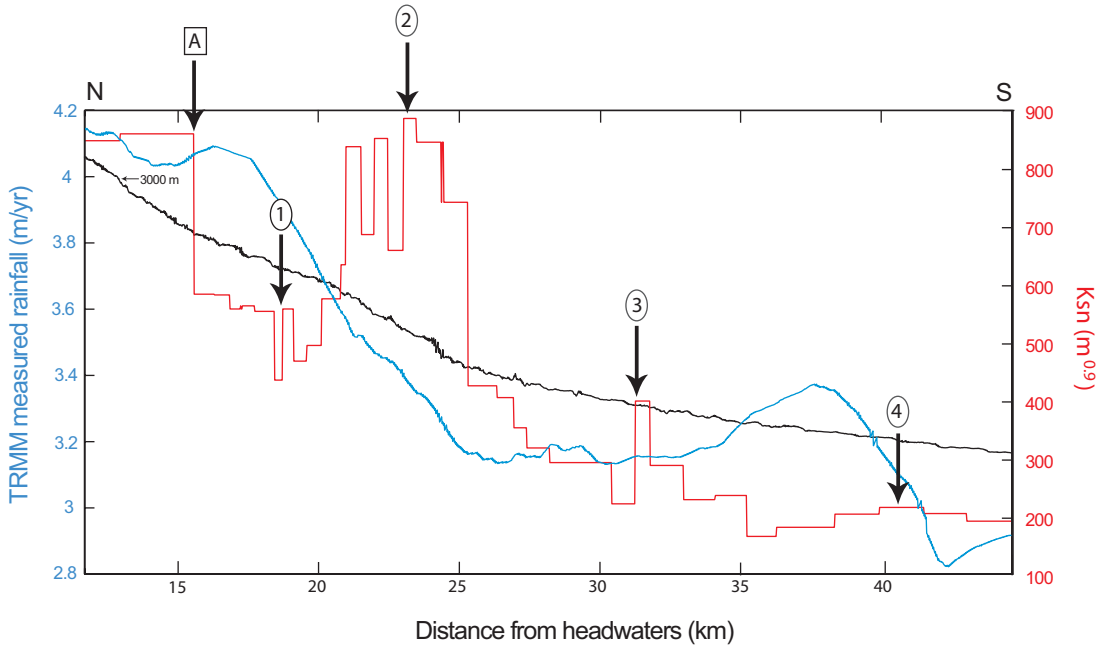

Figure 15: Precipitation on the Modi Khola profile
Variability of rainfall across the Modi Khola profile shown in blue. Precipitation data derived from Tropical Rainfall Measurement Mission (TRMM) data provided by Bodo Bookhagen. River-bed elevation profile shown in black. Locations 1-4, location A, and k_{sn} illustrated as in Figure 13.

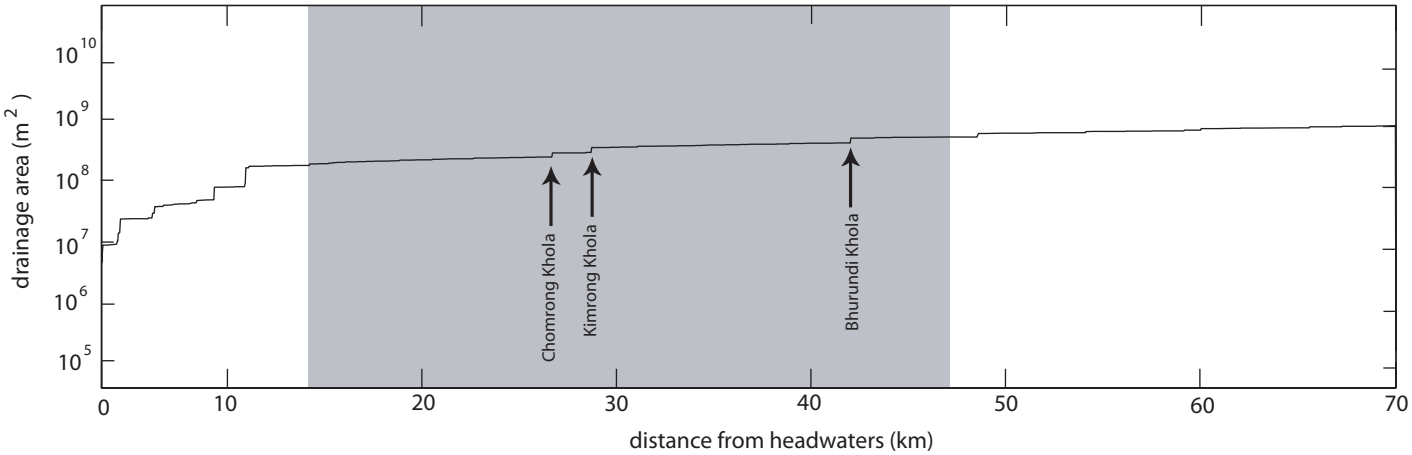

Tributary name	Drainage area north of tributary (m^2)	Drainage area south of tributary (m^2)	Drainage area change at tributary (m^2)	Percent drainage area change
Chomrong Khola	2.289×10^8	2.692×10^8	4.03×10^7	18 %
Kimrong Khola	2.747×10^8	3.361×10^8	6.14×10^7	22 %
Bhurundi Khola	4.025×10^8	4.889×10^8	8.64×10^7	21 %

Figure 16: Drainage area versus distance plot for the Modi Khola profile
The Chomrong, Kimrong, and Bhurundi Kholas, all major tributaries, produce 18-22% increases in drainage area. The grey rectangle represents the high concavity zone on the Modi Khola profile.

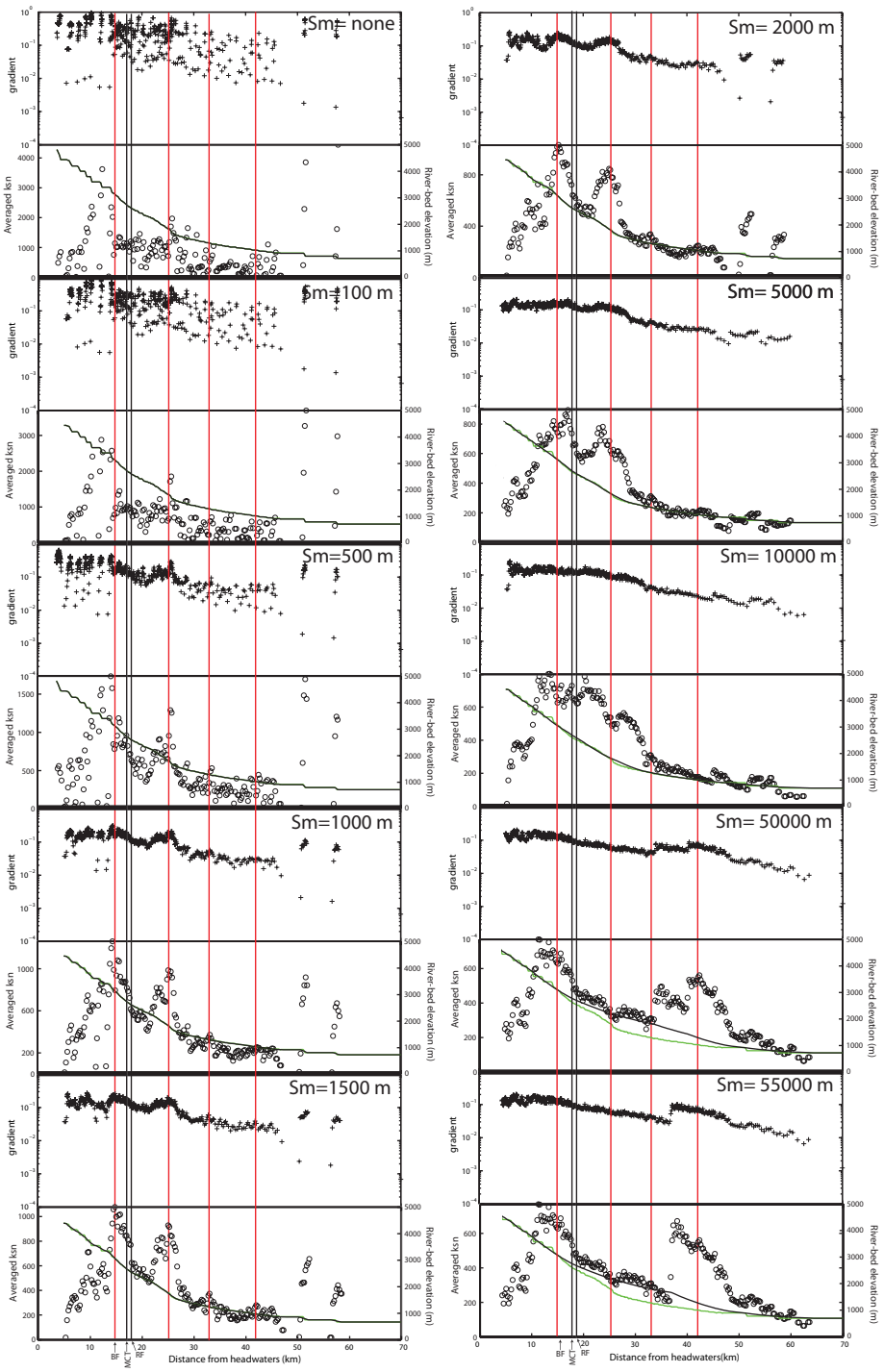

Figure 17: Smoothing windows

Several smoothing windows were tested ranging from none to 55 km. The four steepness peaks, shown by the red lines, as in Figure 12, consistently occur in the same location regardless of smoothing window size. Note the locations of the Bhanuwa Fault (BF), Main Central Thrust (MCT), and Romi Fault (RF) for reference. Plus marks shows raw slope data for each smoothing window size. Open circles represent values of k_{sn} based on log slope versus distance data for the Modi Khola over a 0.5 km window with an assumed reference concavity of 0.45 for each smoothing window size. Black stream profile line is smoothed and green stream profile is unsmoothed.

TABLE 1. RIVER STEEPNESS AND CONCAVITY CHANGES ON THE MODI KHOLA

k_{sn}	$k_{sn}+2\sigma$	$k_{sn}-2\sigma$	A_{min}	A_{max}	θ	$\theta\,2\sigma$	k_s	R^2
846	870	822	1.74E+08	1.84E+08	-7.11	4.39	3.61E-60	0.34
858	867	848	1.84E+08	1.95E+08	5.79	2.19	1.29E+47	0.38
582	606	557	1.95E+08	1.97E+08	-16.59	25.84	2.77E-139	0.25
580	621	540	1.97E+08	2.02E+08	10.28	5.91	2.22E+84	0.8
556	583	529	2.02E+08	2.03E+08	-135.38	216.48	0	0.57
562	596	527	2.03E+08	2.05E+08	16.37	10.25	1.10E+135	0.96
552	577	527	2.05E+08	2.06E+08	-44.91	29.16	0.00E+00	0.7
434	661	207	2.06E+08	2.09E+08	12.52	65.13	1.02E+103	0.86
556	651	462	2.09E+08	2.12E+08	-430.81	780.32	0	0.74
466	527	406	2.1E+08	2.13E+08	-56.45	177.98	0	0.48
494	541	446	2.13E+08	2.14E+08	-68.65	68.41	0	0.77
574	601	546	2.14E+08	2.14E+08	-61.81	147.50	0	0.15
632	1001	264	2.14E+08	2.17E+08	24.60	98.02	1.18E+204	0.91
835	871	800	2.17E+08	2.2E+08	-47.69	58.31	0	0.35
684	711	658	2.2E+08	2.21E+08	-4.85	147.54	4.17E-42	0.0014
850	875	824	2.21E+08	2.23E+08	-2.32	18.11	6.92E-21	0.013
657	680	634	2.23E+08	2.25E+08	10.80	33.14	1.92E+89	0.12
884	944	825	2.25E+08	2.25E+08	-350.07	136.85	0	0.84
843	858	829	2.25E+08	2.28E+08	8.36	17.20	1.08E+69	0.078
740	749	730	2.28E+08	2.29E+08	34.04	97.46	4.24E+283	0.057
424	452	396	2.29E+08	2.7E+08	5.07	6.74	3.68E+41	0.31
404	441	366	2.7E+08	2.71E+08	-36.93	209.42	2.35E-313	0.057
352	415	288	2.71E+08	3.36E+08	-9.46	13.07	8.09E-82	0.83
317	334	300	2.75E+08	3.37E+08	1.94	1.50	1.62E+15	0.85
292	298	286	3.37E+08	3.54E+08	-3.63	2.21	4.30E-33	0.57
221	295	146	3.54E+08	3.56E+08	35.05	298.82	1.83E+298	0.69
398	440	355	3.56E+08	3.58E+08	-78.05	83.10	0.00E+00	0.89
287	300	274	3.58E+08	3.7E+08	26.72	21.08	2.01E+227	0.68
228	284	172	3.64E+08	3.71E+08	-6.08	64.69	2.45E-54	0.029
235	297	173	3.7E+08	3.77E+08	-8.21	70.83	1.31E-72	0.11
165	348	-18	3.77E+08	3.83E+08	32.10	122.52	6.49E+273	0.92
180	198	162	3.83E+08	3.95E+08	-10.34	16.16	4.36E-91	0.44
203	236	170	3.95E+08	4E+08	-37.69	41.66	0	0.73
215	252	177	4E+08	4.02E+08	-58.41	151.25	0	0.33
204	227	181	4.89E+08	5.01E+08	-4.92	27.95	4.21E-45	0.095
191	215	166	5.01E+08	5.05E+08	13.63	123.52	9.75E+116	0.039
183	217	149	5.05E+08	5.09E+08	35.56	167.42	8.57E+307	0.29

Notes: Values extracted from stream segments shown by dashed vertical lines in Figure 5.
All stream segments exist within the High Concavity zone shown in Figure 6.

TABLE 2: MAJOR EXTREMA AND TRANSITIONS IN RIVER STEEPNESS ON THE MODI KHOLA

River steepness extrema or transition location description	Location	k_{sn} (north)	k_{sn} (south)	θ (north)	θ (south)	k_{sn} factor Δ	θ factor Δ
Middle of Formation II	A	858	582	5.79	-16.59	1.5	-0.3
Contact between Formation II and Formation I	1	434	556	12.52	-430.81	0.8	-0.03
Bhanuwa fault	2	884	843	-350.07	8.36	1.0	-41.87
Peak in Kuncha formation south of the Ulleri granite	3	398	287	-78.05	26.72	1.4	-2.92
Peak at contact between Kushma and Kuncha	4	215	204	-58.41	-4.92	1.1	11.87

Notes: Location A is a river steepness transition, location 1 is a river steepness minimum, location 2 is a river steepness maximum, location 3 is a river steepness maximum, location 4 is a river steepness maximum

Chapter 3: Data acquisition

The Shuttle Radar Topography Mission (SRTM) yielded publicly available, high resolutions digital elevation models (DEMs) at 1 arc second (~30 m) resolution in the United States and 3 arc-second (~90m) resolution worldwide. The absolute vertical height accuracy across the entire SRTM dataset is 16 meters. SRTM data have become important for the scientific community and are the only free, public DEM available for Nepal. Unfortunately glaciated and steep topography created voids in the SRTM data, making SRTM DEMs unusable for the Modi Khola valley study site. To address this issue, topographic maps were scanned and digitized, allowing specialized interpolation methods to be incorporated to produce a high resolution DEM at 25 m resolution.

3.1 SRTM data for central Nepal

3.1.1 SRTM data collection

The objective of the SRTM, sponsored as an international project by the National Geospatial-Intelligence Agency and NASA, was to "obtain elevation radar data on a near-global scale to generate the most complete high-resolution digital topographic database of Earth" (JPL, 2000). For 11 days in February of 2000 a unique radar system equipped the Space Shuttle Endeavour allowing mapping of about 80% of Earth's surface elevation. The shuttle was launched into orbit with an inclination of 57 degrees, allowing SRTM's radars to cover regions between 60 degrees north and 56 degrees south (Figure 18).

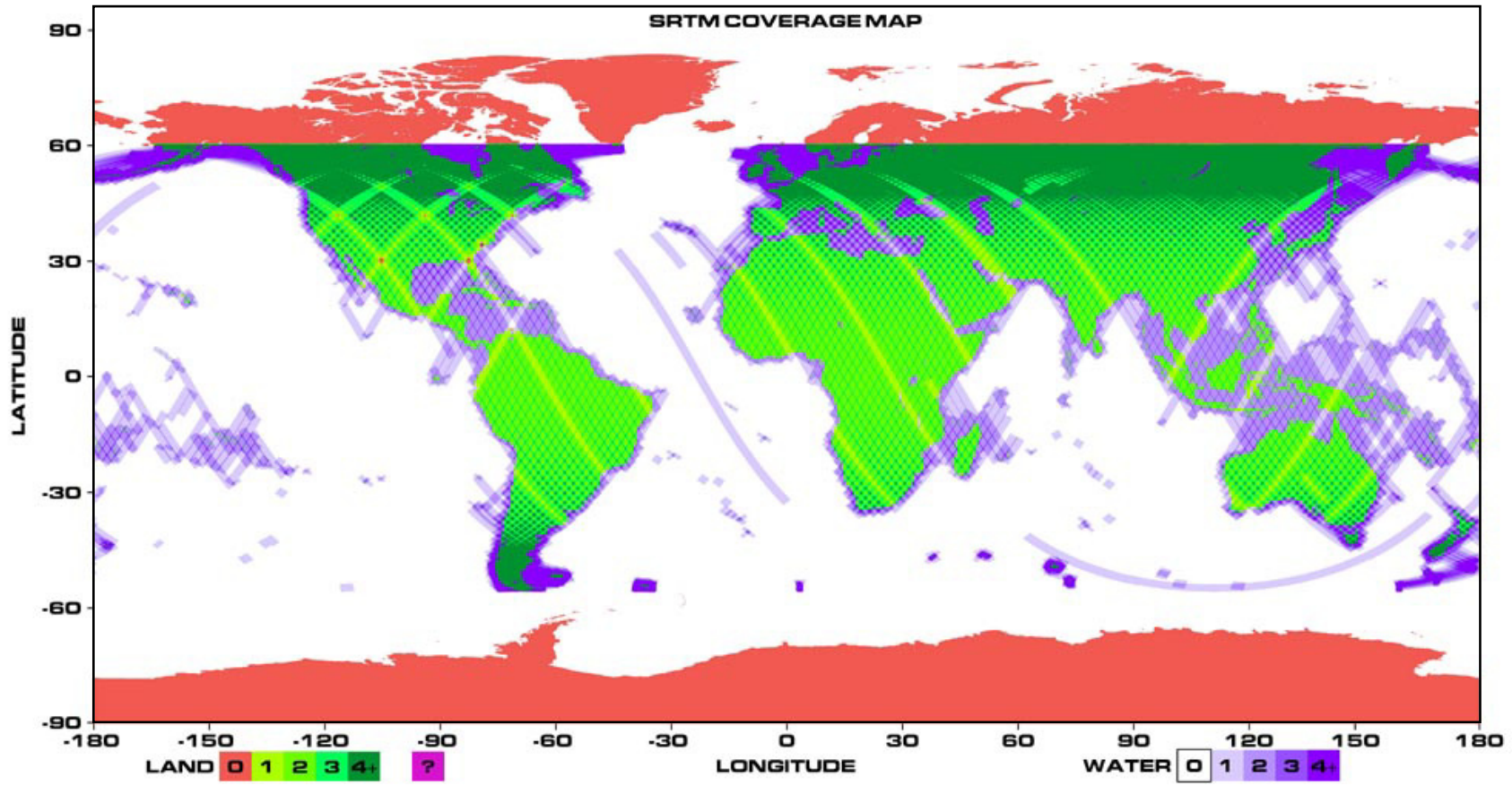

Figure 18: SRTM data coverage map
SRTM data was collected in a swath across the globe spanning in latitude from 60° N to 60° S. The colors of the swaths indicate the number of times the area was imaged by SRTM. For land, green shows regions where data was collected once, yellows-green shows regions where data was collected twice, etc., as shown in the key at the lower left. Over water, data collection is colored in shades of blue as shown in the key at the lower right. Red areas near the poles could not be mapped. As the SRTM mission focused on topography, most data was acquired over land. Only small amounts of data were collected over water for calibration purposes. (Figure from http://www2.jpl.nasa.gov/srtm/coverage.html)

For this mission, two radar antennas were installed, one in the shuttle cargo bay and the other at the end of a 60 m mast extended into space. Radar images were taken concurrently from each antenna allowing interferograms to be created (Figure 19). The two radar beams can be combined or "interfered" to determine a phase difference, extracting topographic data (Bridges, 2000).

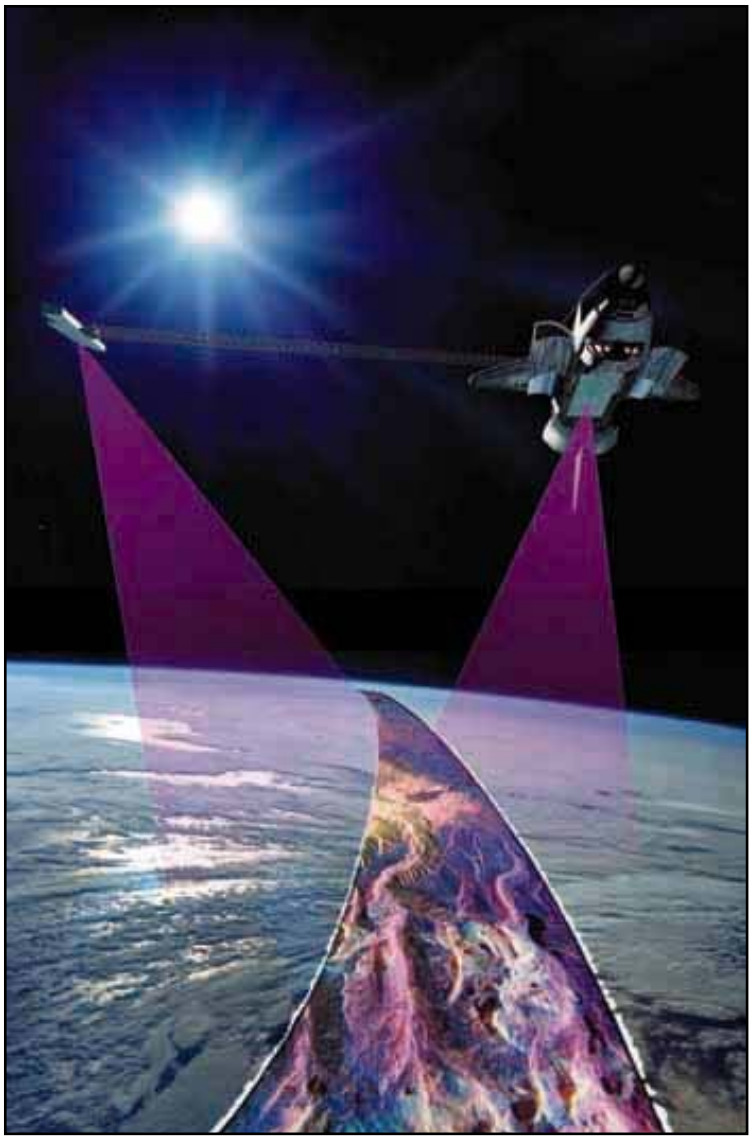

Figure 19: Artist's depiction of SRTM data collection
Title: Radar penetrates clouds and uncovers swath as it flies over Earth. Courtesy of Ball Aerospace & Technologies Corp. (Figure from http://www2.jpl.nasa.gov/srtm/multimed.htm)

The dual radar capability of SRTM has mitigated several problems experienced by conventional imagery, including independence from solar illumination, cloud cover, and forest canopies (Duren, 1998).

3.1.2 SRTM data voids in the Nepalese Himalaya

The accuracy of SRTM data have been assessed from a variety of outside sources including GPS ground points and LIDAR (Light Detection and Ranging) data. Studies by Berthier et al. (2006), Falorni et al. (2005), and Kaab (2005) found that SRTM accuracy depends on the local topography and that errors are greater in mountainous terrain than on planar surfaces (Luedeling et al., 2007).

While SRTM data are approximately 95% complete over the collection area, some of the data exhibit radar artifacts that produce scattered patches of data voids. Shadow and layover effects or poor signal returns over mountainous terrain, and occasional phase wrapping errors create data voids (Dowding et al., 2004). A study by Hall et al. (2005) indicated that data voids comprised only 0.3% of the SRTM dataset for the United States, but comprised 30% of the total coverage area in the mountainous terrain of Nepal.

Shadow occurs when an area is not illuminated by radar signals. Layover is a type of foreshortening where the top of an object is imaged before the bottom. These phenomena cause problems synthesizing two interferometeric channels and create data voids (Dowding et al., 2004). The number of SRTM passes has reduced, but not completely eliminated shadow and layover effects.

Water causes specular reflection of radar signals. When a radar signal hits water or ice it acts like a mirror and reflects the signals away from the SRTM sensor.

Topography with near vertical slopes also diverts radar signals away from the SRTM sensors. The frequency of data voids increases for surface inclinations above 20º because of radar shadowing (Luedeling et al., 2007). Glaciers and near vertical slopes dominate large portions of the Himalayan range. SRTM data for central Nepal contain approximately 4,238,025 km^2 of data void area, which is 9% of the total data area (Figure 20).

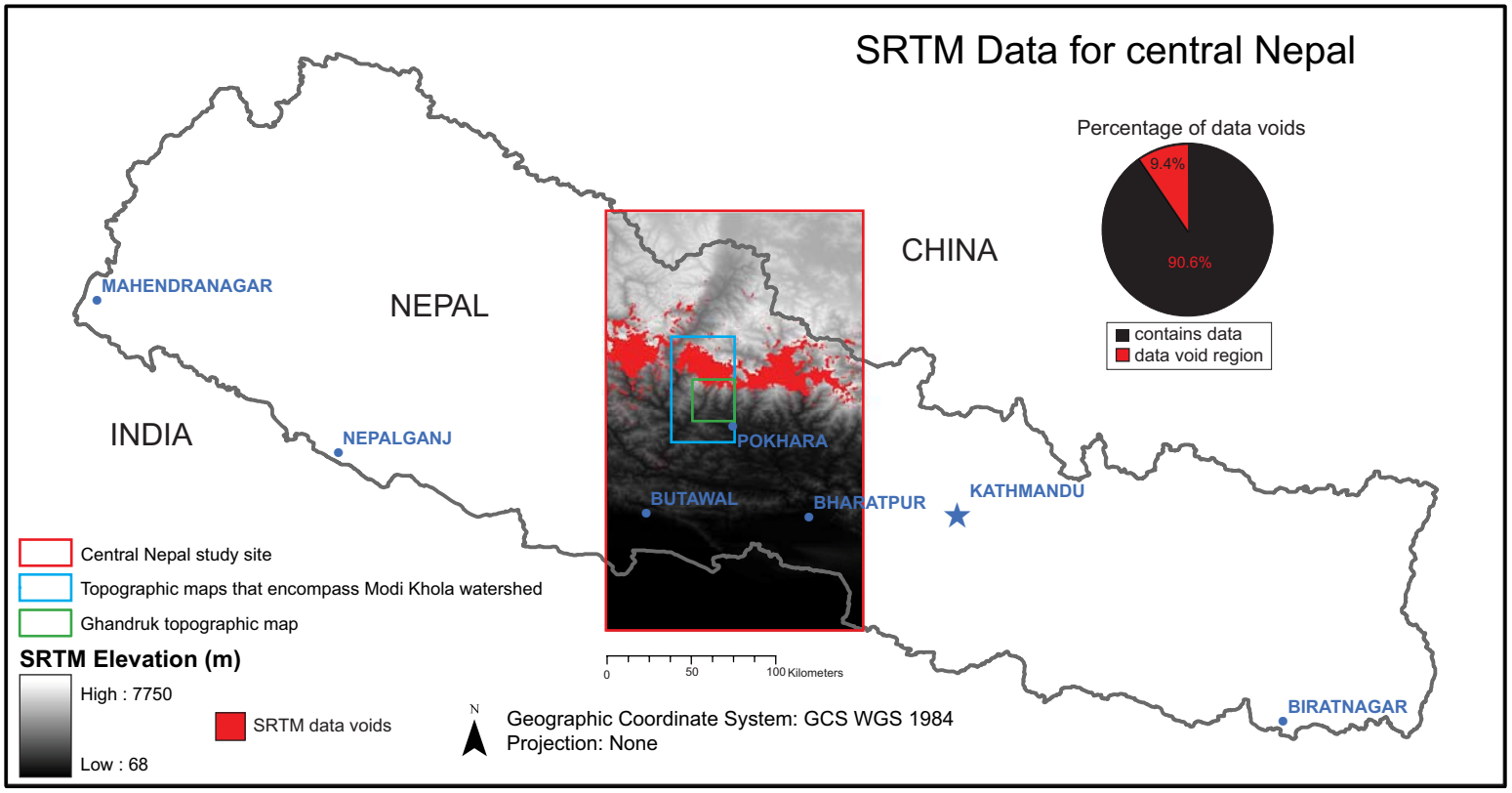

Figure 20: SRTM voids in the central Nepalese Himalaya

3.1.3 SRTM data voids in the Ghandruk topographic map

Within the Ghandruk topographic map, the SRTM data contain 9,713 km^2 of data void area. These voids comprise 23% of the map area, meaning elevation values can only be extracted from 77% of the map area in the Ghandruk region. The data voids dominate the northeast part of the map near Macchapucchare, the highest mountain summit on the map at 6997 m, but also appear in scattered patches throughout the entire map region (Figure 21).

While SRTM data provide quality DEMs for some parts of the world, the large number of voids present in the Ghandruk topographic map makes SRTM data unusable for this analysis. The lack of information in data voids magnifies problems in the dataset when slope is calculated. Since slope is the primary dataset of interest in this analysis, and SRTM data are unusable for this region, an alternate DEM source must be explored.

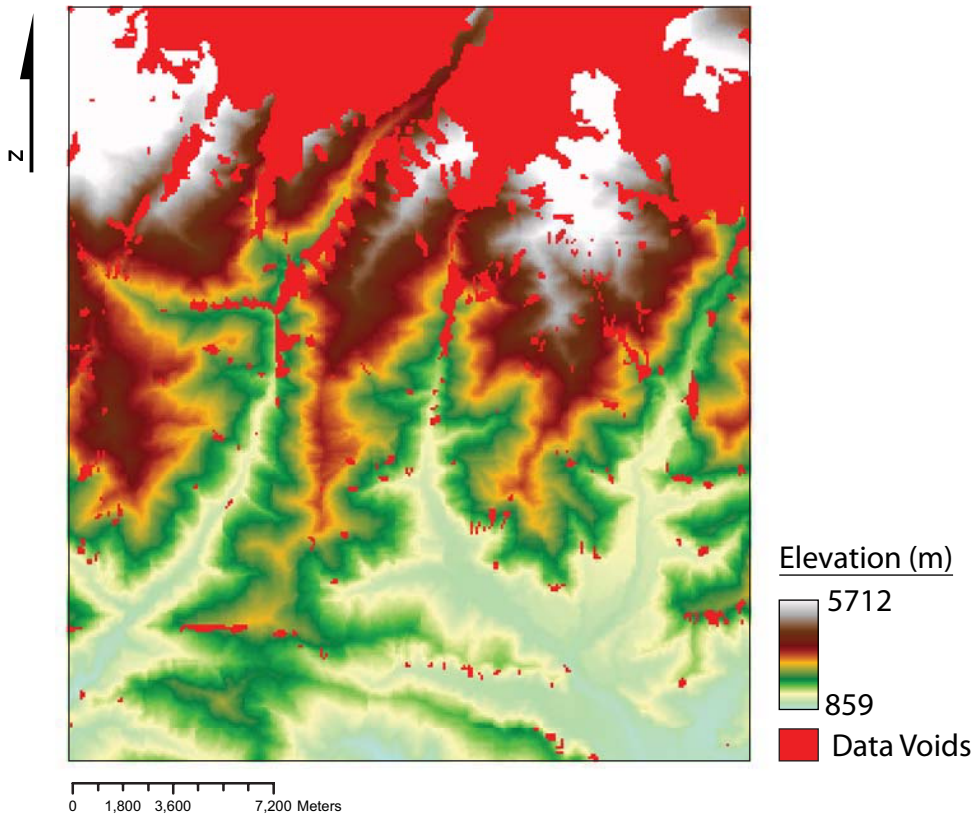

Figure 21: SRTM voids in the Ghandruk topographic map
Geographic coordinate system: WGS 1984 UTM Zone 44N. Projection: Transverse Mercator.

3.2 Digitized topographic maps of central Nepal

To generate a high resolution digital elevation model for Nepal, workers in Nepal digitized 100 m and 200 m contours from topographic maps using an autotrace program in ArcGIS. I corrected errors generated from the autotrace program, yielding a complete digital topographic database for central Nepal. A triangulated irregular network (TIN) was created from contours, making a continuous surface from the contours and projected in three dimensions. While the TIN allowed an adequate visual representation of elevations over a regional scale, it produced false irregular flat terraces in the topography making the DEM problematic at a local scale. For this project, higher resolution contour lines digitized at 40 m instead of 100 m

were acquired from the Nepal Department of Mining and Geology (DMG). Alternate interpolation methods were applied to the contour line data to produce more realistic DEMs that avoid the creation of false flat terraces generated in the TIN method. The specialized interpolation of digitized contour lines made it possible to generate DEMs without data voids and at a high enough resolution (25 m) needed for my analysis.

3.2.1 Topographic maps of central Nepal

The available topographic data for this project encompass the area within the limits of the north and south country borders of Nepal and between 83°15'00" and 84°45'00" longitude and is comprised of 123 topographic maps (Figure 22). Contour lines on these topographic maps were constructed by cartographers using aerial photography and stereoscope projection. The central Nepal topographic data are comprised of 22 fifteen minute topographic maps, at a scale of 1:50,000 and index contours at 200 meters and 101 seven and a half minute topographic maps with a scale of 1:25,000 and index contours digitized at 100 meters. The Japan International Cooperation Agency (JICA) created 23 topographic maps with 50 meter index contours at the 7.5 minute scale because they wanted a detailed map of Buddha's birthplace (red squares in Figure 22). The Japanese maps were digitized by Nepalese workers at 100 meter index contours to be consistent with the other 7.5 minute maps. The remaining seventy-eight 7.5 minute (blue squares) and all the fifteen minute maps (green squares) were produced by the Survey Department of His Majesty's Government of Nepal in cooperation with the Government of Finland, FINNIDA (Figure 22). The fifteen minute maps were created with two times the contour interval than the 7.5' maps because it was difficult to extract topographic data from the high elevations and steep slopes in these regions (Figure 22).

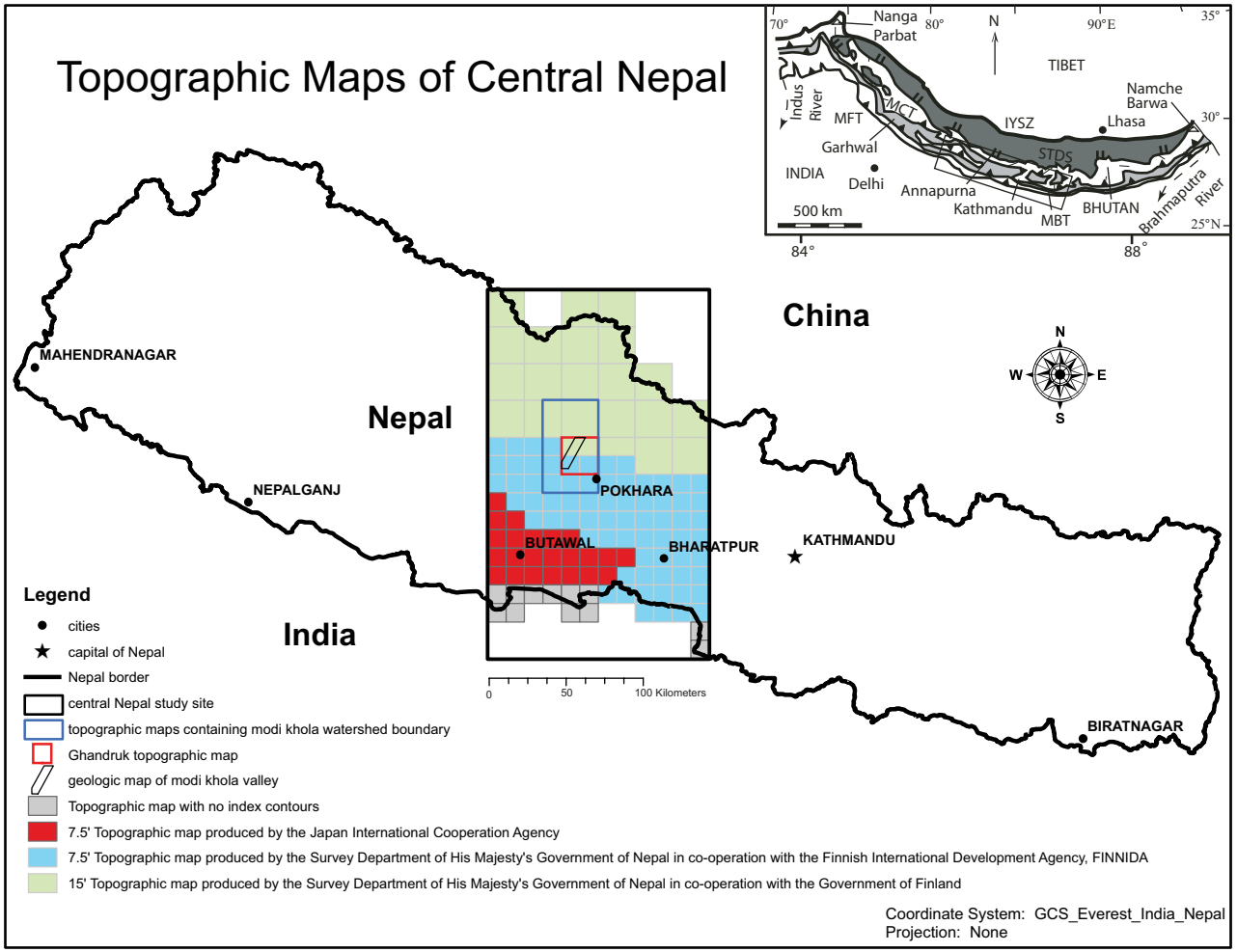

Figure 22: Topographic map index and study site location
Topographic map index outlining the central Nepal study site and organizations that produced topographic maps used in this analysis. Inset: highly generalized geologic map of the Himalyan orogen from Sorkhabi and Macfarlane (1999) (Map in upper right corner extracted from Martin et al., 2005). Geographic coordinate system: GCS Everest India Nepal.

3.2.2 Digitized contour lines and error correction methods

Since a computerized version of these topographic maps is not available, each topographic map was scanned and then rectified in the computer to fit in degrees of longitude and latitude using the GCS Everest India Nepal coordinate system. The rectified topographic maps are located in the grid of longitude and latitude, but have no projection which incorporates the curve of the Earth's surface. Since these digitized maps have no projection, these maps can be easily altered to any projection later, making these data useable in several types of analysis. Nepalese workers digitized the index contours on each topographic map by hand with the aid of ArcScan, a computer assisted autotrace program in ESRI's ArcGIS software. To extract the contour line data digitally, the red contour lines from a scanned topographic map were converted to black and other colors on the map were converted to white and saved as a .TIFF file. The black and white image is ideal for digitally tracing contour lines, but other red symbols and areas where contours were intersected by other attributes of the map introduced impurities into the black and white map template. The autotrace tool produces minor, yet significant errors to occur while the contour lines were digitized. Errors include places where contour lines intersect, are incomplete, or have no assigned elevation value (Figure 23). The use of the autotrace tool enables relatively quick extraction of digital data from topographic maps, but it is important to fix these errors before using this digital data in a geospatial analysis.

Uncorrected contour lines would generate inaccurate results, and thus interpretations, from a spatial analysis of the data. Figure 24 illustrates errors and problems visually by comparing DEMs generated from corrected and uncorrected contour lines.

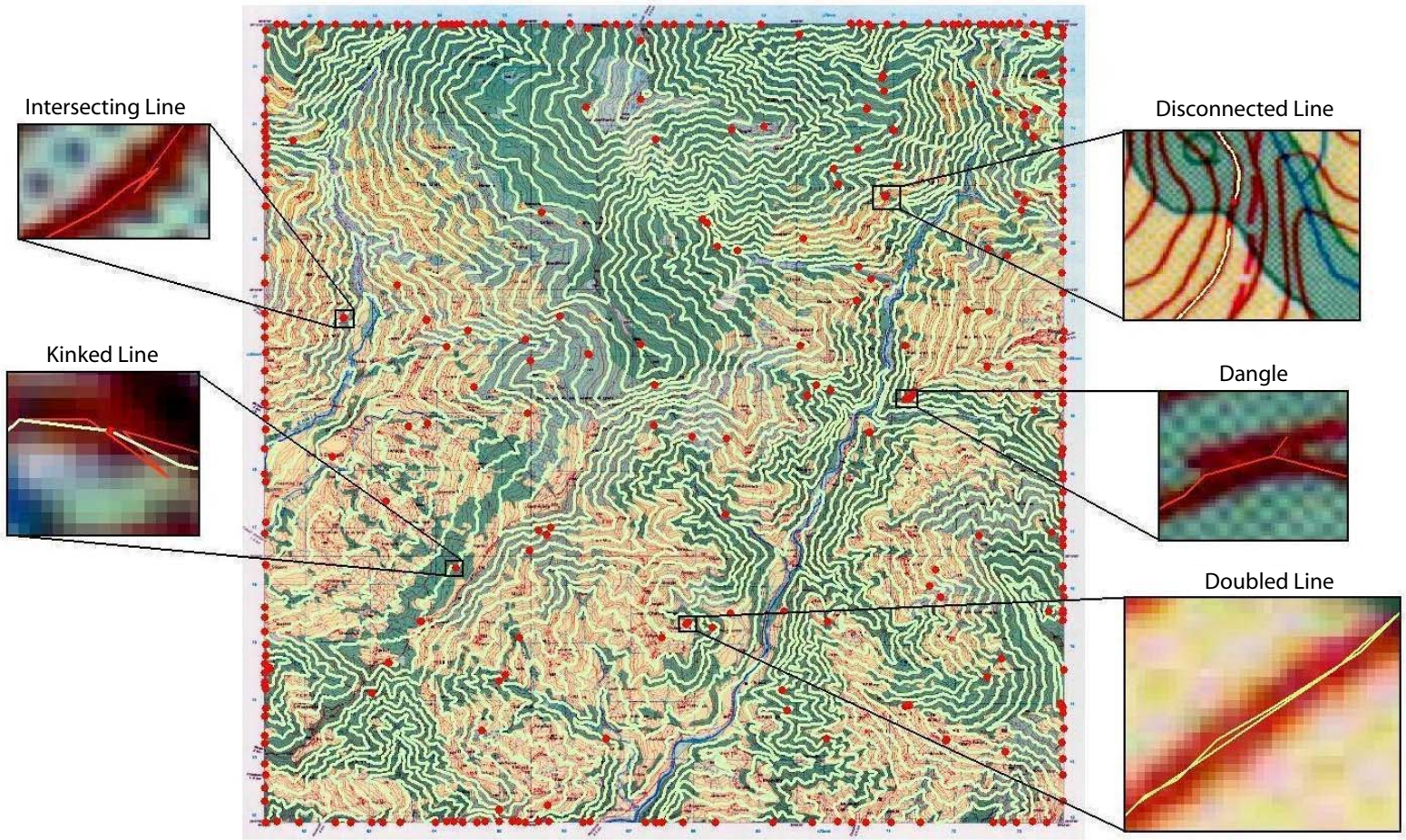

Figure 23: Contour line errors generated by autotrace program

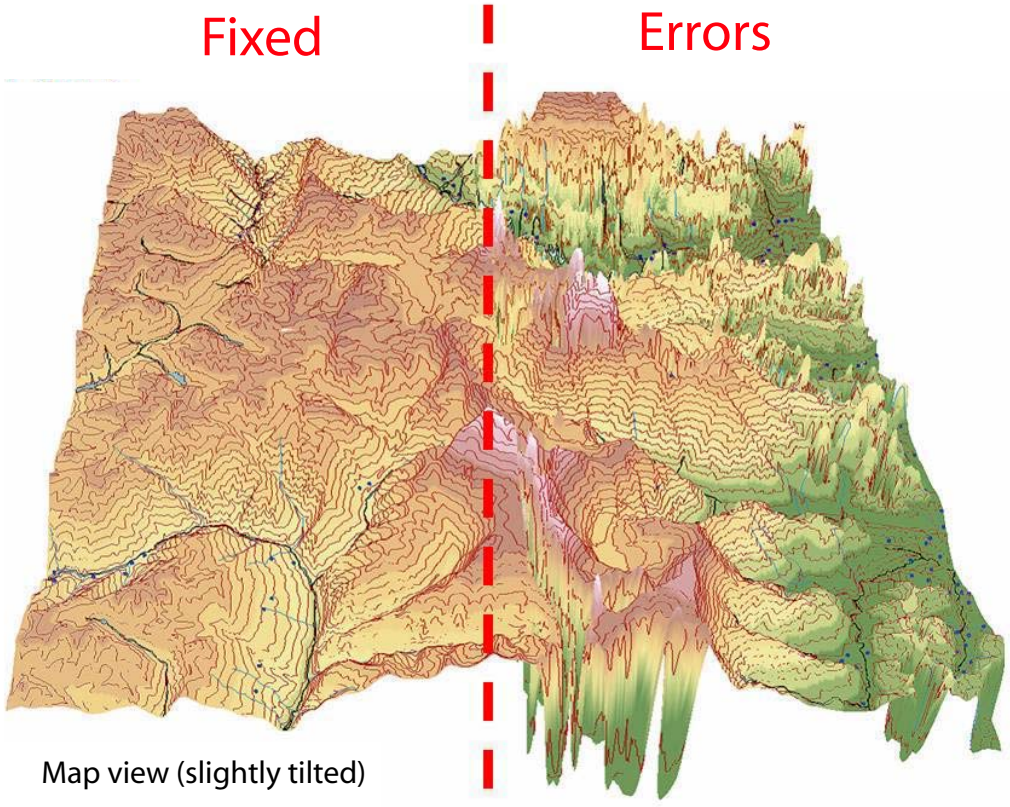

Figure 24: Comparison of DEMs generated from corrected and uncorrected contour lines

3.2.3 Ghandruk topographic map

Once the digital contour lines were corrected for central Nepal, the focus of the study was narrowed to the Modi Khola valley. Choosing the Modi Khola valley as the study site for this analysis offered many benefits, such as access to a detailed geologic map by Martin et al. (2009) (Figure 5) and new exploration opportunities as river steepness has not been assessed for the Modi Khola (Wobus et al., 2006b). The geologic map of the Modi Khola is encompassed by the Ghandruk topographic map (Figure 25). Digital contour lines spaced at 200 m would not yield a high enough resolution map to assess the spatial changes of some lithologic units of interest that spanned as small as 1 km. To address this dilemma, digital contour lines at 40m resolution were purchased from the Nepal Department of Mines and Geology (DMG). It would be expensive to acquire this data for the entirety of central Nepal, but was necessary for detailed analysis in the Modi Khola valley. With more time, the Ghandruk topographic data could have been digitized at the 40 m interval, by utilizing the methods described in this report. Ojha Tank provided this data so I elected to use the DMG data in order to have the most detailed data possible for this analysis. The 200 m digitized contour lines were used to obtain elevation data needed for the watershed, which extends past the Ghandruk topographic map, in order to perform the river profile analysis.

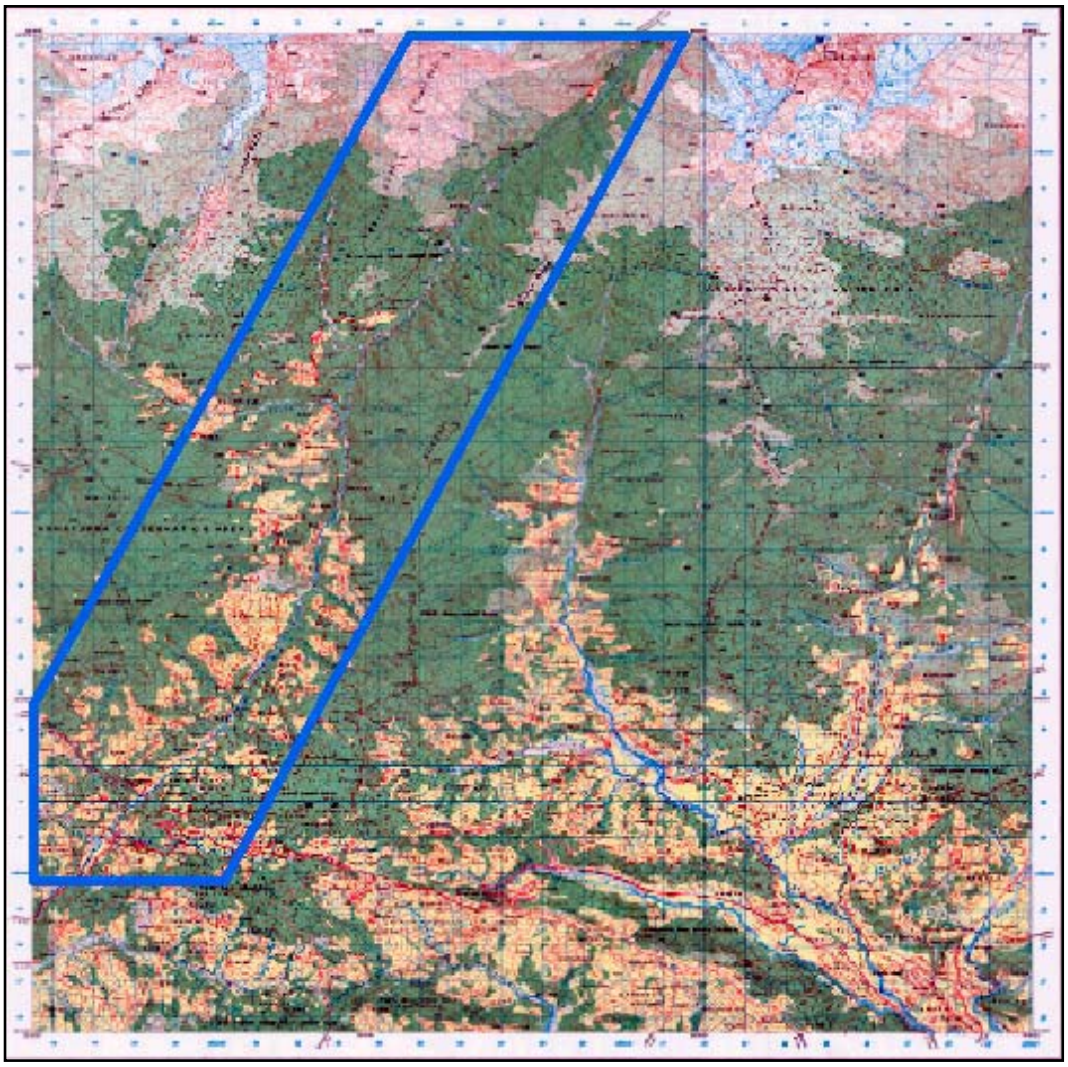

Figure 25: Ghandruk topographic map sheet
Topographic map of the Ghandruk region. Blue border shows location of main study site, the region bounded by the Modi Khola geologic map. Source: The Survey Department of His Majesty's Government of Nepal in cooperation with the Government of Finland, FINNIDA

3.3 Irregular flat terraces from TIN interpolation

3.3.1 TIN interpolation procedure

A triangulated irregular network (TIN) was created from contour line data and used to represent the elevation surface of the Ghandruk topographic map. The points that comprise the contour line become nodes, whose z-values must be incorporated into the TIN triangulation. Every node is joined with its nearest neighbor to form triangle edges. Each edge has only 2 nodes, but a node may be in contact with two or more edges. The slope can be calculated along the edge from one node to another, representing the elevation surface between nodes. The x, y, and z coordinate values of the 3 nodes of each triangle facet can be used to derive slope, aspect, surface area, and surface length. If the 3 node values of the triangle are known, geometry can be used to calculate the x, y, and z values of any point on the triangle facet, making it possible to extract regularly spaced data from the DEM. The ArcGIS TIN calculation follows the Delaunay criterion, in which the triangle facets are drawn with the largest and nearly equilateral angles possible (Worboys, 2004).

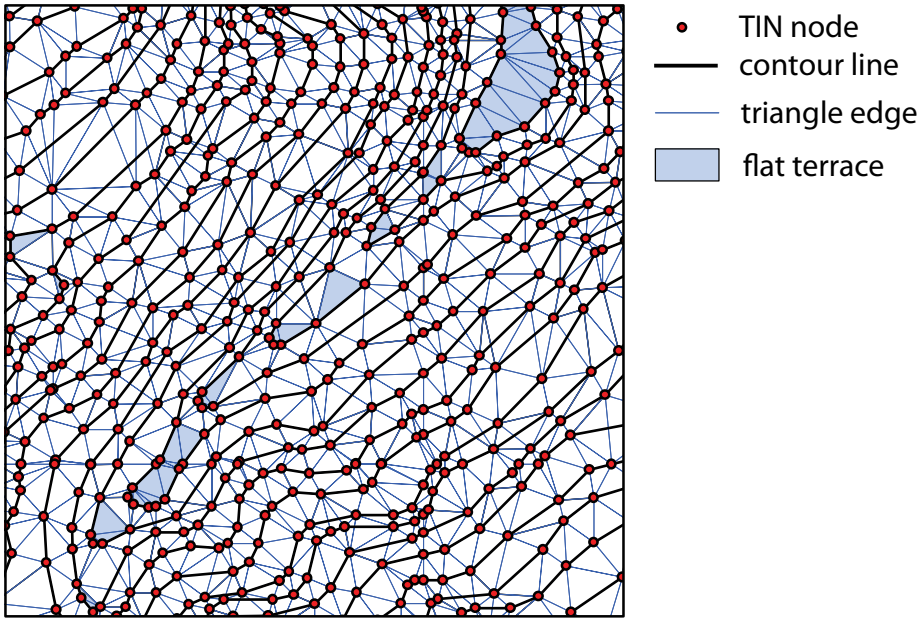

Figure 26: TIN generation
Points that comprise the contour line are used to triangulate a surface

Other studies have experienced the problem of horizontal flat terraces when using the TIN grid interpolation method and have proposed algorithms to solve the problem (Ware, 1998; Barbalic and Omerbegovic, 1999). Figure 27 illustrates the occurrence of the flat irregular terrace problem in the Modi Khola region. The mountain peak shown is Macchapucchare, the highest peak near the Modi Khola valley, known for its steep slopes that form a fish-tail like summit. The characteristic steep slopes of this region should not allow slopes less than 1 degree to be present in the landscape, yet several flat irregular terraces are visible in the landscape when a TIN grid is projected in 3D (green places on 3D slope map).

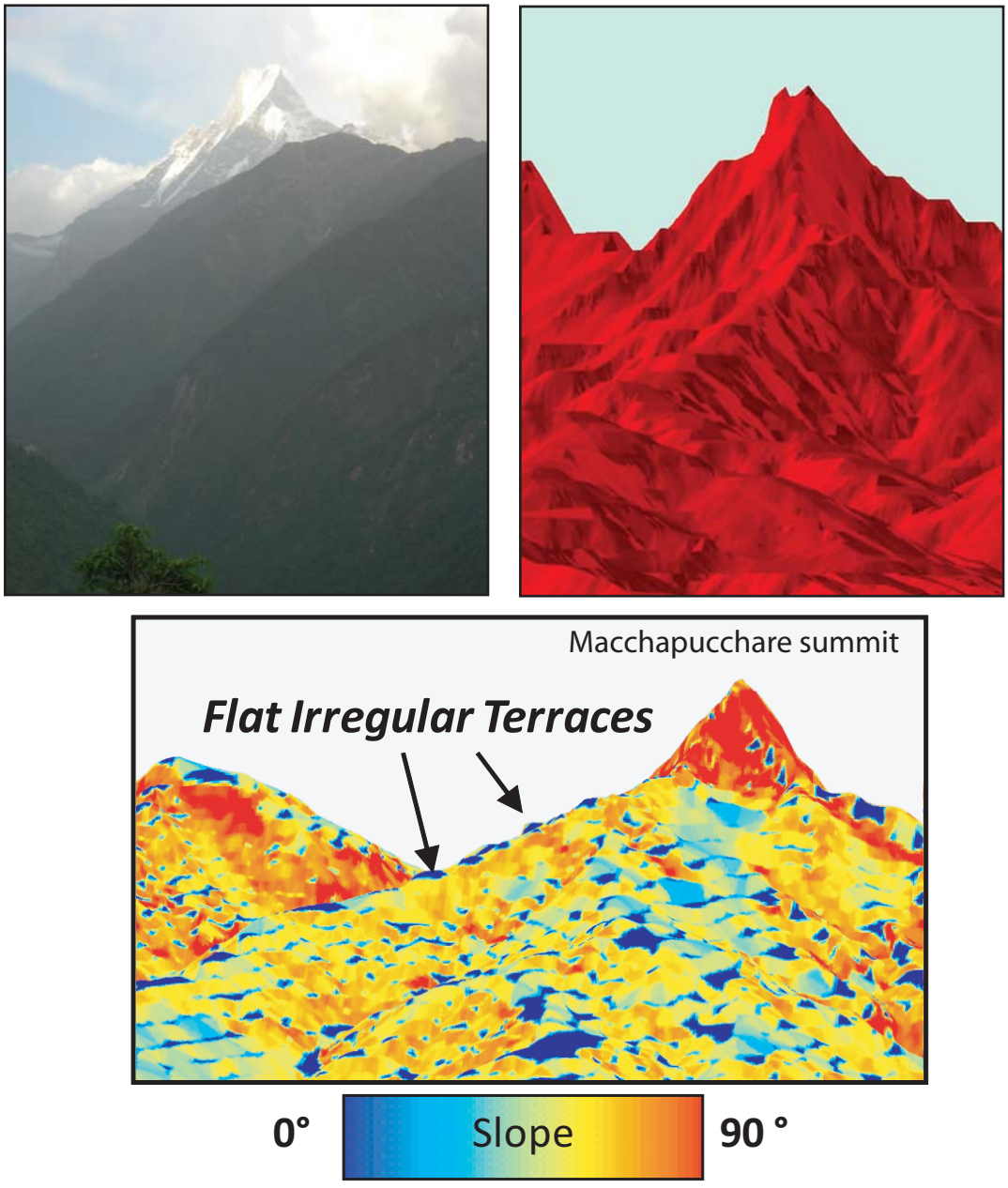

Figure 27: Flat irregular terrace problem shown on Macchapucchare summit
Left image shows a photograph of the Macchapucchare summit looking north up the Modi Khola valley (provided by Kate Burgy). The right image shows a 3D TIN representation of the surface created using ArcGIS. The bottom image shows a 3D TIN model with slope. Blue patches on the slope map that represent flat terraces on the ridge descending from the Macchapucchare summit. These terraces are not realistic since no slopes in the Modi Khola valley are less than 1 degree.

3.3.2 Recontouring

Interpolation errors often occur during the conversion of contour lines into a DEM. These errors produce artificial stair-steps in the landscape which cause several flat terraces with values of zero degree slopes. Some of these problems were alleviated during recontouring during DEM creation, where the raw elevation data was resampled at equal intervals, using the contour interval from the original data source (Figure 28). The TIN was created from the 40m contours and stored as a vector file, then converted to a grid format to facilitate spatial analysis. Recontouring was preformed from the grid reducing the contour interval to 8m. A new TIN was created from the recontoured lines, and then a second grid was generated from the new TIN. This significantly reduced, though did not completely eliminate, the number of flat terraces in the DEM.

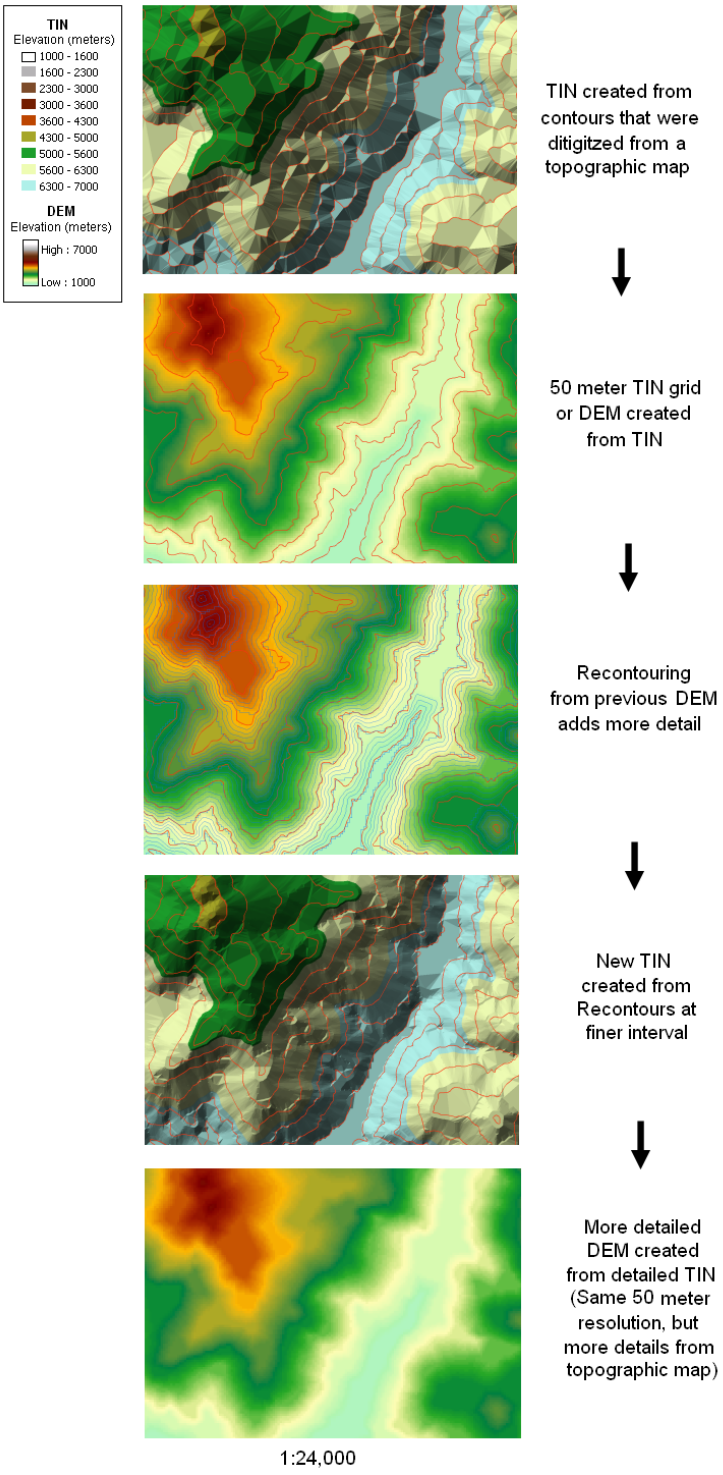

Figure 28: Improving the TIN grid interpolation
These series of figures show recontouring procedures that may improve the TIN grid interpolation results.

3.4 Alternative interpolation methods

To mitigate issues of flat terraces introduced from the TIN interpolation, a raster interpolation approach was adopted to allow exploration of a variety of grid based techniques. Points were extracted from contour lines, characterizing the input dataset as irregularly spaced elevation points. Irregularly spaced data classically are difficult to interpolate. Since point data were only available along contour lines, points were highly concentrated at the contour lines with large gaps of empty space between contour lines. This analysis required a raster DEM in which points are spaced at regular intervals. Interpolation is a procedure used to predict the value of cells at locations the lack data points. The empty space between elevation data points must be interpolated, or calculated, in order to produce a continuous surface at regularly spaced intervals.

Two different interpolation techniques were applied to the data by Karl Schleicher and Tom Fedenczuk allowing a reduction of flat irregular terraces and the creation of a more realistic DEM. Karl Schleicher's method used regularization by inverse linear interpolation to create gridded elevation data with a minimum resolution of 10 m (See Appendix A). Tom Fedenczuk used the multiquadric radial basis function to build an interpolated elevation surface with a minimum resolution of 25 m resolution (See Appendix B, Figure 30).

Later in the study, Ofori Pearson provided us with an alternative elevation dataset for the Modi Khola valley. Ofori Pearson digitized contour lines from the Ghandruk topographic map using similar methods as described in this paper. In addition, Ofori's dataset included digitized spot elevations, rivers, and glacial borders.

These topographic data were interpolated using the ArcGIS Topo to Raster function within ArcToolbox. The Topo to Raster method yields promising results that do not produce flat irregular terraces and can be easily generated at a variety of resolutions. The Ofori Pearson interpolation is used as an alternative dataset for this analysis, allowing me to test the reproducibility and repeatability of the DEM production methods outlined in this thesis. Figure 29 shows DEMs created from all interpolation methods investigated in this analysis.

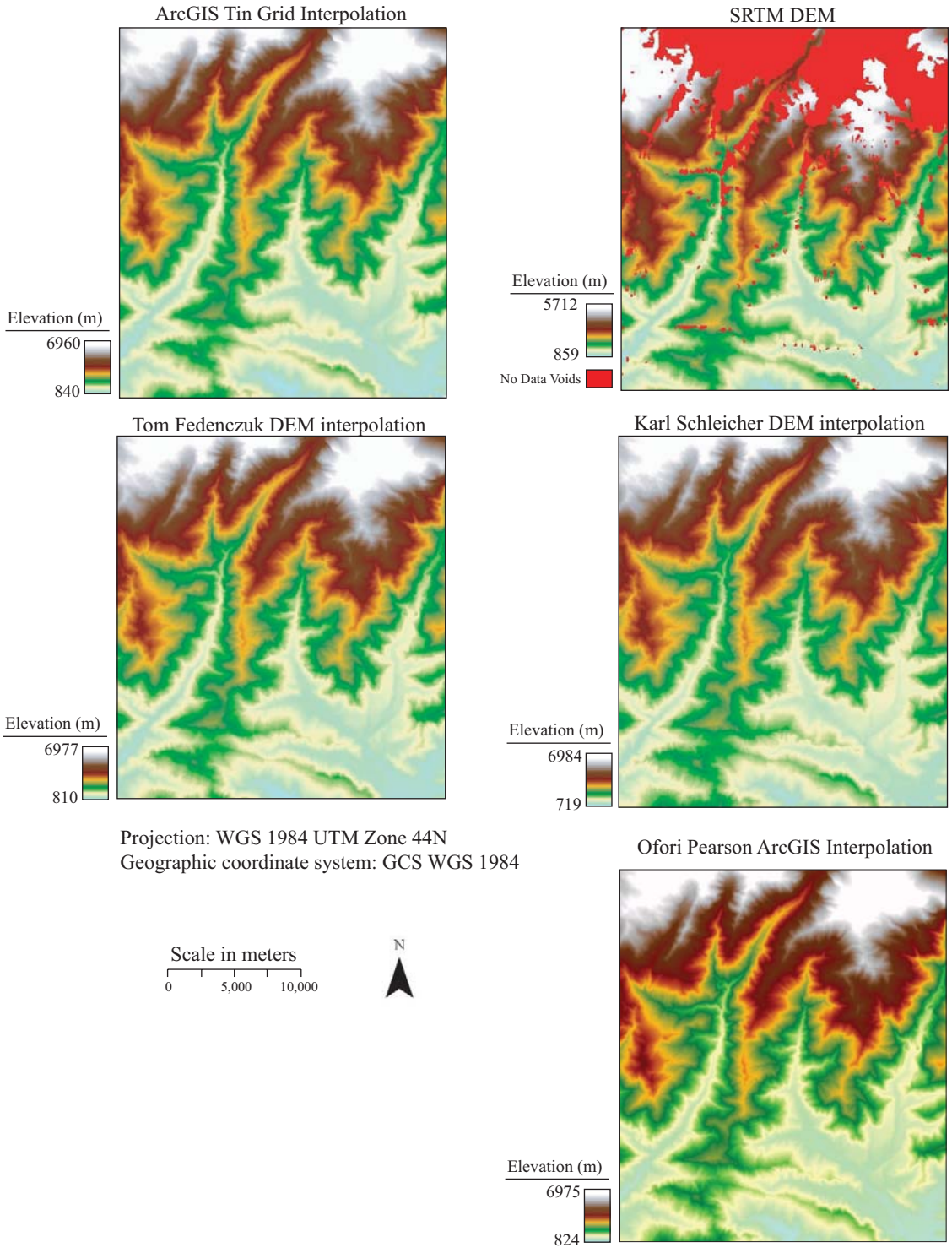

Figure 29: DEM comparison
Maps comparing DEMs created from a variety of interpolation methods (25 m resolution).

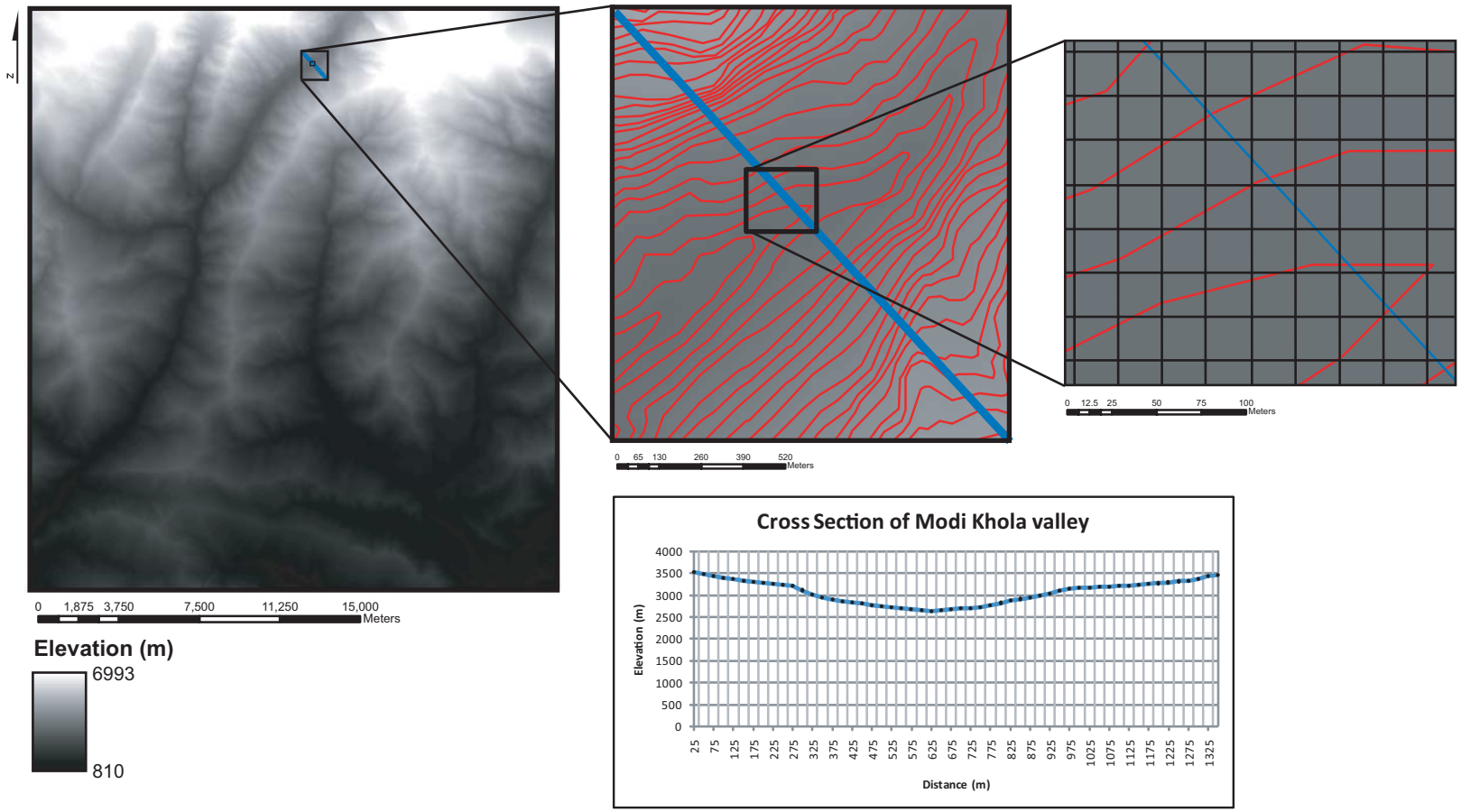

Figure 30: DEM cell size (25 x 25 m) compared to Fedenczuk Interpolation
A sample of the DEM created using the Fedenczuk interpolation method was extracted in order to evaluate the number of DEM cells located between the contour lines and to evaluate the interpolation method by examining a cross-section of the interpolated surface. The image on the upper left shows the DEM for the Modi Khola valley and the location where the DEM was sampled, the upper center image shows the location of the contour lines used to make the DEM with the red lines and the location of the cross-section transect with the blue line, and the image in the upper right shows an inset of the center image to show the relationship between the size of the 25 x 25 m DEM cells and how these cells are arranged between the contour line cells. The value for the DEM cell is taken from the center of the cell. Elevation values were extracted from the interpolated DEM every 25 m along the blue transect line to produce the cross-section of the Modi Khola valley shown in the lower right corner. Black dots shown on the blue profile line in the cross-section plot mark the center point of each 25 m DEM cell.

Chapter 4: Uncertainty in geographical information

The spatial component of geographical data produces unique issues that must be remembered when working with GIS data. The selected scale and data aggregation of an analysis directly affect the results obtained from a spatial analysis. The geographical scale at which a phenomenon is examined can affect the observations we make and should always be considered before analysis (O'Sullivan and Unwin, 2003). This chapter addresses aspects of elevation uncertainty present in spatial data in order to select the interpolation that would allow the greatest reduction of error. I compared elevations from my DEM interpolations with known spot height locations from the Ghandruk topographic map using the root mean squared error (RMSE) technique. I also measured the amount of irregular flat terraces present in each interpolation.

4.1 The problems and potential of spatial data

4.1.1 Geographical scale

For this analysis, I sought to derive the smallest resolution DEM possible by acquiring the highest resolution data available (40 m digitized contour lines) and applying an array of interpolation methods. Other studies used 30 arc second (~1 km) and 90 m DEMs to extract information about tectonics from topography (Finlayson et al., 2002; Finlayson and Montgomery, 2003; Wobus et al., 2006a; Wobus et al., 2003). In general, tectonic signals occur at scales significantly greater than the contour interval (Wobus et al., 2006a). Approximately 25 m resolution DEMs were

used to characterize topographic signatures of rock types in studies by Roering et al. (2005) and Korup (2008). I selected a 25 m resolution for this study in an effort to investigate tectonic signals and rock type signatures. I also explored an array of alternative DEM resolutions for this analysis, including: 10 m, 25 m, 30 m, 40 m, 50m, 90 m, 100 m, 200 m, and 500 m resolution DEMs. The 25 m DEM allowed me to examine the topography with the required detail needed for this analysis, while avoiding the introduction of artifacts observed at 10 m resolution.

4.1.2 MAUP - Modifiable area unit problem

Most geographic data are represented, at least to some extent, by aggregated regions or sampling areas. O'Sullivan and Unwin (2003) provide an excellent example of this using data collection for the national census. National census data are collected by household, but for practical and privacy reasons is reported at various levels of aggregation such as city districts, counties, and states. The problem is that the aggregation units used by the census bureau are arbitrary in relation to spatial phenomena one may investigate. The aggregation of the units will affect statistics solely based on how the data are reported by unit. Different aggregation methods could produce different results and spatial patterns from the same data source. This difficulty is referred to as modifiable area unit problem or MAUP.

Our choice of reference frame significantly determines observable spatial patterns. Politicians utilize the effects of MAUP to ensure the boundaries of electoral districts are defined in the most advantageous way to their parties. MAUP provides one explanation for why Al Gore, who maintained a greater popular vote than George W. Bush in the 2000 US election, still lost the presidency (Example from O'Sullivan

and Unwin, 2003). Decision making processes involving GIS often use publically available, yet still aggregated, maps. Spatial phenomena illuminated by aggregated data are often implemented into policy, but the data may yield very different results if it were examined with an alternative aggregation scheme.

For my research, MAUP plays into the creation and spatial scale of my analysis. The main data source is a DEM that was created by irregularly sampled points from contour lines. The resolution of the DEM greatly affects the spatial patterns which can be observed. The elevation points used to create the DEM are the key information used in the analysis and were sampled arbitrarily with respect to the phenomena I am investigating. Different patterns and relationships may be illuminated in the topography if an alternative resolution or even data source, such as SRTM data, LIDAR, or a geodetic network were used for this analysis. While the MAUP problem cannot be avoided during spatial analysis and data collection, it must be remembered while interpreting geographic data. For this project, I checked to ensure that changes in the topography were not related only to effects from my interpolation method by comparing changes in steepness with contour line location.

4.1.3 Lithologic border location

Geological data were drawn in a vector format or polygons (Figure 6), but spatial analysis of the topography often requires continuous regularly spaced data, or a raster format. This introduces a notable problem at lithologic contacts (Worboys, 2004). When geologic polygons are converted to a raster format, the edges become blocky due to the regular sampling method. Raster cells are bound to land on fault lines or lithologic contacts and will smear the contact by the cell size resolution (25

m). Smearing of geographic data due to a conversion from vector to raster format is termed a fuzzy set (Worboys, 2004). Since the center of the cell must land on one side or the other of a dividing line, this "smearing" extends no more than half the cell size (12.5 m).

4.2 Uncertainty calculations from topographic map spot elevations

4.2.1 RMSE from digitized spot elevations

The RMSE calculation allows quantification of the vertical elevation uncertainty in a DEM. This calculation determined the difference between known spot height elevations acquired from the Ghandruk topographic map ($z_{observed}$) and interpolated elevations from the DEM ($z_{estimated}$). First, 150 spot elevations were randomly digitized from the Ghandruk topographic map with an equal distribution of points from valley bottoms, ridge crests, and hillsides. The following equations were used to calculate RMSE, where n is the number of data points (150), $z_{estimated}$ is the elevation at the point from the interpolated DEM, and $z_{observed}$ is the known elevation point from the topographic map:

(Equation 1)

$$RMSE = \sqrt{\frac{\sum_{i=1}^{n} (z_{estimated} - z_{observed})^2}{n}}$$

Uncertainty values were calculated using the RMSE equation for the SRTM data, TIN grid interpolation, Karl Schleicher interpolation, Tom Fedenczuk interpolation, and Ofori Pearson interpolation, producing the results shown in Table 3.

Table 3: RMSE and average difference values for different interpolation DEMs and SRTM data (from 150 randomly chosen points)

	RMSE of elevation (m)	Average elevation difference (m)
Karl Schleicher Interpolation	64	51
Tom Fedenczuk Interpolation	19	15
A) Ofori Pearson Topo to Raster	20	16
B) Ofori Pearson Topo to Raster (Extra Data Inputs)	15	9
Tin Grid Interpolation	28	23
SRTM data	6471	3158

When the 150 spot elevation points were digitized on the topographic map, 32 points landed in data void regions of the SRTM data, generating an unrealistically high RMSE calculation for the SRTM data. To mitigate this issue, the 32 points that occurred in data void regions were omitted from the RMSE calculation and yielded the results shown in Table 4 and Figure 31.

Table 4: RMSE and average difference values for different interpolation DEMs and SRTM data (from subset 150 randomly chosen points that excludes points that occur in data voids of SRTM data, total 118 points)

	RMSE of elevation (m)	Average elevation difference (m)
Karl Schleicher Interpolation	59	46
Tom Fedenczuk Interpolation	18	14
A) Ofori Pearson Topo to Raster	19	15
B) Ofori Pearson Topo to Raster (Extra Data Inputs)	14	7
Tin Grid Interpolation	27	22
SRTM data	471	144

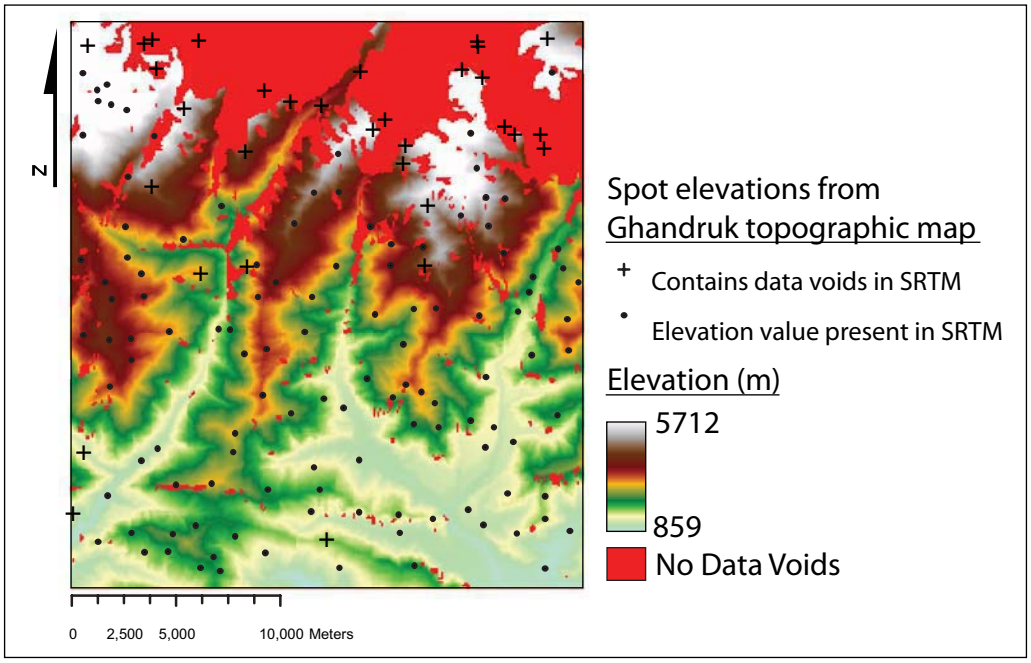

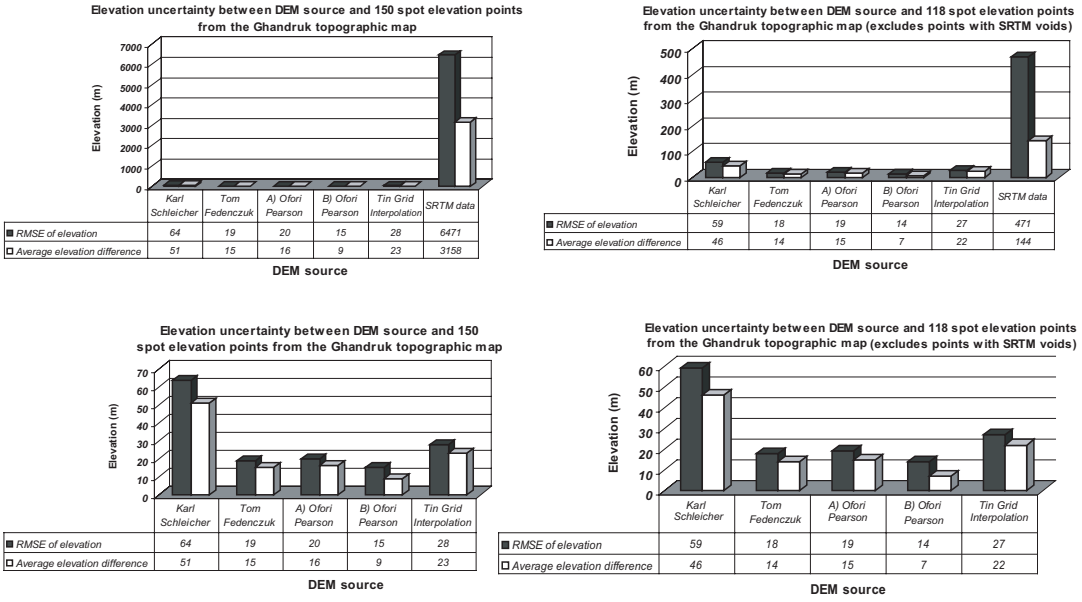

Figure 31: Elevation uncertainty between DEM source and spot heights digitized from Ghandruk topographic map

The Ofori Pearson B interpolation includes extra inputs that were not initially available. These inputs include a stream profile and spot point elevations. The Ofori Pearson B interpolation excludes additional data to allow the DEM to be compared to the other interpolation methods.

4.2.2 RMSE from Ofori Pearson spot elevation points

Ofori Pearson digitized 333 spot elevations on the Ghandruk topographic map. The RMSE calculations from the previous section are repeated here to provide an alternate point dataset for the RMSE calculation. Again, elevations from all 333 spot elevations were compared with elevations within each interpolation method and the SRTM data and are shown in Table 5.

Table 5: RMSE and average difference values for different interpolation DEMs and SRTM data (from 333 spot height elevations digitized by Ofori Pearson)

	RMSE of elevation (m)	Average elevation difference (m)
Karl Schleicher Interpolation	61	48
Tom Fedenczuk Interpolation	17	14
A) Ofori Pearson Topo to Raster	18	15
B) Ofori Pearson Topo to Raster (Extra Data Inputs)	9	5
Tin Grid Interpolation	29	24
SRTM data	2696	2963

Then RMSE was recalculated to omit 66 spot heights that occurred in regions of data voids within SRTM data, reducing the number of spot heights to 267.

Table 6: RMSE and average difference values for different interpolation DEMs and SRTM data (from subset of 333 randomly chosen points that excludes points that occur in data voids of the SRTM data, total 267 points)

	RMSE of elevation (m)	Average elevation difference (m)
Karl Schleicher Interpolation	54	45
Tom Fedenczuk Interpolation	16	13
A) Ofori Pearson Topo to Raster	16	13
B) Ofori Pearson Topo to Raster (Extra Data Inputs)	6	4
Tin Grid Interpolation	27	22
SRTM data	298	239

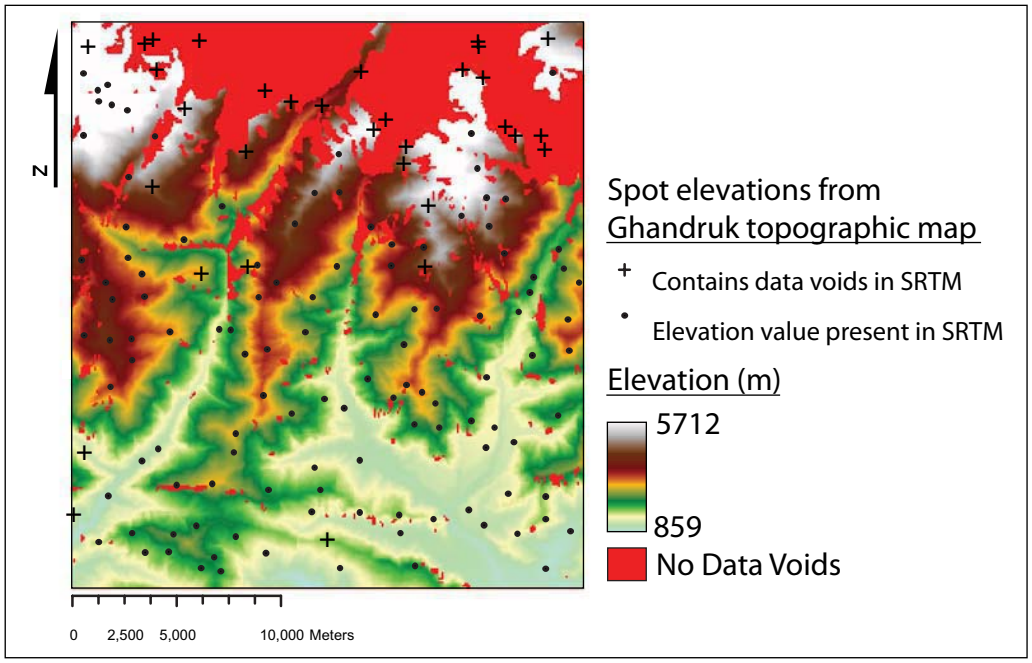

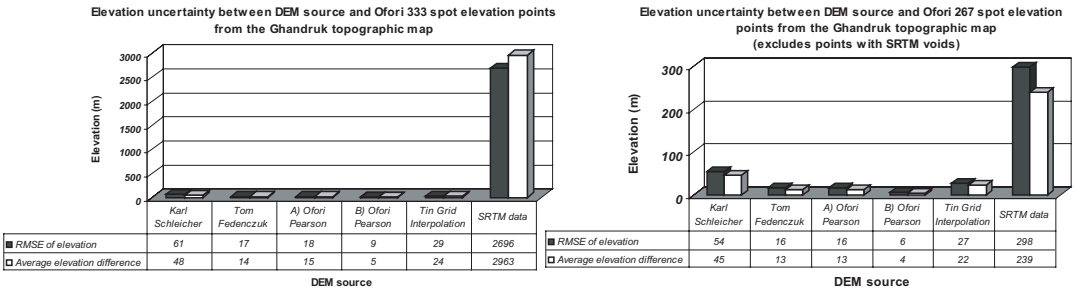

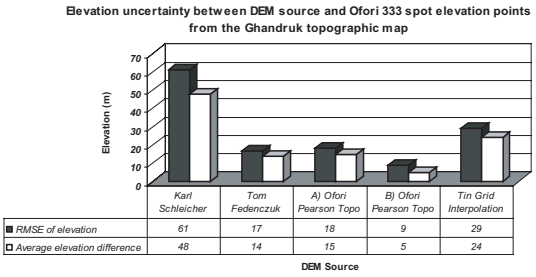

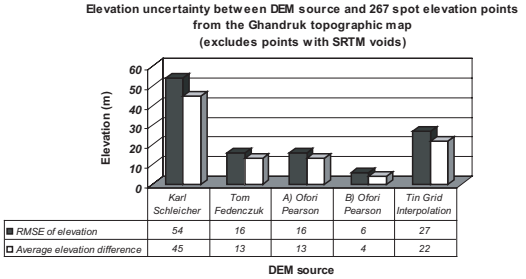

Figure 32: Elevation uncertainty between DEM source and spot heights from Ghandruk topographic map

The Ofori Pearson B interpolation includes extra inputs that were not initially available. These inputs include a stream profile and spot point elevations. The Ofori Pearson B interpolation excludes additional data, allowing comparison of the DEM to other interpolation methods.

4.2.3 RMSE conclusions

Sampling from two different point sets each confirm that the Tom Fedenczuk interpolation generates the smallest RMSE value, indicating that this interpolation maintains a topography that is most similar to the topographic map data. The Ofori Pearson interpolation would also be usable for this analysis, but the data was acquired well after most of the analysis was completed. A random dispersal of points was used to cover the characteristics of valley, ridge, and hillside topography and to prevent biased point selection of the data (Figure 33). Examination of each interpolation method reveals that values of maximum, minimum, and mean elevations from each entire raster dataset are relatively similar (Figure 34). The maximum point value on the topographic map is 6993 m (peak of Macchapucchare) and the minimum is 954 m. The maximum and minimum values were extracted from each DEM for comparison to the map value (Figure 34). All interpolations were able to closely replicate the true peak value of Macchapucchare, with the Karl Schleicher interpolation being the closest at 6984 m. The lowest elevation was harder for all interpolations to resolve, especially for the SRTM data.

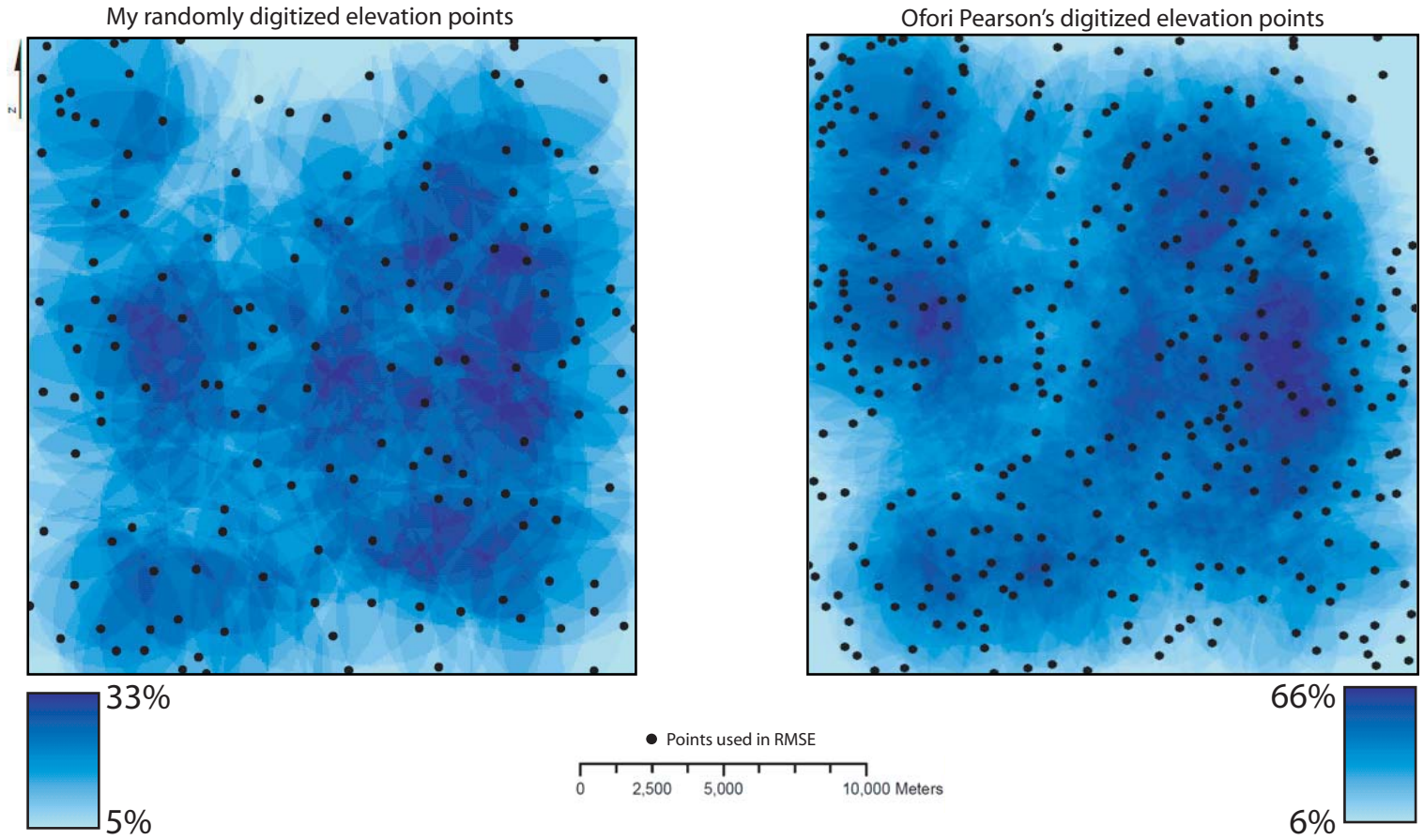

Figure 33: Point density maps
These point density maps illustrate the random distribution of points used in the RMSE calculations. A value of 1 was given for each point, and then a circle radius of 5000 km^2 was drawn around each point. Values show the percentage of points affecting each area based on the 5000 km^2 circle radius. A) Point density map of randomly digitized spot heights on Ghandruk topographic map. B) Point density map of points digitized by Ofori Pearson. Geographic coordinate system: WGS 1984 UTM Zone 44N. Projection: Transverse Mercator.

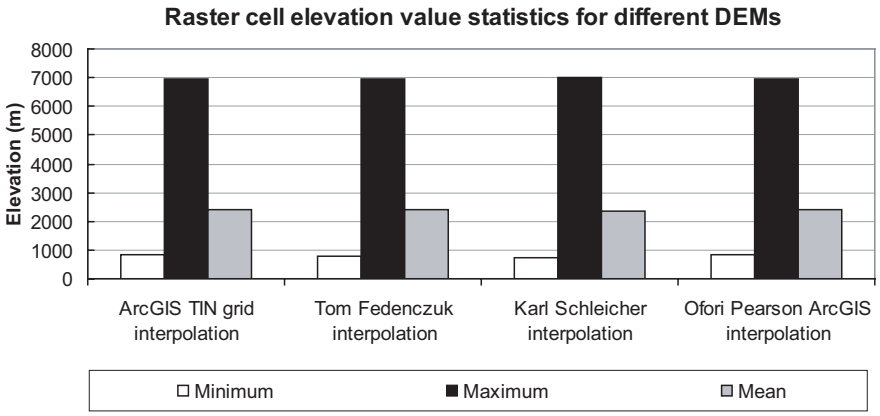

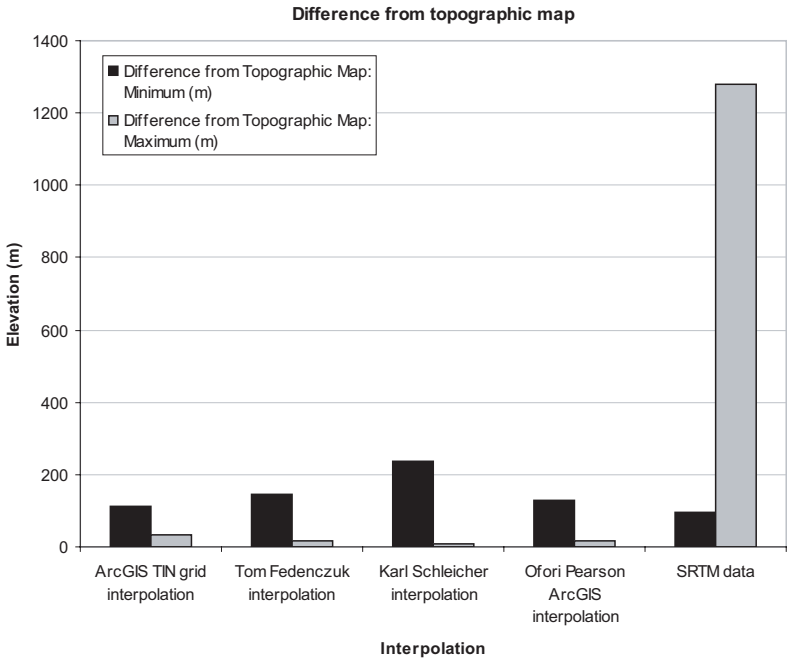

Figure 34: Elevation statistics
Elevation statistics for each interpolation method.

Table 7: DEM elevation comparison

	Minimum (m)	Maximum (m)	Mean (m)
ArcGIS TIN grid interpolation	840	6960	2380
Tom Fedenczuk interpolation	810	6977	2404
Karl Schleicher interpolation	719	6984	2379
Ofori Pearson ArcGIS interpolation	824	6975	2381
SRTM data	859	5712	2167
Real topographic map elevations	*954*	*6993*	*3974*

	Difference from Topographic Map: Minimum (m)	Difference from Topographic Map: Maximum (m)
ArcGIS TIN grid interpolation	114	33
Tom Fedenczuk interpolation	144	16
Karl Schleicher interpolation	235	9
Ofori Pearson ArcGIS interpolation	130	18
SRTM data	95	1281

4.3 Area of flat irregular terraces for different interpolation methods

The TIN interpolation, Ofori Pearson Topo to Raster interpolation, Tom Fedenczuk interpolation, and Karl Schleicher interpolation were compared based on the number of flat irregular terraces, regions where slope is less than 1º, present in the terrain (Figure 35). All interpolations except the TIN interpolation contain less than 1% of regions with less than 1º slope. Alternative interpolation methods, which incorporate an equal interval sampling procedure, create fewer flat terraces than the TIN method. Flat terraces are concentrated at the bottom of the valleys and the crests of ridges. Most of the flat terraces appear in the southeast portion of the map and were avoided in the analysis since Modi Khola geology covers the northwest part of the map. The Karl Schleicher interpolation produces the least amount of flat terraces, followed by the Ofori Pearson interpolation, Tom Fedenczuk interpolation, and finally the TIN grid interpolation (Figure 35). There are only small differences between the Ofori Pearson, Tom Fedenczuk, and Karl Schleicher interpolations, but an order of magnitude difference between these interpolations and the TIN grid interpolation (Figure 35, Table 8).

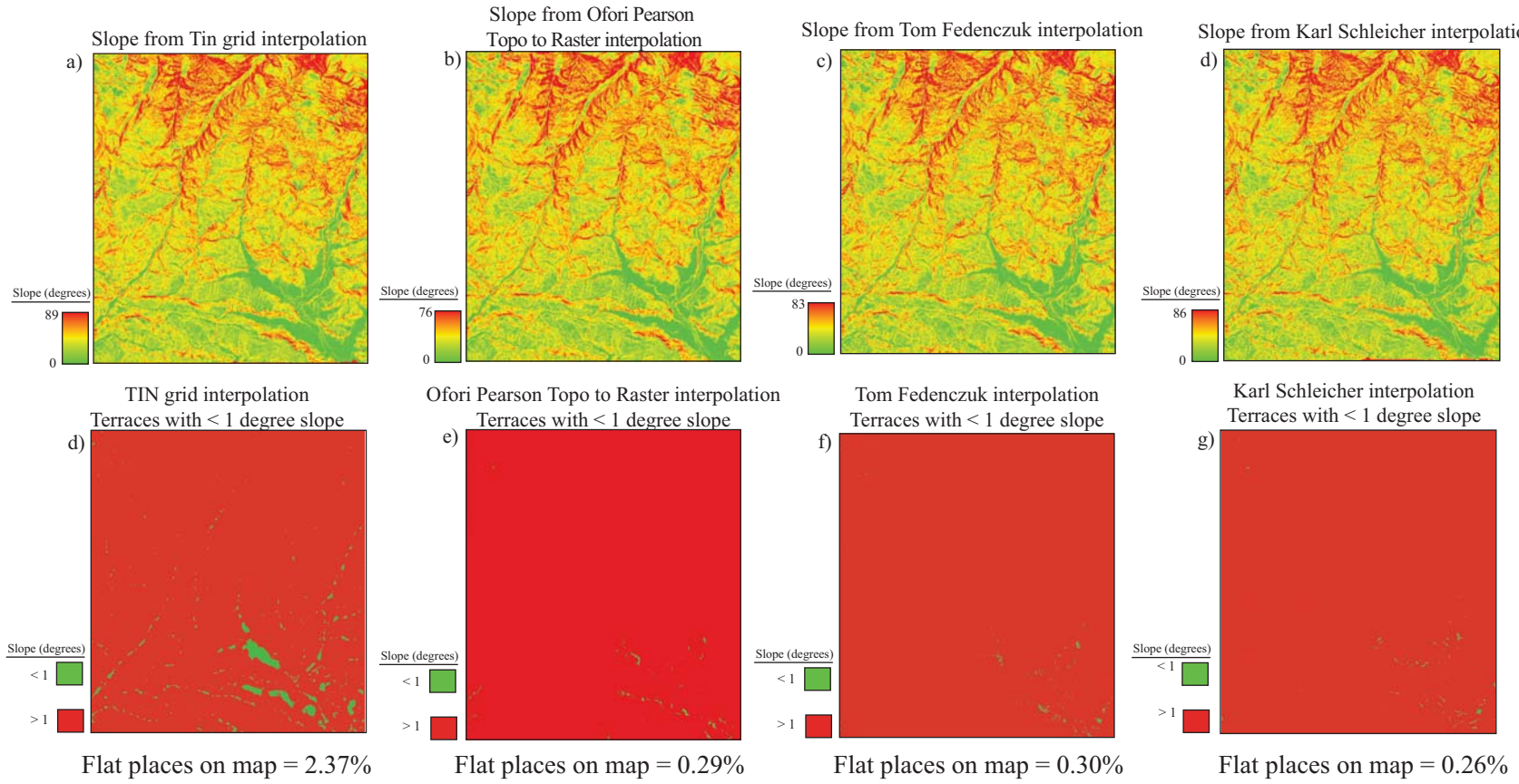

Figure 35: Slope comparison and locations of slope less than 1 degree
Geographic coordinate system: WGS 1984 UTM Zone 44N. Projection: Transverse Mercator.

Table 8: Flat Terraces comparison

DEM interpolation method	Number of cells with < 1 degree slope	Area with < 1 degree slope (m^2)	Total number of cells	% with < 1 degree slope	% with > 1 degree slope
ArcGIS TIN grid interpolation	25179	15736875	1064271	2.37	97.63
Tom Fedenczuk interpolation	3160	1975000	1067434	0.30	99.70
Karl Schleicher interpolation	2852	1782500	1097418	0.26	99.74
Ofori Pearson topo to raster	3184	1990000	1087930	0.29	99.71

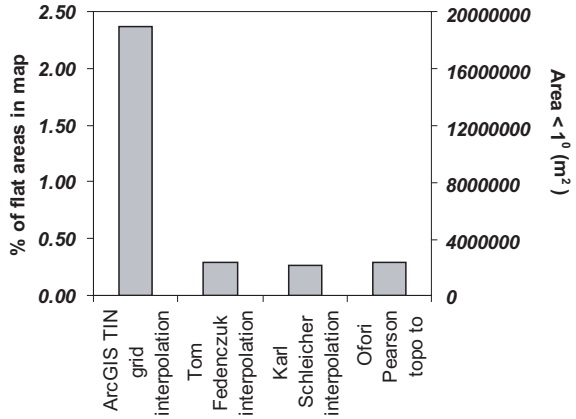

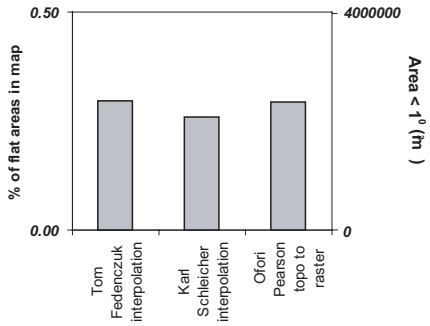

4.4 Comparing interpolations with map algebra

Map algebra was used to subtract different DEMs from one another for comparison with SRTM data (Figure 36) and between interpolation methods (Figure 37). Interpolations tend to differ most in their representations of valley sides. Note that valley and ridges are highlighted by the tan, or zero variability color, indicating that interpolations are most similar on valleys and ridges. Reds or blues dominate the hillsides, demonstrating that interpolations may be shifted slightly. This shifting is an effect of the different methods in which each DEM was interpolated.

These maps illuminate subtle differences that exist between each DEM visually. Holes in the SRTM data and the disadvantage of a low resolution (90 m) DEM are shown in Figure 36. The TIN grid, Tom Fedenczuk interpolation, and Karl Schleicher interpolation all resolve elevation data at 25 m resolution, offering much more detail than SRTM data. Figure 37 illustrates subtle relationships of slope values between my interpolation method choices. The Tom Fedenczuk and Karl Schleicher slope maps clearly differ from the TIN grid interpolation, probably due to the existence of irregular flat terraces in the TIN grid. The Tom Fedenczuk and Karl Schleicher interpolation are the most similar DEMs created for this study, where only subtle differences in how the hillsides were interpolated exist. This indicates that the Tom Fedenczuk and Karl Schleicher interpolations stretch the surface between contour lines in slightly different manners, which is related to the interpolation method used.

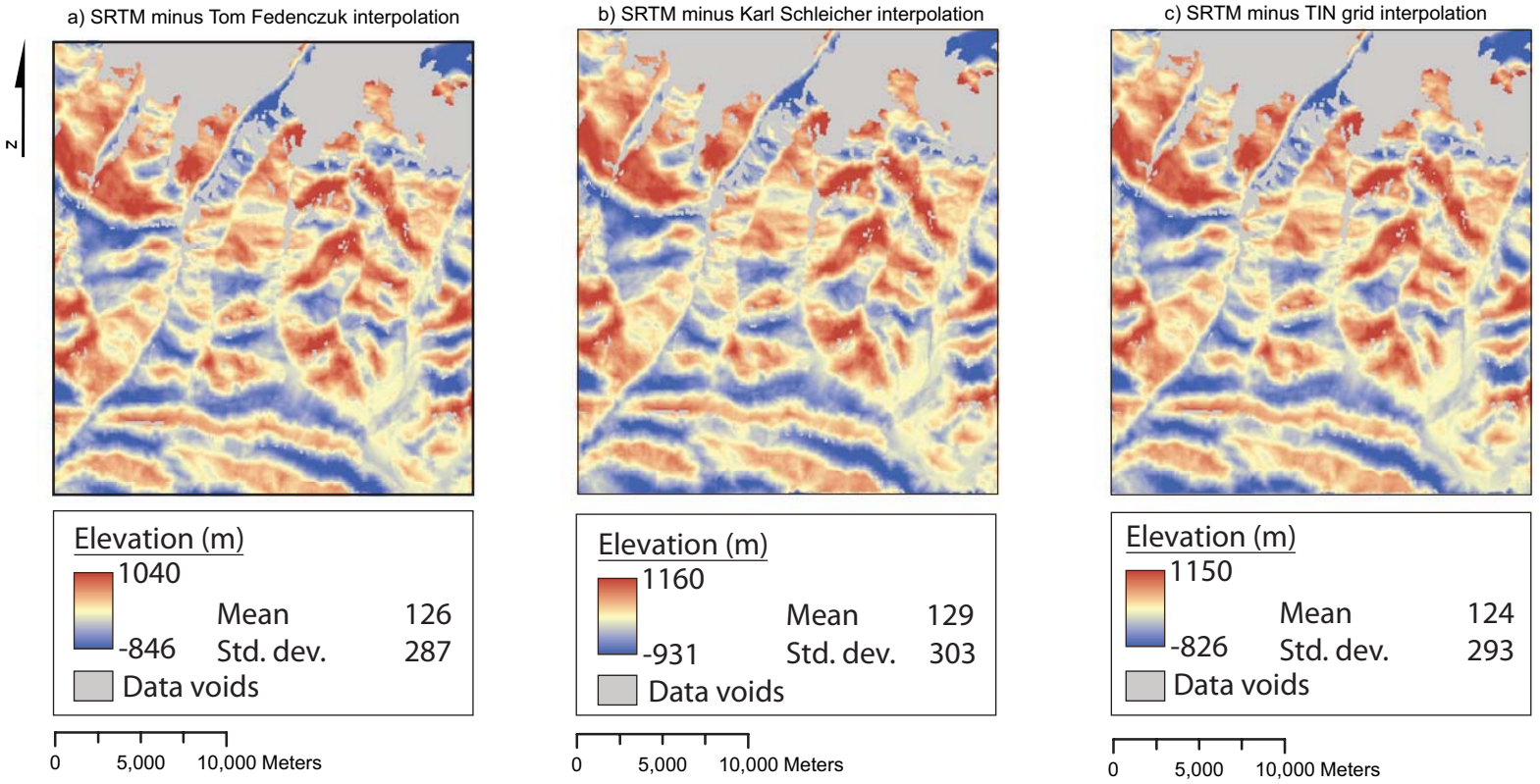

Figure 36: Interpolation elevation comparison with SRTM
SRTM grid elevation was subtracted from alternative DEMs interpolated from contour lines for the Ghandruk topographic map. Grey areas show where holes in SRTM data exist. Differences on the valley sides are likely generated because the SRTM DEM is at 90 m resolution and the alternative interpolations are all at 25 m resolution. Geographic coordinate system: WGS 1984 UTM Zone 44N. Projection: Transverse Mercator.

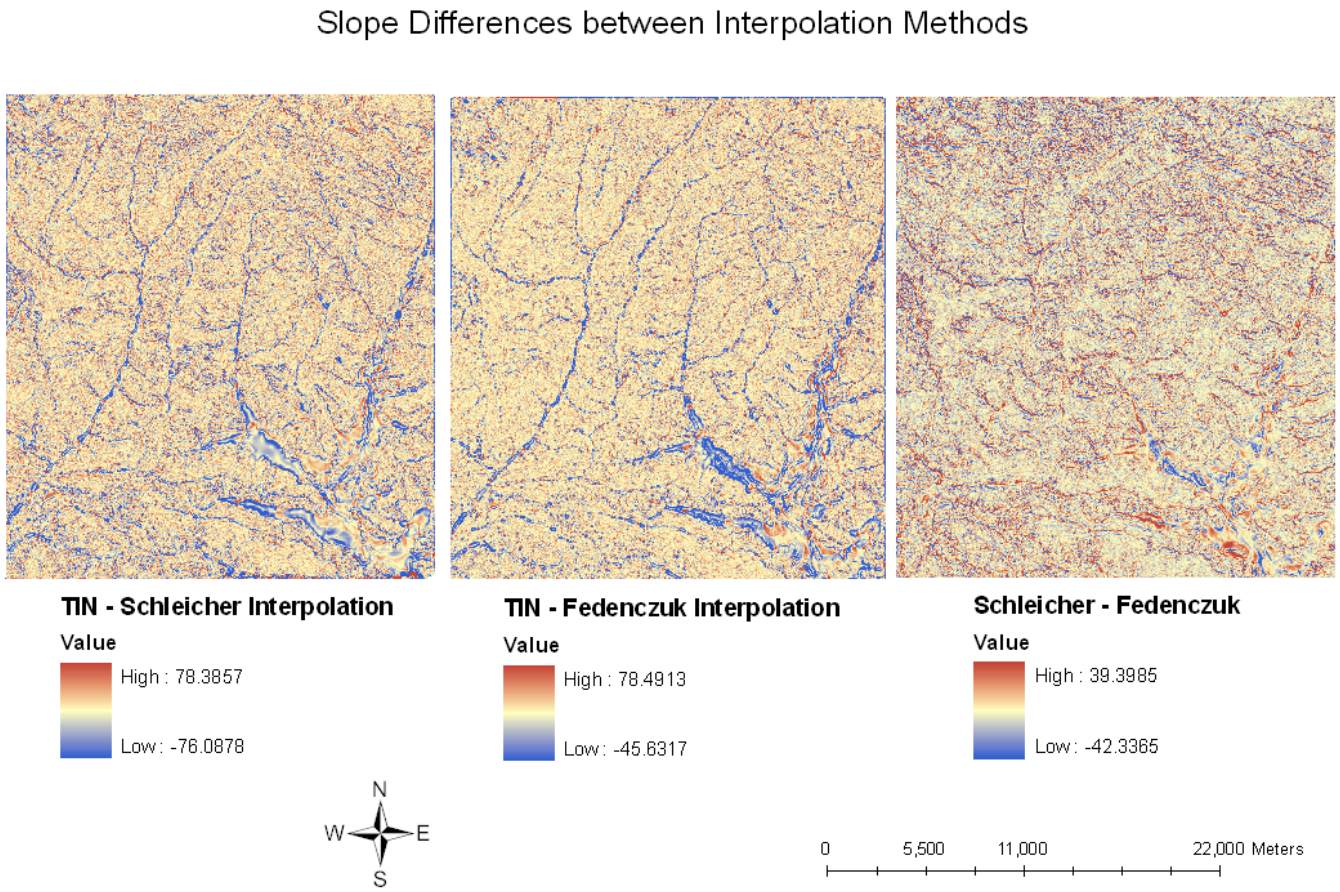

Figure 37: Interpolation slope comparison
Notice that TIN minus Schleicher and TIN minus Fedenczuk rasters have greater differences than the Schleicher minus Fedenczuk raster. This shows that the Schleicher and Fedenczuk interpolations are very similar but also very different from the TIN interpolation. The difference is likely due to the large number of flat terraces in the TIN interpolation, which was mitigated in the Schleicher and Fedenczuk interpolations. Geographic coordinate system: WGS 1984 UTM Zone 44N. Projection: Transverse Mercator.

4.5 Interpolation method choice

Both the Tom Fedenczuk and Karl Schleicher interpolation methods mitigate the problem of flat irregular terraces presented in the TIN grid data. For my data, alternative interpolation methods portray more realistic DEMs than the TIN interpolation easily created in ArcGIS. The Ofori Pearson interpolation method, which uses the ArcGIS Topo to Raster interpolation, demonstrates that realistic interpolations are possible in ArcGIS if additional input information is provided such as spot elevation data and the location of rivers. Subtle differences in the Karl Schleicher and Tom Fedenczuk interpolation grids address the problem of creating a DEM from irregularly spaced contour line data from different perspectives and scales. The Karl Schleicher interpolation method slightly exaggerates elevations at the peaks and valleys in the study site, yet allows DEMs to be produced at smaller resolutions down to 10 m and less than 1% area flat terraces to be produced. If point data along ridges and valleys can be added, it would be possible to use the Karl Schleicher interpolation method to produce higher resolution DEMs for future studies. I choose to use the Tom Fedenczuk interpolation method for this analysis because it limits RMSE values to the smallest value for this dataset and minimizes flat terraces to the extent needed for this study. The small RMSE value, which compares spot elevations from the topographic map and the interpolated elevation, shows that the Fedenczuk interpolation reallistically represents the topography of the Modi Khola valley. A 25 m resolution DEM was chosen because it was the smallest resolution achievable without producing artifacts and was used to successfully distinguish lithologies by the topography in many studies (Roering et al., 2005; Belt et al., 2005; Korup, 2008).

Chapter 5: DEM derivatives

Topographic attributes, such as slope and curvature, can be calculated from derivatives of elevation. These derivatives measure the rate at which elevation changes in response to changes in location x and location y. Slope is the first derivative of elevation and curvature is the second derivative of elevation (Wilson and Gallant, 2000). Slope is defined as the rate of change of elevation, while curvature is defined as the rate of change of slope. Slope was calculated using ArcGIS and curvature was calculated using methods described in Roberts (2001) and the CurvZ program.

5.1 Slope

Slope measures the rate of change of elevation in the direction of the steepest descent (Wilson and Gallant, 2000). Slope was calculated for this project using the slope function within ArcGIS's spatial analyst toolbox. Slope is calculated for each cell of the DEM by calculating the maximum rate of change in value from that cell to its neighbors. The maximum rate of change in elevation over the distance between the cell and its greatest value neighbor identifies the steepest downhill descent. Lower slope values characterize flat terrain, while higher the slope values characterize steep terrain.

The following series of equations (2-5) from Burrough (1998) are used to calculate slope in ArcGIS. Slope is calculated by measuring the rate of change of the surface in the horizontal (dz/dx) and vertical (dz/dy) directions from the center cell.

The geometry of a triangle (Figure 38) can be used to derive the basic equation used to calculate slope as:

(Equation 2)

$$Slope\ (\deg rees) = ATAN(\sqrt{\left(\left[\frac{dz}{dx}\right]^2 + \left[\frac{dz}{dy}\right]^2\right)}$$

Convert (Equation 2 to degrees and the calculation for slope becomes:

(Equation 3)

$$Slope\ (\deg rees) = ATAN(\sqrt{\left(\left[\frac{dz}{dx}\right]^2 + \left[\frac{dz}{dy}\right]^2\right)} \times 57.29578$$

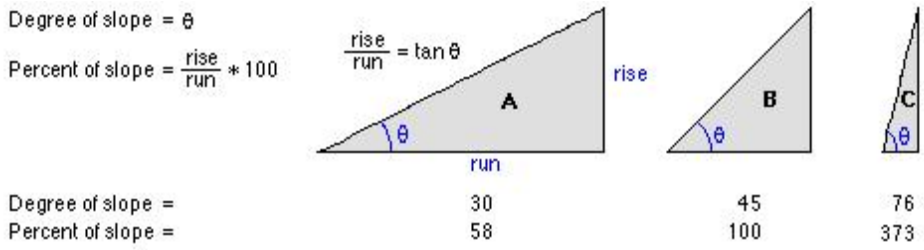

Figure 38: Slope calculation
Figure from ArcGIS help file "How slope works"

The grid in Figure 39 can be used as a reference for slope calculations. The values of the center cell and its eight neighbors determine the horizontal and vertical changes. The neighbors are identified as letters from *a* to *i*, with *e* representing the cell for which the aspect is being calculated.

a	b	c
d	e	f
g	h	i

Figure 39: Grid used for slope calculation
Figure from ArcGIS help file "How slope works"

The rate of change in the x direction for cell *e* is calculated by the following equation:

(Equation 4)

$$\left[\frac{dz}{dx}\right] = \frac{\left((c + 2f + i) - (a + 2d + g)\right)}{\left(8 \times cell\ \ size\right)}$$

The rate of change in the y direction for cell *e* is calculated with the following equation:

(Equation 5)

$$\left[\frac{dz}{dy}\right] = \frac{\left((g + 2h + i) - (a + 2b + c)\right)}{\left(8 \times cell\ \ size\right)}$$

Values of (dz/dx) and (dz/dy) can be plugged into (Equation 3) to calculate slope in degrees. Figure 40 shows the slope map generated with these methods for the Ghandruk topographic map.

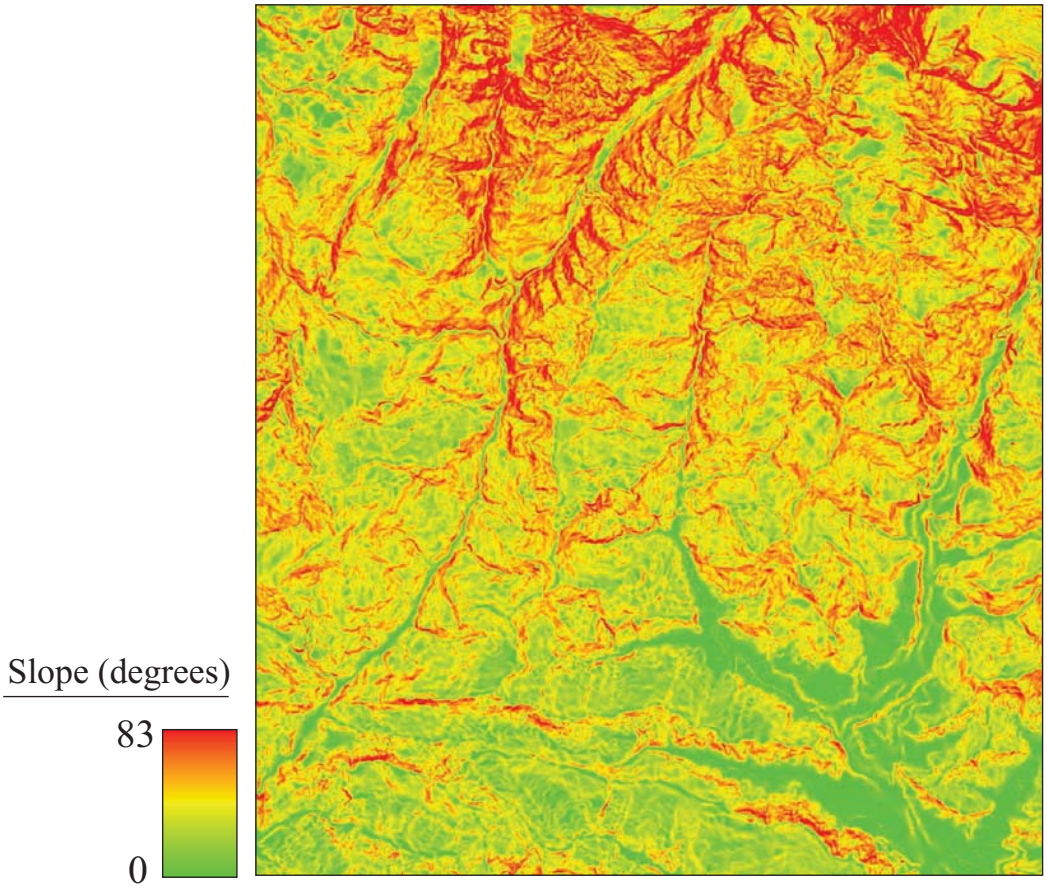

Figure 40: Slope of Ghandruk topographic map

5.2 Curvature

5.2.1 Mathematical definition of curvature

Curvature describes how much a surface is bent at a particular point in the landscape. Mathematically, curvature is defined as the reciprocal of the radius of a circle that is tangent to a point on a curve (Roberts, 2001). Tightly folded terrain has large curvature values, while flat terrain has zero curvature (Figure 41).

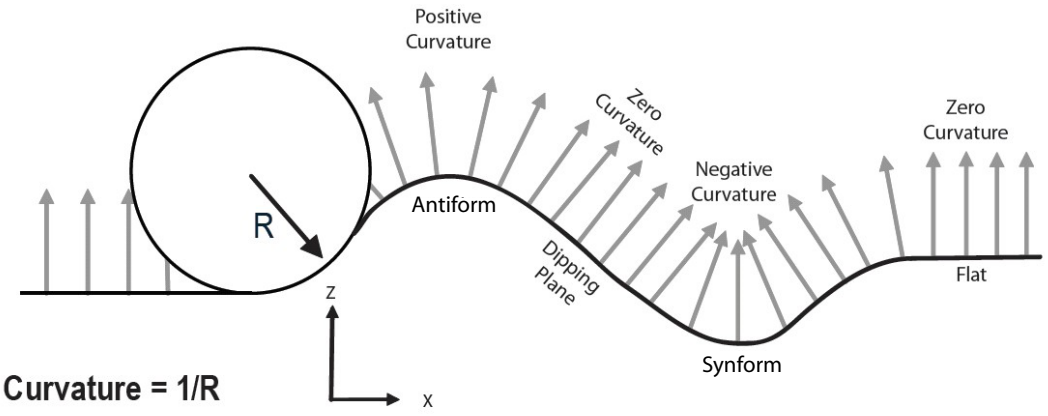

Figure 41: Curvature conventions
Grey arrows represent vectors that are perpendicular to the surface. Curvature is zero where these vectors are parallel on flat or planar dipping surfaces. Where vectors diverge over antiforms, the curvature is defined as positive and where they converge over synforms, the curvature is negative. (Figure modified from Roberts, 2001).

Essentially, curvature is the second derivative or the rate of change of slope (Wilson and Gallant, 2000). There are several ways to calculate curvature from gridded data, but this analysis follows the calculations outlined in Roberts (2001). A local quadratic surface represented by (Equation **6** below is fitted in a least squares sense by using 8 surrounding cell values (Figure 42). Using a 3 x 3 cell aperture, the calculation of the

coefficients in (Equation **6** condense to a series of arithmetic equations (Equation 7 though (Equation 12 as follows:

(Equation 6)

$$y = ax^2 + by^2 + cxy + dx + ey + f$$

(Equation 7)

$$a = \frac{1}{2}\frac{d^2z}{dx^2} = \frac{(z_1 + z_3 + z_4 + z_6 + z_7 + z_9)}{12\Delta x^2} - \frac{(z_2 + z_5 + z_8)}{6\Delta x^2}$$

(Equation 8)

$$b = \frac{1}{2}\frac{d^2z}{dy^2} = \frac{(z_1 + z_2 + z_3 + z_7 + z_8 + z_9)}{12\Delta x^2} - \frac{(z_4 + z_5 + z_6)}{6\Delta x^2}$$

(Equation 9)

$$c = \frac{d^2z}{dxdy} = \frac{(z_3 + z_7 - z_1 - z_9)}{4\Delta x^2}$$

(Equation 10)

$$d = \frac{dz}{dx} = \frac{(z_3 + z_6 + z_9 - z_1 - z_4 - z_7)}{6\Delta x}$$

(Equation 11)

$$e = \frac{dz}{dy} = \frac{(z_1 + z_2 + z_3 - z_7 - z_8 - z_9)}{6\Delta x}$$

(Equation 12)

$$f = \frac{2(z_2 + z_4 + z_6 + z_8) - (z_1 - z_3 - z_7 - z_9) + 5z_5}{9}$$

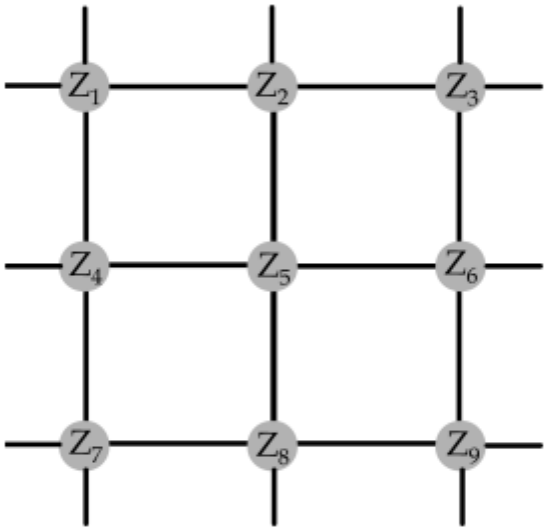

Figure 42: 3 x 3 grid cell for curvature calculation
This is the aperture size used in the computation of all curvature, dip, and azimuth attributes.

The aperture size determines the interval in which the surface is sampled. The scale of the investigation determines the aperture size. Roberts (2001) describes aperture using the analogy of a large mound of stones 100 m across and 10 m high. The mound looks like a smooth hill from a distance, yielding a surface with a small curvature. If the mound is examined at a smaller scale, the curvature of individual stones can be visualized, indicating the mound has a very rough surface. At an even finer scale, each individual stone could be examined. Some of the stones may be rough, while others are smooth and flat. The different scales of study, or the aperture size, yield different curvature results since curvature depends on the sampling scale interval.

A range of aperture sizes were tested for the topographic data of this analysis, at 1 m, 2 m, 3 m, 5 m, 7 m, 10 m, 25 m, and 100 m (Figure 43). Notice that as aperture size increases, the curvature grid output becomes smaller over the map area. The curvature grid size decreases as aperture size increases because the sampling interval can capture less information at the edges of the map as aperture size becomes larger. An aperture size of 3 m was chosen for this analysis since it maintains detailed curvature information and eliminates any artifacts produced during the interpolation process.

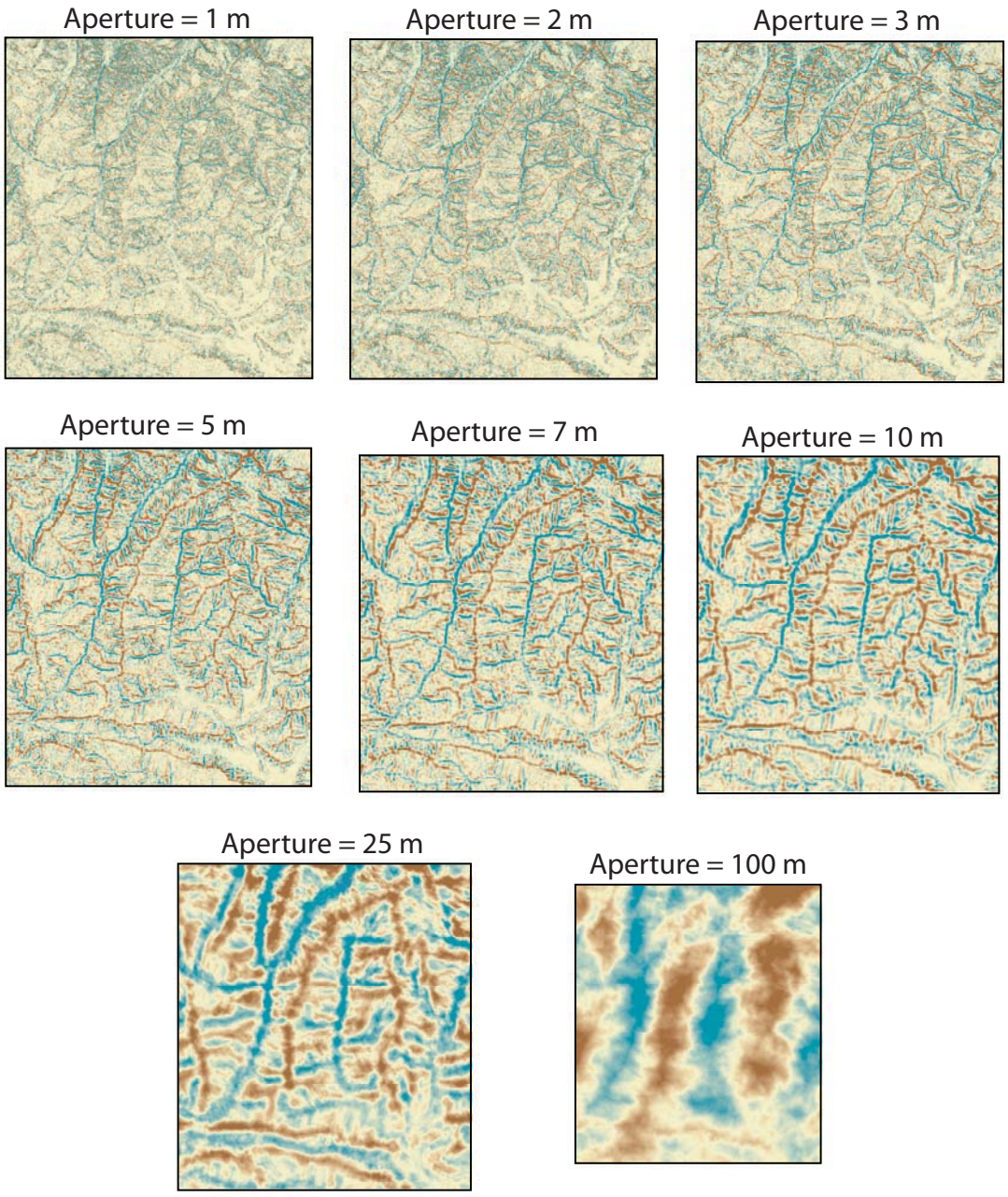

Figure 43: Mean curvature of Ghandruk topography from a range of apertures
Blue represents negative curvature values of valley shaped topography, tan represents zero curvature values of dipping surfaces between valleys and ridges, and brown represents positive curvature values of ridge shaped topography. An aperture of 3 m was chosen for this analysis to preserve curvature detail and eliminate artifacts produced during the interpolation process. Geographic coordinate system: WGS 1984 UTM Zone 44N. Projection: Transverse Mercator.

5.2.2 Types of curvature

The two-dimensional concept of curvature can be extended into three-dimensions, in my case to 3-D topography represented by the DEM. Slicing topography with a plane enables the curvature of a topographic profile to be examined. Roberts (2001) uses the surface skin of an apple and the mathematical plane carved from a knife to help visualize the concept of curvature. A cut made by the knife into the skin of an apple represents the curve. Cutting an apple through the middle creates a circle in which the corresponding curvature can be calculated. But, if the top of the apple is cut off it forms a much smaller circle and thus a much larger curvature. There are an infinite number of cuts that can be made, allowing an infinite number of curvature values to be extracted. The most useful subset of curvatures, according to Roberts (2001), is that defined by planes which are orthogonal to the surface. These planes are called normal curvatures and may be classified into the following categories: maximum curvature (K_{max}), minimum curvature (K_{min}), dip curvature (K_d), and strike curvature (K_s) (Figure 44). Out of the infinite number of normal curvatures that pass through a point on the surface, one curve defines the largest absolute curvature or maximum curvature (K_{max}). The minimum curvature (K_{min}) defines the smallest absolute curvature and is perpendicular to K_{max}. Maximum and minimum curvatures represent the extremes of curvature and are called the principle curvatures. Extracting the curvature in the direction of maximum dip defines the dip curvature (K_d). Strike curvature (K_s) extracts curvature values in the right angle direction from the dip curvature.

The following text describes calculations for the different types of curvature after calculations explained in Roberts (2001). All of the curvatures described in Roberts (2001) were created and projected into ArcGIS for the Ghandruk topographic map, but only the Mean Curvature (K_m) will be used in this analysis.

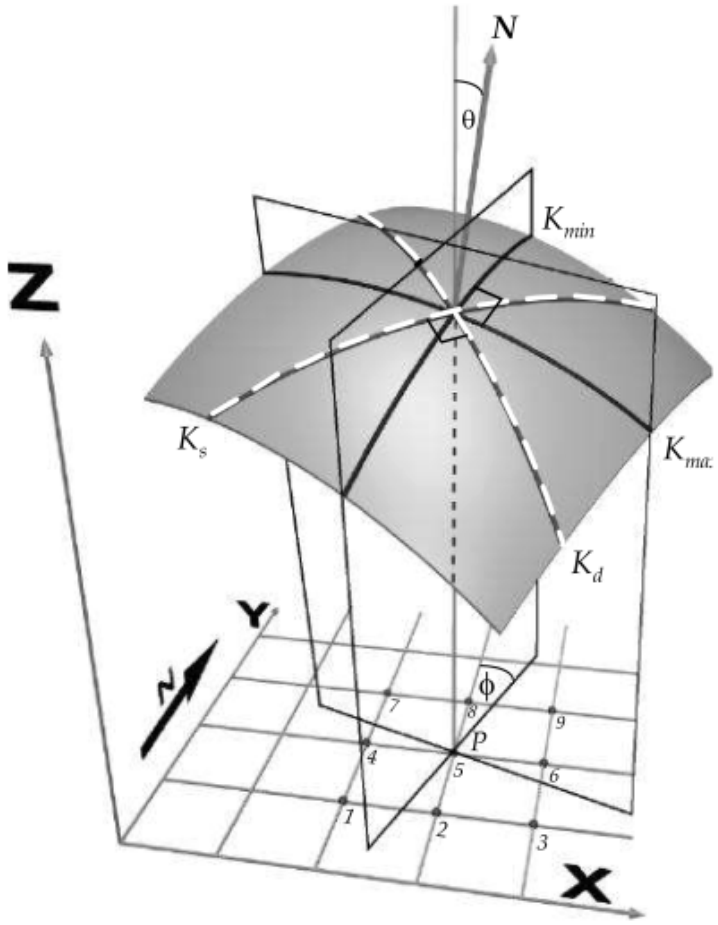

Figure 44: Normal curvatures in three dimensions
X and y represent the map axes, with z representing height. The intersection of the two orthogonal planes with the surface defines the maximum curvature (K_{max}) and the minimum curvature (K_{min}). Two other orthogonal normal curvatures, the dip curvature (K_d) and strike curvature (K_s) also intersect the surface. N is the vector normal to the surface at point P, which makes an angle θ with the vertical, called the dip angle. The location of the underlying gridded map surface has been added for reference, with the additional annotation of nine grid nodes. These represent the 3 x 3 grid cell used in the curvature calculation, where node 5 equals point P whose curvature is being calculated (Grid shown in Figure 42). (Figure from Roberts, 2001)

The normal curvatures can be combined in a variety of ways to illuminate curvature attributes of interest, as defined in Roberts (2001). The average of any two orthogonal normal curvatures is defined as the mean curvature (K_m) where:

(Equation 13)

$$K_m = \frac{K_{\max} + K_{\min}}{2}$$

Mean curvature (K_m) can be expressed by the following equation:

(Equation 14)

$$K_m = \frac{a(1+e^2) + b(1+d^2) - cde}{(1+d^2+e^2)^{3/2}}$$

Gaussian curvature (K_g) describes the bending of a surface and is defined as the produce of the principal curvatures:

(Equation 15)

$$K_g = K_{\max} \times K_{\min}$$

Gaussian curvature is named after Gauss's Theorema Egregium which states that the isometric bending of a surface does not change the Gaussian curvature of points on that surface. This means that Gaussian curvature must remain constant if it is folded in some way, as long as the surface has not been broken, stretched, or squeezed. A flat piece of paper rolled into a cone does not change the Gaussian curvature (Roberts, 2001). This type of surface is called a developable surface. The flat piece of paper has zero curvature in all directions, but a cone has a zero curvature in minimum direction and a non-zero curvature in the maximum direction. Forming a cone with the piece of paper only alters the maximum curvature. The combination of mean curvature and Gaussian curvature may allow the local shape of a surface to be described (Figure 45).

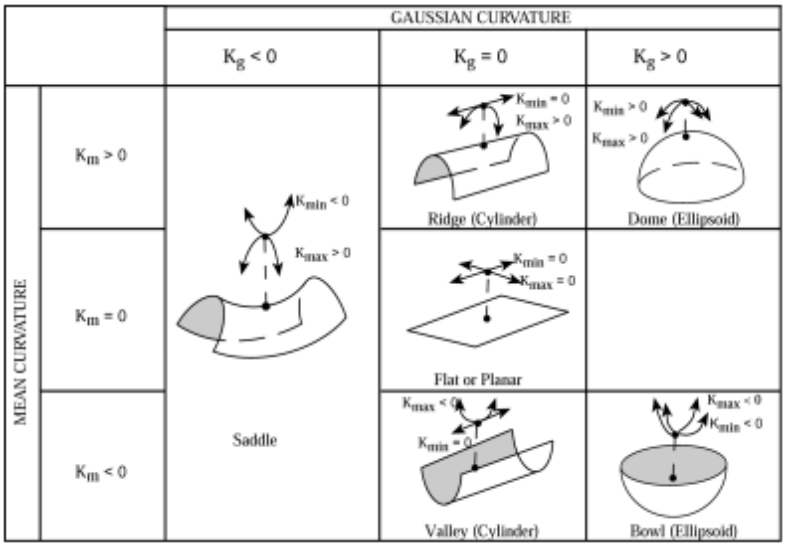

Figure 45: Curvature shape classification
Combination of Gaussian curvature and mean curvature allows the shape of a surface to be described locally and mathematically. (Figure from Roberts, 2001)

Most positive (K_+) and negative (K_-) curvatures are calculated by searching all possible normal curvatures for the most positive and most negative values. This can be obtained by setting coefficients *d* (Equation 10) and *e* (Equation 11) to zero (see Roberts 2001 for more details).

(Equation 16)

$$K_+ = (a+b) + \sqrt{(a-b)^2 + c^2}$$

(Equation 17)

$$K_- = (a+b) - \sqrt{(a-b)^2 + c^2}$$

The shape index (S_i) can be derived by combining maximum and minimum curvature. Shape index results in a qualitative description of shape and can be used to identify bowl shaped features in the landscape.

Dip curvature (K_d) extracts curvature in the direction of maximum dip. This curvature measures the rate of change of dip. This curvature exaggerates local surface relief and can be used to identify channelized sand bodies and debris flows.

(Equation 18)

$$K_d = \frac{2(ad^2 + be^2 + cde)}{(d^2 + e^2)(1 + d^2 + e^2)^{3/2}}$$

Contour curvature (K_c) represents the curvature of the map's contour lines by cutting horizontal planes through the surface at each contour interval. Contour curvature produces very large values at the culmination of anticlines, synclines, ridges and valleys.

(Equation 19)

$$K_c = \frac{2(ae^2 + bd^2 - cde)}{(d^2 + e^2)^{1/2}}$$

And finally, the curvedness (K_n) illustrates the magnitude of surface curvature independent of its shape.

Dip angle (D_a) represents the angle of maximum dip and azimuth (A_z) represents the dip direction of the topography. Dip angle and azimuth are first derivatives that can be extracted from the topography, while the curvature grids are second derivatives extracted from the topography. Dip angle is interchangeable with slope and can be calculated with the following equation:

(Equation 20)

$$Dip\ \ Angle = \tan^{-1}(\sqrt{d^2 + e^2}$$

5.2.3 Curvature program

Bruce Hart, former professor at the University of Oklahoma and current researcher at ConocoPhillips, kindly provided us with a program that can calculate curvature. This curvature program, called CurvZ, was programmed in 2001 by the One Guy Coding Company. The mathematical calculations incorporated into this program were extracted directly from Roberts (2001). Several researchers have utilized curvature attributes in seismic data interpretation. Analysis of seismic attribute data is a growing oil exploration technique, as different types of curvature are shown to correlate well with the location of fractures in sedimentary basins (Chopra and Marfurt, 2007; Hart and Sagan, 2005).

Since CurvZ can only import .txt files, the DEM was converted to points in ArcGIS. This produced rows and columns of points regularly spaced in a grid pattern every 25 m (the resolution of the DEM). Each point contained latitude, longitude, and elevation information and was exported at a .txt file. The .txt file was read into CurvZ and the following grids were calculated and exported as a .txt file: K_m, K_g, D_a, A_z, K_{max}, K_{min}, K_{pos}, K_{neg}, S_i, K_d, K_c, and K_n. Figure 46 shows the CurvZ program interface and Figure 47 shows the .txt output for K_m.

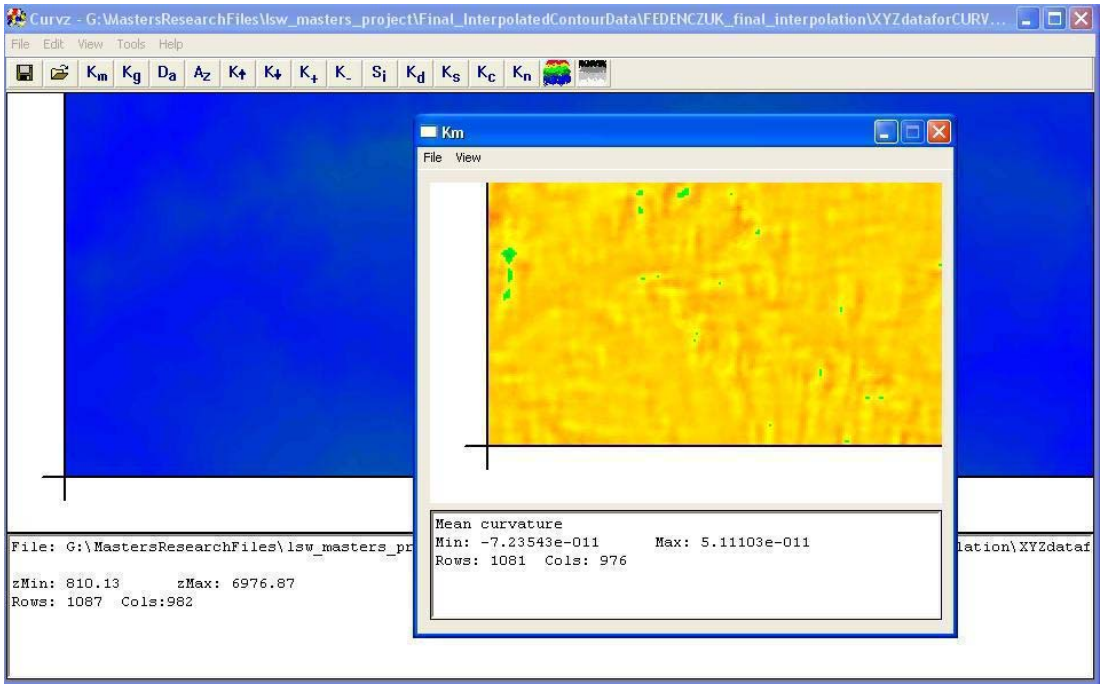

Figure 46: CurvZ program interface
The top window shows a portion of the Mean Curvature (K_m) calculation created from the Ghandruk topographic map elevation data. The back window shows a portion of the DEM grid. Notice buttons for types of curvature that can be calculated with the CurvZ program. The whole grid cannot be seen at once in this program's display, so it must be imported into ArcGIS for full viewing capacity. CURVZ program provided by Bruce Hart.

FORCURVZ_FEDENCZUK_25mptsKm - Notepad

File Edit Format View Help

0	0	475547	3.12622e+006	1.79295e-012
0	1	475572	3.12622e+006	2.10423e-012
0	2	475597	3.12622e+006	2.29785e-012
0	3	475622	3.12622e+006	2.39659e-012
0	4	475647	3.12622e+006	3.39163e-012
0	5	475672	3.12622e+006	4.17841e-012
0	6	475697	3.12622e+006	2.63492e-012
0	7	475722	3.12622e+006	4.65972e-013
0	8	475747	3.12622e+006	-1.32724e-012
0	9	475772	3.12622e+006	-2.71859e-012
0	10	475797	3.12622e+006	-3.60176e-012
0	11	475822	3.12622e+006	-3.68108e-012
0	12	475847	3.12622e+006	-2.90714e-012
0	13	475872	3.12622e+006	-1.82803e-012
0	14	475897	3.12622e+006	-8.79864e-013
0	15	475922	3.12622e+006	1.48023e-012
0	16	475947	3.12622e+006	5.53377e-012
0	17	475972	3.12622e+006	7.69474e-012
0	18	475997	3.12622e+006	4.70673e-012
0	19	476022	3.12622e+006	7.72208e-013
0	20	476047	3.12622e+006	-1.44145e-012
0	21	476072	3.12622e+006	-2.75813e-012
0	22	476097	3.12622e+006	-2.92953e-012
0	23	476122	3.12622e+006	-1.58393e-012
0	24	476147	3.12622e+006	1.85594e-013
0	25	476172	3.12622e+006	-1.36896e-012

Figure 47: Output from CurvZ program
A screenshot of a .txt file output from a Mean Curvature (K_m) calculation made by the CurvZ program. The labels for each column are as follows: row number in grid, column number in grid, latitude, longitude, curvature value.

Once an output .txt file was extracted for each type of curvature, the .txt file was opened in Microsoft Access. Labels were added to each column and then the data were saved. Once the data were saved in a Microsoft Access format, it could be assessed by ArcGIS as a geodatabase. The data became a personal geodatabase table that could be added to ArcGIS. The table was imported into ArcGIS and then the points were used to represent the data by using the option "add XY data" from the geodatabase table. This created a grid of points spaced regularly at 25 m. Since the points were regularly spaced, they were used to create a raster with a 25 m resolution. A raster was created using the curvature value as the value of the raster. When these steps were carried out for each set of curvature data, each type of curvature grid could be viewed in ArcGIS (Figure 48). Each grid was projected to UTM zone 44N, to position the map in the right location on the globe. The CurvZ program exports curvature maps with valleys as positive and ridges as negative. Since this is the opposite of the curvature convention (Figure 41), each grid was multiplied by -1 (Figure 48). The mean curvature (K_m) was chosen for this analysis for simplicity and to represent an average curvature value for the topography (Equation 13).

a) K_m: Mean Curvature

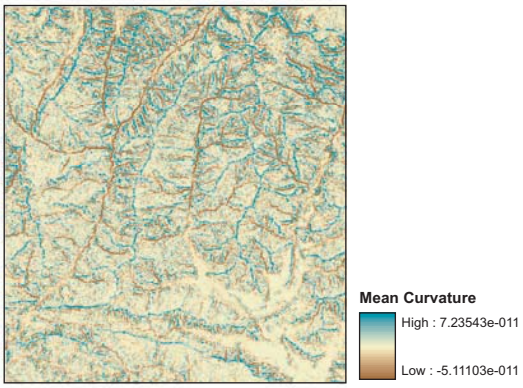

b) K_g: Gaussian Curvature

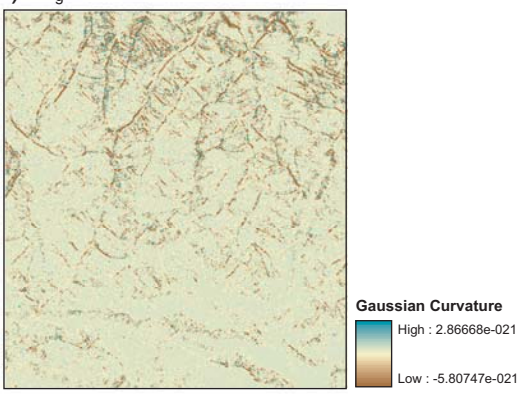

c) K_{max}: Maximum Curvature

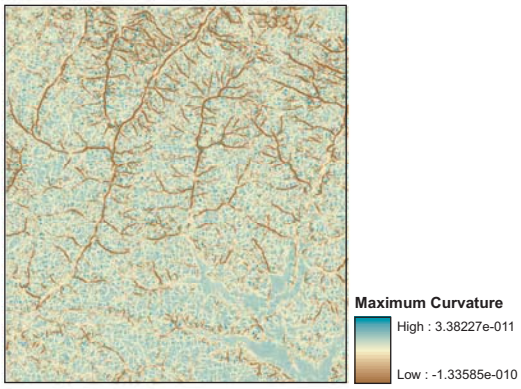

d) K_{min} : Minimum Curvature

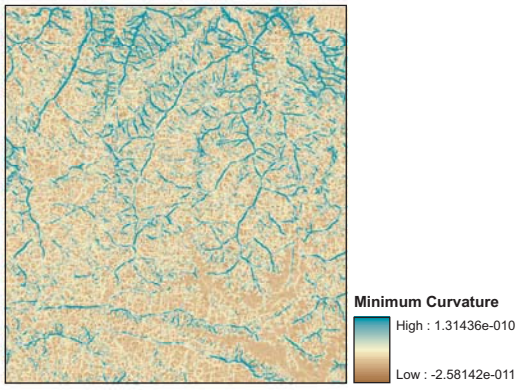

e) K_+: Positive Curvature

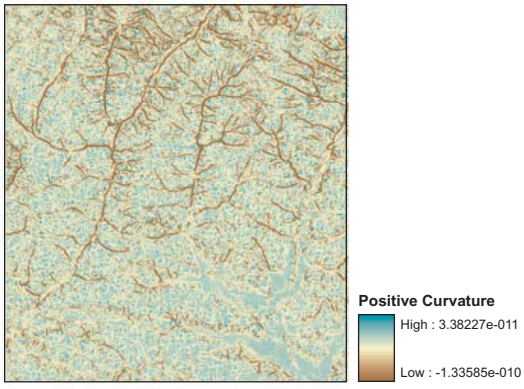

f) K_-: Negative Curvature

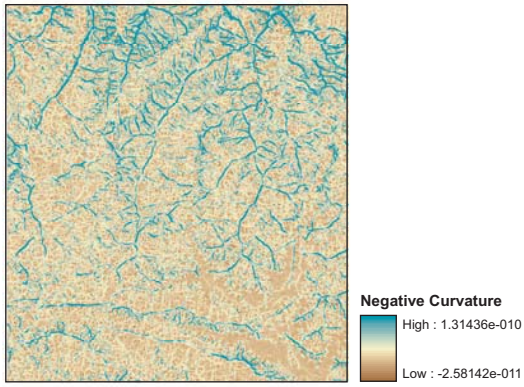

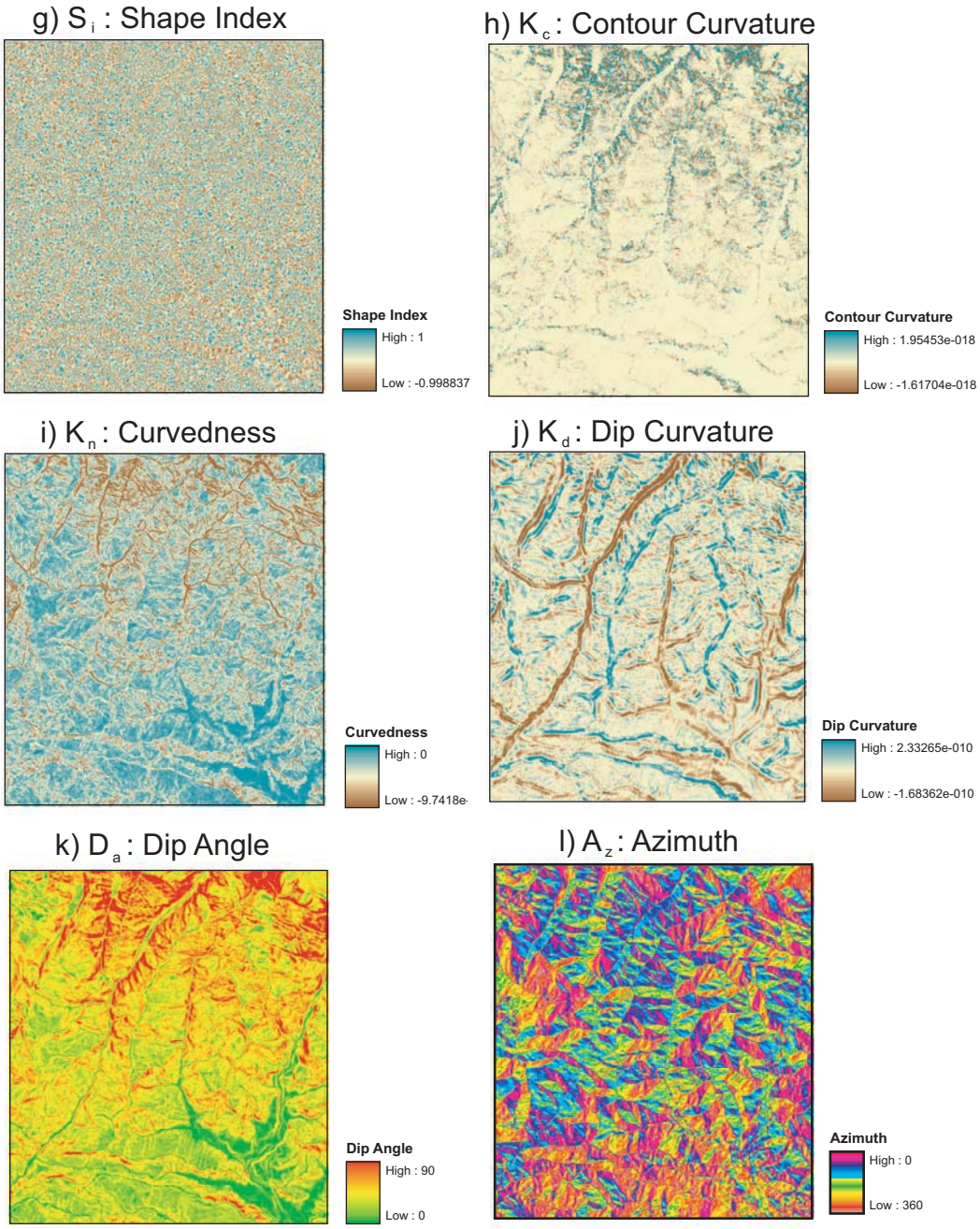

Figure 48: Curvature of Ghandruk topographic map
Curvature calculated from DEM that covers the Ghandruk topographic map. a) Mean curvature (K_m), b) Gaussian curvature (K_g), c) Maximum curvature (K_{max}), d) Minimum curvature (K_{min}), e) Most positive curvature (K_+), f) Most negative curvature (K_-), g) Shape index (S_i), h) Contour curvature (K_c), i) Curvedness (K_n), j) Dip Curvature (K_d), k) Dip angle (D_a), l) Azimuth (A_z). Negative curvature is brown and represents valley shaped topography, zero curvature is tan is represents dipping slopes that connect valley and ridges or flat locations, positive curvature is blue and represents ridge shaped topography. The aperture size for all curvature grids is 3 m. Geographic coordinate system: WGS 1984 UTM Zone 44N. Projection: Transverse Mercator.

5.3 Derivatives for Modi Khola valley

Each DEM derivative was cropped to cover the extent of the Modi Khola geologic map (Figure 5). The DEM and derivatives of the Modi Khola valley comprise the main dataset for this analysis (Figure 49). A hillshade raster shows an illumination of the topography from a hypothetical light source. Note that the hillshade derivative is superimposed beneath the DEM for a three dimensional, more realistic effect.

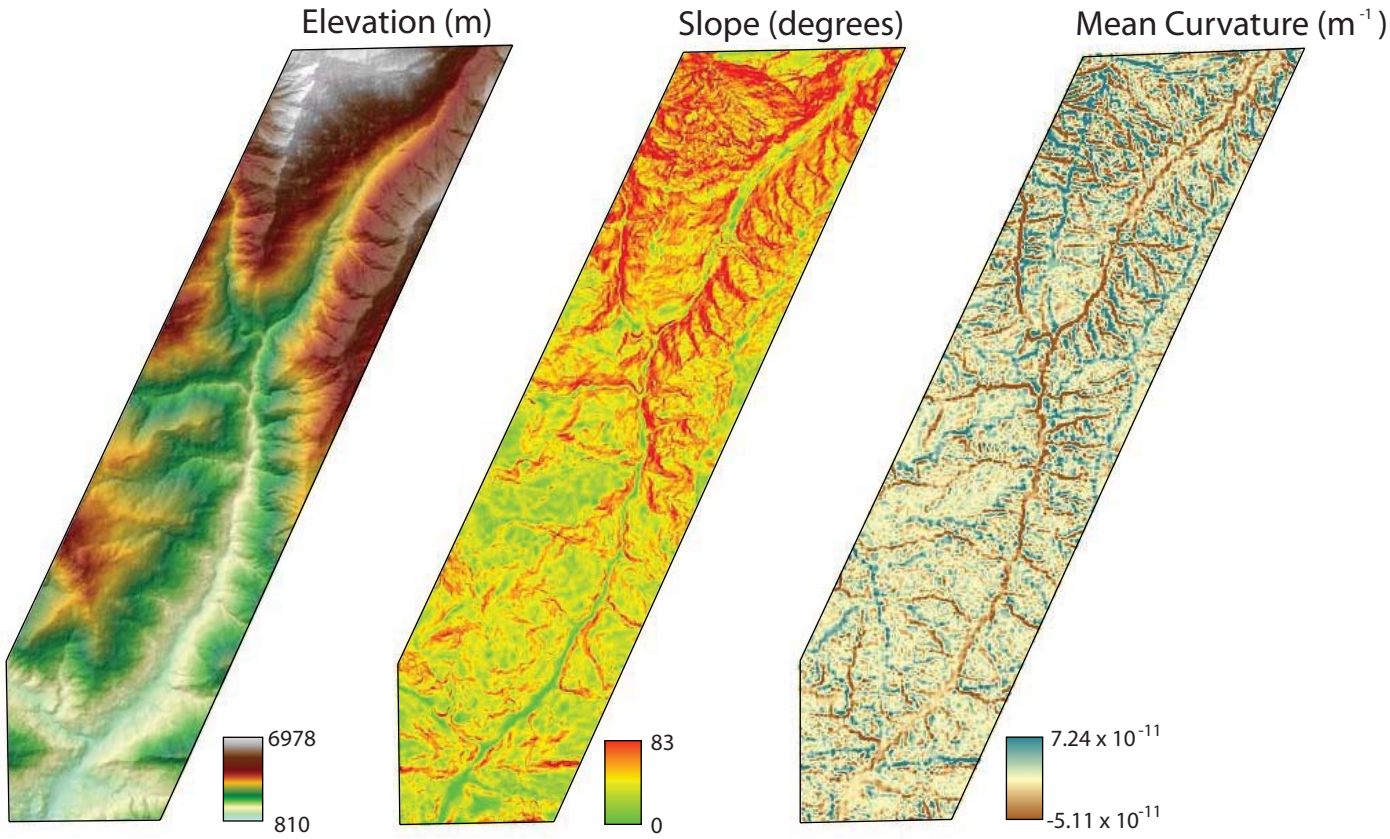

Figure 49: DEM and derivatives of the Modi Khola valley
Geographic coordinate system: WGS 1984 UTM Zone 44N. Projection: Transverse Mercator.

Chapter 6: Topographic signatures of Modi Khola lithologies

Although active faulting is one good explanation for topographic changes in steepness, the possibility that lithologic contacts change measurable aspects of the topography remains underexplored in this region. This study used GIS and spatial statistics to visualize, quantify, and evaluate relationships between bedrock geology and topography. Studies in other parts of the world define the morphologic signature of deep-seated landslides (Roering et al., 2005, Figure 50) or specific rock units (Korup, 2008) from steepness and curvature values. Even subtle variations in nearly flat topography define differences between shale- and sand-prone units (Belt et al., 2005, Figure 51). Hack (1973) initiated one of the first studies of steepness and lithology on the Potomac River and discovered that slope is often strongly correlated to underlying lithology (Figure 52).

Grove Karl Gilbert was one of the first geologists to examine topography and land sculpture to answer geologic questions. The importance of rock resistivity to erosion and its effect on the topography was recognized by Gilbert in the late 1800's during his studies of the Henry Mountains in southern Utah. Gilbert's field notebooks detail the effects of rock resistance and climate on rates of erosion and connect the production of different topographic forms to rock resistivity and erosion processes (Hunt, 1988). Gilbert hypothesized that landscape evolution is driven by ridge erosion which is controlled by slope-dependant processes that give rise to convex slopes and by valley erosion which is controlled by the product of both runoff and slope (Gilbert, 1877; Gilbert, 1909; Montgomery and Dietrich, 1994b).

Landscape erosion can be classified into two end member processes: overland flow and debris flow. Overland flow erosion removes material from the landscape in a particle by particle fashion across the entire landscape. Since different rock types maintain different levels of resistivity to erosion, more resistant lithologies tend to develop more prominent topographic forms in the landscape. Classic overland flow environments include the Grand Canyon and the arid western United States. Overland flow is absent in topography dominated by vegetation and very steep highly permeable soils (Wilson and Dietrich, 1987; Dietrich et al., 1993; Montgomery and Dietrich, 1995).

When overland flow is not present, slope dependant erosion processes, or debris flows, drive landscape evolution. The balance between sediment production from underlying bedrock and erosion or deposition of sediments due to downslope transport of debris is reflected in the spatial pattern in soil thickness across the topography (Dietrich et al., 1995). Sediments converge and accumulate at any indentations in the topography, including valleys, hollows, swales, etc., if there is no stream present to remove the material. Locations where sediments accumulate are convergent transport locations that reflect valley shaped topography. Divergent transport locations occur at ridges or noses where sediment is transported away from the location, allowing only thin layers of sediment to accumulate. Studies have found that the distribution of sediments across the landscape, according to convergent and divergent transportation zones, cause debris flows to typically originate at the tips of the channel network and at the steep, unchanneled convergent valleys (Reneau and Dietrich, 1987).

Research on debris flow-dominated topography suggests that slope and curvature of the surface topography greatly influence the location and frequency of landslide events (Dietrich and Dunne, 1978; Dietrich et al., 1982; Montgomery and Dietrich, 1994a). Transmissitivy, or the ability of the material to transport water down slope, is directly influenced by lithology, as different lithologic compositions control the amount of water that can flow through different rock types. Dietrich and Montgomery (1998) introduced a landscape erosion model called SHALSTAB, to aid in the production of landslide potential maps by measuring slope stability. The SHALSTAB model calculates landslide potential by combining the hydrologic and topographic indices. The hydrologic index integrates the precipitation rate and transmissitivy to determine how likely the ground is to become satuated. Greater saturation would generate a greater chance of hill slope instability. The topographic index (TI), $a/(b\sin\theta)$, quantifies the effect of topographic convergence on concentrating runoff and elevating pore pressures, where a is the distance between the contour lines, b is a selected width length along the contour lines, and θ is the slope angle. The topographic index was first introduced by Beven and Kirkby (1979) and is widely implemented in hydrologic modeling.

Curvature is essentially a representation of convergence and divergence, where negative curvature represents convergent topography and positive curvature represents divergent topography. I extracted values of steepness and curvature for different lithologic units in the Modi Khola valley of central Nepal. While unique values of steepness and curvature may distinguish the expression of different lithologic units in the topography (Belt et al., 2005; Roering et al., 2005; Korup, 2008), the Modi Khola

valley is dominated by steep topography, landslides, and vegetation. Debris flow style erosion potentially wipes the rock type signature out, although lithologies traverse the Modi Khola valley in a manner perpendicular to the river profile allowing the expression of the lithologies in the Modi Khola valley to be easily extracted and examined. Examining steepness and curvature in a debris flow dominated topography allows us to better understand how different lithologies manifest themselves in the topography in this type of environment.

The study described in this chapter was carried out in order to supplement and improve our understanding of the expression of different rock types in the topography of the Modi Khola valley, in an effort to address the role lithologic change plays in landscape evolution. The discovery of physiographic transitions only at lithologic contacts, with no repetitions or omissions of stratigraphy, might explain the breaks of steepness and curvature in the Modi Khola valley without the need for active faults. However, combinations of fault activity and rock type changes also might explain transitions in steepness.

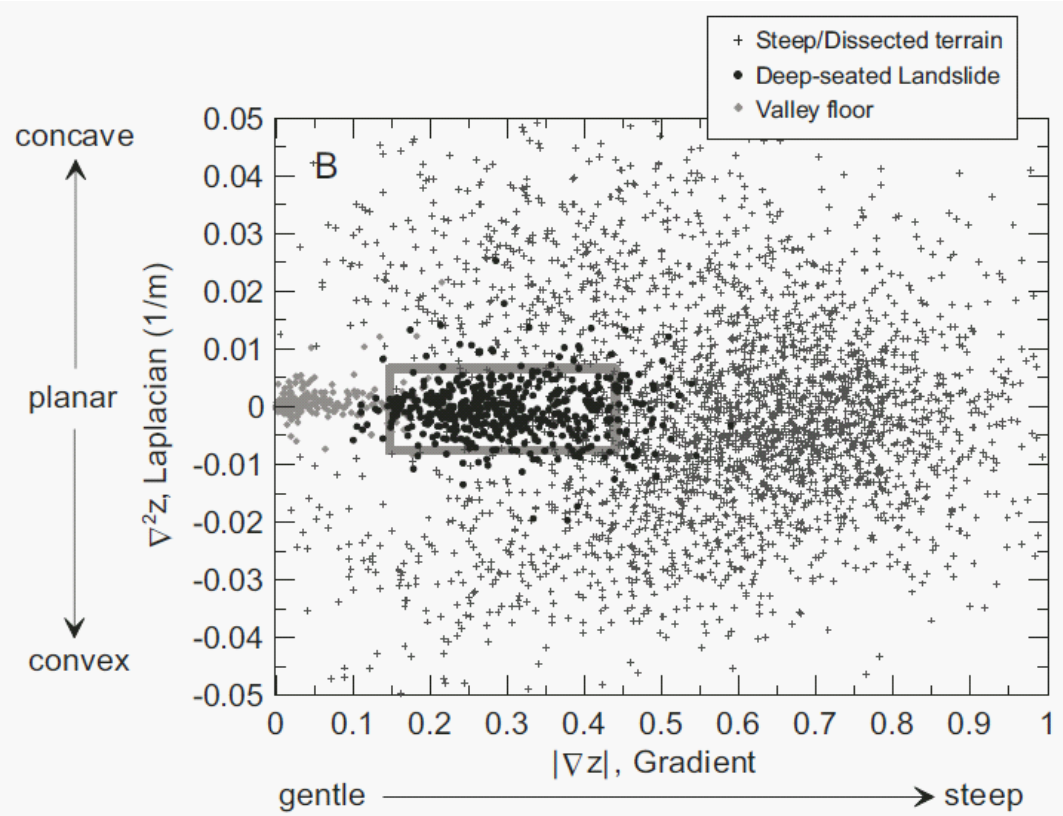

Figure 50: Steepness and curvature of rock types in the Oregon Coastal Range

Plots of gradient ($|\nabla z|$) and curvature ($\nabla 2z$) for two patches of terrain in the Oregon Coastal Range (OCR) studied by Roering et al. (2005). Relationship of gradient and curvature for steep and dissected terrain (crosses), valley floor (filled gray diamonds), and deep-seated landslides (filled circles). The gray box defines the envelope, or morphologic signature of deep-seated slides as defined by Roering et al. (2005). The envelope of deep-seated landslides is distinguishable from of other landforms in the OCR. Over 92% of the deep-seated landslide data points fall within the envelope, while only 4%–8% of the data for other landforms fall within the envelope. (Figure modified from Roering et al., 2005)

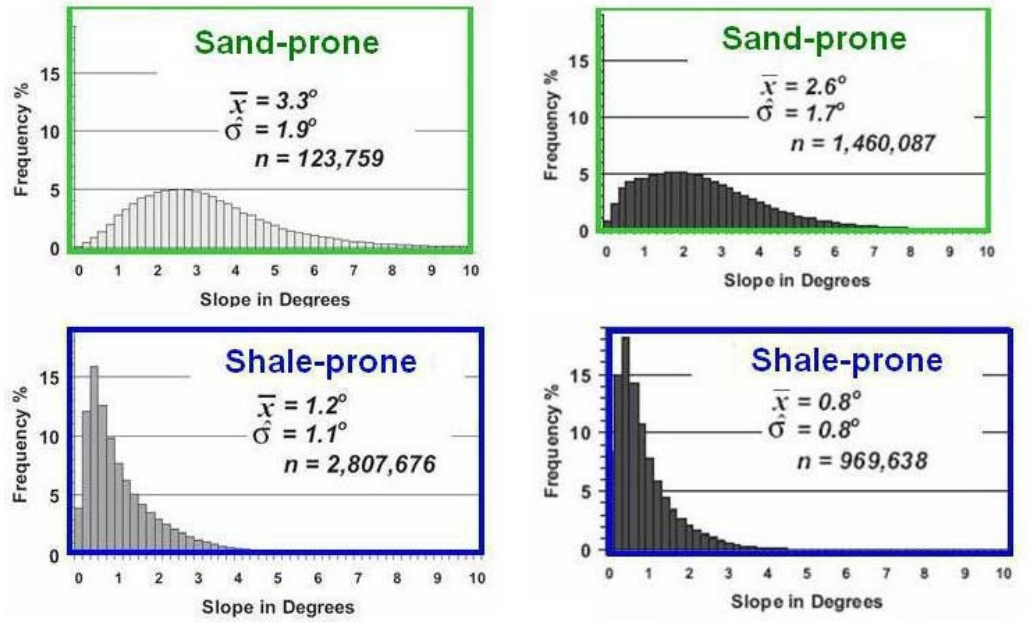

Figure 51: Frequency distributions of slopes for sand-prone and shale-prone lithologies in Oklahoma

Slope angle frequency histograms for sand-prone and shale-prone lithologies in Oklahoma studied by Belt et al. (2005). The top plots outlined in green show the frequency distribution of sand-prone units and the bottom blots outlined in blue show the frequency distribution of shale-prone units. (Figure modified from Belt et al., 2005)

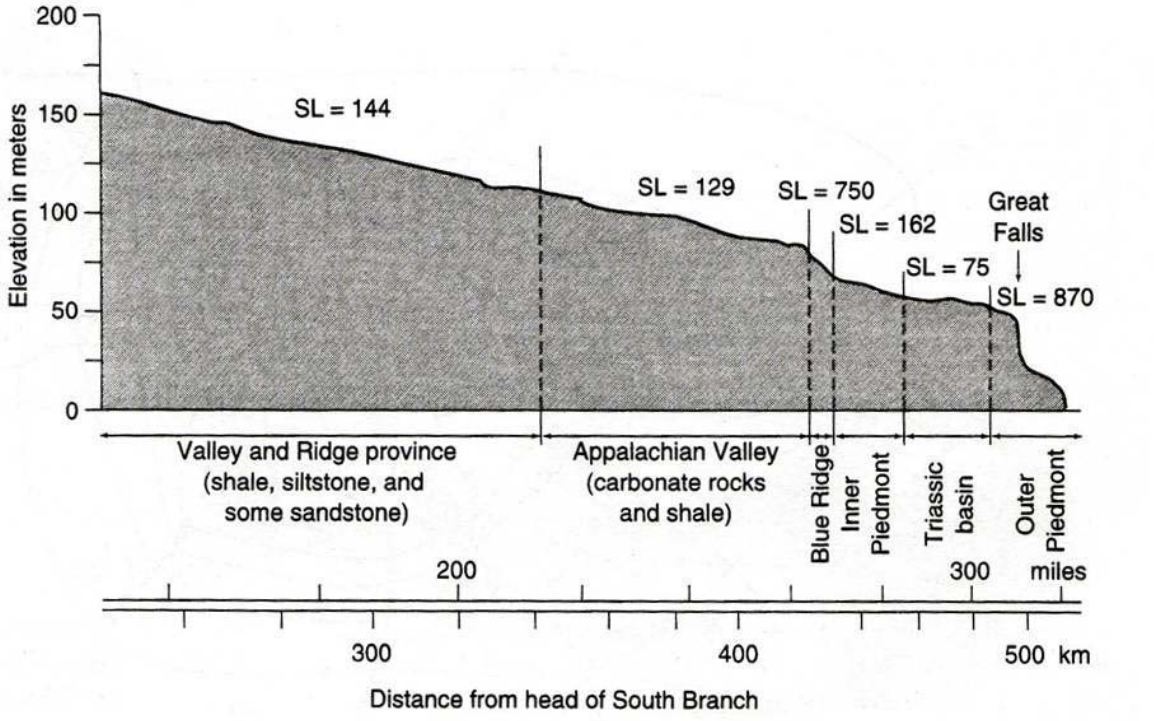

Figure 52: Slope length indices of the Potomac River from Hack 1973
Notice that rocks of the valley and ridge and Appalachian valley have relatively moderate slopes. More resistant rocks of the Blue Ridge create steeper slopes. Then the river changes back to more moderate slopes across the piedmont and Triassic basin until it drops rapidly again across the resistant rocks at great falls. Slope Length index (SL) = change height / change length * total stream length. This figure was extracted from Keller (2002) and is a modified version of the original figure from Hack (1973).

6.1 Pilot study in the Oregon Coast Range (OCR)

Positive values of curvature represent concave terrain such as valleys and hollows, while negative values represent convex forms such as hilltops. Roering et al. (2005) plotted the variation of curvature with gradient for steep and dissected terrain, deep-seated landslide terrain, and nearby valley floors in the OCR. The plot exhibited distinct morphologic signatures in gradient-curvature space for each landform type with minimal overlap, allowing identifications of landslide prone terrain through examination of a DEM.

A pilot study was conducted to quantify the relationship between lithology and slope. To allow comparison to the Roering et al. (2005) study, the same dataset from the OCR was used. A direct cell by cell comparison of slope and lithology showed few correlations, but variations of slope within the bounds of a single lithology could be used to delineate differences between rock types. The Tyee formation contained a high variability of slope values while the Qs formation (lacustrian and fluvial sedimentary rocks) had a low variation of slope values. Also, the average slope was 75º for the Tyee formation and 0.4º for the Qs formation (Figure 53). This analysis verified that no direct correlations between slope and lithology exist, though differences in slope variability within the bounds of a single lithology could be used to distinguish the Tyee and Qs formations in the OCR.

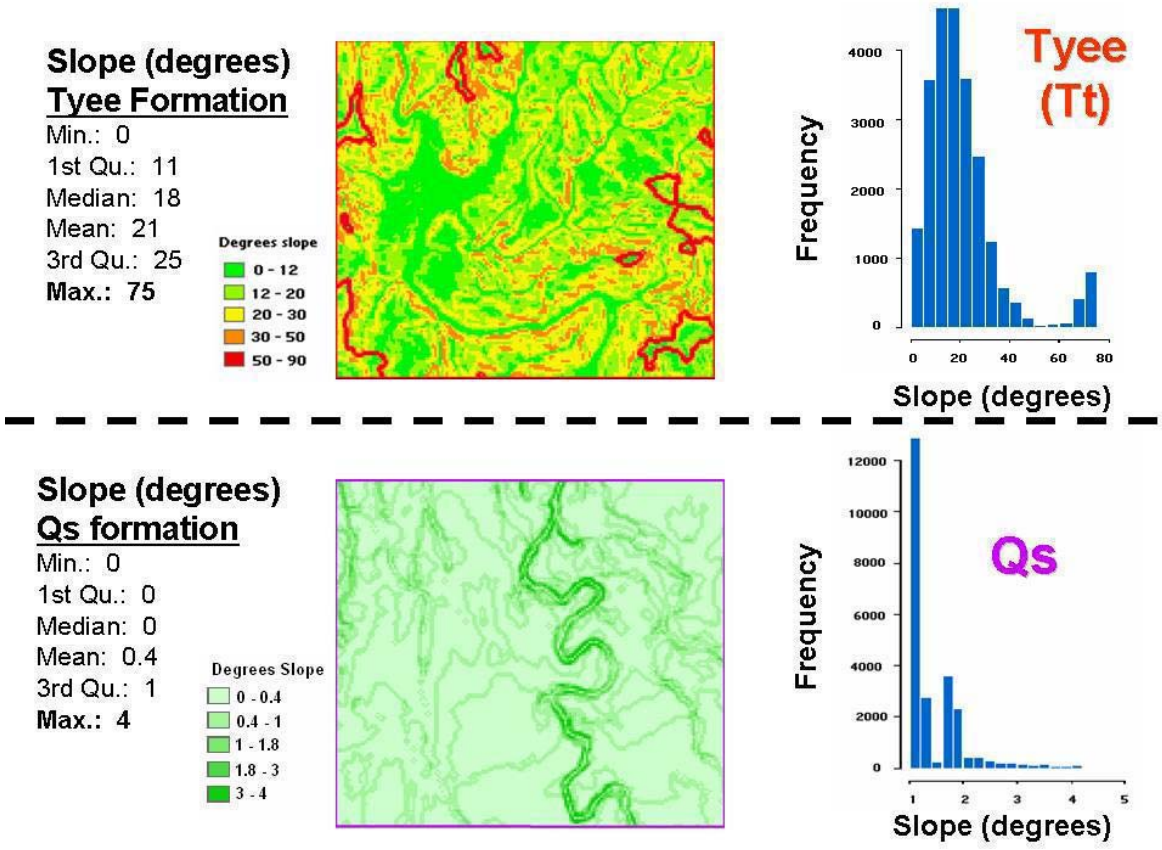

Figure 53: Data from OCR pilot study

6.2 Methods for determining topographic signature of each lithology

The geologic map of the Modi Khola valley was digitized in ArcGIS as a vector format (lines and polygons). Slope and curvature were converted from raster to points, creating grids of points spaced at 25 m. Polygons from each lithology were used to extract all points from the slope and curvature dataset, allowing distributions of slope and curvature to be assessed for each geologic unit.

To constrain the topographic signature of each lithology in the Modi Khola valley, the following graphs and maps were constructed for each lithologic unit: slope histograms (similar to those in Korup, 2008 and Belt et al., 2005), steepness vs. curvature plots (as plotted in Roering et al., 2005), and zonal statistics of elevation, slope, and curvature. Minimum, maximum, mean, and standard deviation of slope were extracted from each histogram. Skewness, kurtosis, and quartile divisions were also calculated from slope histograms in order to examine differences in slope distribution for each rock type. Steepness vs. curvature plots were constructed to determine if different lithologies could be characterized by envelopes of steepness and curvature, as was delineated by Roering et al. (2005) for landslides. Zonal statistics allowed the mean, minimum, maximum, range, and standard deviation of elevation, slope, and curvature for each lithologic unit to be calculated and represented visually in map form.

6.3 Results

6.3.1 Slope distribution comparison

Probability density plots allow the distribution of steepness to be examined within each lithology in the Modi Khola valley (Figure 54). Probability density plots were used instead of histograms because using probability density allowed direct comparison of lithologies that covered different sized areas of the landscape, which would cause a different number of slope data points to be extracted from the topography. To calculate probability density, the slope data were divided into 100 bins. Then the number of counts was determined for each bin and then divided by both the interval width on the x-axis and the total number of data points. This method bins the data by equal intervals of slope, as opposed to ranking the data which emphasizes certain ranges of data that may not have equal intervals of slope. Although the shape and mean values of histograms allowed Belt et al. (2005) to distinguish subtle variations in sand prone and shale prone units, these data do not exhibit any obvious characteristics that correlate to lithology. Probability density lines extracted from these histograms only show subtle changes in skewness and kurtosis (Figure 55), but nothing that allows even rock type groups (sedimentary, igneous, or metamorphic) to be related. When the probability density curves of Tethyan rocks, Greater Himalayan rocks, and Lesser Himalayan rocks are distinguished with color, it becomes apparent that the slope of Greater Himalayan rocks is skewed towards steeper slopes and the slope of Lesser Himalayan rocks is skewed towards gentler slopes (Figure 56). The distribution of slope for Tethyan rocks is skewed the most to the left and has the highest mean slope at 43 degrees.

NORTH

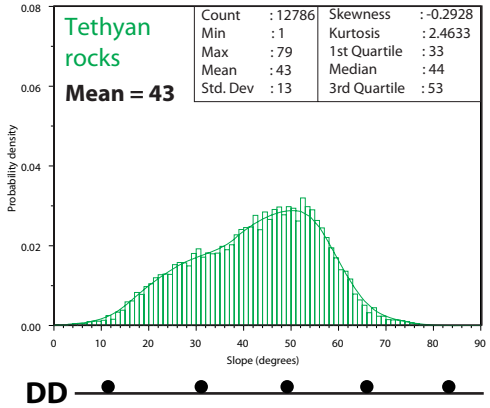

DD

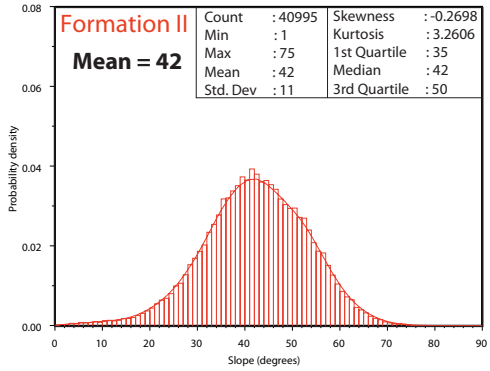

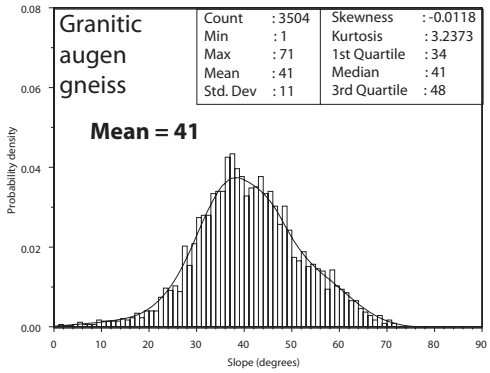

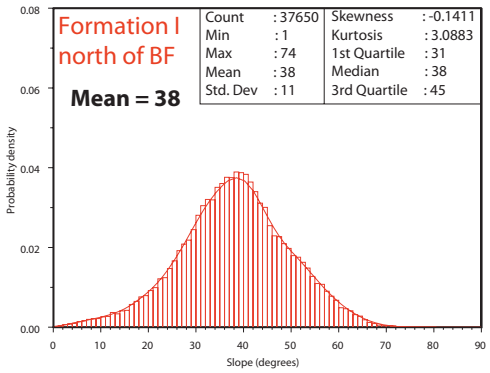

BF

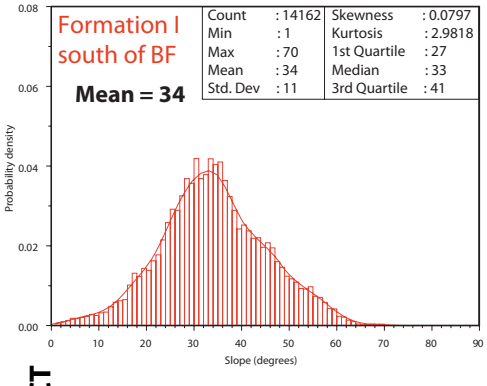

MCT

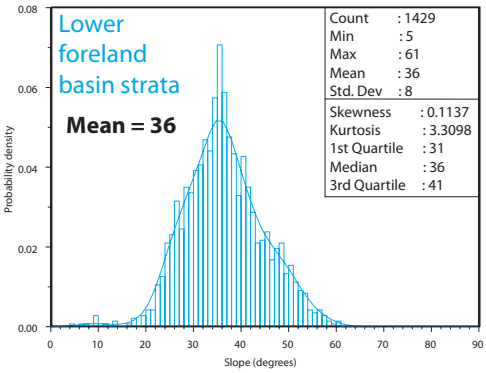

RF

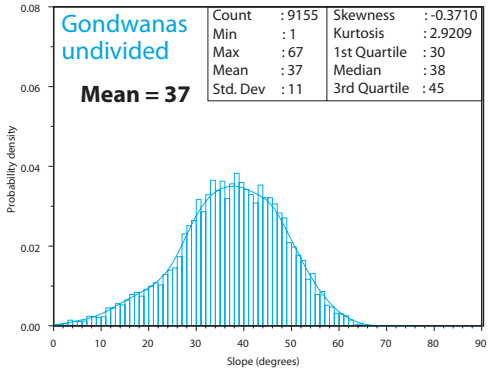

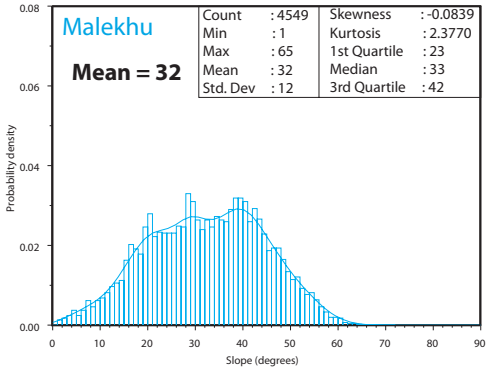

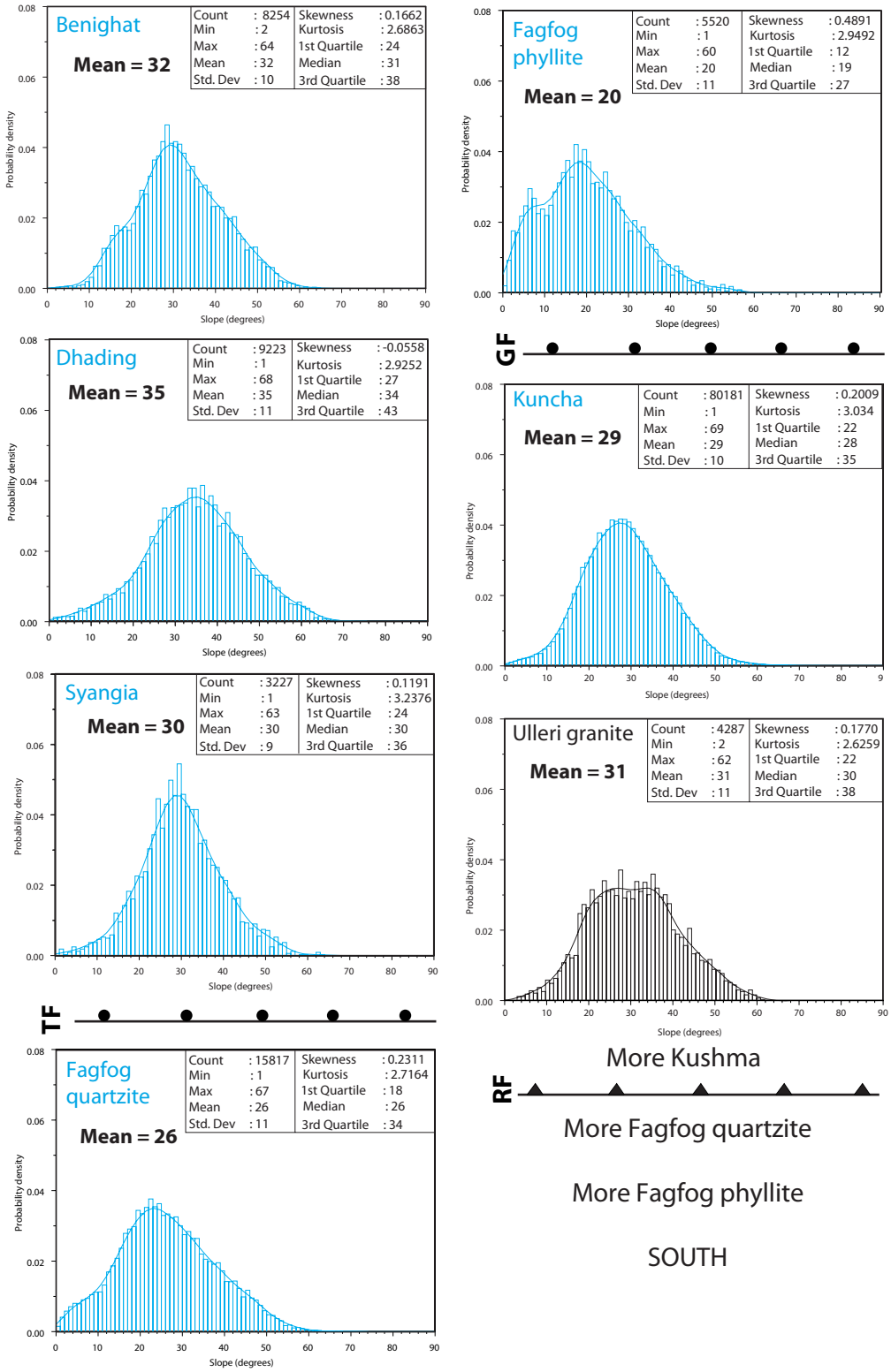

Figure 54: Slope distributions for each lithology in the Modi Khola
Slope distributions are shown by probability density plots and organized in lithologic sequence from north to south. The sequence progresses in vertical columns on the first page and then is continued on the second page of this figure.

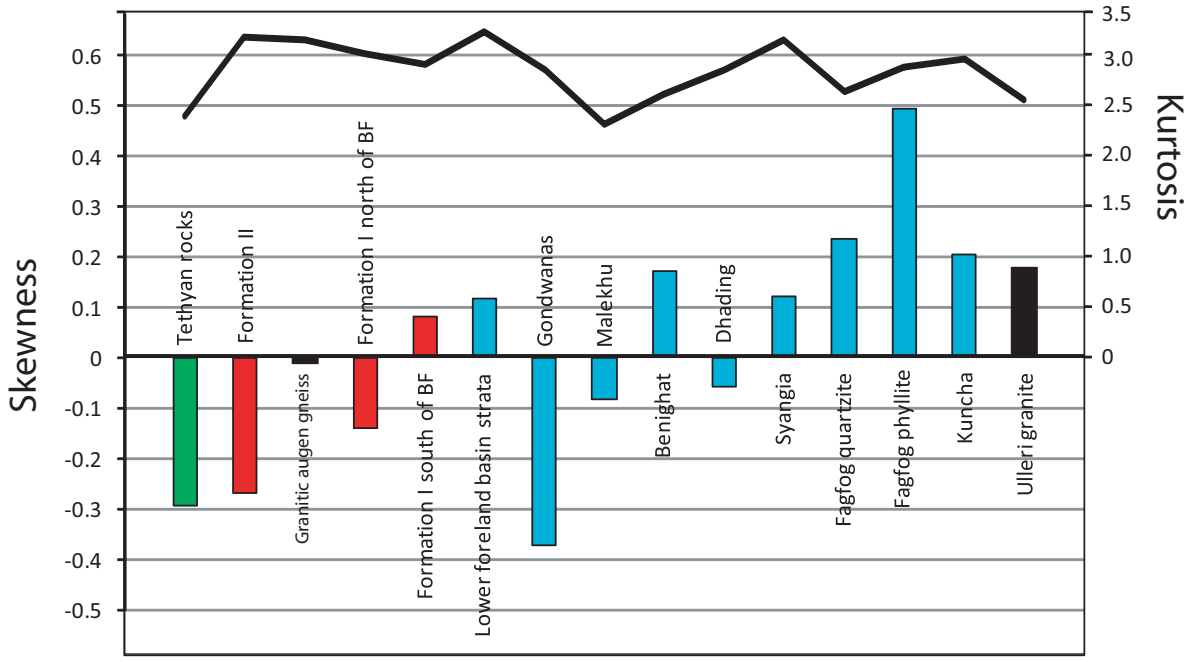

Figure 55: Skewness and kurtosis from slope histograms
Skewness and kurtosis for histograms of each rock type. Kurtosis is shown by the bar graph and skewness is shown by the line. The Tethyan rocks are green, Greater Himalayan rocks are red, and Lesser Himalayan rocks are blue. The granitic augen gneiss and the Ulleri granite are colored black.

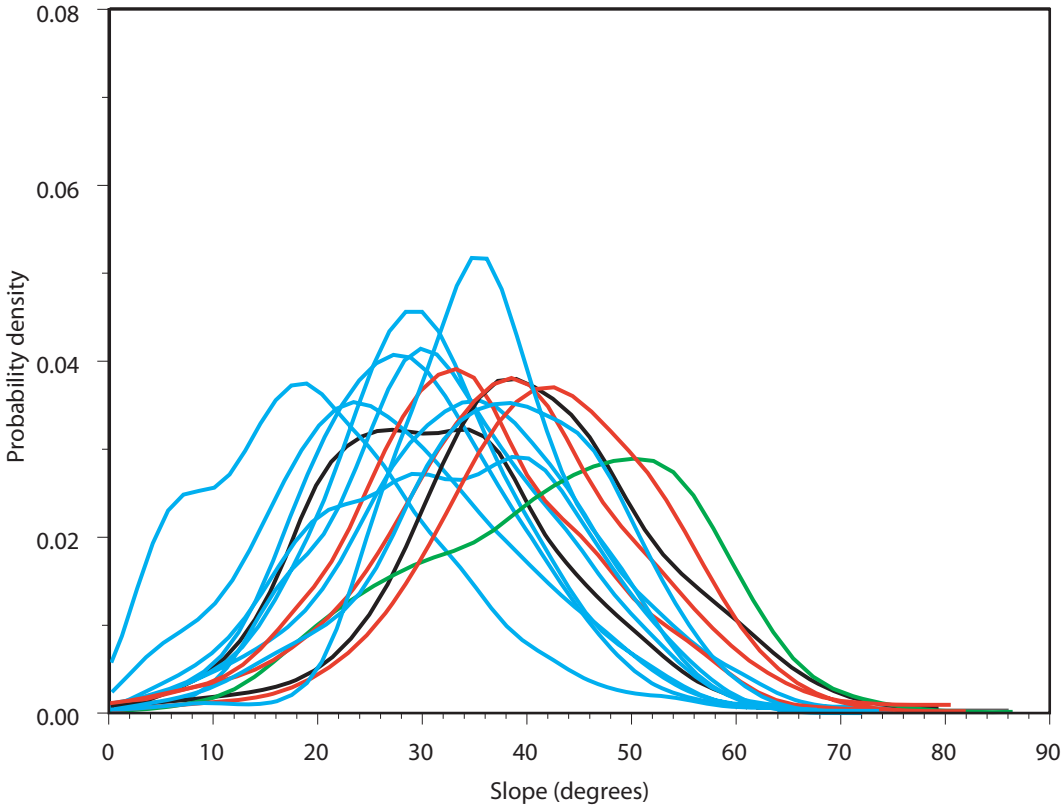

Figure 56: Comparison of probability density curves for Tethyan, Greater Himalayan, and Lesser Himalayan rocks
The green curve represents the probability density of the Tethyan rocks, the red curves represent probability density Greater Himalayan rocks, and the blue curves represent probability density of Lesser Himalayan rocks.

6.3.2 Steepness vs. mean curvature plots

The lithologies of the Modi Khola valley maintain similar envelopes of steepness vs. curvature (Figure 57). Steepness varies from 1 degree to approximately 70 degrees and curvature varies from -2×10^{-11} to 2×10^{-11} m^{-1}. Lithologies for all rock units fall within the limits of the steepness vs. curvature limit described above. More variability of curvature is noticeable to the north of the MCT, but is hard to confirm due to the large number of sampling points in the north per lithology compared to the small number of sampling points per lithology of some units to the south. While Roering et al. (2005) used steepness vs. curvature plots to successfully distinguish deep-seated landslides, steep dissected terrain, and valley floors, this method does not allow the topographic changes of different rock types to be well constrained. The landscape morphology distinguished by Roering et al. (2005) was significantly different. The data suggest that topographic differences of rock types are much more subtle, making it harder to identify features that characterize only specific rock units. At a regional scale, Lesser Himalayan rocks contain noticeably gentler slopes than Greater Himalayan rocks (Figure 58).

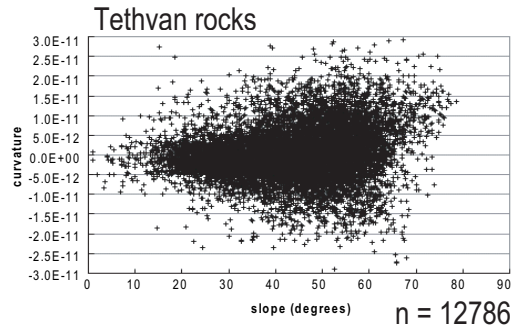
Tethvan rocks
curvature
slope (degrees)
n = 12786

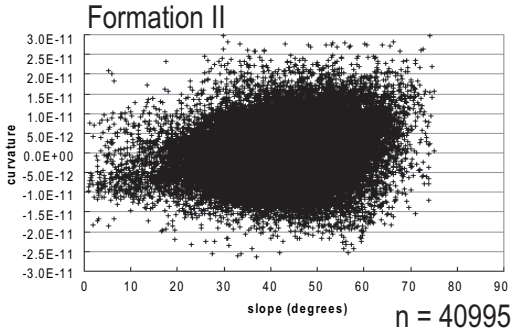
Formation II
curvature
slope (degrees)
n = 40995

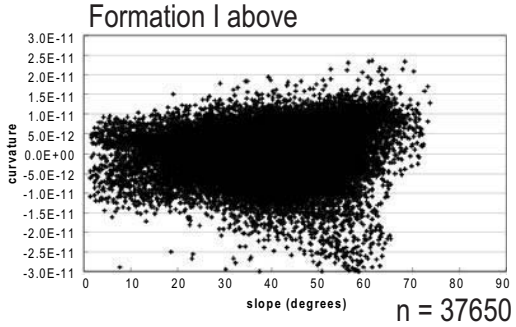
Formation I above
curvature
slope (degrees)
n = 37650

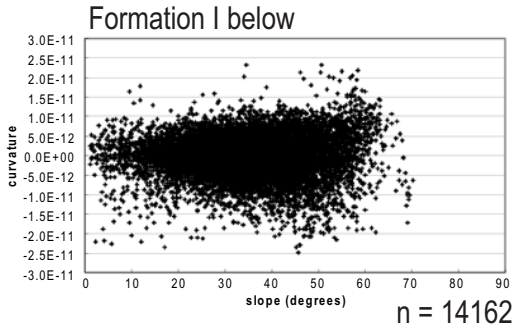
Formation I below
curvature
slope (degrees)
n = 14162

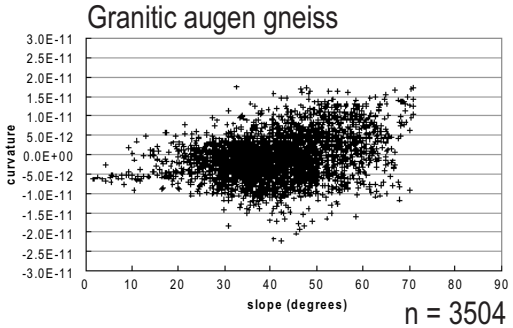
Granitic augen gneiss
curvature
slope (degrees)
n = 3504

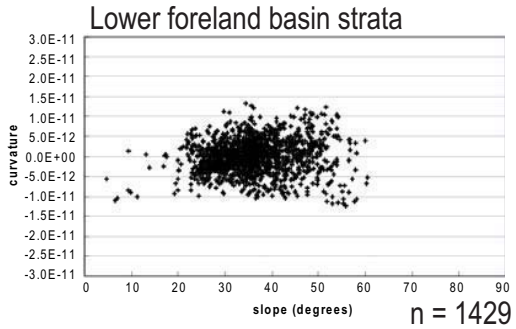
Lower foreland basin strata
curvature
slope (degrees)
n = 1429

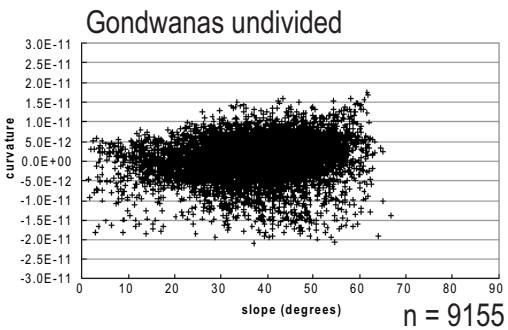
Gondwanas undivided
curvature
slope (degrees)
n = 9155

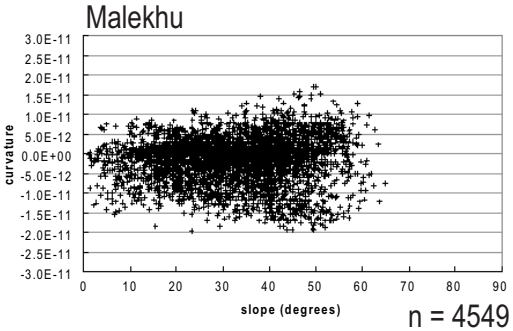
Malekhu
curvature
slope (degrees)
n = 4549

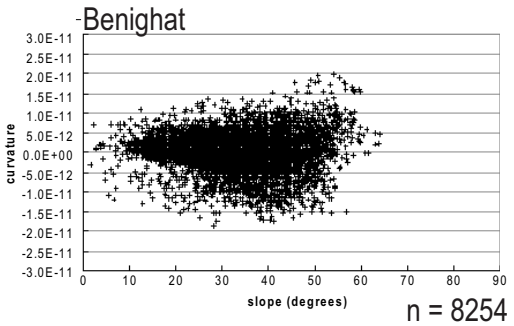
Benighat
curvature
slope (degrees)
n = 8254

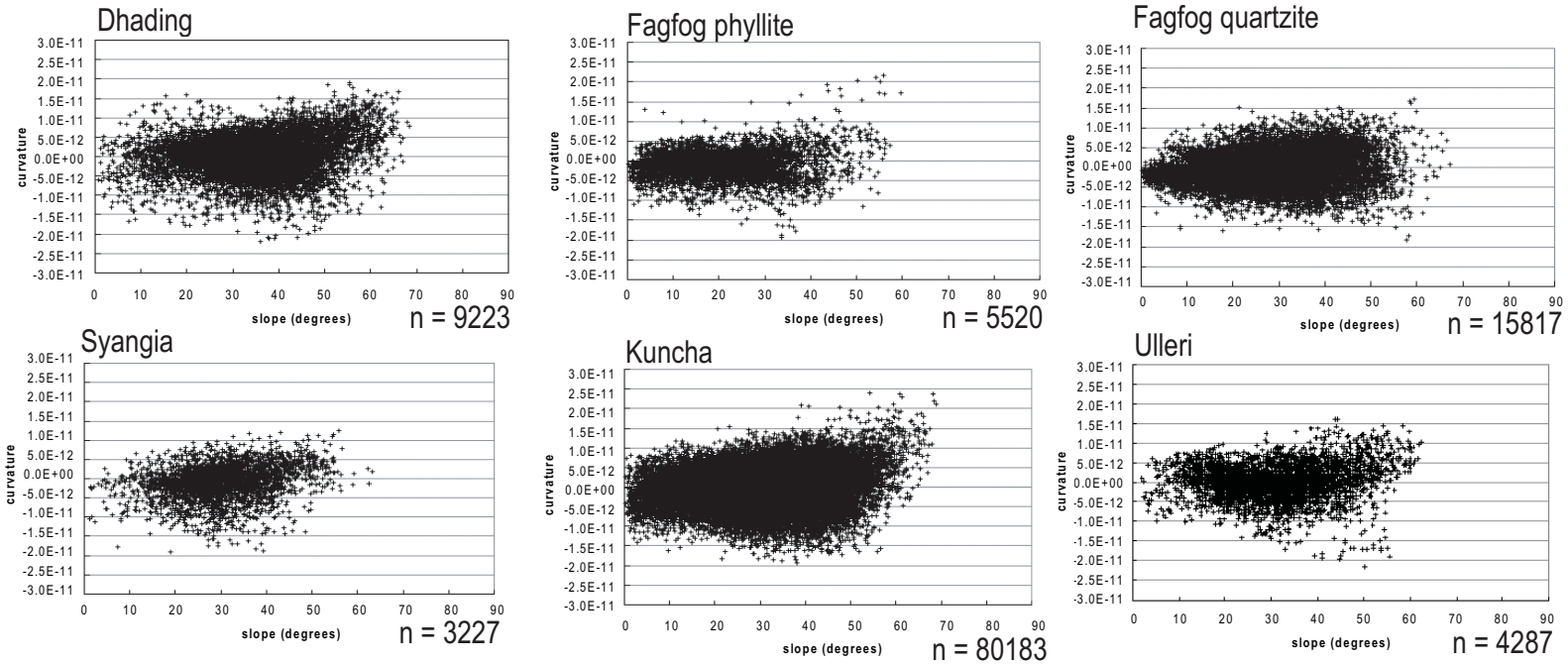

Figure 57: Steepness vs. curvature plots for each lithology
Positive curvature represents convex terrain and negative curvature represents concave terrain. Curvature values are all measured in m^{-1}.

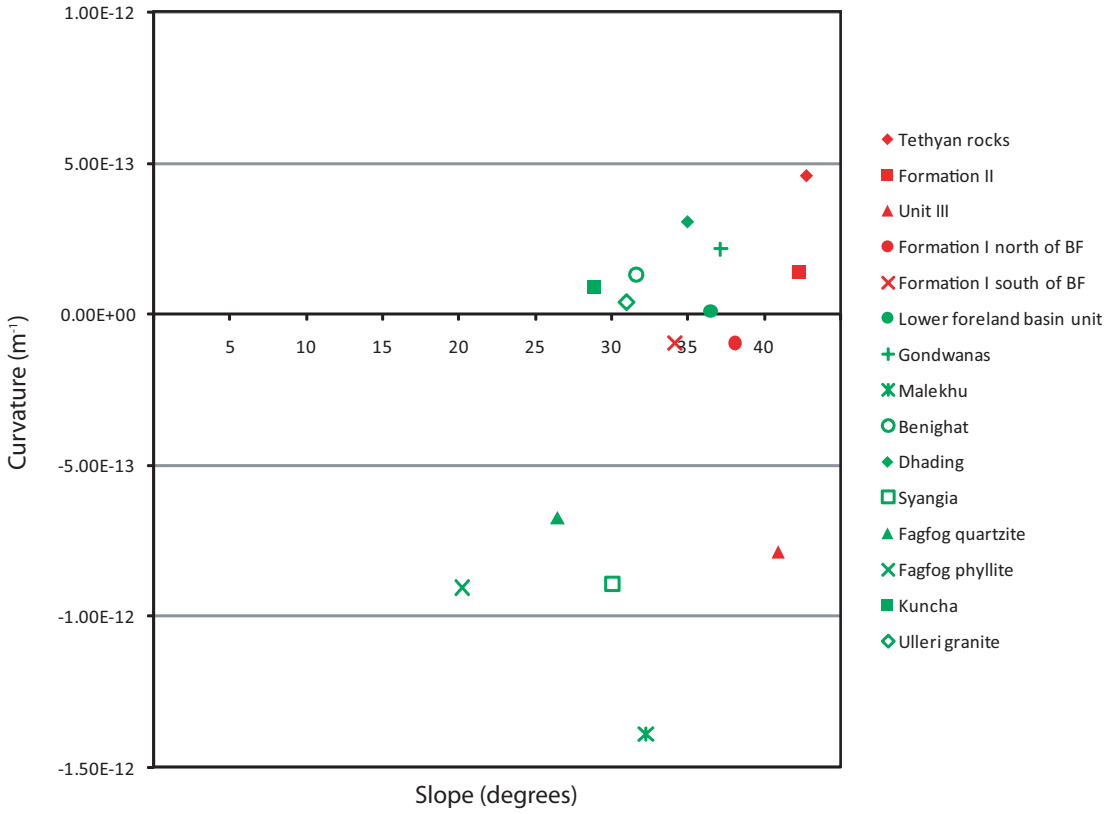

Figure 58: Average steepness vs. curvature plots for each lithology
Each data point represents average steepness and curvature across a particular geologic unit. Greater Himalayan units are colored red and Lesser Himalayan units are colored green. Greater Himalayan rocks appear to maintain higher average slopes than Lesser Himalayan rocks.

6.3.3 Zonal statistics

Zonal maps allow changes in elevation, slope, and curvature across different lithologic units to be analyzed visually. Visual examinations of the zonal elevation statistic maps show that high elevations are concentrated in the Greater Himalayan rocks, while low elevations are concentrated in the Lesser Himalayan rocks (Figure 59, Table 9). The granitic augen gneiss and the Kuncha contain the highest variability, or range in elevation. The zonal slope statistics maps illustrate significantly higher slope values in the Greater Himalayan rocks that vary from 1 to 79 degrees. The Lesser Himalayan rocks tend to have lower slope values than Greater Himalayan rocks and vary only between 1 and 65 degrees (Figure 60, Table 9). Slope values do not increase from south to north consistently, but rather fluctuate as they cross different lithologic units. Formation II, Lower foreland basin strata, Gondwanas undivided, Dhading, and the Ulleri granite all exhibit significantly higher mean slope values than other lithologies (Figure 62, Table 9). Consequently, dips and peaks that occur in slope data from the north to the south are well reflected by the average curvature data. Peaks in slope data correspond to positive curvature values or convex topography, while dips in slope data relate to negative curvature values or concave topography (Figure 62). The zonal mean curvature maps visually delineate this fluctuation of positive to negative curvature across the range (Figure 61).

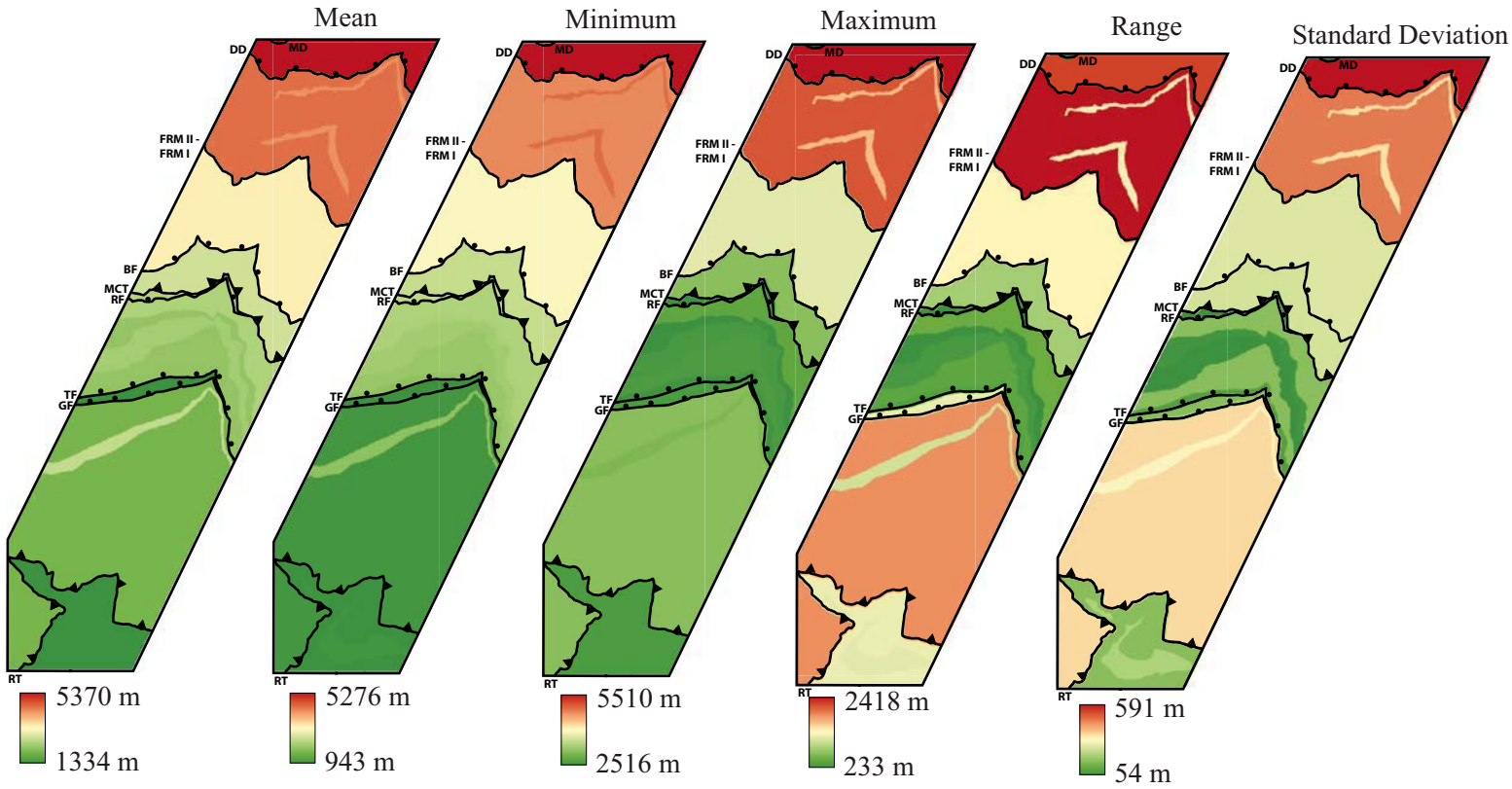

Figure 59: Elevation zonal statistics map

Mean, minimum, maximum, range, standard deviation zonal elevation maps of the Modi Khola valley. Each lithologic unit was used as the zone (or region) to calculate elevation statistics within. Refer to the geologic map of the Modi Khola in Figure 5 to identify lithologic units. MD-Macchapucchare Detachment, DD—Deorali Detachment, FRM II - FRM I— Formation II - Formation I lithologic contact, BF— Bhanuwa Fault, MCT—Main Central thrust, RF—Romi Fault, TF—Tobro Fault, GT—Ghandruk thrust, RT—Ramgarh thrust. Geographic coordinate system: WGS 1984 UTM Zone 44N. Projection: Transverse Mercator.

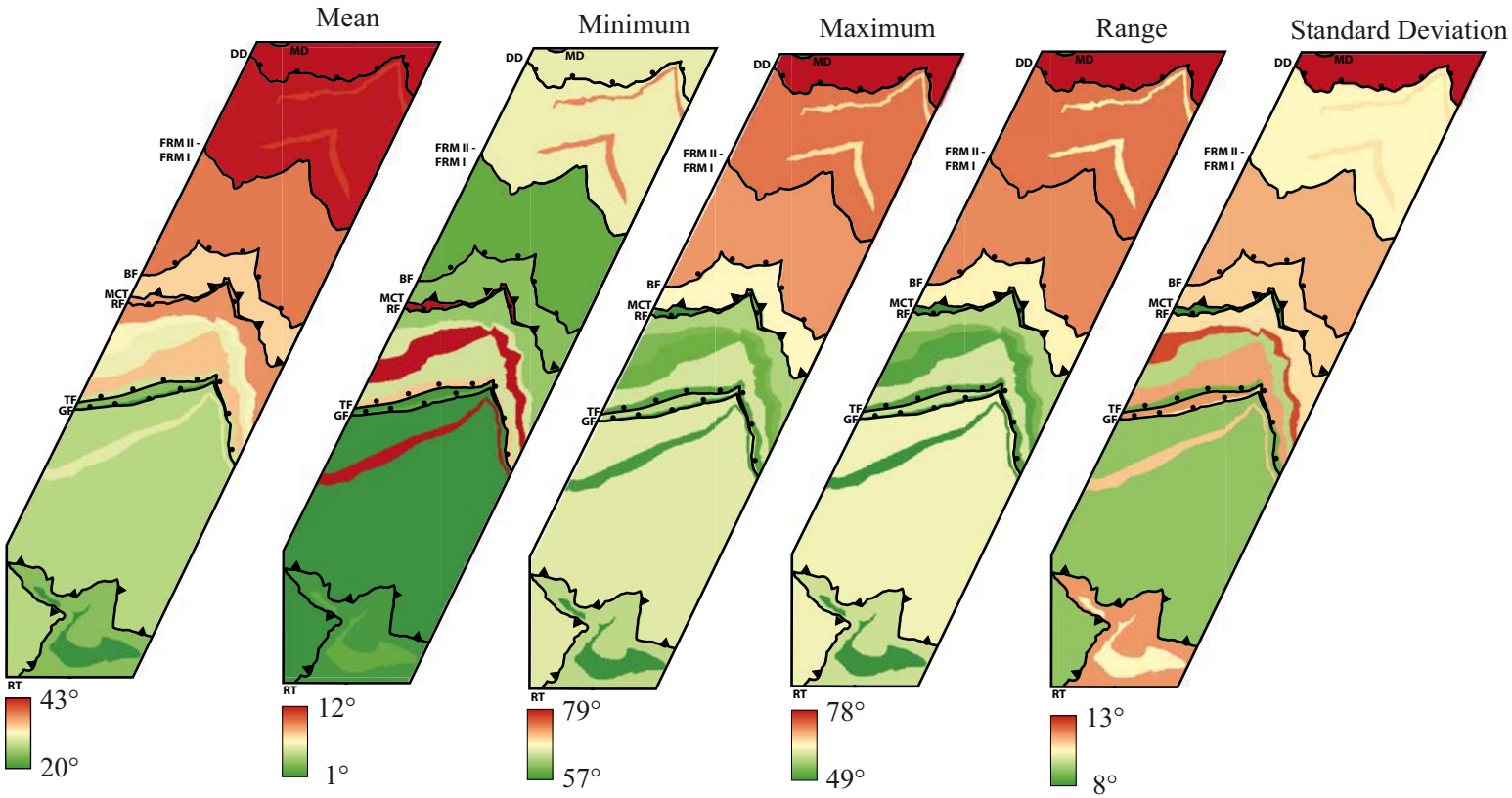

Figure 60: Slope (degrees) zonal statistics map

Mean, minimum, maximum, range, standard deviation zonal slope maps of the Modi Khola valley. Each lithologic unit was used as the zone (or region) to calculate slope statistics within. Refer to the geologic map of the Modi Khola in Figure 5 to identify lithologic units. MD-Macchapucchare Detachment, DD—Deorali Detachment, FRM II - FRM I— Formation II - Formation I lithologic contact, BF— Bhanuwa Fault, MCT—Main Central thrust, RF—Romi Fault, TF—Tobro Fault, GT—Ghandruk thrust, RT—Ramgarh thrust. Geographic coordinate system: WGS 1984 UTM Zone 44N. Projection: Transverse Mercator.

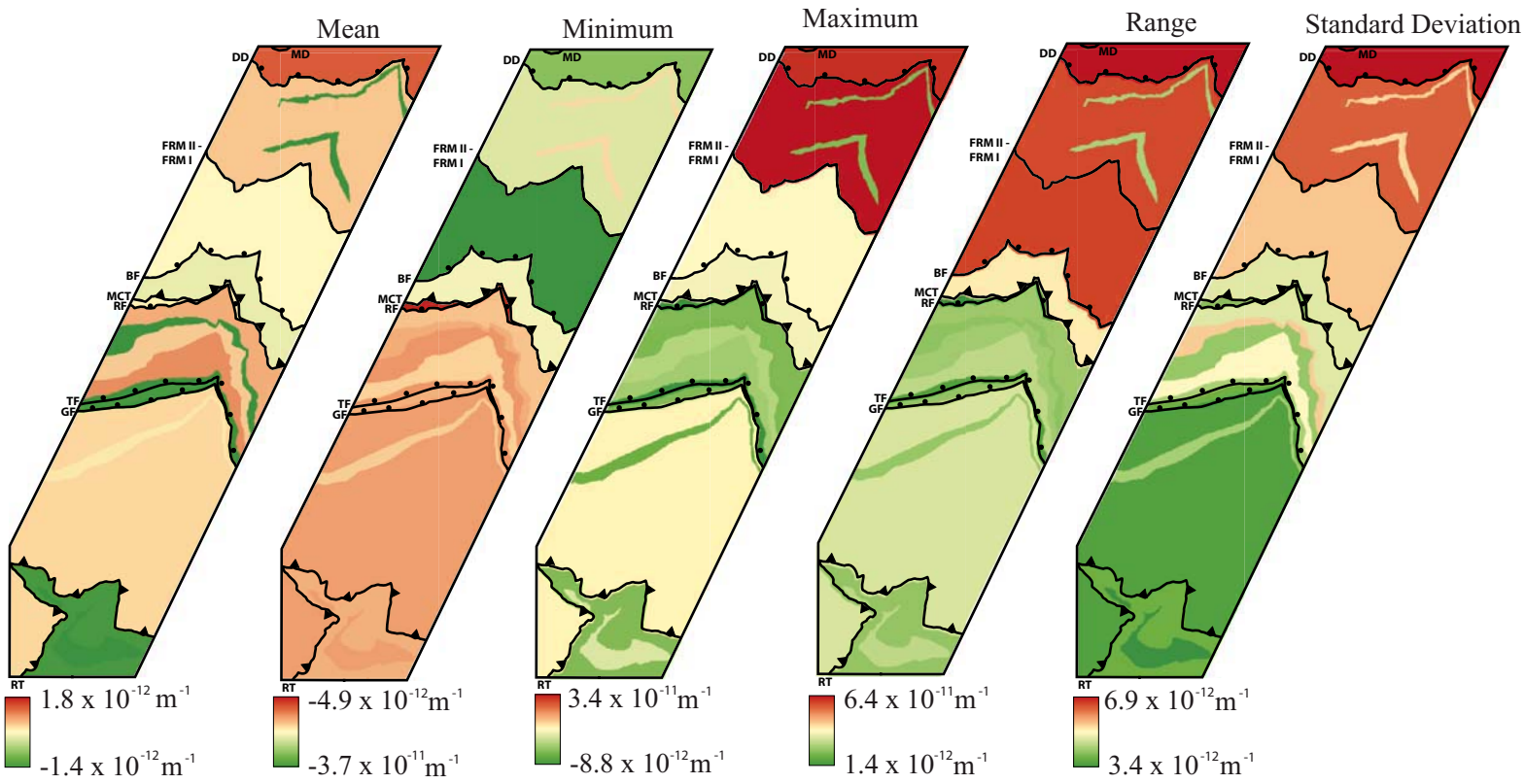

Figure 61: Curvature zonal statistics map

Mean, minimum, maximum, range, standard deviation zonal curvature maps of the Modi Khola valley. Each lithologic unit was used as the zone (or region) to curvature elevation statistics within. Refer to the geologic map of the Modi Khola in Figure 5 to identify lithologic units. MD-Macchapucchare Detachment, DD—Deorali Detachment, FRM II - FRM I— Formation II - Formation I lithologic contact, BF— Bhanuwa Fault, MCT—Main Central thrust, RF—Romi Fault, TF—Tobro Fault, GT—Ghandruk thrust, RT—Ramgarh thrust. Geographic coordinate system: WGS 1984 UTM Zone 44N. Projection: Transverse Mercator.

Table 9: Zonal statistics values for each lithologic unit
Count is the number of 25 x 25 m cells within the lithologic unit. STD is standard deviation.
BF – Bhanuwa fault, Sanctuary unit excluded.

Zonal Elevation (m)

LITHOLOGIC UNIT	COUNT	MINIMUM	MAXIMUM	RANGE	MEAN	STD
Tethyan rocks	12696	3079	5364	2284	4289	591
Formation II	40912	2330	4748	2418	3458	495
Granitic augen gneiss	3485	2452	4162	1709	3266	424
Formation I north of BF	37563	1861	3647	1786	2742	378
Formation I south of BF	14171	1612	3081	1469	2348	370
Lower foreland basin unit	1420	1591	2517	926	2175	234
Gondwanas	9149	1508	2783	1275	2142	312
Malekhu	4530	1498	2516	1017	1972	250
Benighat	8260	1456	2601	1145	2087	234
Dhading	9201	1417	2646	1229	1979	311
Syangia	3230	1372	2560	1188	1950	265
Fagfog	15803	943	2636	1692	1351	311
Fagfog phyllite	5510	983	2658	1675	1340	342
Kuncha	80027	992	3055	2062	1771	428
Ulleri granite	4277	1354	2965	1611	2274	400

Zonal Slope (degrees)

LITHOLOGIC UNIT	COUNT	MINIMUM	MAXIMUM	RANGE	MEAN	STD
Tethyan rocks	12696	1	79	78	43	13
Formation II	40912	1	75	74	42	11
Granitic augen gneiss	3485	1	71	70	41	11
Formation I north of BF	37563	1	74	74	38	11
Formation I south of BF	14171	1	70	70	34	11
Lower foreland basin unit	1420	5	60	56	36	8
Gondwanas	9149	1	67	66	37	11
Malekhu	4530	1	65	64	32	12
Benighat	8260	2	64	62	32	10
Dhading	9201	1	68	68	35	11
Syangia	3230	1	63	62	30	9
Fagfog	15803	1	67	67	26	12
Fagfog phyllite	5510	1	57	57	20	11
Kuncha	80027	1	69	69	29	10
Ulleri granite	4277	2	62	60	31	11

Zonal Curvature (m^{-1})

LITHOLOGIC UNIT	COUNT	MINIMUM	MAXIMUM	RANGE	MEAN	STD
Tethyan rocks	11458	-3.15E-11	3.27E-11	6.42E-11	4.59E-13	6.89E-12
Formation II	8260	-1.87E-11	1.98E-11	3.85E-11	1.30E-13	4.28E-12
Granitic augen gneiss	9201	-2.18E-11	1.90E-11	4.08E-11	3.06E-13	5.15E-12
Formation I north of BF	15803	-2.02E-11	1.73E-11	3.75E-11	-6.74E-13	3.91E-12
Formation I south of BF	5510	-1.92E-11	2.17E-11	4.09E-11	-9.04E-13	3.42E-12
Lower foreland basin unit	37563	-3.70E-11	2.37E-11	6.07E-11	-1.60E-14	5.57E-12
Gondwanas	14171	-2.48E-11	2.31E-11	4.79E-11	-9.46E-14	4.90E-12
Malekhu	40912	-2.64E-11	3.39E-11	6.03E-11	1.38E-13	6.35E-12
Benighat	9149	-2.10E-11	1.72E-11	3.83E-11	2.14E-13	4.88E-12
Dhading	80027	-1.92E-11	2.41E-11	4.33E-11	8.83E-14	3.68E-12
Syangia	4530	-1.98E-11	1.69E-11	3.67E-11	-1.39E-12	5.50E-12
Fagfog	1420	-1.23E-11	1.33E-11	2.56E-11	1.20E-14	4.16E-12
Fagfog phyllite	3230	-1.87E-11	1.27E-11	3.13E-11	-8.93E-13	4.44E-12
Kuncha	4277	-2.16E-11	1.61E-11	3.77E-11	3.94E-14	4.42E-12
Ulleri granite	3485	-2.23E-11	1.72E-11	3.95E-11	-7.87E-13	5.41E-12

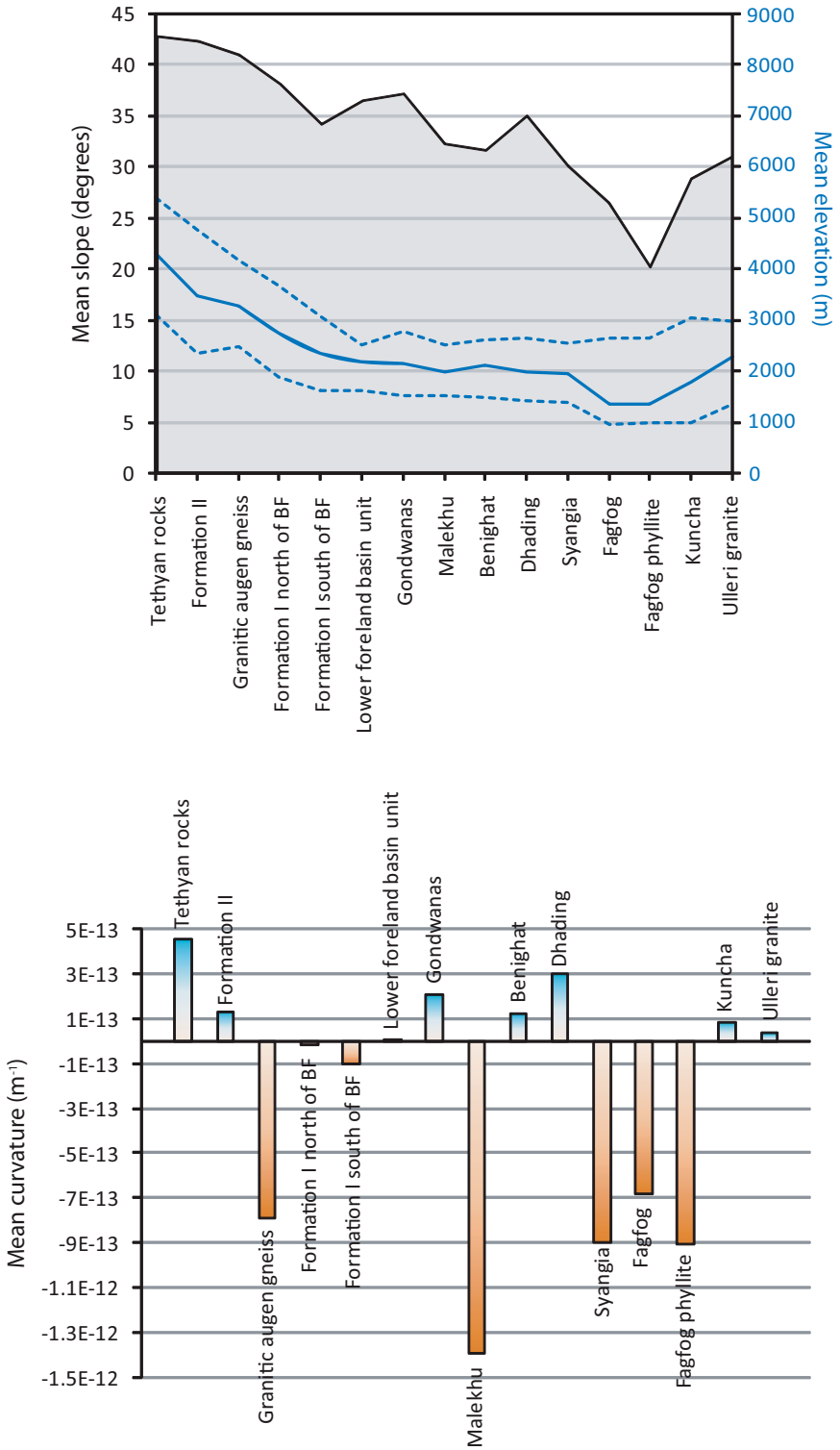

Figure 62: Average elevation, slope, and curvature plots
A graphical representation of average elevation and slope (upper plot) and average curvature (lower plot) for each lithologic unit.

6.4 Conclusions

Only subtle variations in steepness and curvature are observable in the Modi Khola valley. The slope and curvature distributions occurring in lithologies of the Modi Khola valley do not exhibit substantially different variations of slope, as expected and documented by several other studies (Roering et al., 2005; Belt et al., 2005; Korup et al., 2008). These studies indicate that slopes have a natural limit to their steepness, which is determined by a rocks resistivity to erosion, and no amount of rainfall or tectonic uplift can change it (Hartmann, 2008). Korup et al. (2008) analyzed an array of field sites in New Zealand in which each site differed in rates of precipitation and tectonic uplift. The data showed that hillsides composed of greywacke all had the same average slope angle at about 39 degrees. While this study allowed the topographic signature of New Zealand bedrock to be characterized, Korup et al. (2008) emphasize that the topographic signature of underlying bedrock may not be reflected unless hillslopes are at the limit of their mechanical strength which would produce landsliding. While rock type seems to play a pivotal role in landscape evolution, perhaps extreme tectonic and climatic differences, like those that characterize the Himalaya, could make patterns of rock type signature more subtle and harder to detect in the landscape. The following conditions may make lithologic signatures difficult to identify in the Modi Khola valley:

1) The Modi Khola valley is saturated by over 8 m of precipitation annually (TRMM precipitation data, Bookhagen et al., 2006). Intense rains may

cause even the most cohesive rocks to erode more rapidly that predicted in other regions of the world.

2) The slope and curvature variations detected in this analysis are very subtle. Perhaps the variability of topographic signatures would be magnified if resolutions less than 25 m, such as LIDAR data, were attainable for analysis in this region (Snyder, 2009). While topographic signatures of different lithologies were identified in Oklahoma (Belt et al., 2005), the Oregon Coast Range (Roering et al., 2005), and New Zealand (Korup 2008), the topography and climate of the Modi Khola valley is very different than these locations. Perhaps the particular physical characteristics of a particular region determine the ideal DEM resolution size needed to distinguish the topographic expression of different rock types in the landscape (Zhang and Montgomery, 1994).

3) If tectonic events are occuring in the Modi Khola valley, perhaps the tectonic events are occurring at a rate that is quicker than the time it takes for hillslopes to reach threshold angles.

4) Landslide events cover the terrain with debris, resculpting the landscape, regardless of the location of different lithologic units. Landslides frequently occur in the Modi Khola valley and may cover the expected expression of different lithologies in the landscape.

Chapter 7: River profile analysis

The stream profiler tool used to calculate river steepness (k_{sn}) and concavity (θ) in this analysis was acquired from www.geomorphtools.com. This tool was originally developed by Noah Snyder and Kelin Whipple in the 1990s at MIT. The tool was refined later by subsequent graduate students at MIT. An advanced iteration of the tool, which was downloaded from www.geomorphtools.com, is the most recent incarnation of the stream profiler tool and allows integration between Matlab and ArcGIS. Daniel Sheehan and Eric Kirby developed the ArcGIS interface and additional refinements were added by Joel Johnson, Ben Crosby, Cameron Wobus, and Will Ouimet. This tool was presented at a GSA short course offered during the GSA Annual Meeting on October 28, 2007 in Boulder, CO. In this chapter I present a short introduction to the field of tectonic geomorphology and elaborate on the parameters and methods implemented in the river profile analysis discussed in chapter 2.

7.1 Tectonic geomorphology: A short introduction

River profiles can adjust rapidly to landscape changes and thus can act as a proxy to search for active deformation of the Earth's surface. Global sea level change, human driven landscape development, and active tectonic processes all generate profound effects on geomorphic systems (Keller, 2002). The longitudinal elevation profile of an undisturbed stream should exhibit a relatively smooth concave up shape across the entire profile length, where the river maintains gentle gradients downstream and increasingly steeper gradients upstream (Keller, 2002; Schoenbohm

et al., 2004). In tectonically active regions, stream profiles respond to rock uplift by rapid bedrock incision (Whipple, 2004). Localized incision from rock uplift will create a knickpoint in the longitudinal morphology of a stream profile (Crosby et al., 2006; Burbank and Anderson, 2001) (Figure 63). The steepest reach on the stream profile associated with these knickpoints is expected to produce peaks in steepness on log slope versus distance plot and average k_{sn} versus distance plots (Figure 63). Keller (2002) describes the effect of rock uplift on stream profiles with a useful analogy of a ship plowing through calm lake water. Uplift of water, from the motion of the ship, maximizes near the ship's bow and decreases in the wake (Figure 64). Therefore, the steepest location on the profile reflects the location of greatest rock uplift.

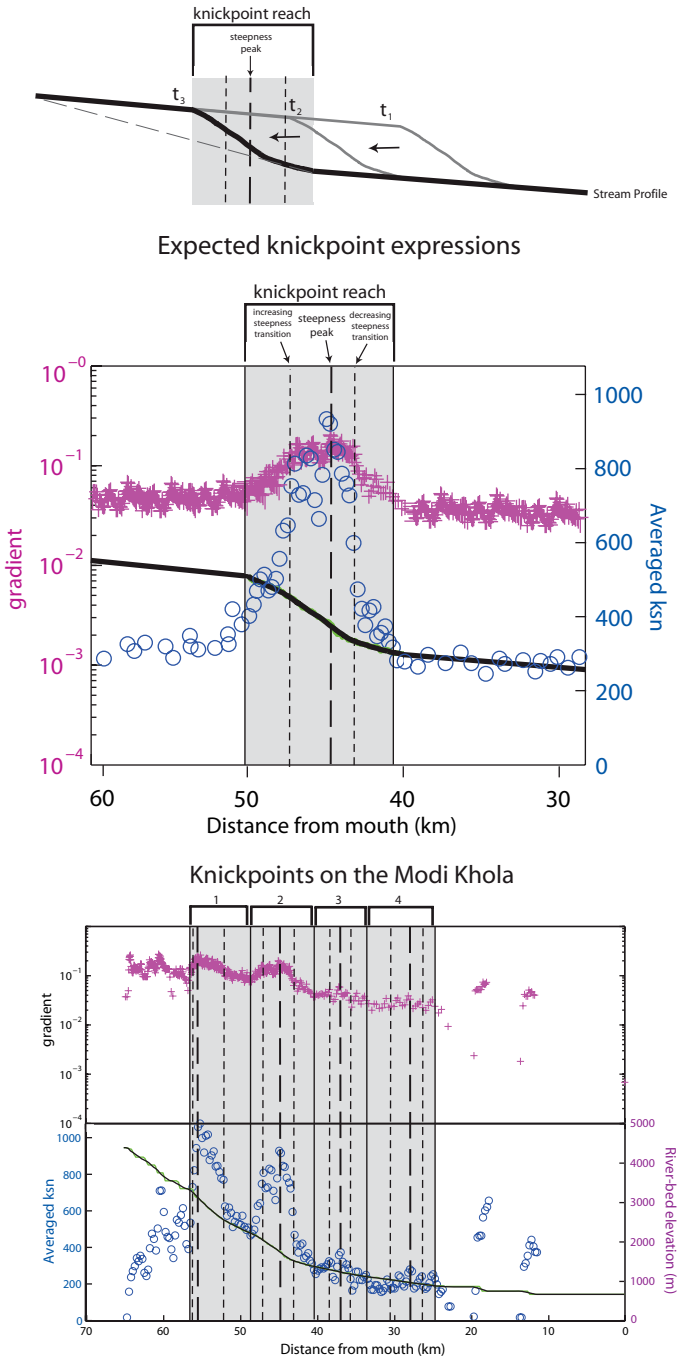

Figure 63: Definition of stream knickpoint
Top diagram shows a stream profile with a knickpoint, or steepened reach of the stream. The center vertical dashed line marks the steepest location on the profile while the surrounding vertical dashed lines mark the location where concavity transitions from negative to positive. The grey shaded box represents the extent of the knickpoint reach. Knickpoints migrate upstream overtime. The grey solid lines show pervious stream profiles. Each time step is marked by t_1 being the oldest stream profile and t_3 is the current stream profile. This diagram is constructed after Burbank and Anderson, 2001. The center plot shows peaks in steepness that are expected on the log slope versus distance and average k_{sn} versus distance plots if a knickpoint exists on a stream profile. The bottom diagram shows data from the Modi Khola profile and the extents of four distinguishable knickpoints.

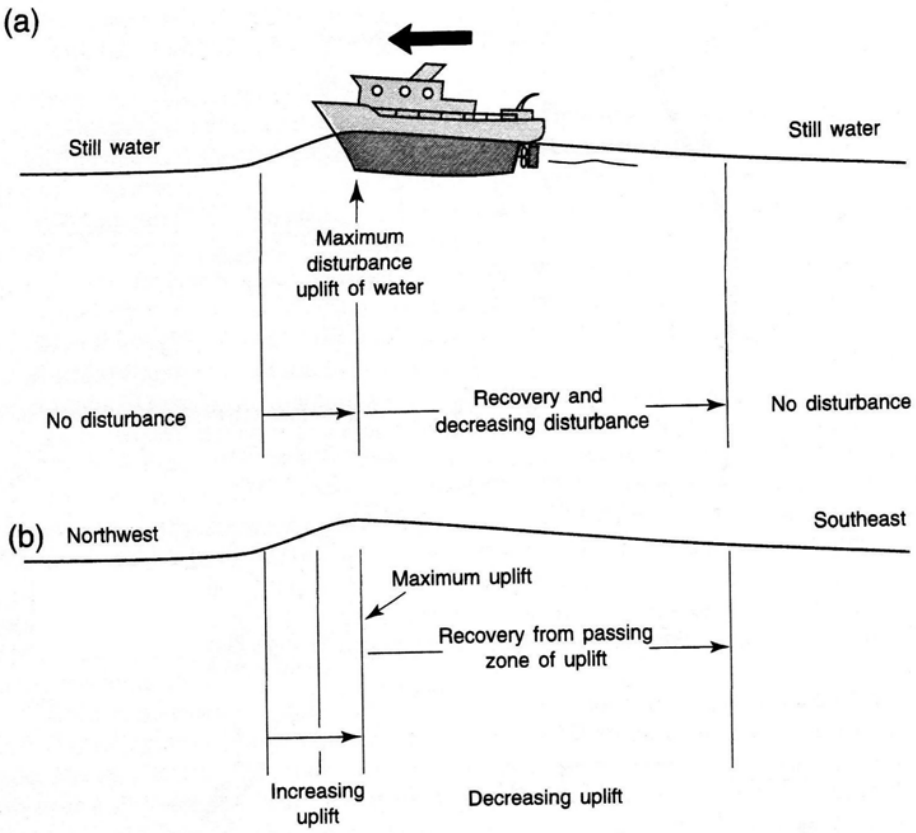

Figure 64: Ship analogy for understanding rock uplift process
An idealized diagram to illustrate rock uplift processes. A) The moving ship represents the surface water uplift. B) Movement on faults produces a similar pattern of rock uplift on a stream profile. (Figure modified from Keller, 2002)

7.2 River profile analysis methods

7.2.1 DEM preparation

Digitized contour lines with a 40 m interval were used to produce a 25 m DEM for the Ghandruk topographic map, which encompasses the extent of the Modi Khola geologic map. To perform the river profile analysis I needed a DEM for the entire Modi Khola watershed. Digitized contours at the 40 m interval were not available so I used contour lines I corrected at a 200 m and 100 m intervals for the topographic maps needed to cover the watershed area (Figure 65). I created a DEM

from the contour lines outside the Ghandruk topographic map using the TIN grid interpolation method. While the multiquadric radial basis function interpolation is necessary for measuring realistic slopes on a DEM, the DEM outside the Ghandruk topographic map is needed only to calculate flow accumulation and direction rasters. The TIN grid interpolation method is sufficient for creating these rasters.

The flow direction and accumulations rasters were created using spatial analyst in ArcGIS as described in the methods outlined by the stream profile tool user manual acquired from www.geomorphtools.org (Whipple et al., 2007). The DEM and flow accumulation rasters are the main input sources to the stream profiler toolbar. Essentially, k_{sn} is derived from the DEM and drainage area is obtained from the flow accumulation raster.

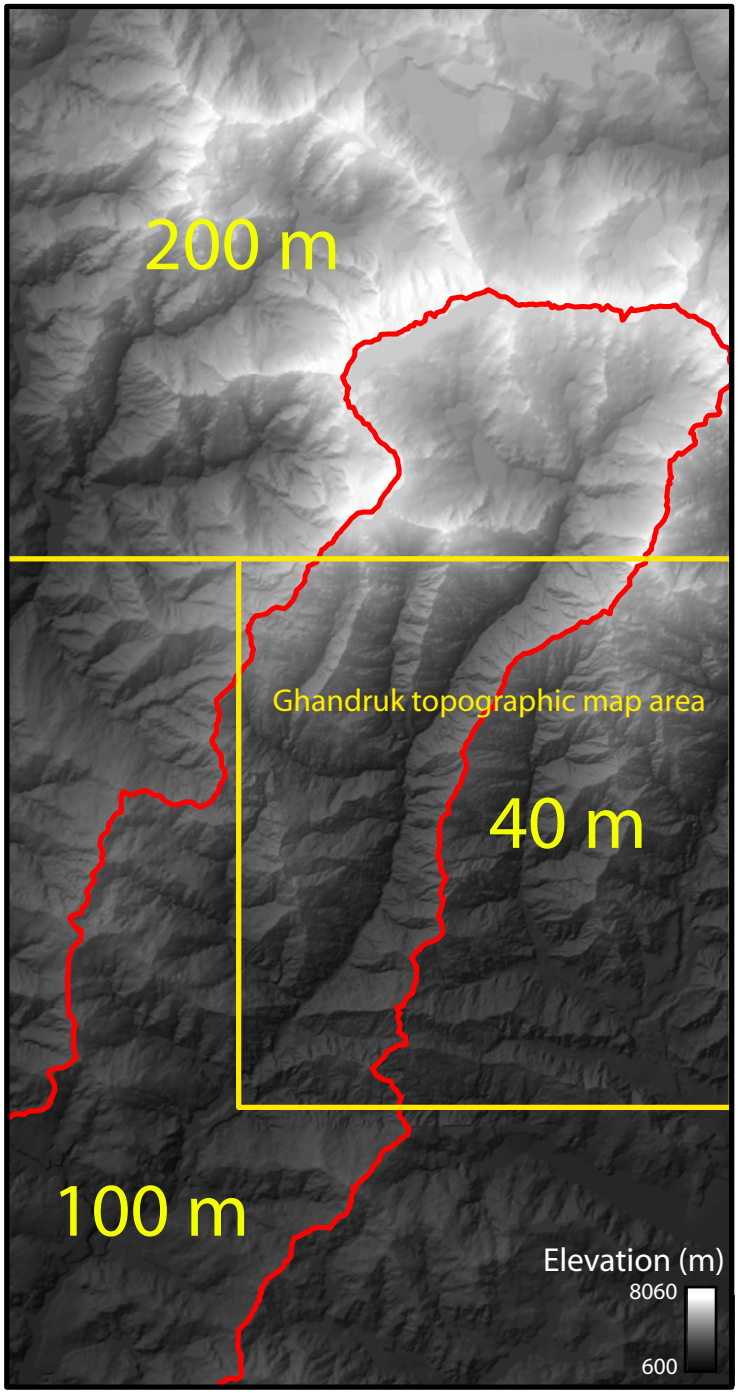

Figure 65: Key to contour line data source for DEM of the Modi Khola watershed and generated DEM for river profile analysis

Red line shows the border of the Modi Khola watershed. Yellow lines show boundaries of topographic maps and digitized contour line intervals used to make DEMs. The Ghandruk topographic map has a 40 m contour interval and was interpolated using the multiquadric radial basis function. Outside the Ghandruk topographic map area, the DEM was created using the TIN interpolation methods from 200 m and 100 m contour intervals from digitized topographic maps. The DEM outside the Ghandruk topographic map was needed to obtain drainage area data from the Modi Khola watershed. Geographic coordinate system: WGS 1984 UTM Zone 44N. Projection: Transverse Mercator.

7.2.2 River analysis parameters

A smoothing window size and contour sampling interval must be selected in order to perform the river steepness analysis using the Stream Profiler Tool and Matlab codes I obtained from www.geomorphtools.org (Whipple et al., 2007). A smoothing window is a moving average window over which the raw river profile is smoothed. Smoothing windows may eliminate noise from log slope – distance data, illuminating distinct and prominent river steepness maxima and transitions. The contour sampling interval is the vertical distance used by Matlab to calculate raw slopes. Choice of contour sampling interval depends on the detail which needs to be captured in the data and the extent to which the data can be examined without noise contamination.

I examined several combinations of smoothing window size and contour sampling intervals. In general, very small smoothing windows produce too much noise to detect changes in k_{sn} and too large of a smoothing window smears out interesting signals in the data (Figure 66 - Figure 68). Whipple et al. (2007) recommend smoothing windows of 250 m for United States Geological Survey (USGS) DEMs (which have cell sizes of 10 and 30 m) and 1000 m for more rough data such as SRTM 3 arc second data. Hodges et al. (2004) use a 10 km smoothing window for a 90 m DEM and were able to detect distinct zones of k_{sn} and θ. Smoothing windows reduce oversampling effects of interpolation methods, which occur when DEMs are created from irregularly spaced elevation data such as contour lines. Wobus et al. (2006a) investigated the problems of using raw pixel-to-pixel channel slopes and conclude that the problem of artificial stair steps associated with

contour lines crossing the stream profile may be mitigated using smoothing windows of a range of sizes. The smoothing window subsamples elevation data on the stream profile, at equal vertical intervals, allowing a smoother and more realistic stream profile to be extracted from the topography. According to studies by Wobus et al. (2006a), the contour sampling interval faithfully reproduces stream profile crossings of contour lines on original USGS topographic maps. DEMs may be accurately subsampled by factors of 5, according to recontouring studies I have conducted on digitized contour lines in central Nepal.

I examined several combinations of smoothing window size and contour sampling intervals. Table 10 displays the smoothing window sizes and contour sampling intervals I applied to river profile data from the Modi Khola. A smoothing window of 1500 m illuminated both prominent and subtle k_{sn} transitions on the Modi Khola, without over-smoothing the data. A contour subsampling interval of 8 m produced suitable log slope – log area and log slope – distance plots for this analysis.

Table 10: Range of parameters tested

Each list column lists the range of smoothing window size and contour sampling interval parameters that were tested. I tried smoothing windows ranging from none to 60,000. Smoothing windows less than 100 failed to run because smoothing window size must be greater than 3 times the resolution (25 m), which would be 75 m. Smoothing windows larger than 60,000 m caused the Matlab program to crash. I tested smoothing windows ranging from 100 to 60,000 in logarithmic steps shown below in the smoothing window column. I then tested smoothing window between 100 and 2000 m at a finer scale, every 100 m, for more detailed investigation. Several combinations of these listed smoothing window values and contour interval values were tested. Smoothing windows between 900 and 16000 m reflected the most detail with the least amount of smoothing. I tested contour interval of 12.192 m because it is the default for the stream profile tool, since it represents the 40 ft contour interval that most USGS DEMs were created from. I also tested a contour interval of 5.55 m since the stream profile user manual (Whipple et al., 2007) recommends a 90 m resolution DEM use 20 m contour interval. Since the DEM is 25 m in resolution, the proportional contour interval to the DEM resolution would be 5.55 m. I tried a 40 m contour interval because the Ghandruk map DEM was created from contours with a 40 m interval. I found that 40 m sampled the data at too large of a scale, and 5.55 m sampled the data at too small of a scale. Since recontouring experiments showed contour lines can be drawn on DEMs a factor of 5 smaller than the original contour line interval I tried 8 m to subsample the original contour interval of 40 m. A contour sampling interval of 8 m and a smoothing window of 1500 m reduced noise in the data the most without over smoothing the results (See Figure 66 and Figure 68).

Smoothing windows tested (m): logarithmic scale for values ranging 0 to 60,000	Smoothing windows tested (m): finer scale between 100 and 2000 at intervals of 100
0 (no smoothing window)	
100	100
200	200
400	300
600	400
800	500
1000	600
2000	700
4000	800
6000	900
8000	1000
10000	1100
20000	1200
40000	1300
60000	1400
	1500
	1600
	1700
	1800
	1900
	2000

Contour sampling intervals tested (m)
5.55
8
12.192
40

Note: Bold red numbers represent smoothing window and contour interval chosen

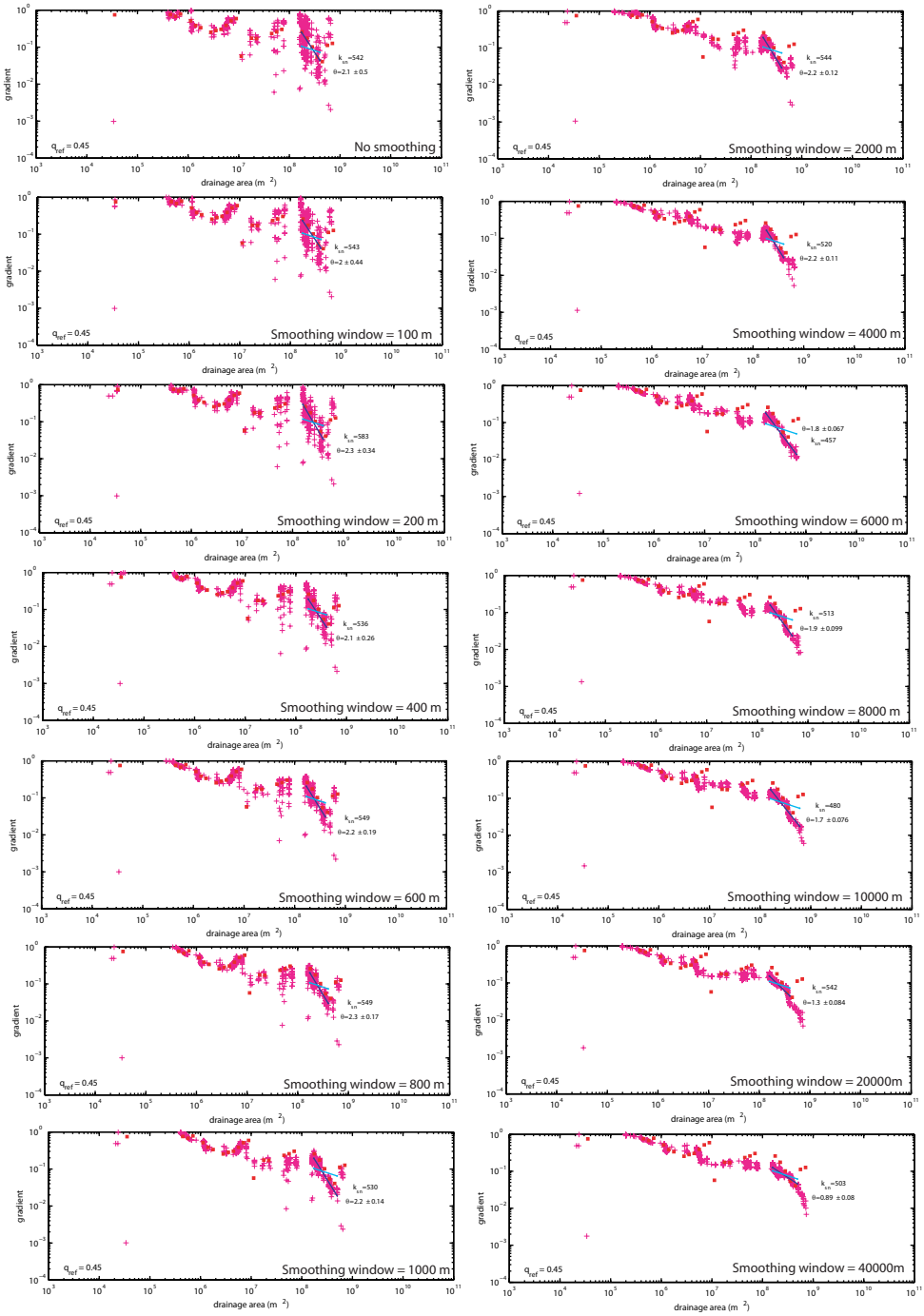

Figure 66: Effect of smoothing on log slope – log drainage area plots
Smoothing windows ranging from 0 to 40,000 m illustrate effect of smoothing on log slope – log drainage area plots. Smoothing causes slope of the data, which represents θ, to become more gradual. Concavity and river steepness values may become slightly altered during the smoothing process, but the location of the high concavity zone on the river profile remains consistent. The dark blue line shows the predicted regressed channel concavity, θ. The cyan lines are the concavity adjusted by normalization to the reference concavity, θ_{ref}. Red squares are logbin averages of the slope – area data and the pink plus marks are raw slope-area data extracted from the specified smoothing window size. These data include all slope – area data from the ridge line to the end of the Modi Khola on the input DEM.

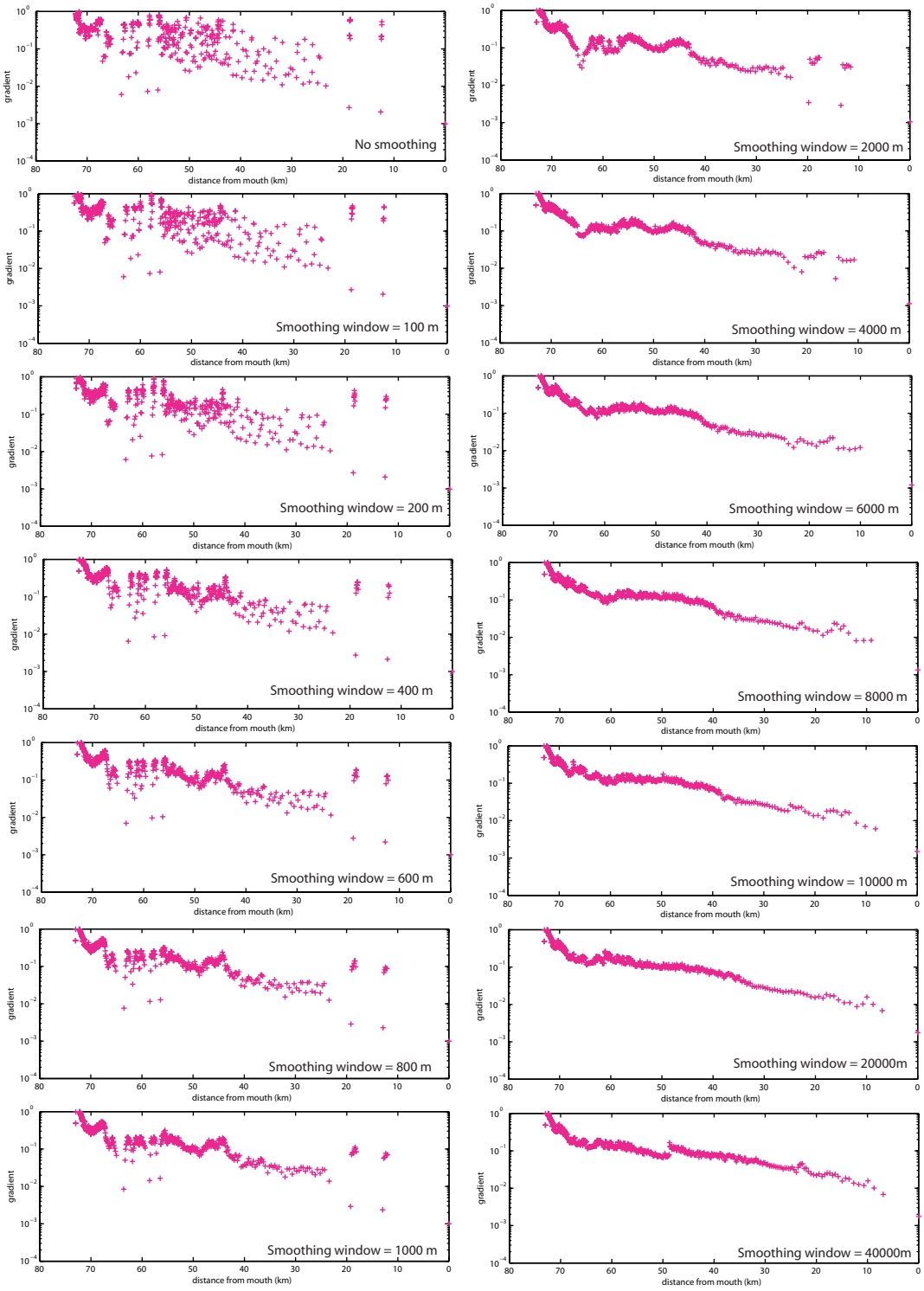

Figure 67: Effect of smoothing on log slope – distance plots
Smoothing windows ranging from 0 to 40000 m illustrate effect of smoothing on log slope – distance plots. Smoothing causes slope of the data, which represents θ, to become more gradual. Concavity and river steepness values may become slightly altered during the smoothing process. The pink plus marks are raw slope-area data extracted from the specified smoothing window size. These data include all slope – area data from the ridge line to the end of the Modi Khola on the input DEM.

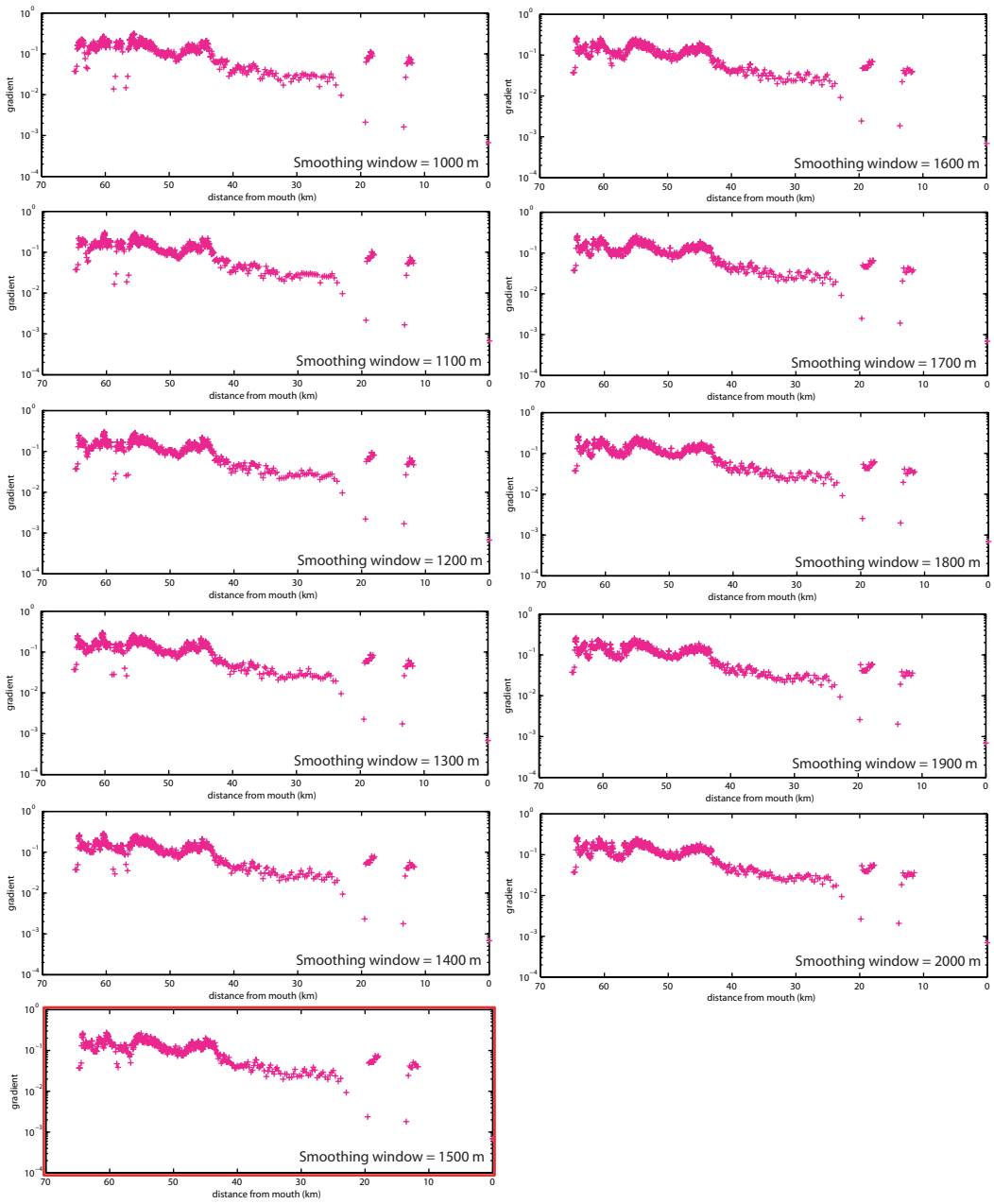

Figure 68: Constrained range of smoothing windows
The initial examination of smoothing effects shown in Figure 66 and Figure 67 showed the most detail and least amount of smoothing appears in the range from 1000 to 2000. Smoothing windows were observed for values between 100 m and 2000 m in intervals of 100 m to select the ideal smoothing window for this analysis. Smoothing windows ranging between 1000 and 2000 exhibited the most detailed log slope – distance data without over smoothing, and are shown above over 100 m intervals. A smoothing window of 1500 m (outlined with red box) was chosen as an average value to represent the range of plots that exhibit both detailed steepness changes and minimal noise reduction in the log S – distance plots. These data include all log slope – distance data from the Ghandruk topographic map only. Glaciated topography and regions north of the high resolution data from the Ghandruk map were excluded to allow the smoothing window test to focus on steepness changes within the high concavity zone.

7.2.3 Choosing regression limits

River steepness (k_{sn}) is calculated over a specific stream length by choosing a boundary in which a least squares regression is preformed on data points within the log slope vs. distance plot. Since k_{sn} can only be calculated across the distance of the chosen stream length, the issue of scale becomes important and determines the detail and extent of river steepness transitions I can interpret. I investigated a variety of spatial scales before narrowing my study to small-scale k_{sn} transitions within the high concavity zone. These methods allowed me to discover the high concavity zone and recognize the importance of detecting changes in steepness within high concavity zones. For each scale of analysis I isolated the high concavity zone, the extent of which I delineated by observing an abrupt reach of steep data on the log slope versus log drainage area plot. In the large-scale analysis I searched for regional changes in k_{sn} and in the small-scale analysis I included subtle and minor variations of k_{sn}. The following regression limits were applied in my analysis of the Modi Khola profile:

1) *Large-scale (includes glaciated):* In this scale I looked for regional k_{sn} changes from the Annapurna ridge line to the end of the stream on the DEM. This regression included glaciated regions so I could observe the effect of glaciations on the river profile (Figure 69, Figure 70, and Table 11).

2) *Large-scale (excludes glaciated):* This scale searched for regional k_{sn} changes from the base of glaciers shown on the topographic map to the end of the stream on the DEM. This scale yielded the same information, but excludes

stream reaches on glaciated terrain (Figure 71, Figure 72, Figure 73, and Table 12).

3) *Large-scale (within high concavity zone):* The previous scales measured both the average k_{sn} of the high concavity zone and k_{sn} changes outside the high concavity zone. This scale narrows the focus of the river analysis to k_{sn} variations only within the high concavity zone at a regional scale. Only large-scale transitions of k_{sn} were recorded at this scale, allowing the average k_{sn} of distinct steepness peaks and transitions to be measured. The study was also narrowed to only the high concavity zone, since regions outside the high concavity zone extended into the DEM outside the Ghandruk topographic map, where the DEM is less realistic and at a higher resolution (Figure 74, Figure 75, Figure 76, and Table 13).

4) *Small-scale (within high concavity zone):* The small-scale regression limits captured minor variations of k_{sn} observed within the high concavity zone on the log slope versus distance plot. The least squared regression was performed across the smallest segments made possible by the Matlab scripts (on the order of 0.25 to 1 km) (Figure 8, Figure 12, Figure 77, and Table 1).

7.3 Results

7.3.1 Regional and local k_{sn} transitions

Glaciated topography reflects gently sloping topography that abruptly steepens near the ridge line on the gradient versus distance plot (Figure 69). The removal of slope – area data in regions of glaciated topography minimizes the potential interpretations of stream reaches that are dominated by glacial processes. Slope-area data from the Modi Khola delineate a high concavity zone that extends approximately 1.5 km between 28°30.5'N and 28°17.5'N (Figure 73). This zone of high concavity has an average θ is 2.12, whereas in the region to the north the average θ is 0.03 and to the south the average θ is -1.2. The high concavity zone is nearly 70 times higher than concavity of the river profile to the north and south. While a high concavity zone of 7.8 exists to the south of my designated 'high concavity zone' it was excluded from this analysis because it lies outside the Ghandruk topographic map where the DEM was created with the TIN method and from contours spaced at 100 m (Figure 65). The presence of the southern high concavity zone suggests that tectonic activity may be occuring south of my study site and would be interesteing to investigate in future studies. The stream profile data north of the high concavity zone were excluded from this analysis because its DEM source was created from 200 m contours using the TIN grid method and because the presence of nearby glaciers would complicate the analysis because of their influence on the topography. Large-scale k_{sn} changes within the high concavity zone are clearly visible, regardless of smoothing window. Small-scale river steepness transitions allowed me to compare k_{sn} variations with mapped geology and more subtle k_{sn} changes to be recognized. The following figures and tables illustrate k_{sn} and θ transitions for each analysis scale:

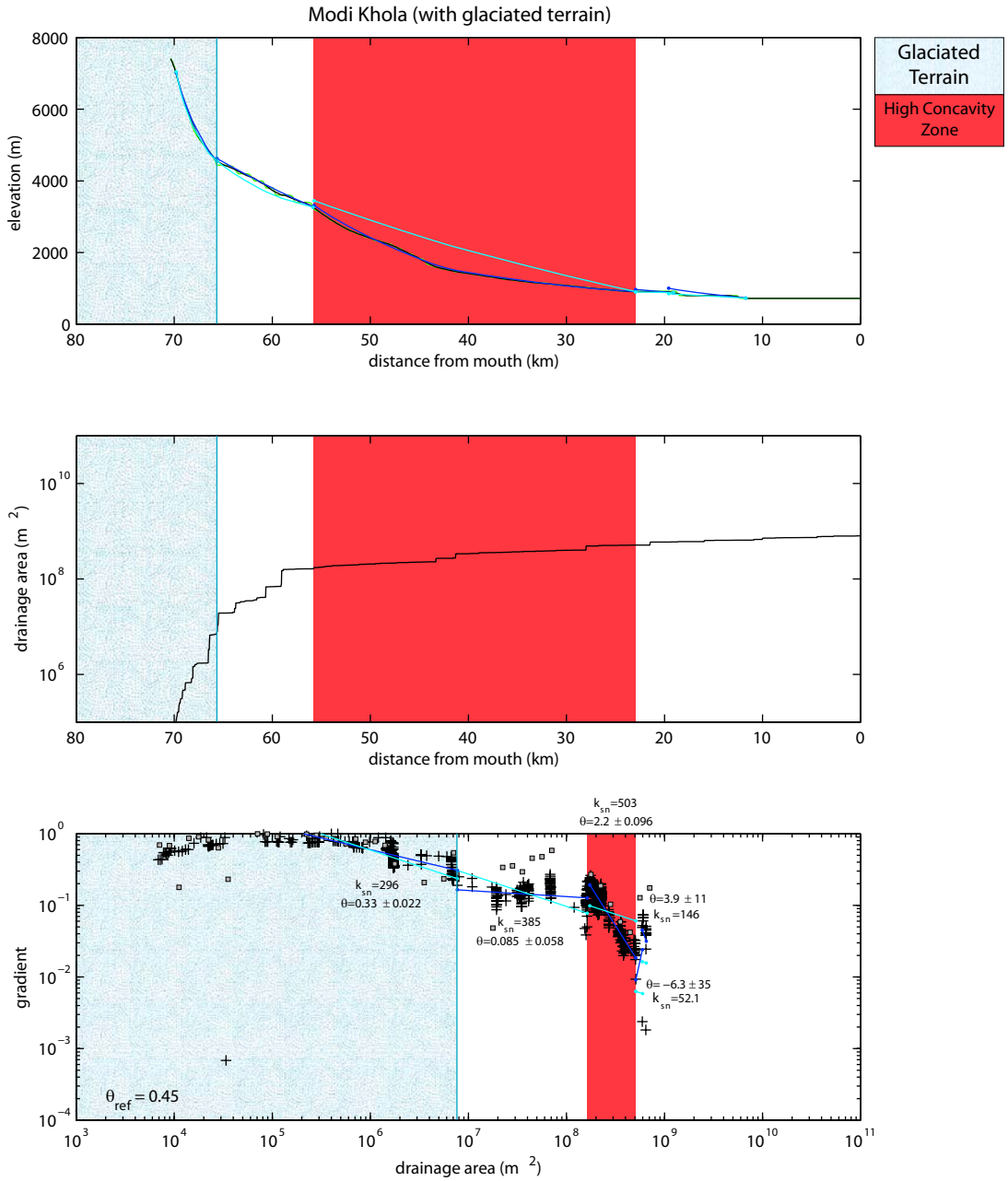

Figure 69: High concavity zone on the Modi Khola including glaciated terrain (Graphs page 1) The red shading marks the extent of a high concavity zone on the Modi Khola. Mapped glaciers are shown to the north of the high concavity zone. On the first page, the top plot shows the stream profile. Raw elevation profile is green and smoothed is black. The dark blue lines represent the stream profile's concavity for a segment of the stream. The cyan lines represent the local concavity adjusted to a reference concavity of 0.45. The middle plot shows changes in drainage area. Distribution of large-scale concavity zones on the Modi Khola, Red shading on slope-area and long river profile plots show extent of the identified high concavity zone seen on the log slope versus log drainage area plot. Note that within the high concavity zone, θ is approximately 70 times larger than the surrounding area. Crosses show the log of slope and drainage area taken at regular intervals along the stream profile, utilizing a 1.5 km moving average smoothing window and 8 m contour interval. Grey squares are log-bin averages of the S-A data and the open circles show the location of knickpoints as plotted on the long river profile.

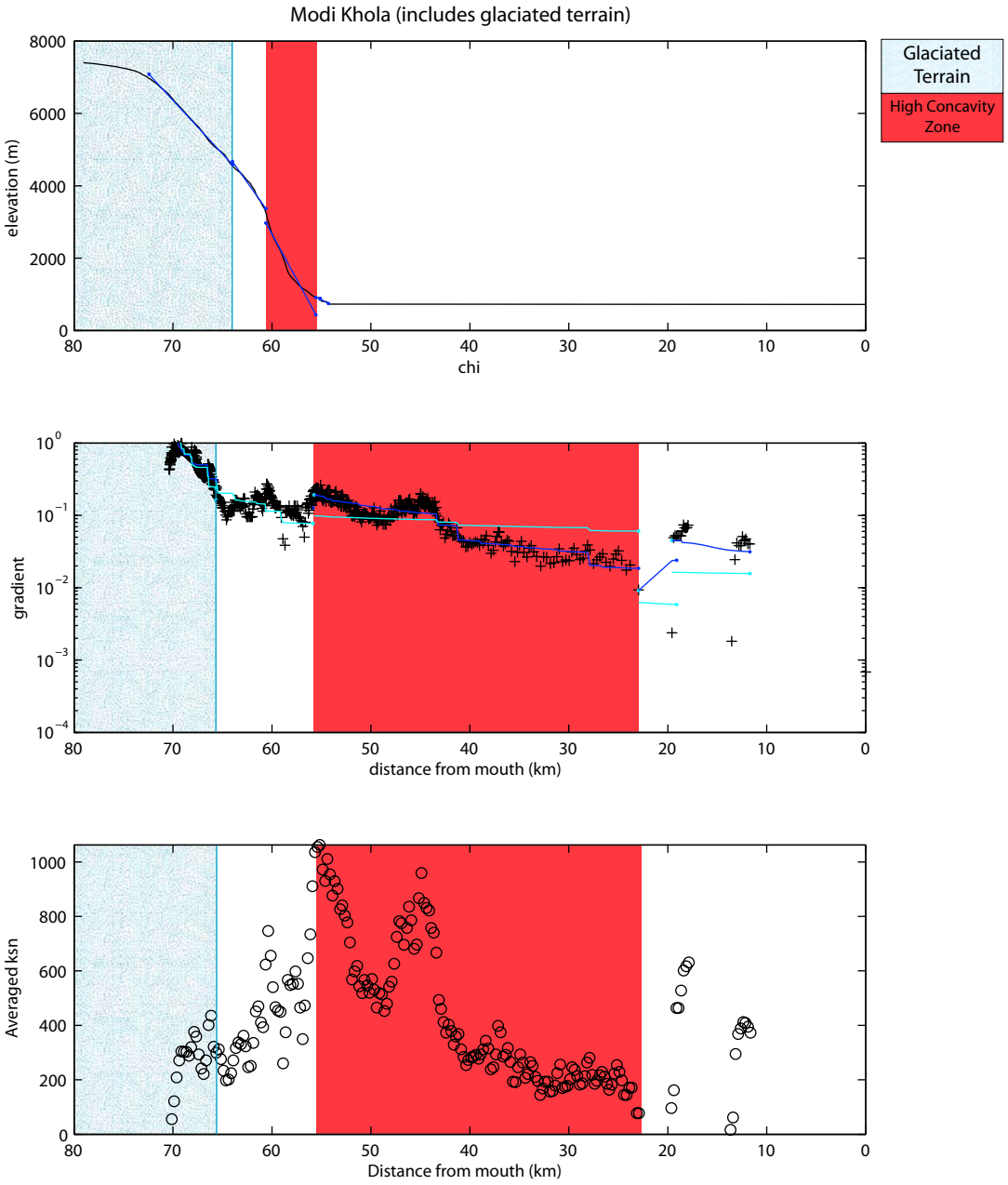

Figure 70: High concavity zone on the Modi Khola including glaciated terrain (Graphs page 2) The red shading marks the extent of a high concavity zone on the Modi Khola. The top plot is the profile data with elevation plotted against chi, the integral of drainage area to that point on the profile. The middle plot is local channel slope versus distance. The dark blue lines represent the stream profile's concavity for a segment of the stream. The cyan lines represent the local concavity adjusted to a reference concavity of 0.45. The lower plot shows normalized river steepness (k_{sn}) 0.5 km moving average window.

Table 11: Data from regression in high concavity zone on the Modi Khola (includes glaciated terrain)

k_{sn}	$k_{sn}+2\sigma$	$k_{sn}-2\sigma$	A_{min}	A_{max}	θ	$\theta\ 2\sigma$	k_s	R^2
296	298	295	1.08E+05	7.90E+06	0.33	0.02	54.19	0.75
385	395	376	7.01E+06	1.64E+08	0.08	0.06	0.63	0.05
503	516	489	1.67E+08	5.37E+08	2.16	0.10	1.29E+17	0.87
52	130	-25	5.1E+08	5.96E+08	-6.27	35.48	2.46E-57	0.10
146	171	120	5.94E+08	6.74E+08	3.86	10.56	3.35E+32	0.10

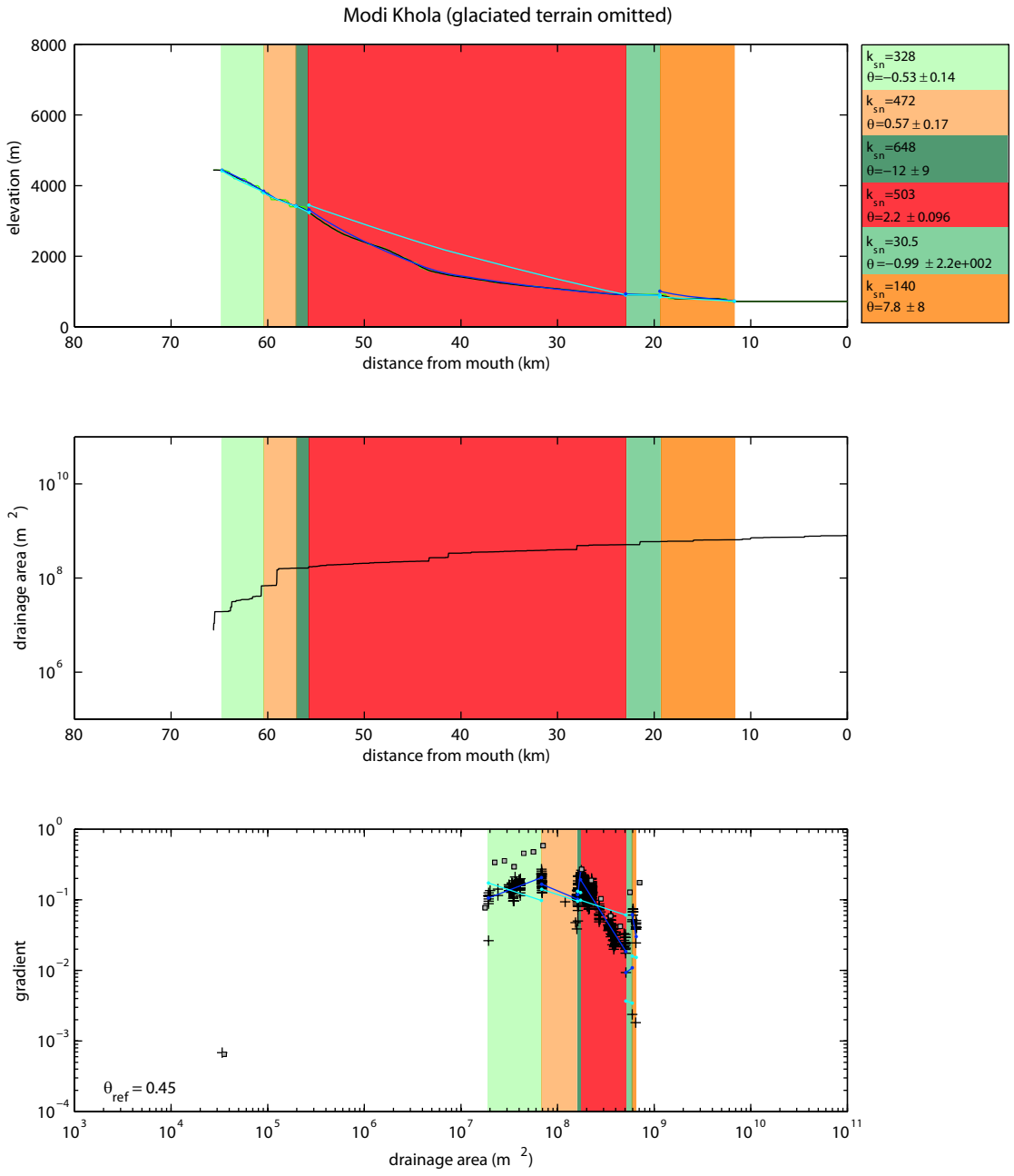

Figure 71: High concavity zone on the Modi Khola (Graphs page 1)
Colored swaths delineate distinct changes in concavity. The top plot shows the stream profile. Raw elevation profile is green and smoothed is black. The dark blue lines represent the stream profile's concavity for a segment of the stream. The cyan lines represent the local concavity adjusted to a reference concavity of 0.45. The middle plot shows changes in drainage area. Distribution of large-scale concavity zones on the Modi Khola, Red shading on slope-area and long river profile plots show extent of the identified high concavity zone seen on the log slope versus log drainage area plot. Note that within the high concavity zone, θ is approximately 70 times larger than the surrounding area. Crosses show the log of slope and drainage area taken at regular intervals along the stream profile, utilizing a 1.5 km moving average smoothing window and 8 m contour interval. Grey squares are log-bin averages of the S-A data and the open circles show the location of knickpoints as plotted on the long river profile. Glaciated terrain is omitted in this figure.

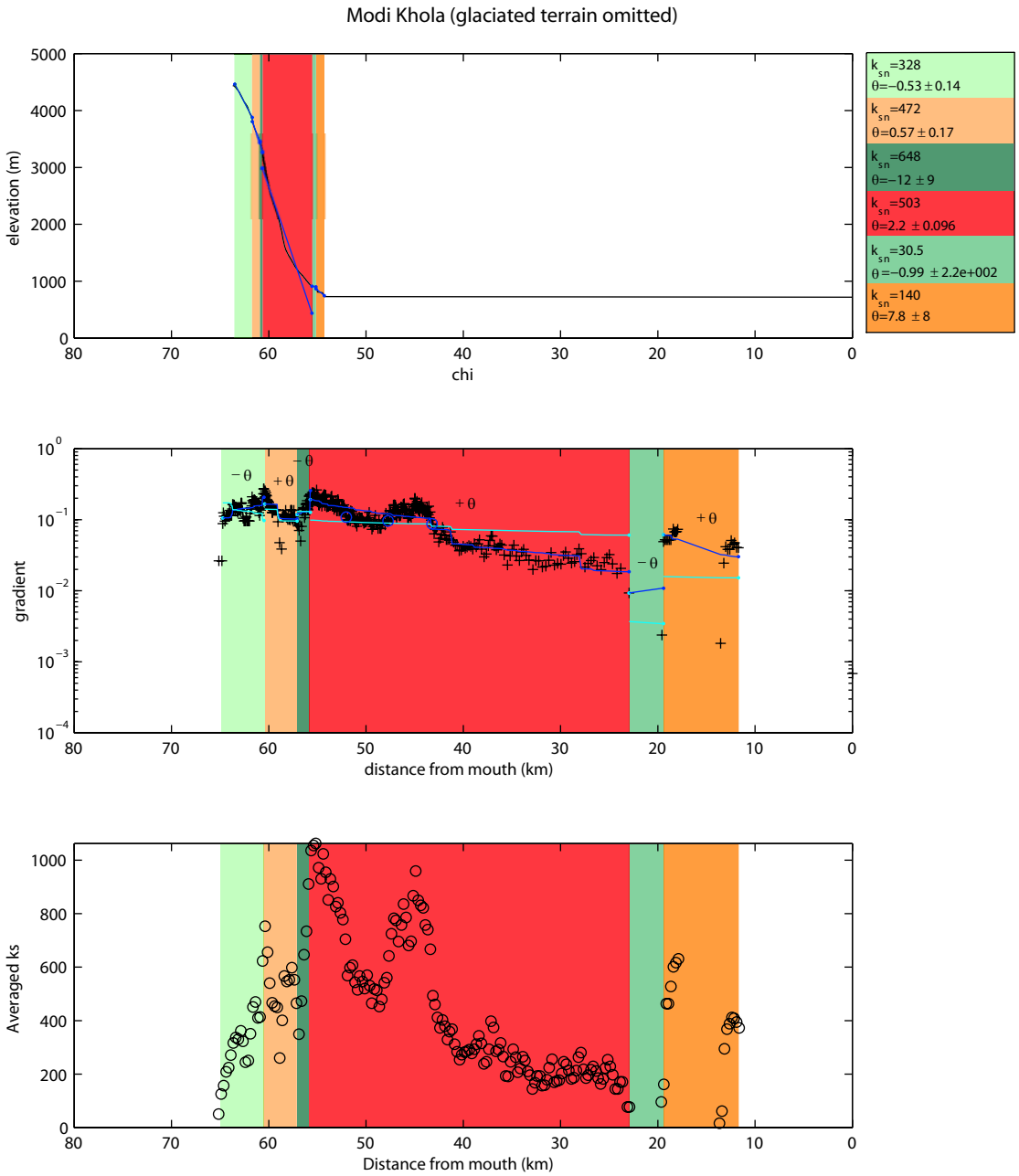

Figure 72: High concavity zone on the Modi Khola (Graphs page 2)
Colored swaths delineate distinct changes in concavity. The top plot is the profile data with elevation plotted against chi, the integral of drainage area to that point on the profile. The middle plot is local channel slope versus distance. The dark blue lines represent the stream profile's concavity for a segment of the stream. The cyan lines represent the local concavity adjusted to a reference concavity of 0.45. The lower plot shows normalized river steepness (k_{sn}) 0.5 km moving average window.

Table 12: Data from regression in high concavity zone (excludes glaciated terrain)

k_{sn}	$k_{sn}+2\sigma$	$k_{sn}-2\sigma$	A_{min}	A_{max}	θ	$\theta\ 2\sigma$	k_s	R^2
328	335	320	1.93E+07	6.85E+07	-0.53	0.14	1.50E-05	0.44
472	482	462	6.85E+07	1.62E+08	0.57	0.17	4.75E+03	0.46
648	700	597	1.62E+08	1.73E+08	-11.59	8.95	8.24E-97	0.26
503	516	489	1.7E+08	5.27E+08	2.16	0.10	1.29E+17	0.87
31	234	-173	5.1E+08	5.95E+08	-0.99	218.40	2.43E-11	0.0033
140	166	115	5.94E+08	6.52E+08	7.83	7.95	2.90E+67	0.17

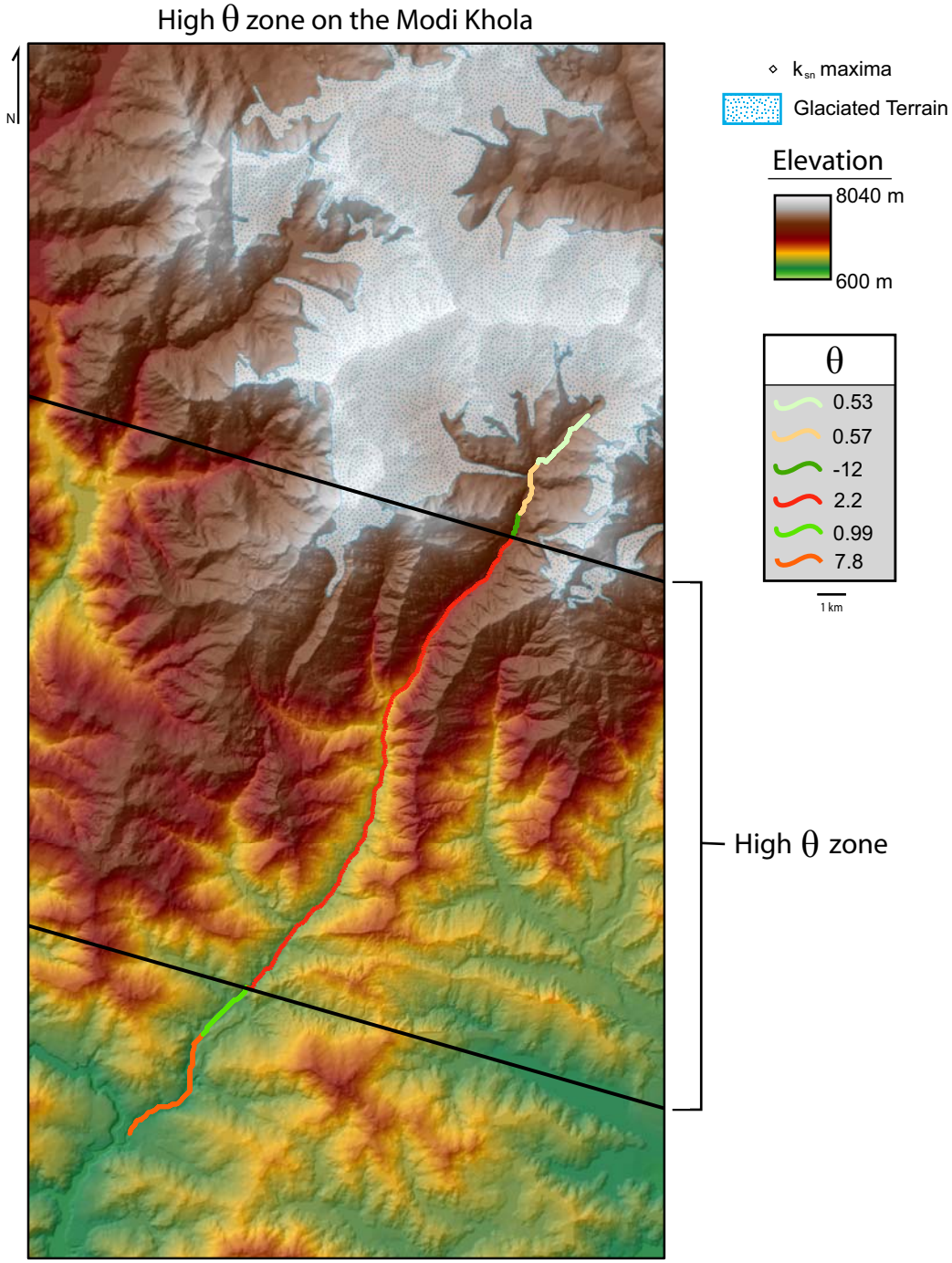

Figure 73: Map of high concavity zone on the Modi Khola (excludes glaciated)
This map shows small regional concavity transitions on the Modi Khola. Solid black lines mark border of high concavity zone. The orange river segment would be considered a high concavity since its θ value is 7.8, but it is excluded from this analysis because the DEM underlying this zone was generated at a lower resolution, making it difficult to compare with the zone with a concavity of 2.2 that lies completely in the Ghandruk topographic map which has higher resolution DEM data (Figure 65). River profile data north of the high concavity zone were excluded because they may be affected by glaciations as well as a lower resolution DEM data source. Geographic coordinate system: WGS 1984 UTM Zone 44N. Projection: Transverse Mercator.

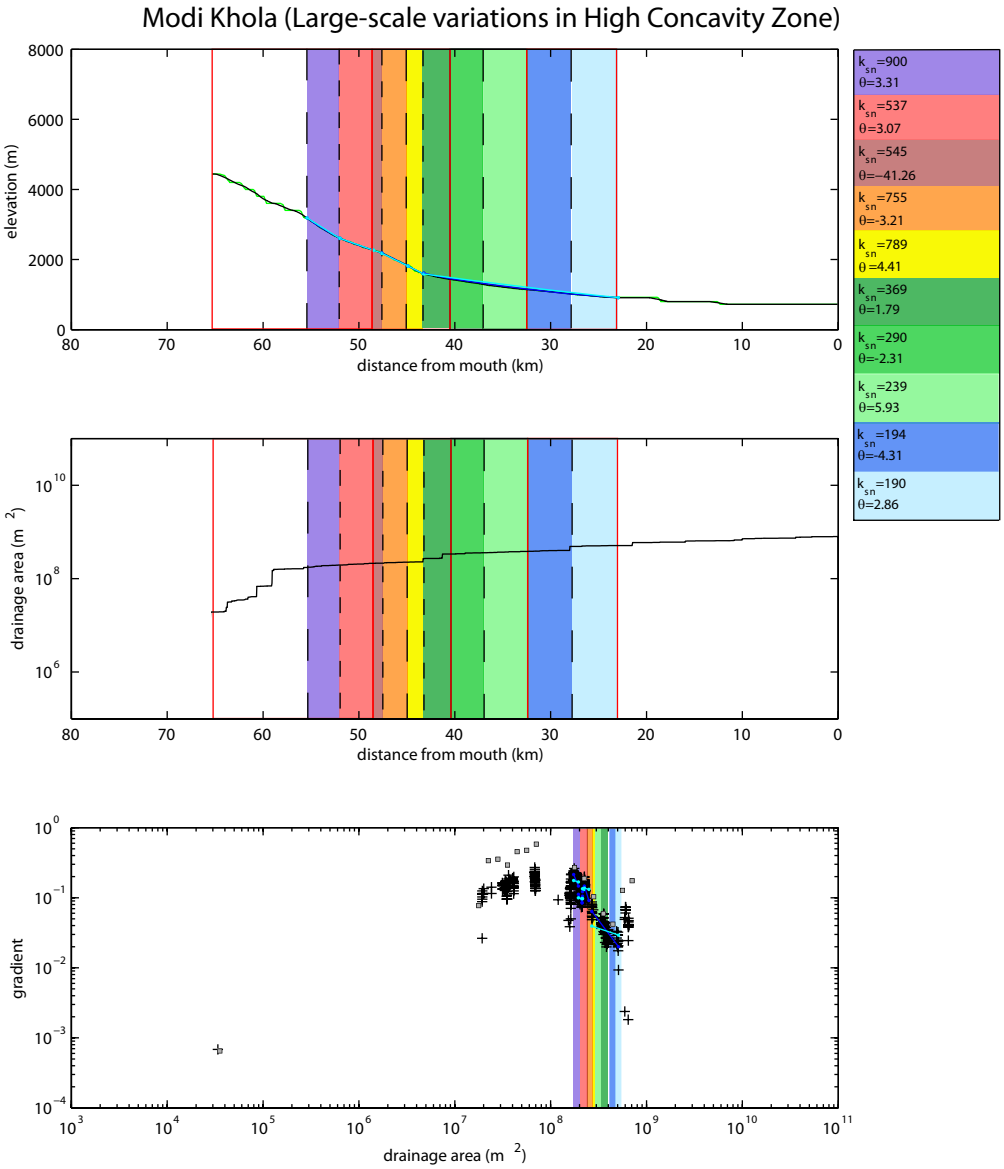

Figure 74: Large-scale steepness changes on the Modi Khola (within the high concavity zone) (Graphs page 1)

Regional k_{sn} and θ changes within the high concavity zone are shown by colored swaths. Colored zones added together mark the extent of the high concavity zone. The top plot shows the stream profile. Raw elevation profile is green and smoothed is black. The dark blue lines represent the stream profile's concavity for a segment of the stream. The cyan lines represent the local concavity adjusted to a reference concavity of 0.45. The middle plot shows changes in drainage area. Distribution of large-scale concavity zones on the Modi Khola, Red shading on slope-area and long river profile plots show extent of the identified high concavity zone seen on the log slope versus log drainage area plot. Note that within the high concavity zone, θ is approximately 70 times larger than the surrounding area. Crosses show the log of slope and drainage area taken at regular intervals along the stream profile, utilizing a 1.5 km moving average smoothing window and 8 m contour interval. Red squares are log-bin averages of the S-A data and the open circles show the location of knickpoints as plotted on the long river profile. Dashed lines show the upper and lower bounds of k_{sn} indices across the high concavity zone. Glaciated terrain is omitted in this figure.

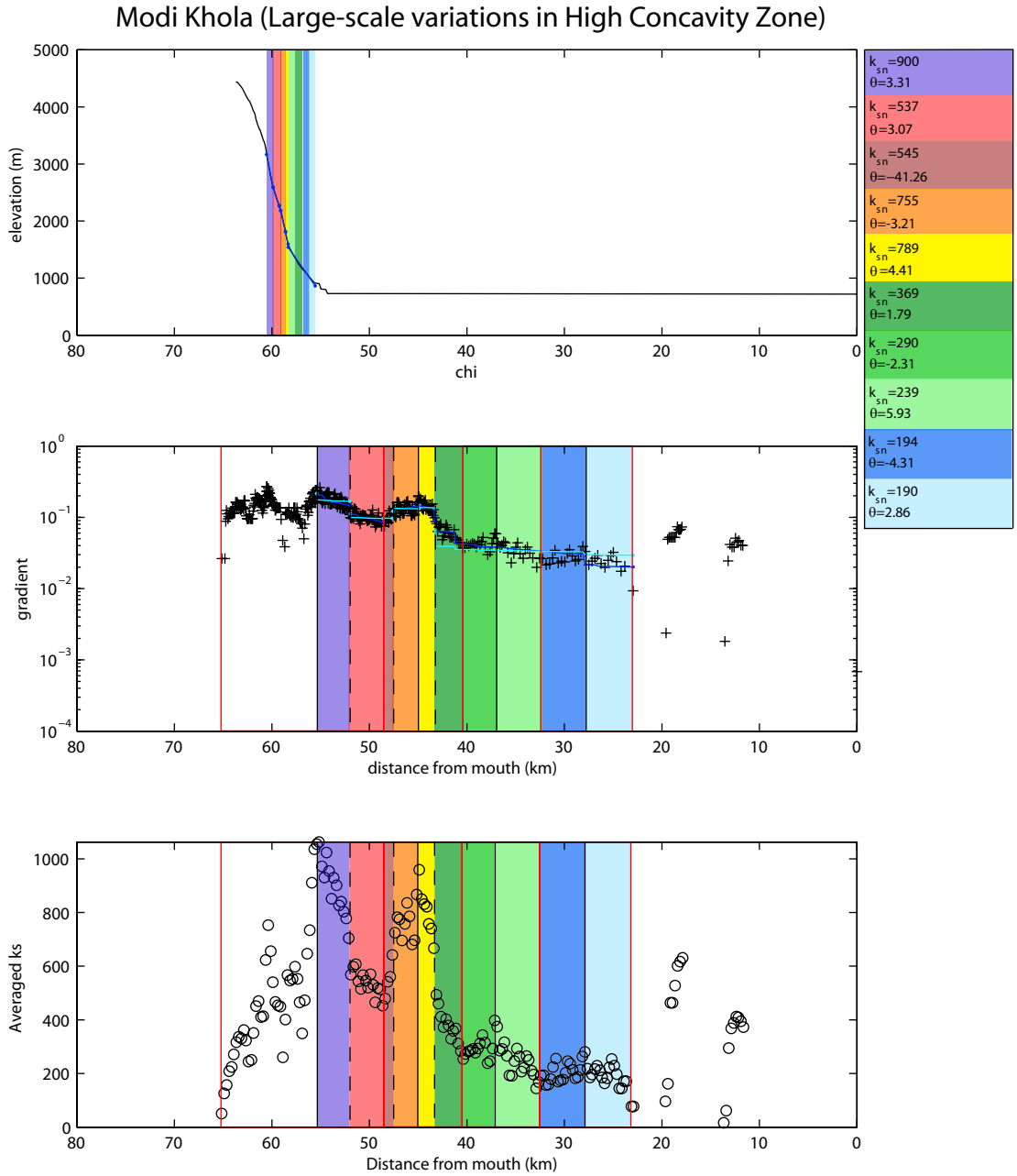

Figure 75: Large-scale steepness changes on the Modi Khola (within the high concavity zone) (Graphs page 2)
Regional k_{sn} and θ changes within the high concavity zone are shown by colored swaths. Colored zones added together mark the extent of the high concavity zone. The top plot is the profile data with elevation plotted against chi, the integral of drainage area to that point on the profile. The middle plot is local channel slope versus distance. The dark blue lines represent the stream profile's concavity for a segment of the stream. The cyan lines represent the local concavity adjusted to a reference concavity of 0.45. The middle plot shows changes in drainage area. The lower plot shows normalized river steepness (k_{sn}) 0.5 km moving average window.

Table 13: Data from regression of large-scale steepness changes analysis (within the high concavity zone)

k_{sn}	$k_{sn}+2\sigma$	$k_{sn}-2\sigma$	A_{min}	A_{max}	θ	$\theta\,2\sigma$	k_s	R^2
900	910	891	1.74E+08	1.95E+08	3.31	0.88	3.70E+26	0.44
537	542	532	1.95E+08	2.13E+08	3.07	1.39	3.35E+24	0.33
545	555	535	2.13E+08	2.14E+08	-41.26	43.50	0	0.34
755	761	749	2.14E+08	2.25E+08	-3.21	3.70	2.15E-28	0.07
789	801	777	2.25E+08	2.69E+08	4.41	2.50	1.05E+36	0.35
369	379	358	2.69E+08	3.37E+08	1.79	0.85	7.64E+13	0.50
290	296	284	3.37E+08	3.58E+08	-2.31	3.92	7.97E-22	0.09
239	245	233	3.58E+08	3.83E+08	5.93	4.87	2.10E+49	0.33
194	199	189	3.78E+08	4.89E+08	-4.31	4.12	2.41E-39	0.23
190	201	178	4.02E+08	5.1E+08	2.86	3.00	1.83E+23	0.25

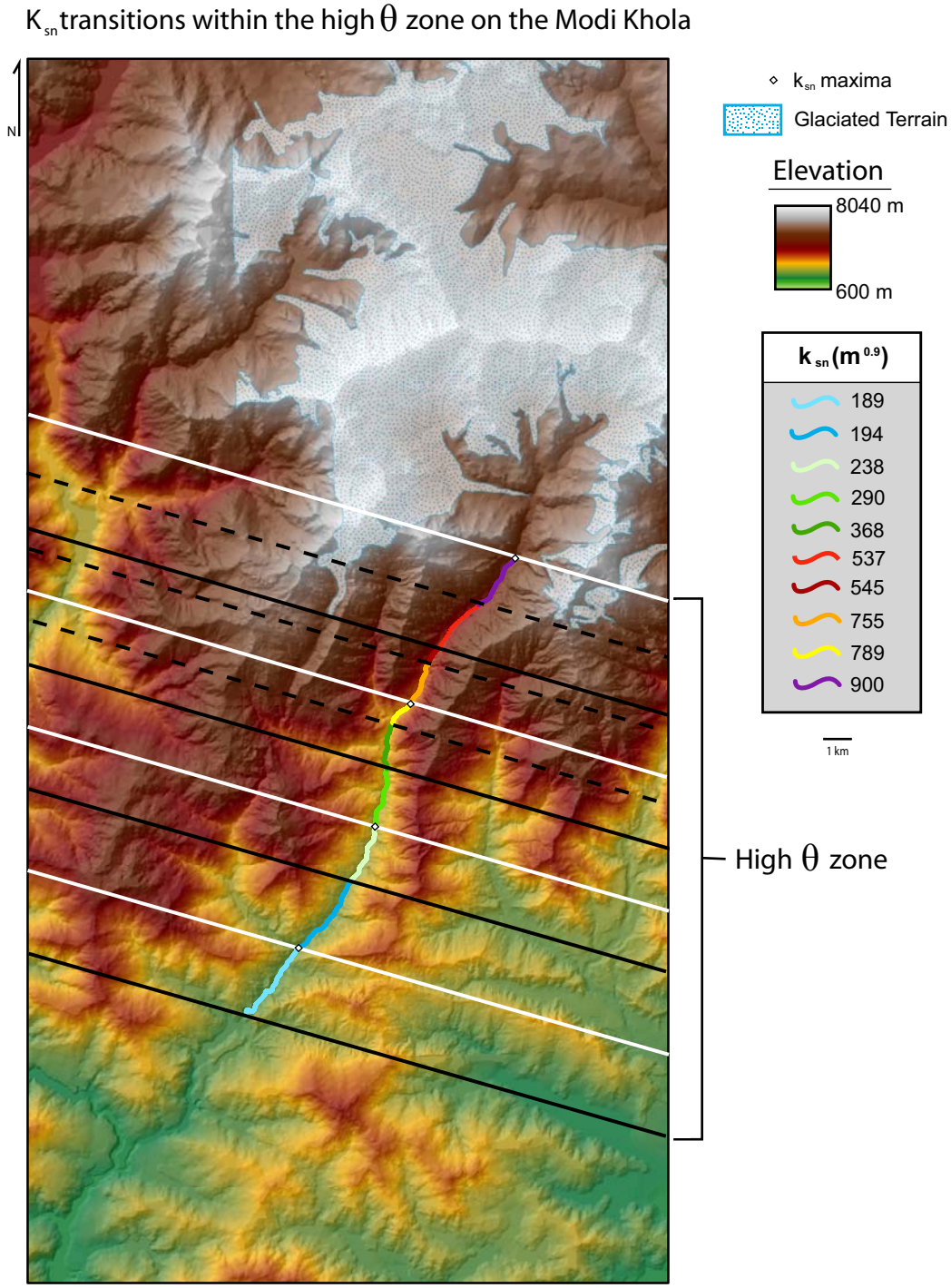

Figure 76: Large-scale steepness changes on the Modi Khola (within the high concavity zone) on the Ghandruk topographic map
This map shows small-scale k_{sn} transitions on the Modi Khola DEM. Solid black lines mark locations of local k_{sn} minimums and solid white lines mark locations of local k_{sn} maximums. Dashed lines mark abrupt transitions between local k_{sn} maximums and minimums. Lines only mark transitions measured at the river profile and do not mark transitions in surrounding topography. White diamonds mark precise location of k_{sn} maximum on the river profile. Geographic coordinate system: WGS 1984 UTM Zone 44N. Projection: Transverse Mercator.

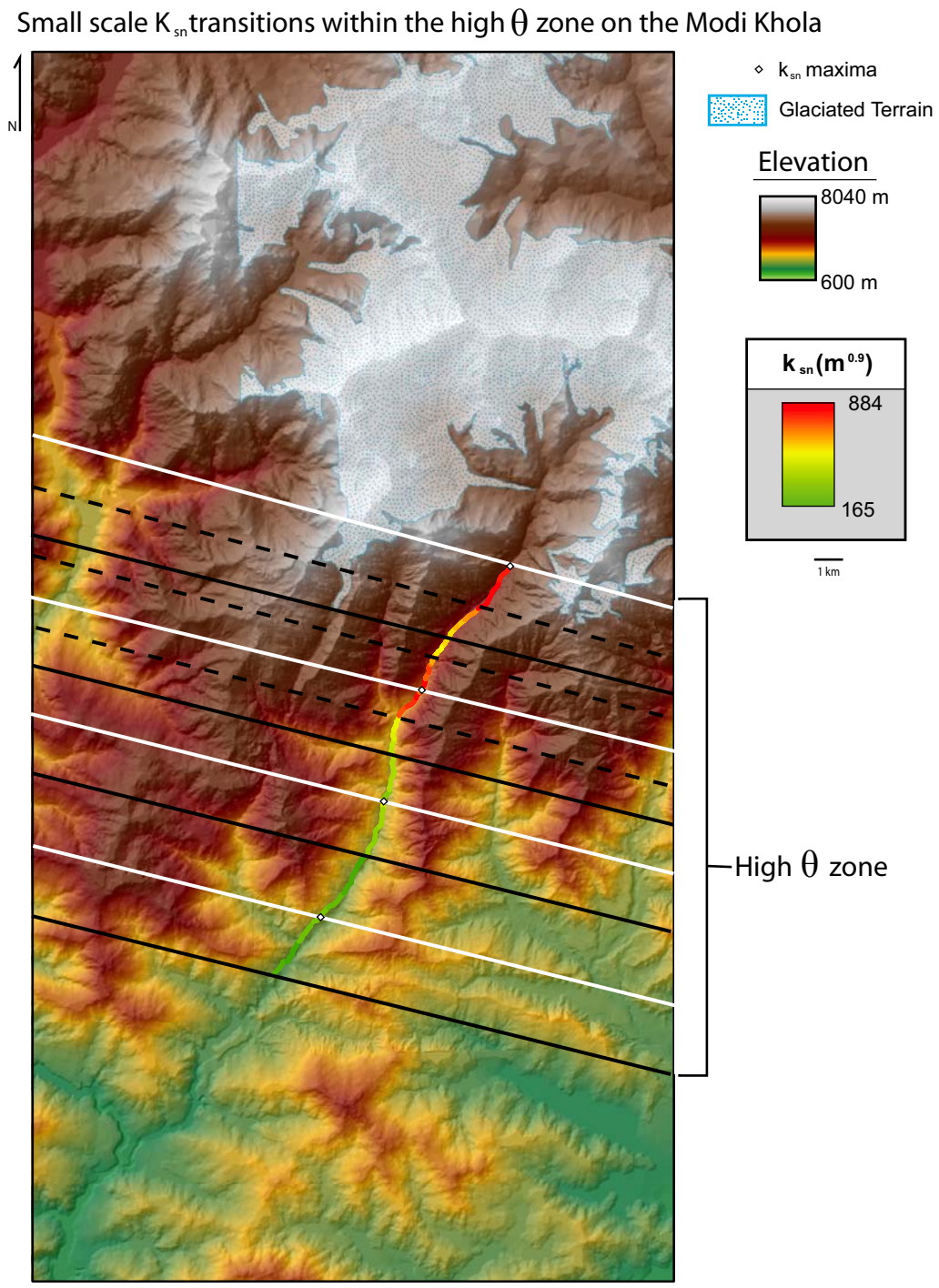

Figure 77: Map of small-scale river steepness transitions on the Modi Khola
Plots and data table for the small-scale transitions can be found in Figure 12 and Table 1 of chapter 2. This map shows small-scale k_{sn} transitions on the Modi Khola DEM. Solid black lines mark locations of local k_{sn} minimums and solid white lines mark locations of local k_{sn} maximums. Dashed lines mark abrupt transitions between local k_{sn} maximums and minimums. Lines only mark transitions measured at the river profile and do not mark transitions in surrounding topography. White diamonds mark precise location of k_{sn} maximum on the river profile. Geographic coordinate system: WGS 1984 UTM Zone 44N. Projection: Transverse Mercator.

7.3.2 Vegetation and human impact on topography

Chapter 2 discusses several mechanisms that may be responsible for k_{sn} and θ transitions on the Modi Khola, including: Precipitation variability, glacial dams, landslide dams, spatial changes in lithology, recent rock uplift on faults, and tributary junctions. Land cover transitions between vegetated and human modified topography also potentially impact landscape evolution. Farms near villages and in cultivated regions of the Modi Khola valley contain large numbers of agricultural rice terraces which possibly divert water flow and withhold or delay rainfall from entering the stream (Figure 78). Human land use increases potential soil erosion and could produce changes in landscape morphology (Hooke, 2006; Clarke and Rendell, 2000). According to the Ghandruk topographic map, several buildings and regions of cultivated land characterize the Modi Khola valley and may contribute to changes in the Modi Khola profile (Figure 79).

Dynamic interactions between vegetation, water flow, and fluvial landforms may also play an important role in landscape evolution (Corenblit et al., 2007) in the Modi Khola valley. Dense vegetation dominates the land in most uncultivated regions, particularly in the northern reaches of the Modi Khola (Figure 79). Hack and Goodlett (1960) showed that different land forms in northwestern Virginia were characterized by distinct differences in vegetation. Changes in vegetation species may reflect the k_{sn} and θ transitions of the Modi Khola, though this need to be confirmed with a more detailed land cover map which includes specific vegetation types. Vegetation dominates the topography at locations A and 1 and do not exhibit any abrupt transition in land cover from vegetated to cultivated land. Interfaces

between vegetated and cultivated land do exist at locations 2, 3, and 4 and could be partially responsible for changes in river steepness at these locations. Particular vegetation species may inhibit erosion at particular stream reaches and should be examined in more detail. A detailed land cover DEM at 25 m resolution, which includes vegetation species and type of cultivation, would be required before determining a quantifiable influence of vegetation and human impact on the topography.

Figure 78: Agricultural rice terraces in central Nepal
Photo of agricultural terraces taken near the Kimrong Khola in the Modi Khola valley of central Nepal. (Photo taken by Aaron Martin)

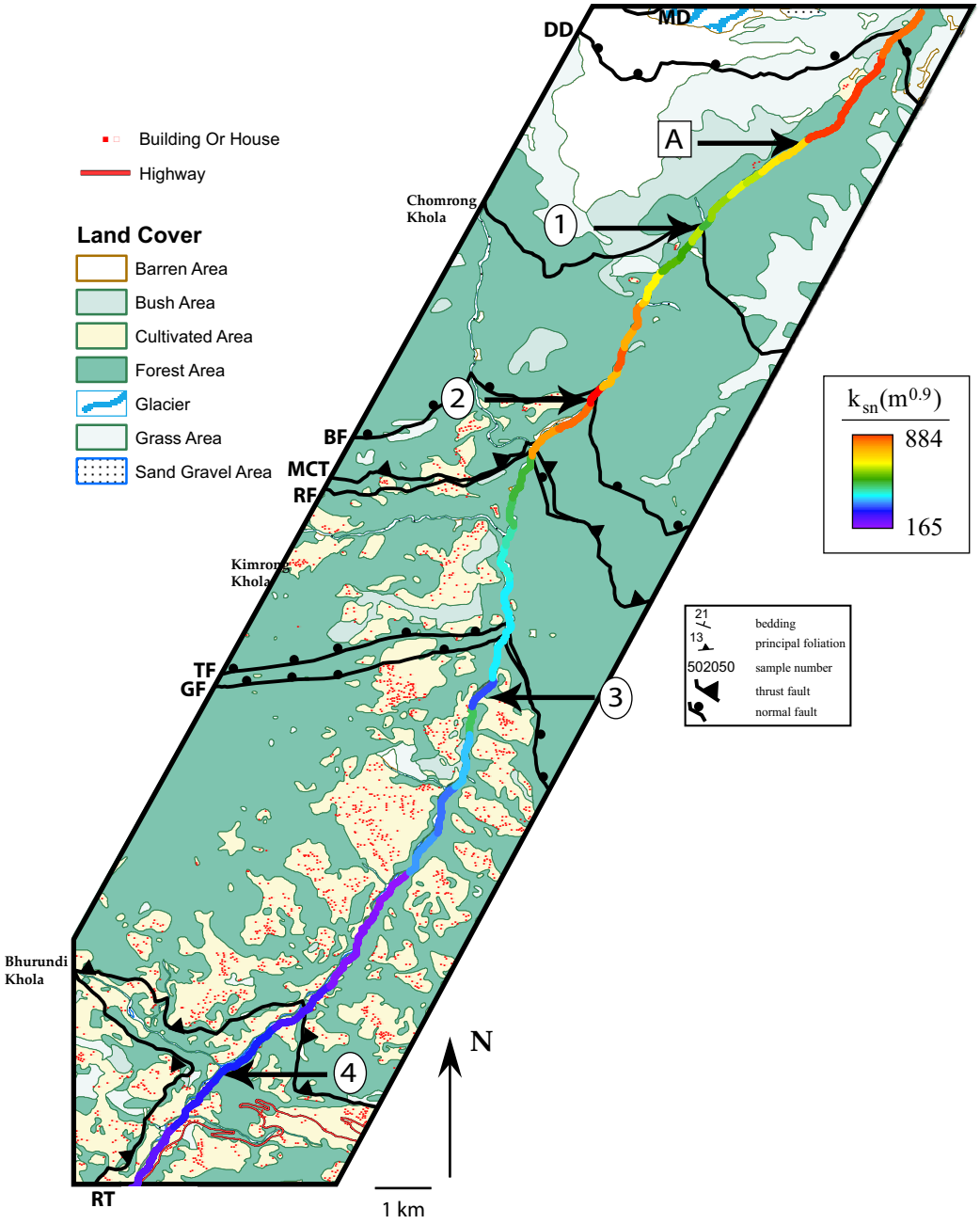

Figure 79: Land cover change for the Ghandruk topographic map and the Modi Khola valley Land cover map digitized and provided by Ofori Pearson. Light yellow regions show cultivated regions. Notice large number of buildings in cultivated areas. These buildings likely are surrounded by rice terraces like those pictured in Figure 78. Green regions represent forested areas, which are the densely vegetated areas mentioned in the text. Numbers represents locations of distinct ksn transitions or peaks that are discussed in chapter 2. Black lines show faults from Martin et al., 2009. MD—Macchapucchare Detachment, DD—Deorali Detachment, FRM II - FRM I— Formation II - Formation I lithologic contact, BF— Bhanuwa Fault, MCT—Main Central thrust, RF—Romi Fault, TF—Tobro Fault, GT—Ghandruk thrust, RT—Ramgarh thrust. Geographic coordinate system: WGS 1984 UTM Zone 44N. Projection: Transverse Mercator.

7.3.3 River steepness on tributaries of the Modi Khola

In the initial analysis of river steepness on the Modi Khola, I calculated k_{sn} for the Modi Khola starting at the headwaters of several tributaries (Figure 80). Tributaries entering the Modi Khola south of the abrupt drop in k_{sn} at the Romi fault do not reflect distinct profile convexities observed on the log slope versus log drainage area plot (shown in green Figure 80 and Figure 81). Tributaries entering the Modi Khola north of the abrupt drop in k_{sn} at the Romi fault do reflect a distinct zone of high concavity when data for that tributary are plotted on the log slope versus log drainage area plot.

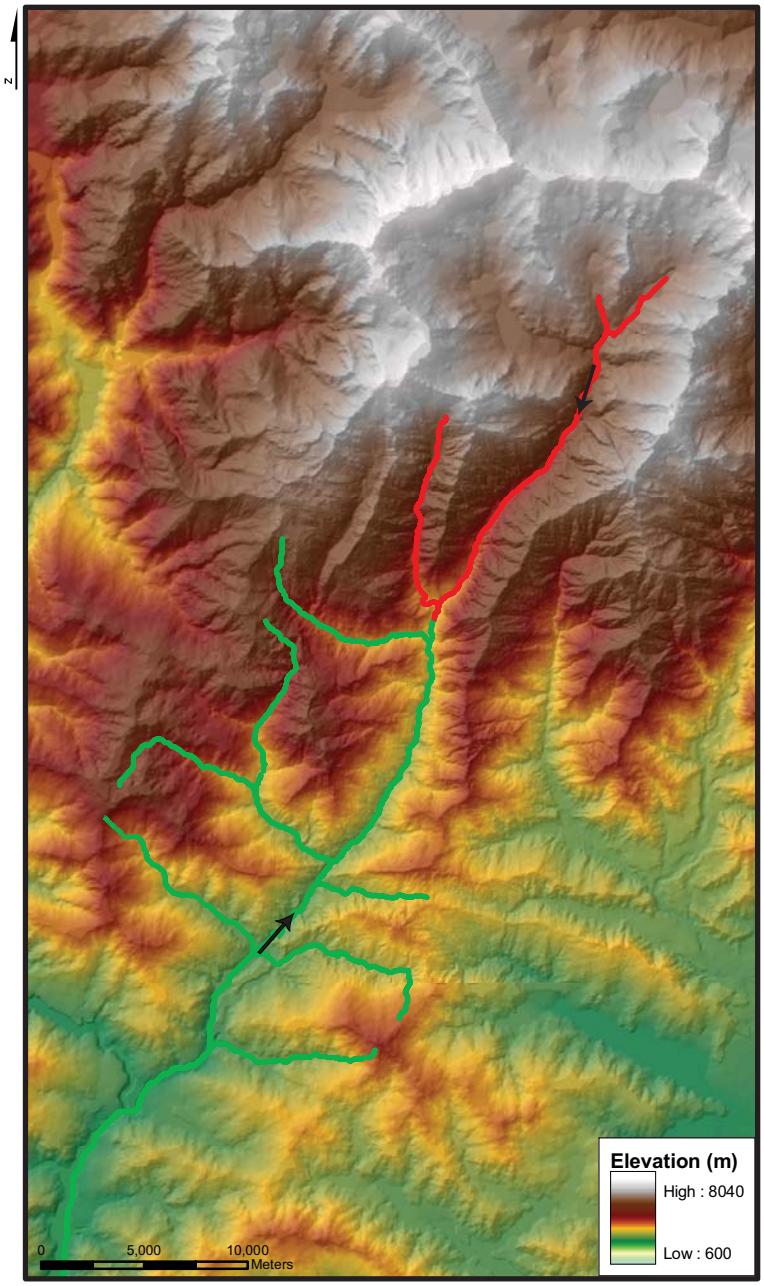

Figure 80: Tributaries examined for the Modi Khola watershed
This map shows tributaries examined in the Modi Khola watershed during the initial assessment of river steepness and concavity on the Modi Khola. Green stream segments show tributaries that maintain significantly lower values of k_{sn} and no high concavity zone on the log slope versus drainage area plot. Red stream segments mark tributaries that maintain high values of k_{sn} and a high concavity zone on the log slope versus log drainage area plot. Black arrows mark the extent of the high concavity zone discussed in chapter 2. Contact between green and red segments marks the abrupt drop in k_{sn} that occurs at the Romi fault, as discussed in chapter 2.

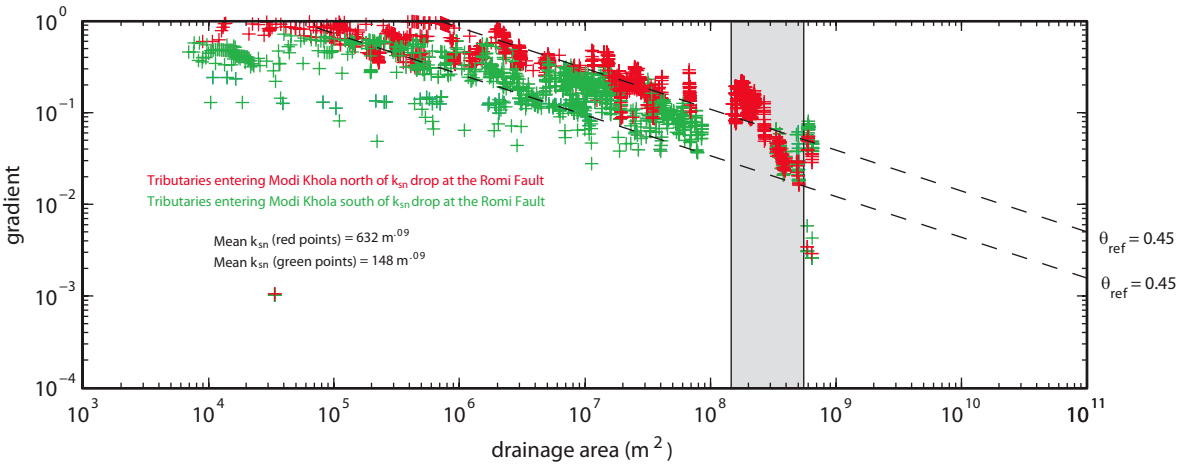

Figure 81: Log slope – log drainage area data compiled for tributaries on the Modi Khola River steepness and drainage area data were analyzed for tributaries entering the Modi Khola trunk stream. The main observation from this analysis was that tributaries entering the Modi Khola south of the abrupt drop of k_{sn} near the Romi fault (green crosses) do not exhibit a zone of high concavity while tributaries entering the Modi Khola north of the abrupt transition in k_{sn} (red crosses) do reflect a zone of high concavity. Grey band shows zone of high concavity. Dashed lines mark the average k_{sn} value for the red and green segments of the stream shown in Figure 80.

7.3.4 Stream profile steepness compared to slope and curvature grids

I used the slope and curvature grids created for the lithologic signature analysis discussed in chapter 6 to extract variations in steepness and curvature across the Modi Khola profile. The global slope maximum occurring in this case occurs between the Bhanuwa fault and the MCT, though these data do not take into account upstream drainage area which has proven to be an important factor in river incision (Wobus et al., 2006a). Variability of slope appears to be much greater north of the steepness maxima and less variable south of the steepness maxima. Curvature is moderately variable across the entire profile length, but exhibits an interesting correlation between maximum curvature, the high concavity zone on the Modi Khola, and the steepness maxima. Maximum curvature centers on the MCT along the Modi Khola profile. Other locations in the topography, which are not at the trace of the Modi Khola, curvature does not appear to always correlate with the MCT when examined visually (Figure 83 - Figure 86). High positive curvature values represent concave down shapes in the topography (Roberts, 2001), as do high concavity zones (Schoenbohm et al., 2004). The apparent correlation between concavity and curvature identify the potential of curvature grids to be implemented into river profile studies. The examination of curvature grids may allow researchers to achieve an initial understanding of river profile morphology without carrying out an entire river analysis study as outlined in this thesis. A visual comparison of slope and curvature grids to k_{sn} transitions and faults can be seen in Figure 83 through Figure 86.

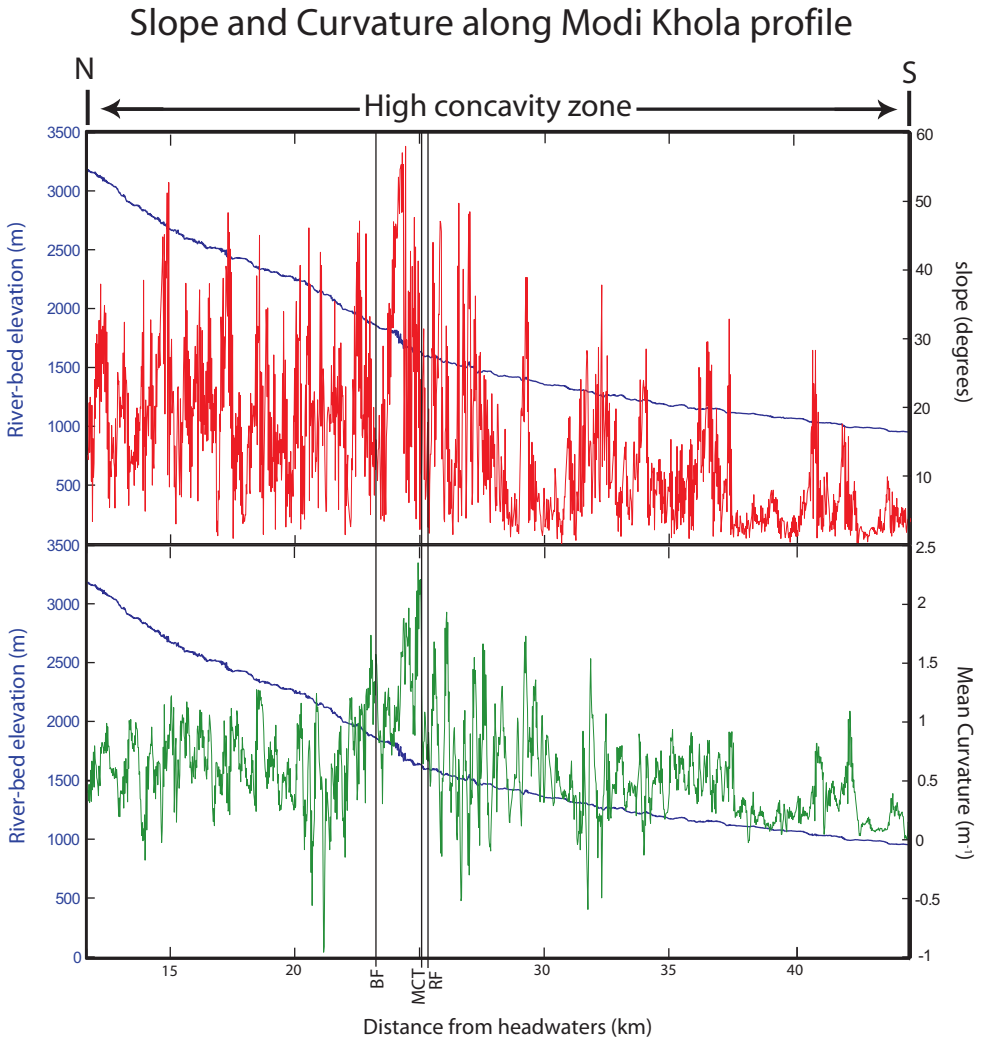

Figure 82: Slope and curvature variability on unsmoothed river profile
Red line on top plot shows changes in slope and green line in bottom plot shows changes in curvature across the Modi Khola profile. These data were extracted from the slope and the curvature grid discussed in chapter 5 from the DEM cells which cover only the trace of the stream. Since the DEM resolution is 25 m, these data represent very local slope and curvature of both the stream profile and the topography of the surrounding inner gorge. These data do not incorporate drainage area, a key component of the river profile analysis that accounts for erosion intensity. The black vertical lines represent faults, BF– Bhanuwa fault, MCT – Main Central thrust, and RF – Romi Fault. These plots include data only from the high concavity zone on the Modi Khola profile.

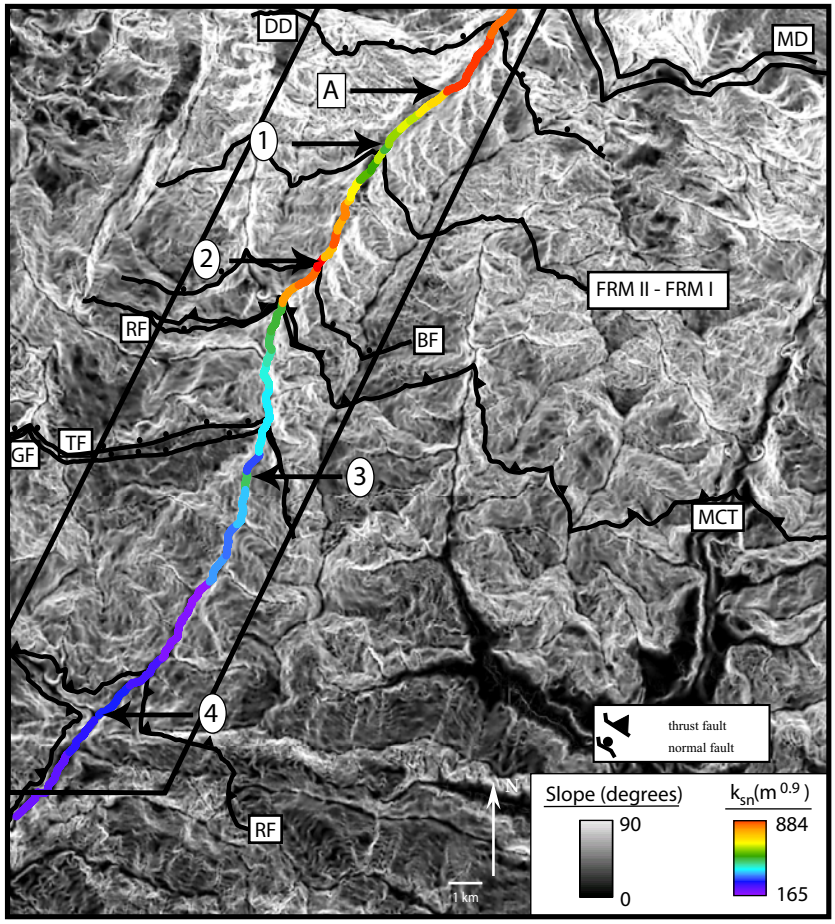

Figure 83: Faults, k_{sn} transitions, and slope grid for the Modi Khola valley
White locations on slope grid show steep topography and black locations on slope grid show gentle topography. Red lettering indicates the names of faults from Martin et al. (2009). MD—Macchapucchare Detachment, DD—Deorali Detachment, FRM II - FRM I— Formation II - Formation I lithologic contact, BF— Bhanuwa Fault, MCT—Main Central thrust, RF—Romi Fault, TF—Tobro Fault, GT—Ghandruk thrust, RT—Ramgarh thrust. Numbers represent distinct transitions of k_{sn} discussed in chapter 2. Black border marks the location of the geologic map shown in Figure 5. Entire map covers span of the Ghandruk topographic map. Resolution of slope map is 25 m. Geographic coordinate system: WGS 1984 UTM Zone 44N, Projection: Transverse Mercator.

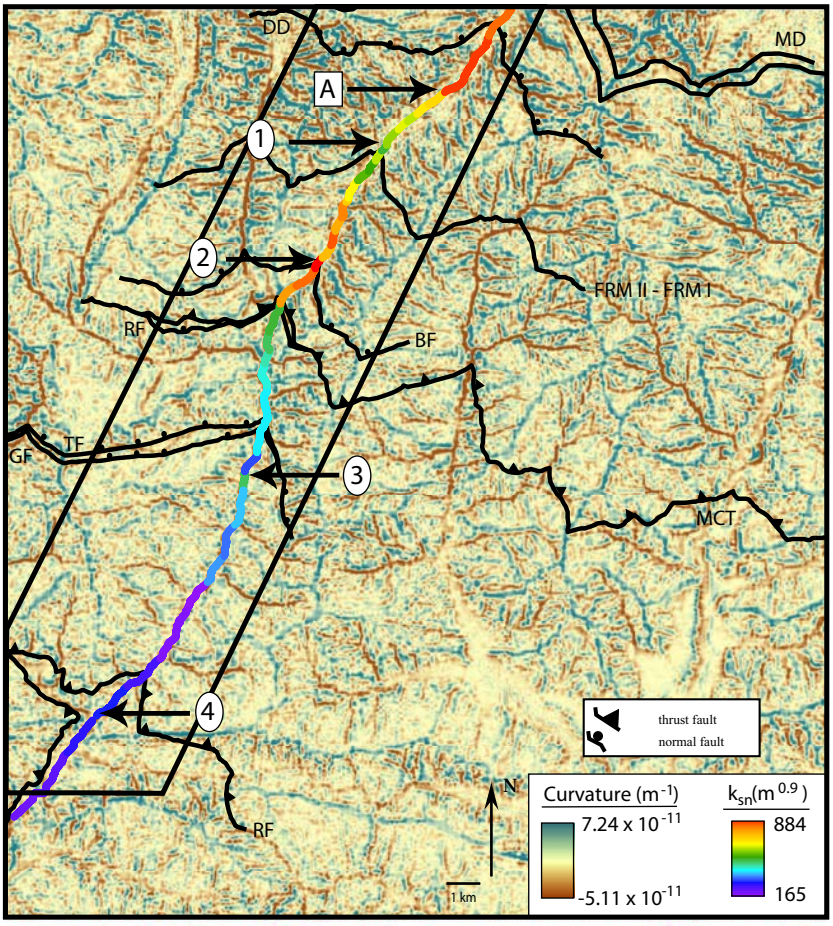

Figure 84: Faults, k_{sn} transitions, and curvature grid for the Modi Khola valley
Brown locations on curvature grid show concave up or valley shaped topography and aqua location on curvature grid show concave down or ridge shaped topography. Tan locations on curvature grid show locations of zero curvature (See Figure 41). Lettering indicates the names of faults from Martin et al. (2009). MD—Macchapucchare Detachment, DD—Deorali Detachment, FRM II - FRM I— Formation II - Formation I lithologic contact, BF— Bhanuwa Fault, MCT—Main Central thrust, RF—Romi Fault, TF—Tobro Fault, GT—Ghandruk thrust, RT—Ramgarh thrust. Numbers represent distinct transitions of k_{sn} discussed in chapter 2. Black border marks the location of the geologic map shown in Figure 5. Entire map covers span of the Ghandruk topographic map. Resolution of curvature map is 25 m. Geographic coordinate system: WGS 1984 UTM Zone 44N, Projection: Transverse Mercator.

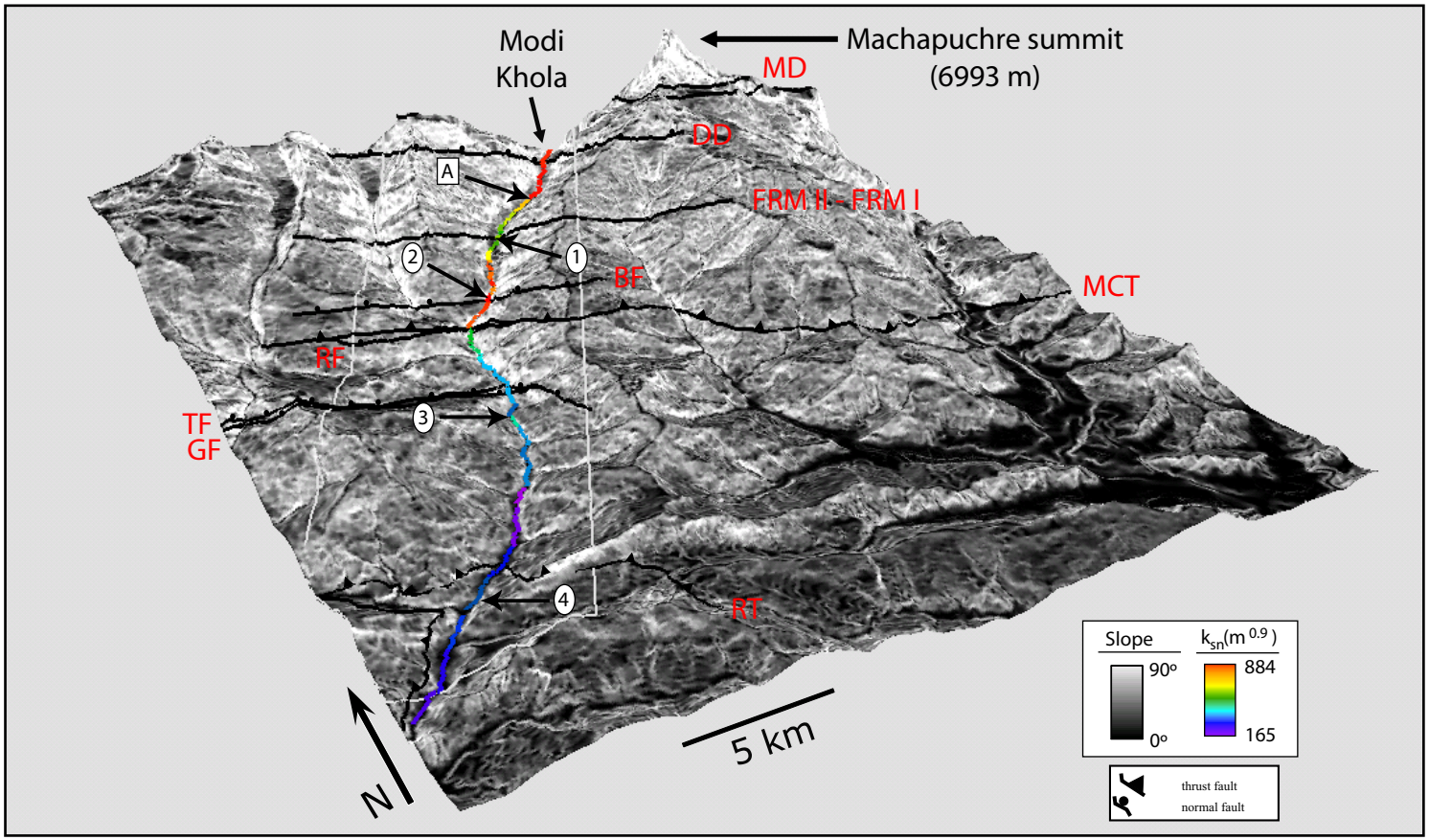

Figure 85: 3-Dimensional Faults, ksn transitions and slope grid for the Modi Khola valley
Same as Figure 83 in 3-dimensions. White locations on slope grid show steep topography and black locations on slope grid show gentle topography. Red lettering indicates the names of faults from Martin et al. (2009). MD—Macchapucchare Detachment, DD—Deorali Detachment, FRM II - FRM I— Formation II - Formation I lithologic contact, BF— Bhanuwa Fault, MCT—Main Central thrust, RF—Romi Fault, TF—Tobro Fault, GT—Ghandruk thrust, RT—Ramgarh thrust. Numbers represent distinct transitions of ksn discussed in chapter 2. Grey border marks the location of the geologic map shown in Figure 5. Entire map covers span of the Ghandruk topographic map. Note the Macchapucchare summit, the highest location on the Ghandruk topographic map. Resolution of slope map is 25 m. Geographic coordinate system: WGS 1984 UTM Zone 44N, Projection: Transverse Mercator.

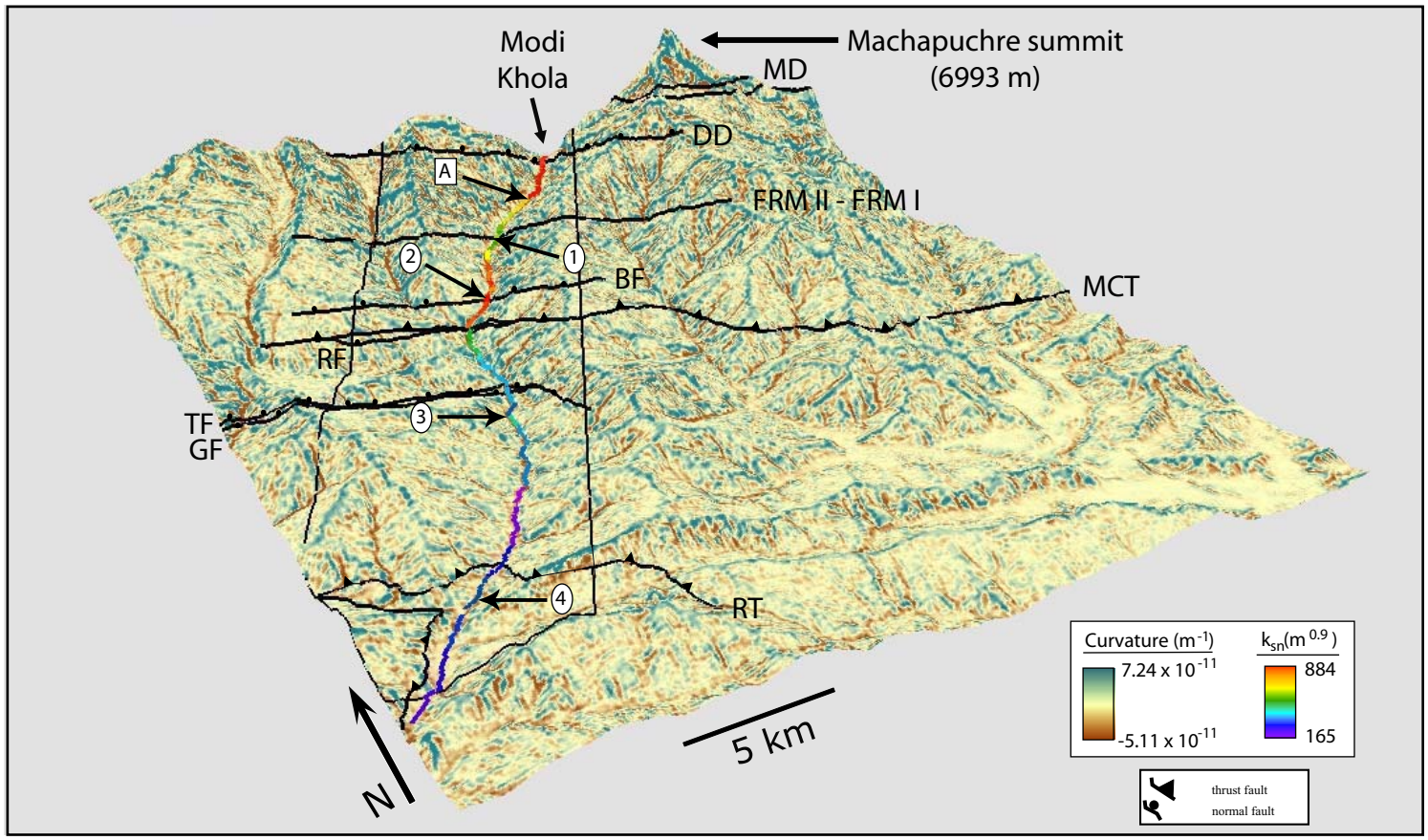

Figure 86: 3-Dimensional Faults, ksn transitions and curvature grid for the Modi Khola valley
Same as Figure 84 in 3-dimensions. Brown locations on curvature grid show concave up or valley shaped topography and aqua location on curvature grid show concave down or ridge shaped topography. Tan locations on curvature grid show locations of zero curvature (See Figure 41). Red lettering indicates the names of faults from Martin et al. (2009). MD—Macchapucchare Detachment, DD—Deorali Detachment, FRM II - FRM I— Formation II - Formation I lithologic contact, BF— Bhanuwa Fault, MCT—Main Central thrust, RF—Romi Fault, TF—Tobro Fault, GT—Ghandruk thrust, RT—Ramgarh thrust. Numbers represent distinct transitions of ksn discussed in chapter 2. Black border marks the location of the geologic map shown in Figure 5. Entire map covers span of the Ghandruk topographic map. Note the Macchapucchare summit, the highest location on the Ghandruk topographic map. Resolution of slope map is 25 m. Geographic coordinate system: WGS 1984 UTM Zone 44N, Projection: Transverse Mercator.

.

7.3.5 Uncertainty of k_{sn} and θ values

Figure 87 shows 2 σ uncertainties for k_{sn} and θ values, also listed in Tables 1 and 2 in chapter 2. The 2 σ uncertainty values mean that there is a 95.4% chance, or confidence interval, the k_{sn} or θ values are accurate within the specified 2 σ uncertainty range. Since k_{sn} or θ values are calculated by a least squares regression over a specified stream segment, the 2 σ uncertainty is calculated using a standard error calculation on the mean. The calculation for standard error is shown below as:

(Equation 21)

$$\sigma = \sqrt{\frac{\Sigma(x - \bar{x})}{n}},$$

where, x is the k_{sn} or θ values calculated from a specific slope and drainage area data point within the stream segment, $\bar{x}$ is the mean of k_{sn} or θ values for all slope and drainage area within the stream segment, and n is the number of slope and drainage area data points within a chosen stream segment. The standard error value can then be converted to a 2 σ confidence interval of 95.4%, assuming the data maintain a normal distribution. The 2 σ k_{sn} or θ values were calculated using a Matlab code embedded in the stream profiler tool.

River steepness and concavity maintain relatively low 2 σ uncertainty values that are about the size of the symbols used plots in Figure 87. The 2 σ uncertainty is approximately 50 $m^{0.9}$ for k_{sn} and 100 for θ. Large 2 σ uncertainty values for both k_{sn} and θ were probably generated when minimal data points or abrupt transitions in the data made it difficult to fit a line through the data during the least squares regression. River steepness and concavity extrema and transitions are mostly unaffected by these uncertainties, except at location 1 at the Formation I – Formation II contact. At

location 1 k_{sn} may fluctuate within the bounds of 2 σ uncertainty by ± 94 $m^{0.9}$ and θ may fluctuate by 390. This means that a local minimum of k_{sn} and large drop in concavity may not exist in the Modi Khola valley at the Formation I-Formation II contact. The k_{sn} maxima at location 2 (the Bhanuwa fault), location 3 (the local k_{sn} maximum in the Kuncha formation), and location 4 (the local k_{sn} maximum between the quartzite- and phyllite- rich members of the Fagfog Formation) are still valid since there are very low 2 σ uncertainties at each of these locations.

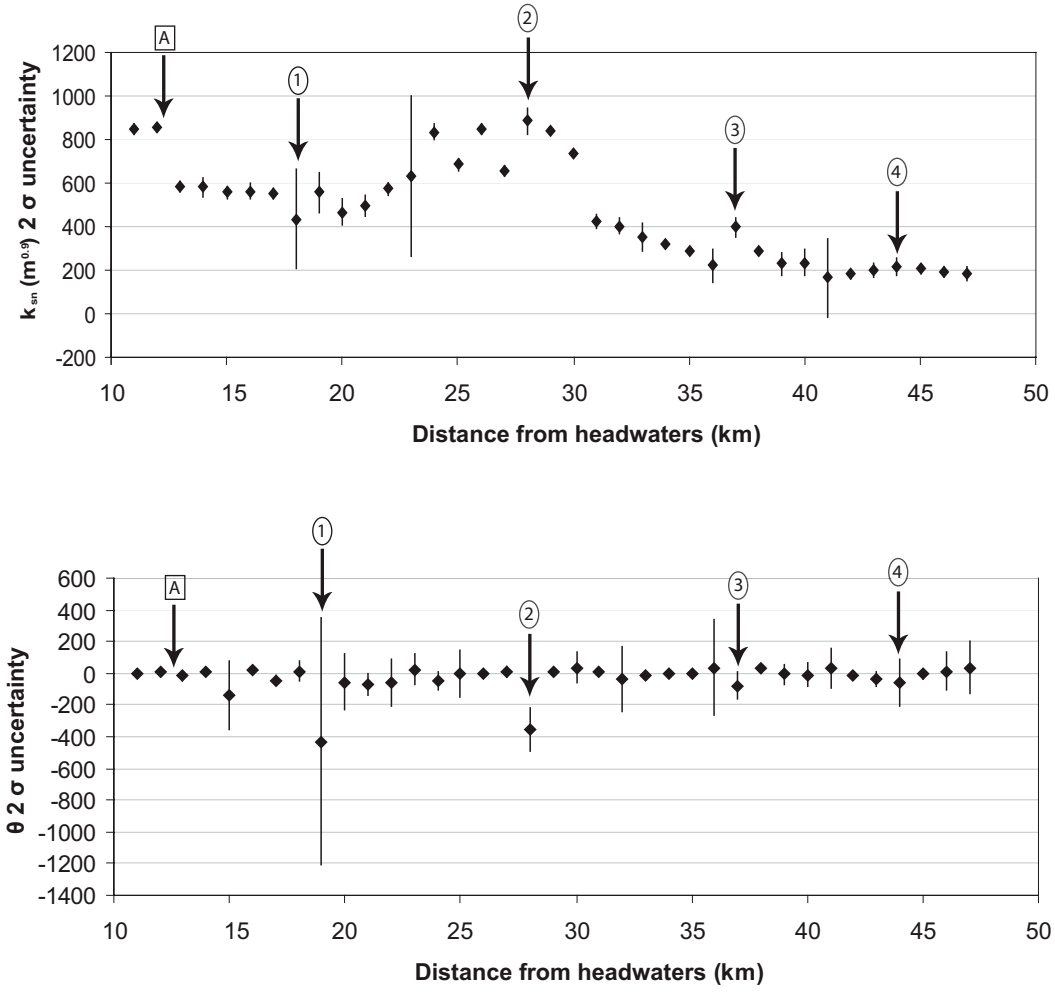

Figure 87: 2σ uncertainty k_{sn} and θ values for regressed stream segments
Numbers mark locations of abrupt k_{sn} transitions and peaks discussed in chapter 2. Each 2σ value was calculated from slope and drainage area data points within the selected stream segment k_{sn} and θ were calculated over.

7.4 Conclusions

A high concavity zone exists on the Modi Khola. Similar zones of high concavity exist on other rivers in central Nepal including the Thopal Khola, Balephi Khola, Burhi Gandaki, Trisuli Khola, and Marsyandi Nadi (Wobus et al., 2003) (Figure 88, Figure 89). Within the high concavity zone river steepness varies significantly, allowing four locations of steepness maxima to be determined. I initiated this study by observing large-scale changes in k_{sn} and θ, then zooming in to observe small-scale changes in k_{sn} and θ. Small-scale variations of k_{sn} within the high concavity zone are discussed in detail in chapter 2.

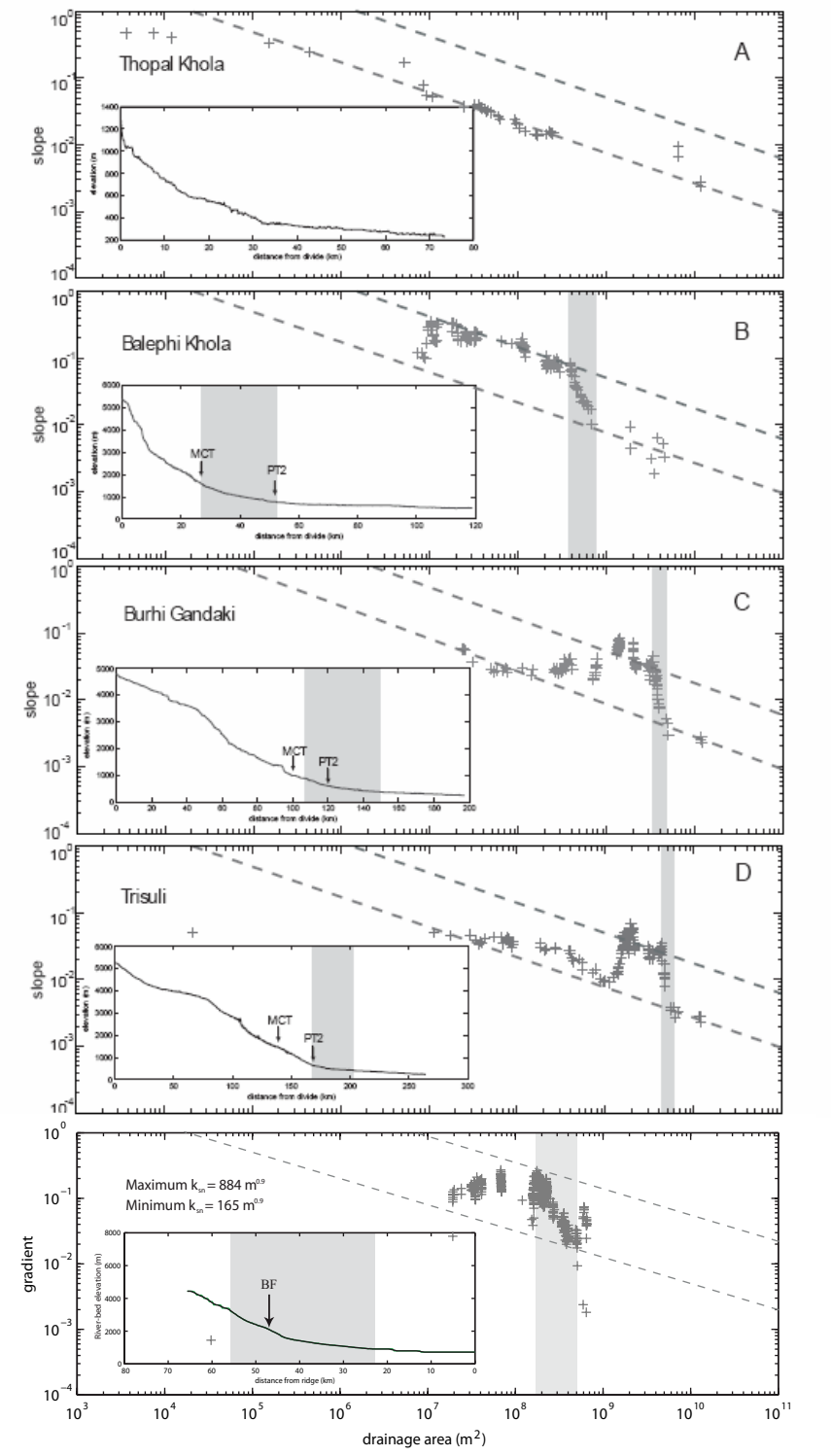

Figure 88: High concavity zone comparison
High concavity zone on the Modi Khola compared with high concavities on the Thopal Khola, Balephi Khola, Burhi Ghandaki, and Trisuli from Wobus et al. (2003) on log slope versus log drainage area plots. Reference concavity for all plots is 0.45. Grey bands show zones of locally high concavity. In Wobus et al. (2003) plots, PT2 represents physiographic transition 2 and MCT represents the Main Central thrust. BF stands for the Bhanuwa fault.

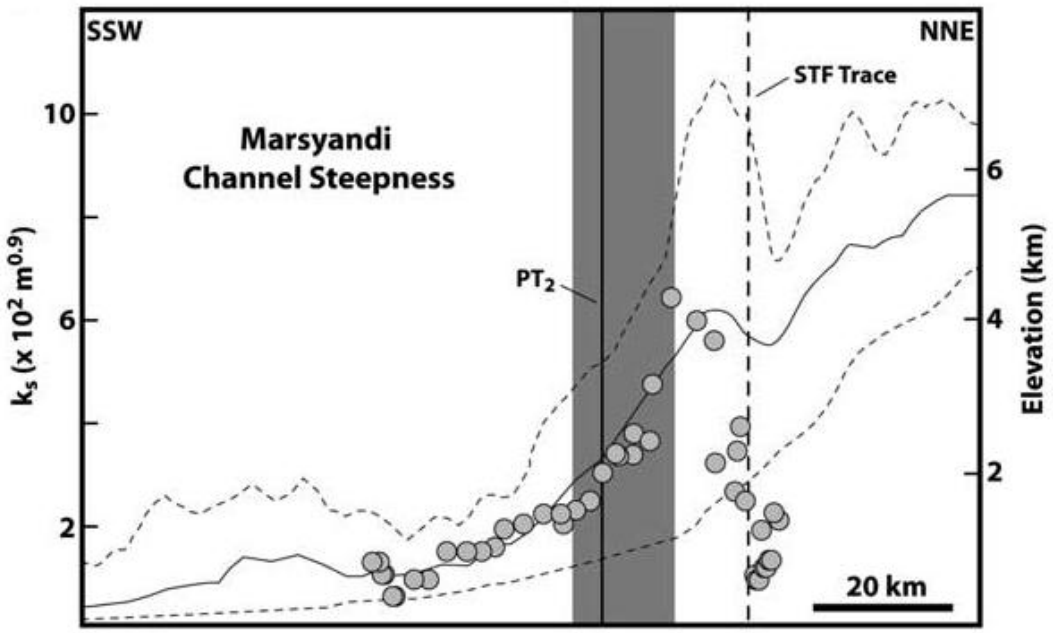

Figure 89: High concavity on Marsyandi Nadi
River steepness versus distance plot illustrating spatial relationships between topography, river steepness, and physiographic transition 2 (PT_2) in the Marsyandi valley from Hodges et al. (2004). The Marsyandi valley is approximately 55 km from the Modi Khola valley. Solid line represents mean elevations along a ~50 km wide transect while dashed lines represent maximum and minimum elevations. Shaded circles show values of k_s based on slope versus drainage area data for 5 km intervals along the Marsyandi trunk stream. Smoothing window is 10 km and reference concavity is 0.45. Dashed vertical line marks approximate location of South Tibetan fault system (STF). (Figure modified from Figure 4 in from Hodges et al., 2004)

Chapter 8: Discussion

8.1 Main conclusions of the thesis

The creation of digital elevation data for central Nepal, search for a topographic signature of rock types in the Modi Khola valley, and detailed examination of river steepness (k_{sn}) and concavity (θ) extrema and transitions on the Modi Khola profile yields several interesting conclusions concerning the examination of topographic data and our resulting understanding of mountain belt evolution, including:

(1) Digitizing topographic maps provide a feasible and successful method to produce a cohesive DEM for the central Nepalese Himalaya. SRTM data for the Himalaya contain too many data voids to allow detailed studies of the topography to be conducted without implementing an alternative interpolation method.

(2) The TIN interpolation, which is available and easily operated in ArcGIS, produces flat irregular terraces which inhibit slope studies in regions with steep topography. The multiquadric radial basis function and the regularization by inverse linear interpolation method allow the creation of high resolution DEMs that avoid flat irregular terraces produced in the TIN grid interpolation. The Topo to Raster function, also within ArcGIS, produces accurate DEMs only if digitized contour data are supplemented with spot heights, rivers, and the map boundary during the DEM creation process.

(3) The topographic signature of lithologies in the Modi Khola valley remains difficult to constrain. Only subtle differences in mean slope characterize different

rock types in the Modi Khola valley. Steepness versus curvature plots reflect relatively similar data dispersal for each lithology, constraining the steepness – curvature envelope where steepness values vary from 1 degree to approximately 70 degrees and curvature ranges from -2 x 10^{-11} to 2 x 10^{-11} m^{-1}. Perhaps underlying tectonic processes and intense erosion dominate landscape evolution in the Himalaya, dampening the expected topographic signature of different rock types.

(4) A high concavity zone traverses part of the Modi Khola, implying fault movement may have occurred in the last 1 My. Spatial changes in k_{sn}, within the high concavity zone, reveal 4 distinct peaks in river steepness. Precipitation variability, glacial dams, landslide dams, spatial changes in lithology, recent rock uplift on faults, and tributary junctions each provide possible mechanisms to explain the distinct changes in k_{sn} observed in the Modi Khola valley. The correlation of the Bhanuwa and Romi faults with the steepest location on the profile and the abrupt drop in river steepness, respectively, suggest normal faults could play a pivotal role in active deformation of the Modi Khola valley. The existence of an active surface breaking fault may explain the local k_{sn} maxima in the Kuncha formation located approximately 1 km south of the Ulleri granite. Alternatively, changes in k_{sn} are explained by compositional changes at the Formation II – Formation I contact and the quartzite – phyllite members of the Fagfog Formation.

(5) The location of lithologic contacts and important structures, such as faults, largely affects the interpretations made when examining the topography and tectonics of a landscape. Two geologists may implement the same DEM in a tectonic geomorphology analysis and reach opposing conclusions if their geologic maps are

different, especially if their faults were in different locations or if different faults were recognized. Geologic maps often change after new field mapping trips and multiple geologists that visit the same field location could interpret the geology differently. Geologists must make flexible and careful interpretations of the relationships between tectonics and the topography, since different geologic interpretations are bound to frequently occur during the production of geologic maps.

8.2 Concluding remarks

The emergence of GIS and digital topography allowed the research, methods, and conclusions of my project to be conducted remotely. Any landscape may be examined using the methods outlined in this thesis, allowing investigation of active deformation of the surface. GIS studies offer great insight and an advantage in selecting potential field site locations for geologic studies. While GIS remains a discipline in itself, this project illustrates the potential positive feedbacks of implementing GIS investigations in geological research. Due to the results of this project, it may be interesting to install a geodetic network near the trace of the Bhanuwa fault to search for active fault movement. The results of this project could be integrated into models which incorporate differing lithologic erosion rates, and extended to develop a landscape evolution model for the Himalaya. The ability of GIS to locate zones of potential deformation may be extended to predict the hazards associated with mountain building, such as landslides or earthquakes.

GIS observations and models of landscape evolution significantly improve our knowledge of mountain belt evolution, but we must gather empirical data from techniques such as seismology, low temperature thermochronology, and GPS to

completely understand the dynamic feedbacks between tectonics and erosion in the Modi Khola valley.

Appendices

Appendix A

In the following text, Karl Schleicher describes the regularization by inverse linear interpolation method (*Note: depth represents height for this project's purpose*):

"The method used to create the gridded elevation data is regularization by inverse linear interpolation. This method inverts for an elevation grid that can be bilinearly interpolated to obtain the original irregularly sampled data. The equations are:

$$A x = z$$

where:

A is the bilinear interpolation operator
x is the unknown elevation grid and
z are the depth samples.

There is one equation for each of the original depth samples. The number of unknowns is the number of points in the unknown grid. Not only are there likely to be fewer equations than unknowns, it may not be possible to exactly fit the original data points. There may be two points with the same (x,y) but different elevations. There are a large number of equations and a large number of unknowns, so conventional matrix inversion methods would be very computationally intensive. Regularization by inverse linear interpolation addresses all of these problems.

The algorithm uses techniques described in Earth Soundings Analysis: Processing versus Inversion (PVI), by Jon Claerbout. Dr. Claerbout calls the algorithm the Congugate Gradient method, but strictly it is the least squares method LSQR (Paige and Saunders). Claerbout's text book explains how to solve these problems without even computing the matrix A, which is very large and sparse. You need only write a computer routine to apply A and transpose A.

The conjugate gradient method is an iterative method. Starting with an initial guess at the solution the algorithm iterates to improve the estimate. The initial guess can be the 0 vector. Mathematically you will get a best fit solution after iterating once for each unknown, but fortunately good results are often obtained after a few iterations.

A serious problem is that more than one elevation grid may optimally fit the data. This is especially a problem where there are large holes in the original, irregularly sampled depth and when you solve for x on a fine grid. This implementation of regularization by inverse linear interpolation uses preconditioning to address this problem. Preconditioning is a change of variables that ensures the elevation grid estimated is smooth. A very smooth elevation grid was estimated. This elevation grid was used as an initial estimate to solve the problem again with less smoothing.

This process was repeated many times so the final solution has rapid elevation variation only in areas where it was required to fit the data."

Appendix B

In the following text, Tom Fedenczuk describes the multiquadric radial basis function employed in his interpolation method:

"The underlying model used to fit a surface to the elevation points, sampled at irregularly spaced positions (x_j,y_j), was a linear combination of *n* radial basis functions (Buhmann 2003):

$$f(x,y) = \sum_{j=1}^{n} \beta_j \phi\left(\sqrt{(x-x_j)^2 + (y-y_j)^2}\right)$$

where β_j are parameters found by fitting the model to the data in a least squares sense, and ϕ is a single variable function. The multiquadric function was used since it has proven to be useful for fitting scattered data (Hardy 1990):

$$\phi(d) = \sqrt{d^2 + r^2}$$

where *r* is a fixed smoothing parameter. The final multiquadric radial basis function model has the form:

$$F(x,y) = \sum_{j=1}^{n} \beta_j \sqrt{(x-x_j)^2 + (y-y_j)^2 + r^2}$$

." An array of raster resolutions was created using the multiquadric radial basis function at a 40m, 30m, and 25m cell size. Artifacts began to appear in valleys and low elevations of rasters created with a cell size of 20m or less. The 25m cell size raster created the highest resolution DEM without the production of artifacts.

References

Anders, A.M., Roe, G.H., Hallet, B., Montgomery, D.R., Finnegan, N.J., and Putkonen, J, 2006, Spatial patterns of precipitation and topography in the Himalaya: Geological Society of America Special Paper 398, p. 39-53, doi:10.1130/2006.2398(03).

Amatya, K.M., and Jnawali, B.M., 1994, Geological Map of Nepal: Kathmandu, Department of Mines and Geology, Government of Nepal, scale 1:1,000,000.

ArcGIS Desktop Help, How slope works, 21 April 2009, http://webhelp.esri.com/arcgisdesktop/9.3/index.cfm?TopicName=How%20Slope%20works.

Attal, M., J. Lavé, and J.P. Masson, 2006, A new experimental device to study pebble abrasion and transpose to natural systems: Journal of Hydraulic Engineering, v. 132, p. 624-628, doi:10.1061/(ASCE)0733-9429(2006)132:6(624).

Barros, A.P., Joshi, M., Putkonen, J., Burbank, D.W., 2000, A study of 1999 monsoon rainfall in a mountainous region in Central Nepal using TRMM products and rain gauge observations: Geophysical Research Letters, v. 27, p. 3683-3686.

Belt, K., and Paxton, S.T., 2005, GIS as an aid to visualizing and mapping geology and rock properties in regions of subtle topography: GSA Bulletin, v. 117, no. 1/2 p. 149-160.

Bettinelli, P., Avouac, J.P., Flouzat, M., Jouanne, F., Bollinger, L., Willis, P., and Chitrakar, G.R., 2006, Plate motion of India and interseismic strain in the Nepal Himalaya of GPS and DORIS measurements, Journal of Geodynamics, v. 80, p. 567-589.

Berthier, E., Arnaud, Y., Vincent, C., and Remy, F., 2006, Biases of SRTM in high-mountain areas: implications for the monitoring of glacier volume changes, Geophysical Research Letters, v. 33, no. 8.

Beven, K. and M. J. Kirkby, 1979, A physically based, variable contributing area model of basin hydrology: Hydrological Sciences Bulletin, v. 24, p. 43-69.

Bollinger, L., Henry, P., and Avoacc, J.P., 2006, Mountain building in the Nepal Himalaya: Thermal and kinematic model: Earth and Planetary Science Letters, v. 244, p. 58-71.

Bolstad, P., Gessler, P., and Lillesand, T.M., 1990, Positional uncertainty in manually digitized map data: International Journal of Geographic Information Systems, v. 4, p. 399-412.

Bookhagen, B. and Burbank, 2006, Topography, relief, and TRMM-derived rainfall variations along the Himalaya: Geophysical Research Letters, v. 33, L08405, doi: 10.1029/2006GL026037.

Bridges, A., 2000, ABCs of Interferometry, http://www.space.com/businesstechnology/technology/sts99_interfer.html

Barbalic and Omerbegovic, 1999, Correction of horizontal areas in TIN terrain modeling – algorithm, ESRI user conference proceedings, http://proceedings.esri.com/library/userconf/proc99/proceed/papers/pap924/p924.htm.

Brocard, G.Y., and van der Beck, P.A., 2006, Influence of incision rate, rock strength, and bedload supply on bedrock river gradients and valley-flat widths: Field-based evidence and calibrations from western Alpine rivers (southeast France): Geological Society of America Special Paper 398, p. 101.

Buhmann, M.D., 2003, Radial Basis Functions: Theory and Implementations, Cambridge University Press, ISBN 0521633389, 780521633383. 259 pages

Burbank, D.W., Blythe, A.E., Putkonen, Pratt-Sitaula, Gabet, E., Oskin, M., Barros, A., and Ojha, T.P., 2003, Decoupling of erosion and precipitation in the Himalayas: Nature, v. 426, p. 652-655.

Burchfiel, B. C., Chen, Z., Hodges, K. V., Liu, Y., Royden, L. H., Deng, C., and Xu, J., 1992, The South Tibetan detachment system, Himalayan orogen: Extension contemporaneous with and parallel to shortening in a collisional mountain belt, Geological Society of America Special Paper 269, 41 p.

Burbank, D.W., 2005, Cracking the Himalaya: Nature, v. 434, p. 963-964.

Burbank, DW., and Anderson, R.S., 2001, Tectonic Geomorphology, Blackwell Science, ISBN 0632043865. 274 pages.

Burrough, P. A. and McDonell, R.A., 1998. Principles of Geographical Information Systems (Oxford University Press, New York), p. 190.

Cattin, R., and Avouac, J.P., 2000, Modeling mountain building and the seismic cycle in the Himalaya of Nepal: Journal of Geophysical Research, v. 105, no. B6, p.13389-13407.

Claerbout, J., 1992, Earth Soundings Analysis: Processing versus Inversion (PVI), Blackwell, ISBN 0865422109.

Clarke, M.L., and Rendell, H., 2000, The impact of the farming practice of remodeling hillslope topography on badland morphology and soil erosion processes: Catena, v. 40, p. 229-250.

Chopra, S., and Marfut, K.J., July 2007, Volumetric curvature attributes add value to 3D seismic data interpretation: The Leading Edge.

Corenblit, D., Tabacchi, E., Steiger, J., and Gurnell, A.M., 2007, Reciprocal interactions and adjustments between fluvial landforms and vegetation dynamics in river corridors: A review of complementary approaches: Earth-Science Reviews, v. 84, p. 56-86.

Crosby, B., and Whipple, K.X., 2006, Knickpoint initiation and distribution within fluvial networks: 236 waterfalls in the Waipaopa river, North Island, New Zeland: Geomorphology, v. 82, p. 16-38.

Davis, D., Suppe, J., and Dahlen, F.A., 1983, Mechanics of fold-and-thrust belts and accretionary wedges: Journal of Geophysical Research, v. 88, p. 1153–1172.

DeCelles, P. G., Gehrels, G. E., Quade, J., LaReau, B., and Spurlin, M., 2000, Tectonic implications of U-Pb zircon ages of the Himalayan orogenic belt in Nepal: Science, v. 288, no. 5465, p. 497-499.

DeCelles, P.G., and DeCelles, P.C., 2001, Rates of shortening, propagation, underthrusting, and flexural wave migration in continental orogenic systems: Geology, v. 29, no. 2, p. 135-138.

Dhalen, F.A., 1990, Critical taper model of fold and thrust belts and accretionary wedges: Annual Reviews of Earth and Planetary Science Letters, v. 18, p. 55-99.

Dietrich, W. E., and T. Dunne, 1978, Sediment budget for a small catchment in mountainous terrain: Zeit. für Geomorph., v. 29, p.191-206.

Dietrich, W. E., Dunne, T., Humphrey, N. F., and Reid, L. M., 1982, Construction of sediment budgets for drainage basins, in Sediment Budgets and Routing in Forested Drainage Basins: edited by F. J. Swanson, R. J. Janda, T. Dunne, and D. N. Swanston, General Technical Report PNW-141, Forest Service, U.S. Dept. of Agriculture, p. 5 - 23.

Dietrich, W. E., Wilson, C. J., Montgomery, D. R., McKean, J., 1993, Analysis of Erosion Thresholds, Channel Networks and Landscape Morphology Using a Digital Terrain Model: Journal of Geology, v. 101, p. 259-278.

Dietrich, W. E., Reiss, R., Hsu, M.-L., and Montgomery, D. R., 1995, A process-based model for colluvial soil depth and shallow landsliding using digital elevation data: Hydrological Processes, v. 9, p. 383-400.

Dietrich, W.E., and Montgomery, D.R., 1998, SHALSTAB: A digital terrain model for mapping shallow landslide potential. http://calm.geo.berkeley.edu/geomorph/shalstab/index.htm.

Dowding, S., Kuuskivi, T., and Li, X., 2004, Void fill of SRTM elevation data – principles, processes, and performance, ASPRS Images to Decision: Remote Sensing Foundation for GIS Applications, September 12-14, Kansas City, Missouri.

Duren, R., Wong, E., Breckenridge, B., Shaffer, S., Duncan, C., Tubbs, E., and Saloman, P., 1998, Metrology, attitude, and orbit determination for spaceborne interferometric synthetic aperture radar, NASA, Jet Propulsion Laboratory, California Institute of Technology, SPIE AeroSense Conference on Acquisition, Tracking and Pointing XII.

England and Molnar, 1990, Surface uplift, uplift of rocks, and exhumation of rocks: Geology, v. 18, p.1173-1177.

Falorni, G., Teles, V., Vivoni, E.R., Bras, R.L., and Amaratunga, K.S., 2005, Analysis and characterization of the vertical accuracy of digital elevation models from the Shuttle Radar Topography Mission. Journal of Geophysical Research-Earth Surface, v. 110, (F2).

Fort, M., 2000, Glaciers and mass wasting processes: their influence on the shaping of the Kali Gandaki valley (higher Himalaya of Nepal): Quaternary International, v. 65/66, 101–119.

Finlayson, D.P., Montgomery, D.R., and Hallet, B., 2002, Spatial coincidence of rapid inferred erosion with young metamorphic massifs in the Himalayas: Geology, v. 30, p. 219–222, doi: 10.1130/0091-7613(2002)030<0219:SCORIE>2.0.CO;2.

Gabet, E., Pratt-Sitaula, B., and Burbank, D., 2004, Climatic controls on hillslope angle and relief in the Himalayas: Geology v. 32, no. 7, p.629.

Garzanti, E., Vezzoli, G., Ando, S., Lave, J., Attal, M., France-Lanord, and DeCelles, P., 2007, Quantifying sand provenance and Erosion (Marsyandi River, Nepal Himalaya): Earth and Planetary Science Letters, v. 258, p.500 (2007).

Gilbert, G.K., 1877, Report on the geology of the Henry Mountains: US Department of the Interior, US Geographical and Geological Survey of the Rocky Mountain Region, Washington, D.C., Government Printing Office. 160 pp.

Gilbert, G.K., 1909, The convexity of hill tops: Journal of Geology, v. 17, p. 344-350.

Hack, T.J., 1973, Stream-profile analysis and stream-gradient index: U.S. Geological Survey Journal of Research, v. 1, no. 4, p. 421-429.

Hack, J.T., and Goodlett, J.C., 1960, Geomorphology and forest ecology of a mountain region in the central Appalachians; Geomorphology, v. 13, p. 1-20.

Hardy, R.L. 1990. Theory and Applications of the Multiquadric BiHarmonic Method, Computers and mathematics with applications, v. 19, 163-208.

Hall, O., Falorni, G., and Bras, R., 2005, Characterization and quantification of data voids in the Shuttle Radar Topography Mission, IEEE Geoscience and Remote Sensing Letters, v. 2, no. 2, p. 177-181.

Hart, B.S., and Sagan, J.A., 2005, Horizon attribute curvature aids stratigraphic interpretation, Search and Discovery Article #40172.

Hartmann, A., October 2008, Hillslope hypothesis falls into place: Earth Magazine.

Hilley, G.E., and Arrowsmith, J.R, 2008, Geomorphic response to uplift along the Dragon's Back pressure ridge, Carrizo Plain, California, Geology, v. 36, no. 5, p. 367–370; doi: 10.1130/G24517A.1.

Hodges, K. V., Parrish, R. R., and Searle, M. P., 1996, Tectonic evolution of the central Annapurna Range, Nepalese Himalayas: Tectonics, v. 15, no. 6, p. 1264-1291.

Hodges, K.V., 2000, Tectonics of the Himalaya and southern Tibet from two perspectives: Geological Society of America Bulletin, v. 112, p. 324–350.

Hodges, K., Hurtado, J. M. and Whipple, K, 2001, Southward extrusion of Tibetan crust and its effect on Himalayan tectonics: Tectonics v. 20, p. 799–809.

Hodges, K.V., Wobus, C., Ruhl, K., Schildgen, T., and Whipple, K., 2004, Quaternary deformation, river steepening, and heavy precipitation at the front of the Higher Himalayan ranges, Earth and Planetary Science Letters, v. 220, p. 379-389.

Hooke, J.M., 2006, Human impacts on fluvial systems in the Mediterranean region: Geomorphology, v. 79, p. 311-335.

Hoth, S., Adams, J., Kukowski, and Oncken, O., 2006, Influence of erosion on the kinematics of bivergent orogens: Results from scaled sandbox simulations: Geological Society of America Special Paper 398, Penrose Conference Series, p. 201-225.

Howard, A.D., and Kerby, G., 1983, Channel changes in badlands, Geological Society of America Bulletin, v.94, p. 739-752.

Hunt, C.B., 1988, Geology of the Henry Mountains, Utah, as recorded in the notebooks of G.K. Gilbert, 1875-76. The Geological Society of America, Inc., Boulder, CO, ISBN 0813711673. 229 pages.

Jet Propulsion Laboratory (JPL), NASA, California Institute of Technology, 2000, Shuttle Radar Topography Mission: The mission to map the world. http://www2.jpl.nasa.gov/srtm/

Kääb, A., 2005. Combination of SRTM3 and repeat ASTER data for deriving alpine glacier flow velocities in the Bhutan Himalaya, Remote Sensing of Environment, v. 94 (4), p. 463-474.

Keller, E.A., 2002, Active Tectonics: Earthquakes, uplift, and landscape. Prentice Hall. 228 pages.

Kirby, E., and Whipple, K., 2001, Quantifying differential rock-uplift rates via stream profile analysis, Geology, v. 29, no. 5, p. 415-418.

Kirby, E., and Whipple, K.X., 2003, Distribution of active rock uplift along the eastern margin of the Tibetan Plateau: Inferences from bedrock channel longitudinal profiles: Journal of Geophysical Research, v. 108, no. B4, 2217, doi:10.1029/2001JB000861.

Korup, O., Strom, A.L., Weidinger, J.T., 2006, Fluvial response to large rock-slope failures: examples from the Himalayas, the Tien Shan, and the Southern Alps in New Zealand: Geomorphology, v. 78, 3–21.

Korup, O., Clague, J.J., Hermanns, R.L., Hewitt, K., Strom, A.L., Weidinger, J.T., 2007, Giant landslides, topography, and erosion: Earth and Planetary Science Letters, v. 261, 578–589.

Korup, O., and Tweed, F., 2007, Ice, moraine, and landslide dams in mountainous terrain: Quaternary Science Reviews, v. 26, p. 3406-3422.

Korup, O., 2008, Rock type leaves topographic signature in landslide-dominated mountain ranges, Geophysical Research Letters, v. 35, L11402, doi: 10.1029/2008GL034157.

Korup, O., and Montgomery, D.R., 2008, Tibetan plateau river incision inhibited by glacial stabilization of the Tsangpo gorge: Nature, v.455, p. 786-790, doi:10.1038/nature07322.

Lave, J., and J.P. Avouac, 2000, Active folding of fluvial terraces across the Siwaliks Hills (Himalayas of central Nepal), J. Geophys Res., v. 105, p. 5735-5770.

LeFort, P., 1975, Himalayas: the collided range. Present knowledge of the continental arc: American Journal of Science, v. 275-a, p. 1-44.

Luedeling et al., 2007, Filling the voids in the SRTM elevation model – A TIN-based delta surface approach, ISPRS, Journal of Photogrammertry & Remote Sensing, v. 62, p. 283-294.

Martin, A.J., DeCelles, P.G., Gehrels, G.E., Patchett, P.J., and Isachsen, C., 2005, Isotopic and microstructural constraints on the location of the Main Central thrust in the Annapurna Range, central Nepal Himalaya, GSA Bulletin, v. 117, no. 7/8, p. 926-944.

Martin, A.J., Gehrels, G.E., and DeCelles, P.G., 2007, The tectonic significance of (U, Th)/Pb ages of monazite inclusions in garnet from the Himalaya of central Nepal: Chemical Geology, v. 224, p. 1-24.

Martin, A.J., Ganguly, J., and DeCelles, P. G., 2009, Metamorphism of Greater and Lesser Himalayan rocks exposed in the Modi Khola valley, central Nepal: Contributions to Mineralogy and Petrology, in press.

Montgomery, D. R., and Dietrich, W. E., 1994a, A Physically-Based Model for the Topographic Control on Shallow Landsliding: Water Resources Research, v. 30, p. 1153-1171.

Montgomery, D. R., and Dietrich, W. E., 1994b, Landscape dissection and Drainage Area-Slope Thresholds: Process Models and Theoretical Geomorphology, p. 222-246.

Montgomery, D. R., and Dietrich, W. E., 1995, Hydrologic Processes in a Low-Gradient Source Area: Water Resources Research, v. 31, p. 1-10.

O'Sullivan, D., and Unwin, D., 2003, Geographic Information Analysis, John Wiley & Sons, Inc., ISBN 0471211761. 436 pages.

Owen, L.A., Finkel, R.C., Barnard, P.L., Haizhou, M., Asahi, K., Caffee, M.W., and Derbyshire, E., 2005, Climatic and topographic controls on the style and timing of Late Quaternary glaciation throughout Tibet and the Himalaya defined by ^{10}Be cosmogenic radionuclide surface exposure dating: Quaternary Science Reviews, v. 24, p. 1391-1411.

Paige, C.C., and Saunders, M.A., 1982, LSQR: An algorithm for sparse linear equations and sparse least squares: ACM Transactions on Mathematical Software, v. 8., no. 1, p. 43-71.

Pandey, M. R., Tandukar, R. P., Avouac, J. P., Lave, J. and Massot, J. P., 1995, Interseismic strain accumulation on the Himalayan crustal ramp (Nepal): Geophysical Research Letters, v. 22, p. 751–754.

Pearson, O. N., 2002, Structural evolution of the central Nepal fold-thrust belt and regional tectonic and structural significance of the Ramgarh thrust [Ph.D. Dissertation thesis]: University of Arizona, 231 pages.

Pratt-Sitaula, B., Garde, M., Burbank, D.W., Oskin, M., Heimsath, A., and Gabet, E., 2007, Bedload-to-suspended load ratio and rapid bedrock incision from Himalayan landside-dam lake record: Quaternary Research, v. 68, p. 111-120.

Reneau, S. L., and W. E. Dietrich, 1987, Size and location of colluvial landslides in a steep forested landscape, in Erosion and Sedimentation in the Pacific Rim: edited by R. L. Beschta, T. Blinn, G. E. Grant, F. J. Swanson, and G. G. Ice, International Association Hydrological Sciences publications, v. 165, p. 39-49.

Roe, G.H., Montgomery, D.R., Hallet B., 2002, Effects of orographic precipitation variations on the concavity of steady-state river profiles: Geology, v. 30, no. 2, p.143-146.

Roe, G.H., Stolar, D.B., and Willet, S.D., 2006, Response of a steady-state critical wedge orogen to changes in climate and tectonic forcing: Geological Society of America Special Paper 398, Penrose Conference Series, p. 227-239.

Roberts, A., 2001, Curvature attributes and their application to 3D interpreted horizons: First Break, v. 19.2, p. 85-100.

Robinson, D. M., DeCelles, P. G., Garzione, C. N., Pearson, O. N., Harrison, T. M., and Catlos, E. J., 2003, Kinematic model for the Main Central thrust in Nepal: Geology, v. 31, no. 4, p. 359-362.

Robinson, D.M., 2006, Tectonic evolution of the Himalayan thrust belt in western Nepal: Implications for channel flow models: GSA Bulletin, v. 118, no. 7/8, p. 865-885 doi:10.1130/B25911.1.

Robinson, D.M., 2008, Forward modeling the kinematic sequence of the central Nepal Himalayan thrust belt, western Nepal: Geosphere, v. 4, no. 5, p. 785-801, doi:10.1130/GES00163.1.

Roering, J.J., Kirchner, J.W., and Dietrich, W.E., 2005, Characterizing structural and lithologic controls on deep-seared landsliding: Implications for topographic relief and landscape evolution in the Oregon Coast Range, USA, GSA Bulletin, v. 117, no. 5/6, p. 654-668.

Schoenbohm, L.M., Whipple, K.X., Burchfiel, B.C., and Chen, L., 2009, Geomorphic constraints on surface uplift, exhumation, and plateau growth in the Red River region, Yunnan Province, China: GSA Bulletin, v. 116, no. 7/8, p. 895-909, doi:10.1130/B25364.1.

Searle, M. P., and Godin, L., 2003, The South Tibetan detachment and the Manaslu Leucogranite: a structural reinterpretation and restoration of the Annapurna-Manaslu Himalaya, Nepal: Journal of Geology, v. 111, no. 5, p. 505-523.

Searle, M. P., Simpson, R. L., Law, R. D., Parrish, R. R., and Waters, D. J., 2003, The structural geometry, metamorphic and magmatic evolution of the Everest Massif, High Himalaya of Nepal-South Tibet: Journal of the Geological Society of London, v. 160, no. 3, p. 345-366.

Seeber, L., and Gornitz, V., 1983, River profiles along the Himalayan arc as indicators of active tectonics: Tectonophysics, v. 92, p. 335–367.

Selzer, C., Buiter, S.J.H., and Pfiffner, O.A., 2007, Sensitivity of shear zones in orogenic wedges to surface processes and strain softening: Tectonophysics, v. 473, p. 51-70.

Snyder, N., Whipple, K., Tucker, G., and Merritts, D., 2000, Landscape response to tectonic forcing: DEM analysis of stream profiles in the Mendocino triple junction region, northern California: Geological Society of America Bulletin, v. 112, p. 1250–1263.

Snyder, N.P., February 2009, Studying stream morphology with airborne laser elevation data: EOS, American Geophysical Union.

Stolar, D.B., Willett, S.D., and Roe, G.H., 2006, Climatic and tectonic forcing of a critical orogen: Geological Society of America Special Paper 398, Penrose Conference Series, p. 241-250.

Thiede, R.C., Bookhagen, B., Arrowsmith, J.R., Sobel, E.R., and Strecker, M.R., 2004, Climatic control on rapid exhumation along the southern Himalayan front: Earth and Planetary Science Letters, v. 222, p. 791–806, doi: 10.1016/j.epsl.2004.03.015.

Tucker, G.E., and Bras, R.L., 2000, A stochastic approach to modeling the role of rainfall variability in drainage basin evolution: Water Resources Research, v. 36, p. 1953–1964.

VanLaningham, S., Meigs, A., and Goldfinger, C., 2006, The effects of rock uplift and rock resistance on river morphology in a subduction zone forearc, Oregon, USA: Earth Surface Processes and Landforms, doi:10.1002/esp.1326.

Ware, J.M., 1998, A procedure for automatically correcting invalid flat triangles occurring in triangulated contour data: Computers & Geosciences, v. 24, No. 2, p. 141-150.

Weidinger, J.T., 2006, Predesign, failure and displacement mechanisms of large rockslides in the Annapurna Himalayas, Nepal: Engineering Geology v. 83, 201–216.

Whipple, K.X., and Tucker, G.E., 1999, Dynamics of stream-power river incision model: Implications for height limits of mountain ranges, landscape response timescales, and research needs: Journal of Geophysical Research, v. 104, no. B8, p. 17661-17674.

Whipple, K.X., Hancock, G.S., and Anderson, R.S., 2000, River incision into bedrock: Mechanics and relative efficacy of plucking, abrasion, and cavitation: GSA Bulletin, v. 112, no. 3, p.490-503.

Whipple, K.X., 2004, Bedrock rivers and the geomorphology of active orogens: Annual Reviews of Earth and Planetary Science Letters, v. 32, p. 151-85, doi:10.1146/annurev.earth.32.101802.120356.

Whipple, K.X., and Meade, B.J., 2004, Controls on the strength of coupling among climate, erosion, and deformation in two-sided, frictional orogenic wedges at steady state: Journal of Geophysical Research, v. 109, F01011, doi:10.1029/2003JF000019.

Whipple, K., Wobus, C., Crosby, B., Kirby, E., and Sheehan, D., 2007, New tools for quantitative geomorphology: Extraction and interpretation of stream profiles from digital topographic data. http://www.geomorphtools.org/Tools/StPro/Tutorials/StPro_UserGuidees_Final.pdf

Whittaker, A.C., Attal, M., Cowie, P.A., Tucker, G.E., and Roberts, G., 2008, Decoding temporal and spatial patterns of fault uplift using transient river long profiles: Geomorphology, v. 100, p.506-526.

Wilson, C. J., and W. E. Dietrich, 1987, The contribution of bedrock groundwater flow to storm runoff and high pore pressure development in hollows, in Erosion and Sedimentation in the Pacific Rim: edited by R. L. Beschta, T. Blinn, G. E. Grant, G. G. Ice, and F. J. Swanson, International Association Hydrological Sciences publications, v. 165, p. 49-60.

Wilson, J.P., and Gallant, J.C., 2000, Terrain Analysis: Principles and Applications, John Wiley & Sons, Inc., New York.

Wobus, C.W., Hodges, K.V., and Whipple, K.X., 2003, Has focused denudation sustained active thrusting at the Himalayan topographic front, Geology, v. 31, no. 10, p. 861-864.

Wobus, C., Heimsath, A., Whipple, K., and Hodges, K., 2005, Active out-of-sequence thrust faulting in the central Nepalese Himalaya, Nature, v. 434, p. 1008-1011.

Wobus, C.W., Whipple, K.X, Kirby, E., Snyder, N., Johnson, J., Spyropolou, K., Crosby, B., and Sheehan, D., 2006a, Tectonics and topography: Procedures, promise, and pitfalls, Geological Society of America Bulletin, Special Paper 398, p. 55-74.

Wobus, C.W., Whipple, K.X., and Hodges, K.V., 2006b, Neotectonics of central Nepalese Himalaya: Constraints from geomorphology, detrital 40Ar/39Ar thermochronology, and thermal modeling, Tectonics, v. 25, TC4011.

Worboys, M., and Duckham, M., 2004, GIS a computing perspective, second edition, CRC press, Washington, DC.

Zang, J., and Goodchild, M., 2002, Uncertainty in geographical information, Taylor & Francis Inc., ISBN 041527723X. 266 pages.

Zhang, W., and Montgomery, D. R., 1994, Digital Elevation Model Grid Size, Landscape Representation, and Hydrologic Simulations: Water Resources Research, v. 30, p. 1019-1028.

Zech, T., Zech, M., Kubik, P.W., Kharki, K., and Zech, W., 2009, Deglaciation and landscape history around Annapurna, Nepal, based on ^{10}Be surface exposure dating: Quaternary Science, v. 28, p. 1106-1118.